npg

Research Highlight

Nanodiamond delivery circumvents tumor resistance to doxorubicin

Xiao-wei MA, Yu-liang ZHAO, Xing-jie LIANG*

Intrinsic and acquired drug resistance is a common problem causing the recurring of malignant tumors, such as breast and liver cancers[1, 2]. Successful chemotherapy is often limited due to significant side effects and development of drug resistance[3]. With the rapid development of nanotechnology, overcoming drug resistance and improving the efficacy of antitumor drugs with scalable and biocompatible nanotherapies have been extensively explored.

Up to date many attempts have been made. Nanoparticles that stimulate the endocytosis of drug resistant cells to raise intracellular drug concentration have been proved an effective way to reverse the acquired resistance of cisplatin-resistant cells[4]. For the resistant tumor cells that pump drugs out through ATP-binding cassette (ABC) transporters, which is considered as a common mechanism for drug resistance[5], one of current approaches is to seek nanoparticle-mediated drug delivery system with prolonged retention time to prevent drug efflux and retain therapeutic concentration for maximized tumor inhibition.

Laboratory of Nanomedicine and Nanosafety, Division of Nanomedicine and Nanobiology, National Center for Nanoscience and Technology, China, and CAS Key Laboratory for Biomedical Effects of Nanomaterials and Nanosafety, Chinese Academy of Sciences, Beijing 100190, China
Correspondence: Xing-jie LIANG
(liangxj@nanoctr.cn)

Doxorubicin (Dox) has been established as one of the most useful chemotherapeutics with a broad spectrum of activity against human neoplasms. In Dox-resistant cells, the drug can be actively pumped out by ABC transporters[6]. Nanometer-sized diamonds (NDs) have been used for fluorescent cellular biolabeling[7], biomedical imaging[8], and as drug carriers[9]. Chow and colleagues recently developed a biocompatible nanodiamond drug carrier system at 2 to 8 nm in diameter with Dox binding to its surfaces electrostatically, forming NDX complexes with an average size of ~80 nm. The complexes not only reversed the drug efflux-based chemoresistance to Dox, but also avoided the toxic side effects to healthy tissues often occurred with unconjugated free Dox[10].

The authors used various Dox-resistant tumor cell lines to determine the ability of NDX in maintaining intracellular drug concentration. The cells retained more Dox when treated with NDX as compared to unmodified Dox treatment. While free Dox was intensively pumped out of these cells by ABC-transporters, sustained release of functional drugs from NDs counteracted the efflux of Dox from the tumor cells. Furthermore, the killing of tumor cells by NDs was not affected by the ABC transporter inhibitor verapamil, suggesting NDs delivery may be used as a nonspecific method for overcoming drug efflux. They also demonstrated *in vivo* that NDX treatment effectively

improved tumor inhibition rate, survival probability and increased apoptosis specifically in murine LT2-Myc liver and 4T1 mammary tumors without affecting adjacent normal tissues (Figure 1).

Effective chemotherapy requires maintaining chemotherapeutic agents at therapeutic concentration for a prolonged period, maximizing tumor inhibition and minimizing normal tissue toxicity[11, 12]. The reason for the advantages of NDX over free Dox is likely due to the gradual release of the drug from nanodiamonds, which allows for increased drug retention in blood circulation and tumor, and therefore maintained the Dox concentration below a toxic level to normal tissues. It prevents the "burst effect" — a majority of Dox released in a rapid and uncontrollable fashion, which creates unpredictable pharmacokinetics, and thereby making effective dose regimens difficult to predict and acute toxicity to normal organs/tissues[13].

Although high-dosage of chemotherapeutic administered as a single dose may exert some effect on tumor, it is also accompanied by significant toxicity. For a solid tumor with a long doubling time, prolonged exposure to an active drug at a minimally effective concentration can affect a greater number of tumor cells while minimizing toxicity to normal organs[11]. Chow and colleagues' work demonstrates that nanodiamond delivery systems may greatly increase the efficacy of traditional anticancer drugs by preventing drugs from being pumped
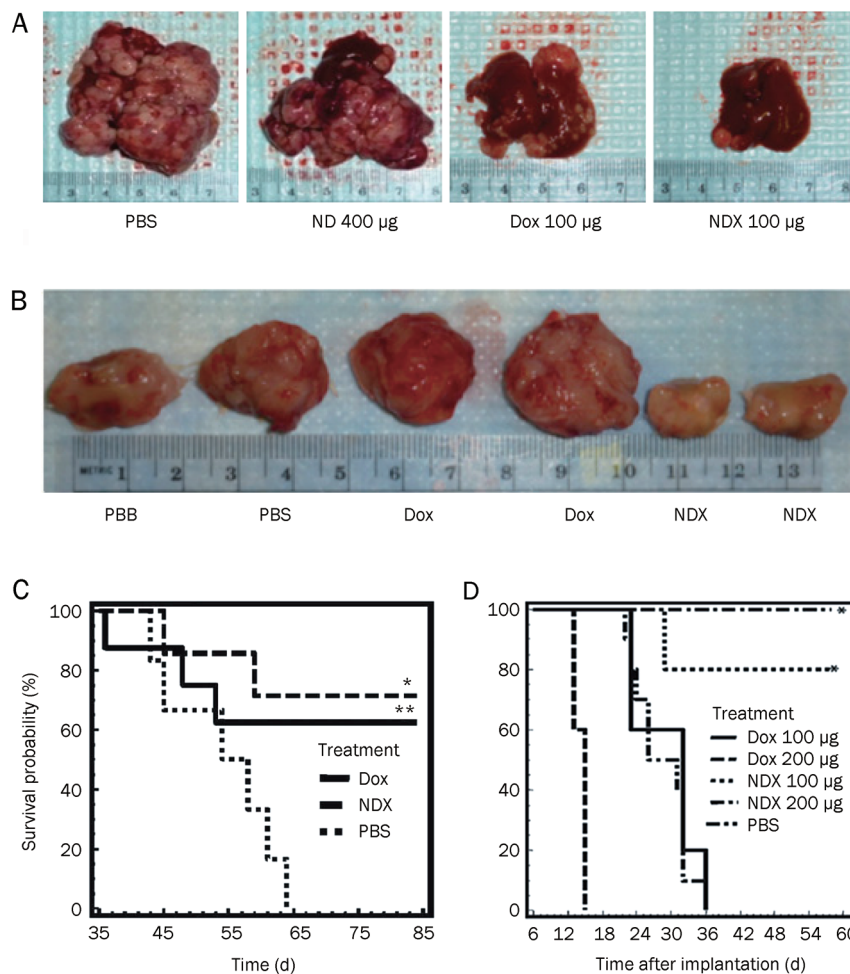
Figure 1. ND delivery of Dox inhibits tumor growth in murine liver tumor models and mammary carcinoma model[10]. (A) Images of livers/tumors from PBS, Dox, ND, or NDX treated LT2-Myc liver tumor bearing mice. (B) Representative images of excised tumors from PBS, Dox, or NDX treated 4T1 mammary tumor bearing mice. (C) Kaplan-Meier survival plot for LT2-Myc mice treated with PBS ($n=5$), Dox (100 mg) ($n=8$), or NDX (100 mg of Dox equivalent) ($n=7$) by tail vein injection every 7 d. *$P<0.03$; **$P<0.06$. (D) Kaplan-Meier survival plot for 4T1 mice treated with PBS ($n=7$), Dox (100 mg) ($n=10$), NDX (100 mg of Dox equivalent) ($n=10$), Dox (200 mg) ($n=5$), or NDX (200 mg of Dox equivalent) ($n=5$) by tail vein injection every 6 d. *$P<0.003$. Reprinted with permission from AAAS: Science Translational Medicine, copyright 2011.

siRNA, proteins and some other hydrophilic/hydrophobic drugs) through either covalent or noncovalent bonds. This implies that NDs have a great potential to be used for a wide range of drug delivery in treatment of a variety of diseases. Diamonds at nanoscale may entertain new expectation for treatment of malignant tumors in future.

out of tumor cells, allowing anticancer drugs to kill drug-resistant cells at a lower dosage, thus lowering the drug toxicity to normal organs and tissues. Compared to other nanoparticles, nanodiamond is small in diameter and can be cleared out of body within a certain period after administration. Meanwhile, no immune response or liver toxicity was observed with NDs even at high dosage, demonstrating its good biocompatibility. Moreover, surface modification with different functionalities would allow NDs binding with different types of therapeutics and biomolecules (such as imaging contrast agent, therapeutic

1 Giaccone G, Linn SC, Pinedo HM. Multidrug resistance in breast cancer: mechanisms, strategies. Eur J Cancer 1995; 31A: S15–7.
2 Chenivesse X, Franco D, Brechot C. MDR1 (multidrug resistance) gene expression in human primary liver cancer and cirrhosis. J Hepatol 1993; 18: 168–72.
3 Gillet JP, Gottesman MM. Mechanisms of multidrug resistance in cancer. Methods Mol Biol 2010; 596: 47–76.
4 Liang XJ, Meng H, Wang Y, He H, Meng J, Lu J, et al. Metallofullerene nanoparticles circumvent tumor resistance to cisplatin by reactivating endocytosis. Proc Natl Acad Sci U S A 2010; 107: 7449–54.
5 Krishna R, Mayer LD. Multidrug resistance (MDR) in cancer. Mechanisms, reversal using modulators of MDR and the role of MDR modulators in influencing the pharmacokinetics of anticancer drugs. Eur J Pharm Sci 2000; 11: 265–83.
6 Shen F, Chu S, Bence AK, Bailey B, Xue X, Erickson PA, et al. Quantitation of doxorubicin uptake, efflux, and modulation of multidrug resistance (MDR) in MDR human cancer cells. J Pharmacol Exp Ther 2008; 324: 95–102.
7 Mkandawire M, Pohl A, Gubarevich T, Lapina V, Appelhans D, Rodel G, et al. Selective targeting of green fluorescent nanodiamond conjugates to mitochondria in HeLa cells. J Biophotonics 2009; 2: 596–606.
8 Mochalin VN, Gogotsi Y. Wet chemistry route to hydrophobic blue fluorescent nanodiamond. J Am Chem Soc 2009; 131: 4594–5.
9 Huang H, Pierstorff E, Osawa E, Ho D. Active nanodiamond hydrogels for chemotherapeutic delivery. Nano Lett 2007; 7: 3305–14.
10 Chow EK, Zhang XQ, Chen M, Lam R, Robinson E, Huang H, et al. Nanodiamond therapeutic delivery agents mediate enhanced chemoresistant tumor treatment. Sci Transl Med 2011; 3: 73ra21.
11 Kamen BA, Rubin E, Aisner J, Glatstein E. High-time chemotherapy or high time for low dose. J Clin Oncol 2000; 18: 2935–7.
12 Wang YZ, Huang B, Lv J, Liang XJ. Current status of nanotechnology applied in biomedicine. Acta Biophys Sin 2009; 25: 168–4.
13 Lenzhofer R, Ganzinger U, Rameis H, Moser K. Acute cardiac toxicity in patients after doxorubicin treatment and the effect of combined tocopherol and nifedipine pretreatment. J Cancer Res Clin Oncol 1983; 106: 143–7.

npg

Review

Small molecule inhibitors of amyloid β peptide aggregation as a potential therapeutic strategy for Alzheimer's disease

Qin NIE[1, #], Xiao-guang DU[2, #], Mei-yu GENG[1, 2, *]

[1]Department of Pharmacology and Glycobiology, School of Medicine and Pharmacy, Ocean University of China, Qingdao 266003, China; [2]Division of Anti-tumor Pharmacology, State Key Laboratory of Drug Research, Shanghai Institute of Materia Medica, Chinese Academy of Sciences, Shanghai 201203, China

Amyloid β (Aβ) peptides have long been viewed as a potential target for Alzheimer's disease (AD). Aggregation of Aβ peptides in the brain tissue is believed to be an exclusively pathological process. Therefore, blocking the initial stages of Aβ peptide aggregation with small molecules could hold considerable promise as the starting point for the development of new therapies for AD. Recent rapid progresses in our understanding of toxic amyloid assembly provide a fresh impetus for this interesting approach. Here, we discuss the problems, challenges and new concepts in targeting Aβ peptides.

Keywords: Alzheimer's disease; amyloid β peptide; protein-protein interaction; small molecule

Introduction

More than 100 years have passed since Alzheimer's disease (AD) was first characterized. However, due to the lack of effective treatment, AD remains pandemic in the 21st century, imposing enormous social, and economic burdens on patients and their families[1]. Modern demographic trends compound the problem; our aging global population has led to a steep increase in the number of individuals with AD. In the United States alone, more than 13 million individuals are predicted to be afflicted with AD by the year 2050[2], leading to an overburden of scarce healthcare resources. Some studies estimate that the present availability of a treatment that can delay disease onset by 6.7 years would decrease the prevalence of AD 38% by 2050[3]. Such disease-modifying treatments would lower the annual cost of individual patient care by up to $24 000, thereby reducing the national cost of AD by trillions of dollars through the year 2050[4, 5].

Unfortunately, currently available treatments, *eg*, Aricept and Memantine, usually provide at best only temporary and incomplete symptomatic relief. The marginal benefits provided by current therapies emphasize the urgent need to develop effective disease-modifying AD treatments.

Amyloid β–targeting strategies

Disease-modifying strategies currently being pursued for AD mainly focus on two AD-related proteins, amyloid β (Aβ) and Tau. Of these, Aβ has attracted the most attention by far.

Substantial data derived from genetics, animal modeling, and biochemical studies support the idea that Aβ, the major component of senile plaques, plays a central role in AD pathophysiology[6, 7]. Paradoxically, Aβ peptides — the seeds of AD — are present at birth, and these neurotoxic peptides are continuously produced throughout life. Thus, the most direct target in anti-Aβ therapy is reduction of Aβ production, which has led naturally to a focus on β- and γ-secretase inhibitors[8–13]. However, despite considerable effort on this front, few novel chemical compounds based on this strategy have reached clinic trials. Safety issues are the overriding reason; because γ-secretase has many physiologically essential substrates, undesirable side effects are inevitable. One such substrate is the Notch signaling protein, which plays an intermediate and essential role in the differentiation and proliferation of many cell types. The consequences of γ-secretase inhibition include impaired lymphocyte differentiation and altered intestinal goblet cell structure[14–16]. Thus, although the use of small-molecule γ-secretase modulators is receiving increasing attention as a promising therapeutic approach[17], many com-

panies have abandoned γ-secretase as a potential target.

In theory, inhibiting β-secretase should not carry the same risk of toxicity as γ-secretase inhibition. However, designing β-secretase inhibitors has been challenging. The β-secretase protein contains a large catalytic pocket; thus, the β-secretase inhibitors that have been developed to date are too large to penetrate the blood-brain barrier[18-20]. There may also be conceptual drawbacks to targeting β-secretase. The development of Aβ secretase inhibitors is based on the hypothesis that Aβ deposition in the brain is due to overproduction or poor clearance of Aβ. However, this is likely only true for cases of familial AD caused by genetic mutation. Non-genetic AD cases, which represent the majority of AD patients, do not carry mutations and do not necessarily have overproduction of amyloid precursor protein (APP)[21]. More importantly, a deeper understanding of Aβ has revealed that Aβ isoforms also serve as endogenous positive regulators of release probability at hippocampal synapses, with some studies suggesting that monomeric Aβ is beneficial for neurons[22, 23]. Thus, because Aβ production may be important for physiological health, inhibiting Aβ generation may not necessarily be a sound strategy. An alternative tactic is to focus on Aβ clearance. One approach is to enhance the peripheral Aβ "sink action" by sequestering plasma Aβ, for example using Aβ immunotherapy. The AN1792 Aβ vaccine was designed for this purpose; however, it failed in Phase II clinical trials due to the development of meningoencephalitis[24]. Nevertheless, it might be possible to circumvent such complications by targeting the proteolytic machinery in the brain. However, from a therapeutic point of view, it remains to be seen whether any of the relevant proteases will serve as a viable AD drug target[25].

Aβ can aggregate into fibrils and oligomers (Figure 1). It was originally believed that only the large fibrils constituting mature neuritic amyloid plaques are toxic. However, in recent years research focus has shifted towards Aβ oligomers. Currently, Aβ peptide aggregation into toxic, prefibrillar oligomers is considered the key pathogenic event in the onset of AD[26, 27]. Consistent with this view, Aβ oligomers can: i) directly induce synaptic dysfunction and neuronal death, both which are responsible for AD initiation and progression[28–30]; and ii) trigger events such as oxidative damage and inflammation, which contribute to the progression of AD[31–33]. Although generation of Aβ monomers is, in and of itself, a physiologically relevant event, their aggregation into oligomers and
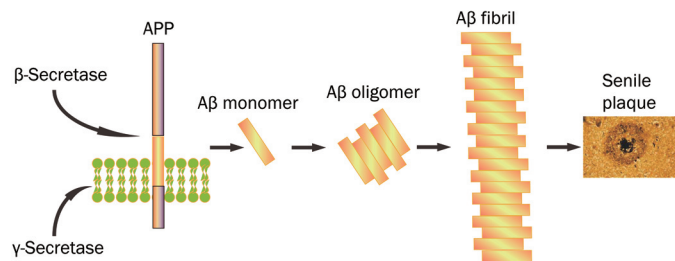
fibrils is pathogenic. Thus, blocking aggregation (while sparing Aβ generation) should not lead to mechanism-based toxicity. Hence, the strategy of inhibiting aggregation of Aβ, more specifically the Aβ42 isoform, has emerged as a valid disease-modifying therapy for AD[34].

Problems associated with inhibiting Aβ aggregation

Tremendous effort has been expended in recent years on developing small molecules that are capable of inhibiting Aβ aggregation. However, to date, no compounds have entered into clinical use. This is because the inhibition of Aβ aggregation requires blocking interactions between Aβ monomers, and historically, protein–protein interaction interfaces are particularly difficult drug targets. Thus, inhibiting Aβ aggregation has been deemed intractable[35, 36]. The challenges associated with targeting Aβ aggregation are substantial, with the most obvious obstacle being the sheer size and geometry of the protein interaction surface. First, the regions of protein–protein interactions are approximately 1500–3000 $Å^2$ [37–40], whereas protein–small molecule interaction regions are only about 300–1000 $Å^2$ [41, 42]. Thus, small molecules are often unable to produce sufficient steric hindrance to inhibit Aβ aggregation[43]. Second, the regions of protein–protein interactions are often relatively featureless, devoid of grooves or pockets into which a small molecule could dock in an energetically favorable manner[43–47]. The binding energy that drives protein–protein contacts is typically distributed over a large area that lacks a defined "hotspot" for pharmacological intervention[48]. Third, the highly plastic nature of protein surfaces can accommodate small molecules, thereby thwarting inhibition[48]. Together, these problems place severe restrictions on the development of Aβ aggregation inhibitors.

Designing solutions to these problems

To tackle these challenges, researchers have envisioned a Trojan horse strategy in which a small bifunctional molecule gains access to the relevant biological compartment, binds tightly to a chaperone, and thereby provides the necessary steric bulk to disrupt protein–protein interactions[48]. A second approach is to directly target the important chaperones, such as metals, in the brain. A growing body of evidence suggests that the presence of excess zinc, iron, copper and/or aluminum within senile plaques exacerbates Aβ-mediated oxidative damage and acts as a catalyst for Aβ aggregation in AD[49]. Thus, chelation therapies aimed at disrupting aberrant interactions between Aβ and metals have attracted considerable attention; one such example is PBT2, which is currently in Phase IIa clinical trials[50]. Unfortunately, to date, no new compounds employing this strategy have entered into clinical use.

The discovery that Aβ fibril formation is controlled by specific amino acids within the Aβ peptide itself has given renewed life to the idea that small molecules might occlude Aβ aggregation. Studies have demonstrated that various Aβ peptide regions contribute differently to Aβ aggregation and have identified important interactions among specific peptide regions that control this process[51]. For instance, the N-termi-

Figure 1. The plaque formation.

nus[52, 53], hydrophobic core[54, 55], hinge or turn regions[51, 56, 57] and C-terminus[58, 59] of Aβ41-42 are all crucial for the peptide's ability to aggregate and promote neurotoxicity.

The importance of the His13–Lys16 (HHQK) region in oligomerization, fibril propagation and neurotoxicity is well known[60–62]. This four-residue region is also an essential component of the heparin-binding site for glycosaminoglycans (GAGs), which assist the HHQK motif in effecting a change in the Aβ secondary structure from a soluble, unordered α-helix to a stable β-sheet–rich conformation. These β-sheet–rich structures, in turn, have an affinity for associating with other monomers to form oligomers, protofibrils and fibrils that aggregate into plaques[60]. The β-hairpin structure serves to nucleate the folding of Aβ monomers, which is the rate-limiting step in fibril formation[56, 57, 63]. The formation of hinge or turn regions brings together two hydrophobic segments in space and produces the β-strand structure. In this region, Lys28 forms a salt bridge with Asp23/Glu22, which further stabilizes the structure[63–65]. Electrostatic and hydrophobic interactions between these non-native side chains bring the peptides together, allowing native backbone−backbone interactions to initiate the assembly of β-sheets, albeit in non-native β-sheet registries[64]. The hydrophobic segments are the main core of Aβ aggregates, and hydrophobic interactions are an important driving force in Aβ aggregate formation[66, 67]. Based on these observations, a β-sheet breaker was first investigated as a potential inhibitor of Aβ aggregation[68]. A substantial body of evidence suggests that the C-terminus of Aβ42 plays a key role in controlling oligomerization; indeed, several studies of prefibrillar Aβ have suggested that the C-terminus of Aβ42 is more rigid than the C-terminus of the more abundant but less toxic Aβ40[69–71]. This increased rigidity has been attributed to interactions involving C-terminal residues Ile41 and Ala42, which stabilize a putative turn conformation[71]. Although these subregions contribute differently to structure formation, each is important for Aβ aggregation.

By targeting these subregions for binding, a small molecule will be more likely to directly occlude Aβ aggregation. In fact, most inhibitors that have entered clinical trials target these specific subregions within the Aβ sequence (Figure 2). Tramiprosate (3-aminopropanesulfonic acid), a mimic of GAGs, targets the HHQK subregion at the N-terminus. Although the structural simplicity of tramiprosate makes it highly specific to Aβ, it ultimately failed in the late stages of a Phase III clinical trial[72]. Despite this setback, the data obtained provided evidence that inhibitors targeting specific Aβ subregions represent a viable approach for AD treatment[73]. The agents targeting C-terminus feature one scaffold, the cyclohexanehexol stereoisomers. Among these, scyllo-inositol, which interferes with Aβ fibril assembly by competing with endogenous phosphatidylinositol for binding to Aβ41-42[59], has shown promise in current Phase II trials. The hydrophobic central region is yet another promising target for Aβ fibrillation inhibitors, which include RS-0406[74].

The quest for small molecules that target Aβ

As the strategy of inhibiting Aβ aggregation has increasingly gained acceptance, greater numbers of inhibitors have been developed and the structure-activity relationships of potent inhibitors have been systematically explored[75]. These studies revealed that typical Aβ aggregation inhibitors such as Congo red (CR), chrysamine G (CG) and curcumin share a similar chemical scaffold. These molecules contain two aromatic groups or inositol groups (with a suitable substituted
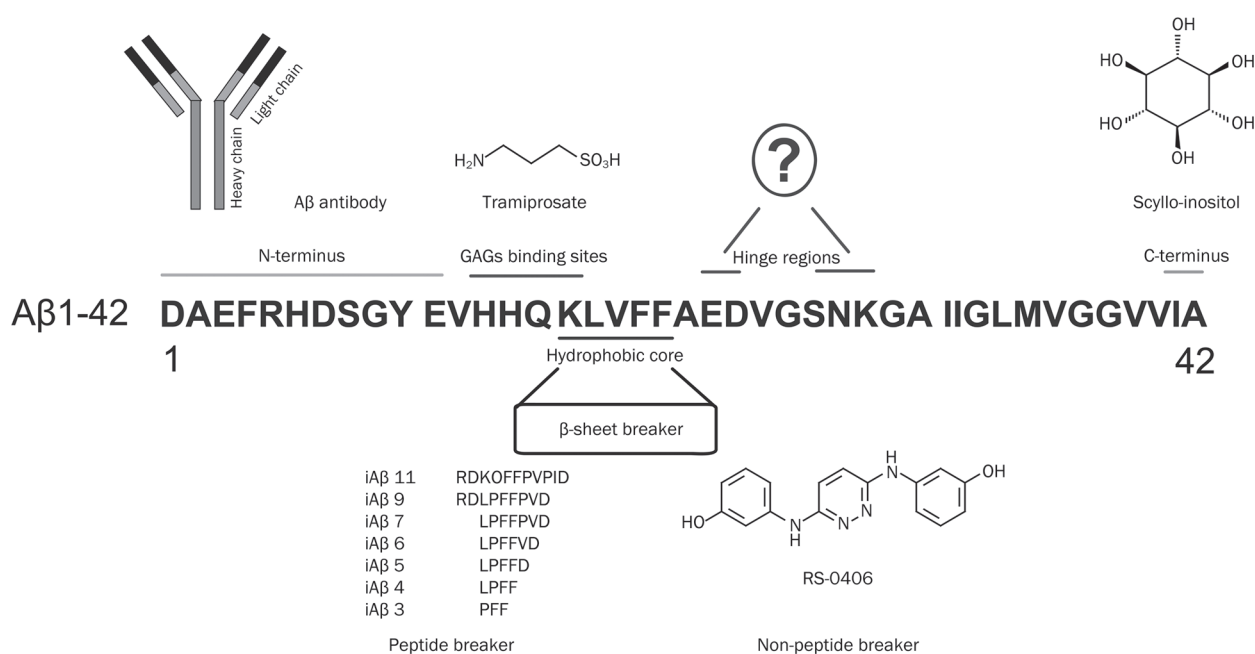

Figure 2. The subregion-targets in Aβ.

group) separated by a backbone of the appropriate length[75]. We speculate that the two terminal groups interact with Aβ protein residues to provide the binding affinity, whereas the linker facilitates binding of inhibitors to specific subregions. Determining which subregion the inhibitors target will be key to future research efforts. A molecule that targets a specific subregion should satisfy the following design criteria: (1) it should contain terminal groups suitable for interacting with residues in, or adjacent to, the subregion; and (2) the linker should be of an appropriate length to join the two terminal groups, span the subregion, and provide sufficient steric hindrance. Molecules designed according to these specifications would therefore be capable of inhibiting Aβ aggregation by binding to a specific subregion.

The handful of inhibitors that have been developed to date do not possess this chemical scaffold. Scyllo-inositol contains only one terminal group and can therefore target only a very small region. Fortunately, scyllo-inositol targets the C-terminus, which is important for Aβ aggregation. However, the presence of a single terminal group restricts the area of the targeted subregion to the C-terminus, and the lack of a linker prevents scyllo-inositol from modulating other targeted subregions. Additionally, a single terminal group results in a weaker binding avidity. In the case of tramiprosate, its simple structure provides specificity for Aβ, yet, for unknown reasons it failed in Phase III clinical trials[72]. Thus, although these atypical molecules possess inhibitory activity, they are severely limited by their weak binding affinity and small occupied region.

To our knowledge, most inhibitors target only one subregion. In fact, if inhibitors could target multiple specific subregions in concert, they might act synergistically to effectively inhibit Aβ aggregation. Thus, in our view, the ideal Aβ-targeting inhibitor should be of appropriate length and suitable flexibility, and should contain multiple groups that interact with Aβ residues. These multiple groups would both convey tighter binding avidity and permit targeting of multiple subregions. In addition, having sufficient length and flexibility would enable the inhibitor to capture the entire Aβ peptide and accommodate conformational changes in the target. Unfortunately, our current lack of the Aβ peptide's detailed molecular structure precludes designing such inhibitors. The successful creation of these new inhibitors will require gaining a better understanding of the modules necessary for activity as well as the key elements in the amyloid surface required for aggregation and toxicity. Alternatively, it might also be possible to employ a combination of multiple molecules.

Future perspectives

Compounds such as peptide-based inhibitors, antibodies and small molecules that target specific Aβ subregions represent the first generation of amyloid-based therapeutics with the potential to demonstrate disease-modifying activity. Although the results of ongoing clinical trials are inconclusive, these compounds hold the promise of a new day in the development of disease-modifying therapies for AD; some Aβ aggregation

inhibitors are listed in Table 1. As we gain additional insights into amyloid biology and AD itself, this will likely guide the development of the next generation of inhibitors.
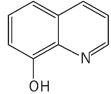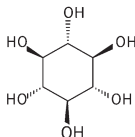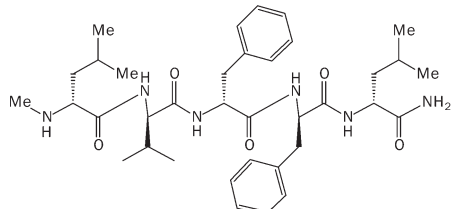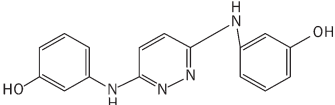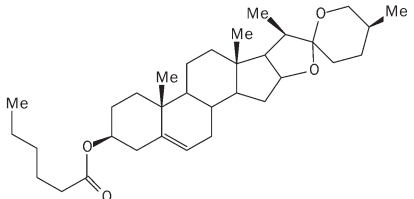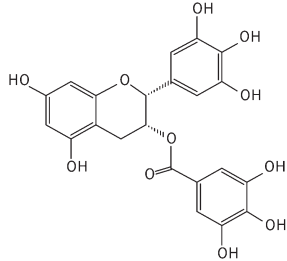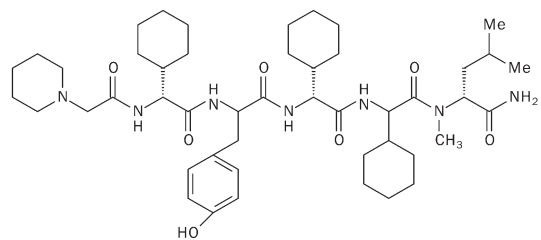
References

1 Wimo A, Winblad B, Jonsson L. The worldwide societal costs of dementia: Estimates for 2009. Alzheimers Dement 2010; 6: 98–103.

2 Hebert LE, Scherr PA, Bienias JL, Bennett DA, Evans DA. Alzheimer disease in the US population: prevalence estimates using the 2000 census. Arch Neurol 2003; 60: 1119–22.

3 Sloane PD, Zimmerman S, Suchindran C, Reed P, Wang L, Boustani M, *et al*. The public health impact of Alzheimer's disease, 2000–2050: potential implication of treatment advances. Annu Rev Public Health 2002; 23: 213–31.

4 Zhu CW, Torgan R, Scarmeas N, Albert M, Brandt J, Blacker D, *et al*. Home health and informal care utilization and costs over time in Alzheimer's disease. Home Health Care Serv Q 2008; 27: 1–20.

5 Leon J, Cheng CK, Neumann PJ. Alzheimer's disease care: costs and potential savings. Health Aff (Millwood) 1998; 17: 206–16.

6 Cras P, Kawai M, Lowery D, Gonzalez-DeWhitt P, Greenberg B, Perry G. Senile plaque neurites in Alzheimer disease accumulate amyloid precursor protein. Proc Natl Acad Sci U S A 1991; 88: 7552–6.

7 Blanquet V, Goldgaber D, Turleau C, Creau-Goldberg N, Delabar J, Sinet PM, *et al*. The beta amyloid protein (AD-AP) cDNA hybridizes in normal and Alzheimer individuals near the interface of 21q21 and q22.1. Ann Genet 1987; 30: 68–9.

8 Vassar R, Bennett BD, Babu-Khan S, Kahn S, Mendiaz EA, Denis P, *et al*. Beta-secretase cleavage of Alzheimer's amyloid precursor protein by the transmembrane aspartic protease BACE. Science 1999; 286: 735–41.

9 Vassar R, Citron M. Abeta-generating enzymes: recent advances in beta- and gamma-secretase research. Neuron 2000; 27: 419–22.

10 Gao Y, Pimplikar SW. The gamma-secretase-cleaved C-terminal fragment of amyloid precursor protein mediates signaling to the nucleus. Proc Natl Acad Sci U S A 2001; 98: 14979–84.

11 Kitazume S, Tachida Y, Oka R, Shirotani K, Saido TC, Hashimoto Y. Alzheimer's beta-secretase, beta-site amyloid precursor protein-cleaving enzyme, is responsible for cleavage secretion of a Golgi-resident sialyltransferase. Proc Natl Acad Sci U S A 2001; 98: 13554–9.

12 Luo Y, Bolon B, Kahn S, Bennett BD, Babu-Khan S, Denis P, *et al*. Mice deficient in BACE1, the Alzheimer's beta-secretase, have normal phenotype and abolished beta-amyloid generation. Nat Neurosci 2001; 4: 231–2.

13 Yang LB, Lindholm K, Yan R, Citron M, Xia W, Yang XL, *et al*. Elevated beta-secretase expression and enzymatic activity detected in sporadic Alzheimer disease. Nat Med 2003; 9: 3–4.

14 van Es JH, van Gijn ME, Riccio O, van den Born M, Vooijs M, Begthel H, *et al*. Notch/gamma-secretase inhibition turns proliferative cells in intestinal crypts and adenomas into goblet cells. Nature 2005; 435: 959–63.

15 Tarassishin L, Yin YI, Bassit B, Li YM. Processing of Notch and amyloid precursor protein by gamma-secretase is spatially distinct. Proc Natl Acad Sci U S A 2004; 101: 17050–5.

16 Leissring MA, Murphy MP, Mead TR, Akbari Y, Sugarman MC,

Table 1. Some chemical inhibitors of amyloid beta aggregation.

Chemical compound	Structure	Current trial state
Bapineuzumab	Monoclonal antibody	Phase III
Tramiprosate	H_2N—SO_3H	Failed in phase III
PTB2		Phase IIa
Scyllo-inositol		Phase II
PPI1019		Completed phase II
RS0406		Phase II
SP-233		Phase I
EGCG		Phase II
Exebryl-1	No structural details are available	Phase I
SEN606		Preclinical

Jannatipour M, *et al*. A physiologic signaling role for the gamma-secretase-derived intracellular fragment of APP. Proc Natl Acad Sci U S A 2002; 99: 4697–702.

17 Tomita T. At the frontline of Alzheimer's disease treatment: gamma-secretase inhibitor/modulator mechanism. Naunyn Schmiedebergs Arch Pharmacol 2008; 377: 295–300.

18 Citron M. Strategies for disease modification in Alzheimer's disease. Nat Rev Neurosci 2004; 5: 677–85.

19 Opar A. Mixed results for disease-modification strategies for Alzheimer's disease. Nat Rev Drug Discov 2008; 7: 717–8.

20 Citron M. Alzheimer's disease: strategies for disease modification. Nat Rev Drug Discov 2010; 9: 387–98.

21 Nishitomi K, Sakaguchi G, Horikoshi Y, Gray AJ, Maeda M, Hirata-Fukae C, et al. BACE1 inhibition reduces endogenous Abeta and alters APP processing in wild-type mice. J Neurochem 2006; 99: 1555–63.

22 Giuffrida ML, Caraci F, Pignataro B, Cataldo S, De Bona P, Bruno V, et al. Beta-amyloid monomers are neuroprotective. J Neurosci 2009; 29: 10582–7.

23 Abramov E, Dolev I, Fogel H, Ciccotosto GD, Ruff E, Slutsky I. Amyloid-beta as a positive endogenous regulator of release probability at hippocampal synapses. Nat Neurosci 2009; 12: 1567–76.

24 Lemere CA, Masliah E. Can Alzheimer disease be prevented by amyloid-beta immunotherapy? Nat Rev Neurol 2010; 6: 108–19.

25 De Strooper B. Proteases and proteolysis in Alzheimer disease: a multifactorial view on the disease process. Physiol Rev 2010; 90: 465–94.

26 Resende R, Ferreiro E, Pereira C, Resende de Oliveira C. Neurotoxic effect of oligomeric and fibrillar species of amyloid-beta peptide 1-42: involvement of endoplasmic reticulum calcium release in oligomer-induced cell death. Neuroscience 2008; 155: 725–37.

27 Walsh DM, Selkoe DJ. Deciphering the molecular basis of memory failure in Alzheimer's disease. Neuron 2004; 44: 181–93.

28 Reddy PH, Beal MF. Amyloid beta, mitochondrial dysfunction and synaptic damage: implications for cognitive decline in aging and Alzheimer's disease. Trends Mol Med 2008; 14: 45–53.

29 Hu NW, Smith IM, Walsh DM, Rowan MJ. Soluble amyloid-beta peptides potently disrupt hippocampal synaptic plasticity in the absence of cerebrovascular dysfunction in vivo. Brain 2008; 131: 2414–24.

30 Rowan MJ, Klyubin I, Wang Q, Hu NW, Anwyl R. Synaptic memory mechanisms: Alzheimer's disease amyloid beta-peptide-induced dysfunction. Biochem Soc Trans 2007; 35: 1219–23.

31 Salminen A, Ojala J, Kauppinen A, Kaarniranta K, Suuronen T. Inflammation in Alzheimer's disease: amyloid-beta oligomers trigger innate immunity defence via pattern recognition receptors. Prog Neurobiol 2009; 87: 181–94.

32 Ruan L, Kang Z, Pei G, Le Y. Amyloid deposition and inflammation in APPswe/PS1dE9 mouse model of Alzheimer's disease. Curr Alzheimer Res 2009; 6: 531–40.

33 Ali-Khan Z, Sipe JD, Du T, Riml H. Echinococcus multilocularis: relationship between persistent inflammation, serum amyloid A protein response and amyloidosis in four mouse strains. Exp Parasitol 1988; 67: 334–45.

34 Estrada LD, Soto C. Disrupting beta-amyloid aggregation for Alzheimer disease treatment. Curr Top Med Chem 2007; 7: 115–26.

35 Whitty A, Kumaravel G. Between a rock and a hard place? Nat Chem Biol 2006; 2: 112–8.

36 Hajduk PJ, Burns DJ. Integration of NMR and high-throughput screening. Comb Chem High Throughput Screen 2002; 5: 613–21.

37 Lo Conte L, Chothia C, Janin J. The atomic structure of protein-protein recognition sites. J Mol Biol 1999; 285: 2177–98.

38 Jones S, Thornton JM. Principles of protein-protein interactions. Proc Natl Acad Sci U S A 1996; 93: 13–20.

39 Teichmann SA. Principles of protein-protein interactions. Bioinformatics 2002; 18: S249.

40 Keskin O, Gursoy A, Ma B, Nussinov R. Principles of protein-protein interactions: what are the preferred ways for proteins to interact? Chem

Rev 2008; 108: 1225–44.

41 Smith RD, Hu L, Falkner JA, Benson ML, Nerothin JP, Carlson HA. Exploring protein-ligand recognition with Binding MOAD. J Mol Graph Model 2006; 24: 414–25.

42 Cheng AC, Coleman RG, Smyth KT, Cao Q, Soulard P, Caffrey DR, et al. Structure-based maximal affinity model predicts small-molecule druggability. Nat Biotechnol 2007; 25: 71–5.

43 Wells JA, McClendon CL. Reaching for high-hanging fruit in drug discovery at protein-protein interfaces. Nature 2007; 450: 1001–9.

44 Arkin MR, Wells JA. Small-molecule inhibitors of protein-protein interactions: progressing towards the dream. Nat Rev Drug Discov 2004; 3: 301–17.

45 Plewczynski D, Rychlewski L. Meta-basic estimates the size of druggable human genome. J Mol Model 2009; 15: 695–9.

46 Hambly K, Danzer J, Muskal S, Debe DA. Interrogating the druggable genome with structural informatics. Mol Divers 2006; 10: 273–81.

47 Hopkins AL, Groom CR. The druggable genome. Nat Rev Drug Discov 2002; 1: 727–30.

48 Gestwicki JE, Crabtree GR, Graef IA. Harnessing chaperones to generate small-molecule inhibitors of amyloid beta aggregation. Science 2004; 306: 865–9.

49 Dong J, Canfield JM, Mehta AK, Shokes JE, Tian B, Childers WS, et al. Engineering metal ion coordination to regulate amyloid fibril assembly and toxicity. Proc Natl Acad Sci U S A 2007; 104: 13313–8.

50 Adlard PA, Cherny RA, Finkelstein DI, Gautier E, Robb E, Cortes M, et al. Rapid restoration of cognition in Alzheimer's transgenic mice with 8-hydroxy quinoline analogs is associated with decreased interstitial Abeta. Neuron 2008; 59: 43–55.

51 Maji SK, Ogorzalek Loo RR, Inayathullah M, Spring SM, Vollers SS, Condron MM, et al. Amino acid position-specific contributions to amyloid beta-protein oligomerization. J Biol Chem 2009; 284: 23580–91.

52 Gardberg AS, Dice LT, Ou S, Rich RL, Helmbrecht E, Ko J, et al. Molecular basis for passive immunotherapy of Alzheimer's disease. Proc Natl Acad Sci U S A 2007; 104: 15659–64.

53 McLaurin J, Cecal R, Kierstead ME, Tian X, Phinney AL, Manea M, et al. Therapeutically effective antibodies against amyloid-beta peptide target amyloid-beta residues 4-10 and inhibit cytotoxicity and fibrillogenesis. Nat Med 2002; 8: 1263–9.

54 Wasmer C, Lange A, Van Melckebeke H, Siemer AB, Riek R, Meier BH. Amyloid fibrils of the HET-s (218–289) prion form a beta solenoid with a triangular hydrophobic core. Science 2008; 319: 1523–6.

55 Permanne B, Adessi C, Saborio GP, Fraga S, Frossard MJ, Van Dorpe J, et al. Reduction of amyloid load and cerebral damage in a transgenic mouse model of Alzheimer's disease by treatment with a beta-sheet breaker peptide. FASEB J 2002; 16: 860–2.

56 Hoyer W, Gronwall C, Jonsson A, Stahl S, Hard T. Stabilization of a beta-hairpin in monomeric Alzheimer's amyloid-beta peptide inhibits amyloid formation. Proc Natl Acad Sci U S A 2008; 105: 5099–104.

57 Fawzi NL, Phillips AH, Ruscio JZ, Doucleff M, Wemmer DE, Head-Gordon T. Structure and dynamics of the Abeta (21–30) peptide from the interplay of NMR experiments and molecular simulations. J Am Chem Soc 2008; 130: 6145–58.

58 Fradinger EA, Monien BH, Urbanc B, Lomakin A, Tan M, Li H, et al. C-terminal peptides coassemble into Abeta42 oligomers and protect neurons against Abeta42-induced neurotoxicity. Proc Natl Acad Sci U S A 2008; 105: 14175–80.

59 McLaurin J, Kierstead ME, Brown ME, Hawkes CA, Lambermon MH, Phinney AL, et al. Cyclohexanehexol inhibitors of Abeta aggregation prevent and reverse Alzheimer phenotype in a mouse model. Nat Med 2006; 12: 801–8.

60 Bartolini M, Bertucci C, Bolognesi ML, Cavalli A, Melchiorre C, An-

drisano V. Insight into the kinetic of amyloid beta (1–42) peptide self-aggregation: elucidation of inhibitors' mechanism of action. Chem-biochem 2007; 8: 2152–61.

61 Williamson MP, Suzuki Y, Bourne NT, Asakura T. Binding of amyloid beta-peptide to ganglioside micelles is dependent on histidine-13. Biochem J 2006; 397: 483–90.

62 Watson DJ, Lander AD, Selkoe DJ. Heparin-binding properties of the amyloidogenic peptides Abeta and amylin. Dependence on aggregation state and inhibition by Congo red. J Biol Chem 1997; 272: 31617–24.

63 Melquiond A, Dong X, Mousseau N, Derreumaux P. Role of the region 23–28 in Abeta fibril formation: insights from simulations of the monomers and dimers of Alzheimer's peptides Abeta40 and Abeta42. Curr Alzheimer Res 2008; 5: 244–50.

64 Buchete NV, Hummer G. Structure and dynamics of parallel beta-sheets, hydrophobic core, and loops in Alzheimer's A beta fibrils. Biophys J 2007; 92: 3032-9.

65 Sciarretta KL, Gordon DJ, Petkova AT, Tycko R, Meredith SC. Abeta40-Lactam (D23/K28) models a conformation highly favorable for nucleation of amyloid. Biochemistry 2005; 44: 6003–14.

66 Lu X, Wintrode PL, Surewicz WK. Beta-sheet core of human prion protein amyloid fibrils as determined by hydrogen/deuterium exchange. Proc Natl Acad Sci U S A 2007; 104: 1510–5.

67 Chimon S, Shaibat MA, Jones CR, Calero DC, Aizezi B, Ishii Y. Evidence of fibril-like beta-sheet structures in a neurotoxic amyloid intermediate of Alzheimer's beta-amyloid. Nat Struct Mol Biol 2007; 14: 1157-64.

68 Soto C, Sigurdsson EM, Morelli L, Kumar RA, Castano EM, Frangione B. Beta-sheet breaker peptides inhibit fibrillogenesis in a rat brain model of amyloidosis: implications for Alzheimer's therapy. Nat Med 1998; 4: 822–6.

69 Murakami K, Irie K, Ohigashi H, Hara H, Nagao M, Shimizu T, *et al*. Formation and stabilization model of the 42-mer Abeta radical: implications for the long-lasting oxidative stress in Alzheimer's disease. J Am Chem Soc 2005; 127: 15168–74.

70 Lazo ND, Grant MA, Condron MC, Rigby AC, Teplow DB. On the nucleation of amyloid beta-protein monomer folding. Protein Sci 2005; 14: 1581–96.

71 Urbanc B, Cruz L, Yun S, Buldyrev SV, Bitan G, Teplow DB, *et al*. In silico study of amyloid beta-protein folding and oligomerization. Proc Natl Acad Sci U S A 2004; 101: 17345–50.

72 Rauk A. Why is the amyloid beta peptide of Alzheimer's disease neurotoxic? Dalton Trans 2008; 10: 1273–82.

73 Blazer LL, Neubig RR. Small molecule protein-protein interaction inhibitors as CNS therapeutic agents: current progress and future hurdles. Neuropsychopharmacology 2009; 34: 126–41.

74 Nakagami Y, Nishimura S, Murasugi T, Kaneko I, Meguro M, Marumoto S, *et al*. A novel beta-sheet breaker, RS-0406, reverses amyloid beta-induced cytotoxicity and impairment of long-term potentiation *in vitro*. Br J Pharmacol 2002; 137: 676–82.

75 Reinke AA, Gestwicki JE. Structure-activity relationships of amyloid beta-aggregation inhibitors based on curcumin: influence of linker length and flexibility. Chem Biol Drug Des 2007; 70: 206–15.

Review

Epithelial cell polarity and tumorigenesis: new perspectives for cancer detection and treatment

Danila CORADINI[1,*], Claudia CASARSA[2], Saro ORIANA[3]

[1]Biostatistics for Bioinformatics and Clinical Translational Research, Institute of Medical Statistics and Biometry, University of Milano, 20133 Milano, Italy; [2]Life Sciences Department, University of Trieste, 34127 Trieste, Italy; [3]Senology Center, Casa di Cura Ambrosiana, Sacra Famiglia, 20090 Cesano Boscone, Milano, Italy

Loss of cell-cell adhesion and cell polarity is commonly observed in tumors of epithelial origin and correlates with their invasion into adjacent tissues and formation of metastases. Growing evidence indicates that loss of cell polarity and cell-cell adhesion may also be important in early stage of cancer. In first part of this review, we delineate the current understanding of the mechanisms that establish and maintain the polarity of epithelial tissues and discuss the involvement of cell polarity and apical junctional complex components in tumor pathogenesis. In the second part we address the clinical significance of cell polarity and junctional complex components in cancer diagnosis and prognosis. Finally, we explore their potential use as therapeutic targets in the treatment of cancer.

Keywords: cell polarity; epithelial tumors; differential diagnosis

Introduction

In humans, more than 80% of all tumors are carcinomas and originate from epithelial tissues[1]. A characteristic hallmark for almost carcinomas is the loss of epithelial morphology and the acquisition of a mesenchymal-like phenotype, through a process called epithelial-to-mesenchymal transition (EMT)[2, 3]. Activated during embryogenesis and adult tissue remodelling[4, 5], EMT is a complex molecular program by which epithelial cells shed their differentiated characteristics and acquire mesenchymal features, including motility, invasiveness and a heightened resistance to apoptosis[6, 7].

A strong correlation between malignancy and loss of epithelial organization has been histologically documented for almost types of tumor deriving from epithelial cells[8–10], and disruption of cell-cell adhesion *per se* has been found to promote the development of some cancers[11, 12]. Thus, understanding the molecular mechanisms that regulate tissue organization and how such mechanisms are disrupted during neoplastic transformation, could provide important and useful insights to be exploited for diagnostic and therapeutic purposes.

* To whom correspondence should be addressed.
E-mail danila.coradini@yahoo.it

Epithelial cells and the apical junctional complex

Generally located at the interface between the organism and the outside world or at the free surface of tubes or cavities as in the case of digestive, respiratory, urinary and reproductive tract, epithelial cells are organized in mono- or multi-layered sheets in which any single cell is strictly in contact with neighboring cells by specific cell-cell adhesion structures. To allow a correct sheet alignment, each epithelial cell presents a well-defined orientation with an apical pole directly in contact with the luminal space and a basal pole in contact with basement membrane (Figure 1A). In contrast, mesenchymal cells display a fusiform or spindle-like morphology, do not form organized cell layers, are not polarized, contact the neighboring cells only focally, are not associated with the basement membrane and tend to be highly mobile (Figure 1B).

The characteristic polarization of epithelial cells is obtained by an asymmetric distribution of cellular components along the internal apicobasal axis. This property, known as apicobasolateral polarity, is part of a crucial differentiation process, termed epithelial polarity program that governs the spatial asymmetry required for a correct epithelial cell morphology and tissue homeostasis[13]. Schematically, the epithelial polarity program utilizes three cellular machineries dynamically interplaying: the polarized trafficking machinery, the domain-identity machinery and the 3D-organization machinery[14]. The polarized trafficking machinery is an adaptation of secretory and endocytic systems to sort and deliver proteins and
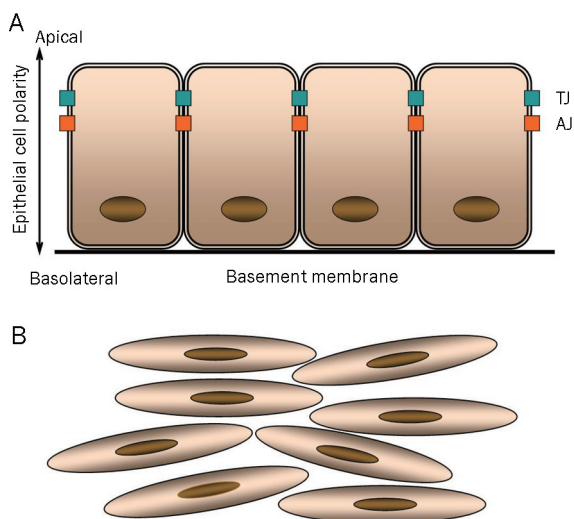
Figure 1. Epithelial cells (A) are organized in mono- or multi-layered sheets in which any single cell is strictly in contact with neighboring cells by specific cell-cell adhesion structures: tight junction (TJ) and adherens junction (AJ). Conversely, mesenchymal cells (B) display a fusiform or spindle-like morphology, do not form organized cell layers, are not polarized, contact the neighboring cells only focally, are not associated with the basement membrane and tend to be highly mobile.

lipids to apical and basolateral plasma membrane domains; the domain-identity machinery governs a highly conserved set of proteins and lipids to the task of generating and maintaining the 'identity' of the apical and basolateral domains; the 3D-organization machinery controls cytoskeleton organization and coordinates extracellular signals with the polarized trafficking and domain-identity machineries.

Among the cellular processes under the domain-identity machinery control there is the establishment of the apical junctional complex, which is formed by two specific cell-cell membrane structures: adherens (AJs) and tight junctions (TJs). Also known as zonula adherens (ZA) and zonula occludens (ZO), these structures are located in the upper portion of a polarized epithelial cell and are composed of transmembrane proteins that interact outside with homotypically molecules in the adjacent cells, and several intracellular scaffolding proteins and signaling molecules connected with the cytoskeletal network[15, 16]. Whereas the main function of AJs is to provide a strong cell-cell adhesion, TJs form a continuous, circumferential, belt-like, selective barrier to solutes leakage across the cellular sheet, and serve, at the same time, as a boundary between apical and basolateral membrane domains to prevent the diffusion of integral proteins and lipids from one to the other domain[17]. As well, TJs are also critical for the polarized location of ion channels, receptors, and enzymes to the membrane domains necessary for structurally and functionally developed epithelia, a function referred to as the "fence" function. In addition, to these barrier and fence functions, TJs are an important site for regulation of epithelial cell differentiation and proliferation due to the interactions of some scaffolding proteins with a large number of signaling molecules[18, 19].

Initially described as membrane "kissing points" (the external leaflets of the lateral plasma membrane of opposing cells appear fused), TJs are located at the apical end of the basolateral domain just above AJs that form a continuous adhesion belt with a sealing function apparently less stronger than that of TJs because the opposing cell membranes are 15−20 nm distant (Figure 2). However, electron microscopy has revealed that the intercellular space of the AJs is not empty but stuffed by the extracellular portion of several transmembrane proteins, and that at the cytoplasmic side, they are characterized by a "plaque" into which actin microfilaments are particularly condensed and connected with the actin filaments forming the cytoskeleton[20].

Both TJs and AJs are composed of a variety of membrane-localized cell adhesion molecules (CAMs) and cytoplasm-localized adaptor proteins that are responsible, respectively, for the mutual recognition and adhesion of adjacent cells in an epithelial layer and for the anchorage of TJ and AJ structure to the cytoskeleton (Figure 2).

The molecular composition of TJs

To date four types of CAMs or transmembrane proteins have been found in TJs: claudin protein family (mammals express about 24 claudins)[21], occludin[22], tricellulin[23] and junctional adhesion molecules (JAMs)[24] (Table 1).

Claudins, occludin and tricellulin are tetraspan proteins that exhibit two extracellular loops, through which they establish contact with homotypic molecules located in the corresponding TJ region of adjacent cells (Figure 2). Experimental evidence from knock-out animals, fibroblasts and epithelial cell lines transfected with different claudin constructs, as well as clinical evidence from human pathological conditions[25, 26]
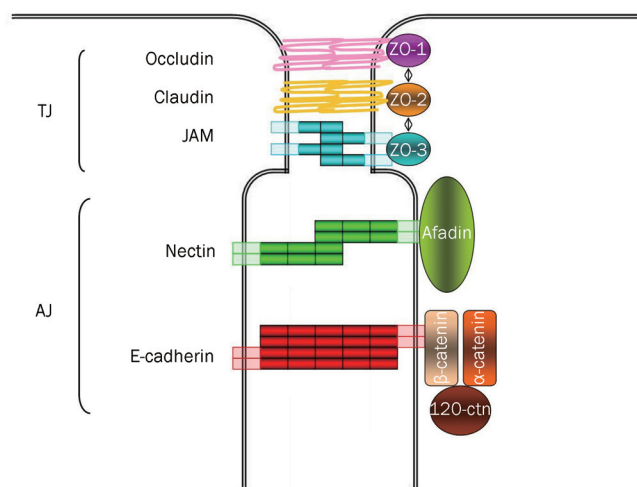
Figure 2. Tight and adherens junctions components. Tight junctions (TJs) are the most apical intercellular junctions in epithelial cells. Their major transmembrane components are the claudins, occludin and adhesion molecules (JAMs) whereas their cytoplasmic components are zonula occludens (ZOs) proteins. Adherens junction (AJs) are localized just below TJs; their transmembrane components are cadherins and nectins that complex respectively the cytoplasmic components β-catenin and afadin.

Table 1. Apical junctional complex components.

	Cell adhesion molecules (transmembrane proteins)	Adaptor proteins (cytoplasmic proteins)
Tight junction	Claudins (about 24 members)	Proteins without PDZ domains
		• Cingulin
	Occludin	• Symplekin
		• Junction-enriched and junction-associated protein (JEAP)
	Tricellulin	
		Proteins with PDZ domains
	Junctional adhesion molecules	*MAGUK protein family*
	• JAM-1	• ZO-1
	• JAM-2	• ZO-2
	• JAM-3	• ZO-3
		• Pals1
		MAGUK inverted proteins
		• MAGI-1
		• MAGI-2
		• MAGI-3
		multi-PDZ domain proteins
		• MUPP-1
		• PATJ
Adherens junction	Cadherins (over 80 members)	Catenins
	Nectins	• α-catenin
	• Nectin-1	• β-catenin
	• Nectin-2	• p120 catenin
	• Nectin-3	Afadin
	• Nectin-4	

indicate that claudin proteins constitute the molecular backbone of TJs and are responsible for the tissue-specific barrier properties of such structures according to the different claudins combination[27]. On the contrary, the role of occludin on TJ structure and function remains rather controversial since occludin knock-out mice are viable and exhibit TJs with an apparent normal morphology[22]. Finally, tricellulin, the latest TJ integral protein to be identified, is concentrated at contact points of three epithelial cells and it appears to play a crucial role in the paracellular barrier mechanism[23].

JAMs belong to a family of type I proteins characterized by two extracellular immunoglobulin-like domains, a single transmembrane region and a cytoplasmic domain that ends with a canonical PDZ domain. The latter is a module of about 80−90 amino acid residues, that derived its name from the first three proteins in which it was found: postsynaptic density protein PSD-95, the *Drosophila* lethal disc large tumor suppressor protein Dlg and the TJ scaffold protein zonula occludens 1, ZO-1. The length of the cytoplasmic tail differs among JAMs, and this difference affects their association to different sets of molecules containing one or more PDZ domains. JAMs appear essential for TJs assembly[28] and growing evidence indicates that they contribute to the regulation of paracellular permeability.

At the cytoplasmic side of TJs, a wide spectrum of scaffold proteins is found. Named peripheral proteins or cytoplas-

mic adaptor proteins, they can be classified according to the presence or absence of PDZ domains in their sequences, a feature that gives them the possibility of establishing specific protein-protein interactions (Table 1).

Among the cytoplasmic adaptor proteins without PDZ domains there are cingulin[29], symplekin[30] and the junction-enriched and junction-associated protein (JEAP), a component of TJs specifically expressed in exocrine cells but not in the epithelial cells of the small intestine[31].

Among the cytoplasmic adaptor proteins with one or more PDZ domains, at least three subgroups can be distinguished. The first one corresponds to the membrane-associated guanylate kinase (MAGUK) protein family and it includes ZO-1, ZO-2, ZO-3, and Pals1[32, 33]. The establishment of cultured epithelial cells in which the expression of ZO-1 and ZO-2 is suppressed by RNA interference, has given crucial clues for understanding the role of these proteins in TJ strand formation: ZO-1 and ZO-2 are essential for the polymerization of claudins and to determine their correct localization at the uppermost portion of the lateral membrane[34].

The second subgroup corresponds to the MAGUK inverted proteins MAGI-1, MAGI-2, and MAGI-3 in which, differently from ZO proteins, the guanylate kinase domain is located at the amino portion of the molecule and PDZ domains are at the carboxyl region[35]. The experimental evidence that MAGI proteins can bind and counteract viral oncoproteins and may

interact with PTEN (phosphatase and tensin homologue) tumor suppressor suggests possible role of MAGIs in the recruitment of growth suppressors[36–38].

The third subgroup includes the multi-PDZ domain protein 1 (MUPP-1) and Pals1-associated TJ protein (PATJ) that, respectively, contain 13 and 10 PDZ domains[39, 40]. MUPP-1 is exclusively localized to the TJ of polarized epithelial cells, where it binds to claudin-1 via PDZ10 domain and to claudin-8 via PDZ9 domain. Like ZO-1, MUPP-1 also links to the membrane-associated JAM-1 protein suggesting a pivotal role of MUPP-1 as multivalent scaffolding protein to recruit several other proteins and participate in the regulation of epithelial cell growth and differentiation.

The molecular composition of AJs

AJs consist of two basic adhesive units: the cadherin/catenin and nectin/afadin complexes (Figure 2)[16]. Classic cadherins are type I, single-pass transmembrane glycoproteins that mediate Ca^{2+}-dependent intercellular adhesion[41]. They consist of over 80 members, among which, E-cadherin is primarily expressed in epithelia. Specific adhesive binding is conferred by the extracellular portion that serves as a template and engages an identical molecule on the surface of neighboring cells. Conversely, the cytoplasmic domain, highly conserved in length, sequence and interaction partners, mediates key structural and signaling activities by the interaction with some cytoplasmic adaptor proteins belonging to the class of catenins (specifically, α-catenin, β-catenin or the highly homologous γ-catenin/plakoglobin and p120 catenin)[42–44]. In particular, an E-cadherin-β-catenin complex is required for the transport of newly synthesized E-cadherin molecules to the plasma membrane where they contribute to the formation of structured AJs[45]. Once at the plasma membrane, the E-cadherin-β-catenin complex rapidly recruits α-catenin, which is essential to reinforce the association of E-cadherin to filamentous actin (F-actin) by linking other actin-binding proteins, including α-actinin, zyxin and vinculin[42, 46]. Cadherins also associate with p120 catenin that specifically prevents cadherin degradation enhancing its surface clustering and helping the formation of strong and more "compacted" structures[47].

In addition to the association with F-actin, α-catenin binds to afadin, the main cytoplasmic binding partner of nectins, recruiting in this way, the second basic adhesive unit (nectin/afadin) that cooperatively organizes AJs[48].

The four nectins till now identified, are members of the immunoglobulin (Ig) superfamily of calcium-independent cell adhesion molecules and are characterized by an extracellular domain with three IgG-like loops, a single transmembrane region, and a cytoplasmic tail that binds to afadin through a C-terminal PDZ binding domain[49]. Nectin-1, nectin-2, and nectin-3 are ubiquitously expressed in a variety of cells including epithelial cells, neurons, and fibroblasts whereas nectin-4 is mainly expressed in the placenta[50]. Experimental evidence indicates that similar to cadherins, nectins are thought to form cis-homodimers and trans-homodimers with similar molecules of adjacent cells[51] (Figure 2).

Cell polarity complexes and formation of the junctional complex

A key event in the establishment of cell-cell junctional complex is the polarization of epithelial cells. In fact, upon establishing a cell-cell contact and before forming AJs and TJs, epithelial cells must reorganize their cytoskeleton and polarize trafficking routes[52]. However, to correctly assemble and localize the junctional complex components, a set of evolutionarily conserved polarity proteins that cross-regulate one each other and interplay with cytoskeleton structures is required (Figure 3).

Originally identified by genetic experiments in *Drosophila melanogaster* and *Caenorhabditis elegans*, in mammals, core polarity regulators are organized in three distinct polarity complexes: (1) the PARtition (PAR) (Par3/Par6/atypical protein kinase (aPKC)) complex; (2) the CRB (Crb/Pals1/Patj) complex; and (3) the SCRIB (Scrib/Dlg/Lgl) complex[53–55].

The PAR complex was initially identified in *Caenorhabditis elegans* mutants (partitioning-defective) as involved in the regulation of the anterior-posterior cell polarity of the one-cell embryo[56]. In mammals, it is composed of two scaffold proteins (Par3 and Par6) and aPKC that form a ternary complex able to bind JAMs and nectins through the PDZ-domain of Par3. PAR complex is localized to the apical junction domain and significant evidence indicates that it has a critical role in TJ formation and epithelial polarization[55, 57].

The CRB and SCRIB complexes were initially identified in the fruit fly *Drosophila melanogaster*, as responsible for epithelial defects: fly embryos the lack Crumbs and stardust proteins fail to form a zonula adherens (the *Drosophila* homolog of TJ) and display a disruption of the apico-basal polarity[54]. In mammals, Crumbs3, one of the three mammalian homologs of Crumbs protein, is localized to the apical membrane where it forms a complex with Pals1 (the mammalian homolog of *Drosophila* stardust protein), and Patj (Pals-associated tight junction protein) the mammalian homolog of *Drosophila* Dlt (Disc lost)[58]. By the binding of the amino terminus of Pals1 and the PDZ domain of Par6, the CRB complex interacts with PAR complex and together regulate TJ assembly[59].

The mammalian SCRIB complex is composed of three proteins, Scribble (Scrib), Disc large (Dlg) and Lethal giant larvae (Lgl)[60]. While Scrib colocalizes with Dlg and overlaps with the AJs, the localization of Lgl depends on its phosphorylation status, which is mediated by aPKC. In fact, phosphorylated Lgl is unable to localize to the membrane and is inactive[61].

In addition to these three core complexes, further components and protein kinases, including Rac1/Cdc42 GTPase, are increasingly being implicated in the organization of cell polarity[54].

Based on the work mainly performed in *Drosophila* and *Caenorhabditis elegans*, the formation of apical polarity seems to be a hierarchical and interactive process in which PAR and CRB complexes cooperate in establishing the apical domain and in the assembly of TJs, whereas SCRIB complex should define the basolateral plasma membrane domain.

Experimental evidence indicates that, in mammals, the earliest stage of junction biogenesis consists of the trans-interaction

of nectins that recruit E-cadherin and JAMs to the apical side of AJs[51]. JAMs and nectins then recruit Par3 protein, which in turn recruits Par6, the second element of the PAR complex characterized by a binding site for aPKC[62]. Experimental evidence indicates that the recruitment of aPKC by Par6 and the following phosphorylation of Par3, that allows the activation of the ternary complex, is a critical step for the maturation of the junctional complex into distinct TJ and AJs. In fact, the localization of active PAR complex to the apical domain is stabilized by the CRB complex whose distribution is reciprocally dependent on the PAR complex. As a consequence, CRB complex forces TJs to remain lateroapical by maintaining the PAR complex in this plasma membrane region[63, 64]. At the same time, the basolaterally located SCRIB complex antagonizes the apical localization of the active PAR complex. In fact, Lgl protein, one of the SCRIB complex components, competes with Par3 for binding to the PAR complex, thereby sequestering the PAR complex away from the apical junctional domain. Such an antagonist function of SCRIB complex is controlled by aPKC as the aPKC-dependent phosphorylation of Lgl protein inactivates the SCRIB complex[54] (Figure 3).
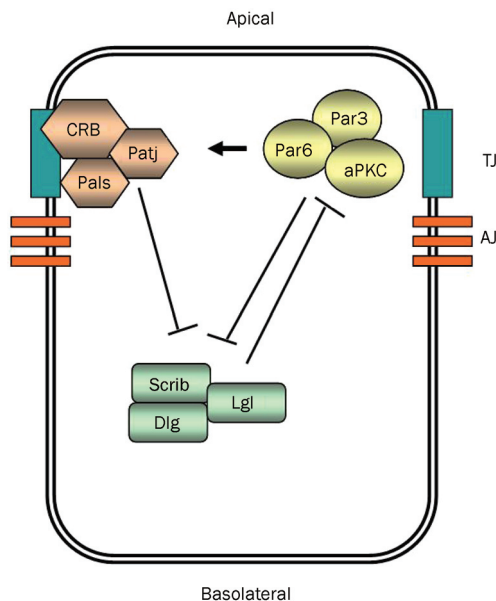
Figure 3. Epithelial cells are polarized along their apicobasal axis, due to the action of three polarity complexes. PAR (Par3/Par6/aPKC) and CRB (Crumbs/Pals1/Patj) complexes are localized to the apical region and promote apical membrane identity. SCRIB complex is localized to the basolateral region, antagonizes the function of the PAR complex and promotes basal membrane identity. SCRIB complex is reciprocally inactivated by aPKC-dependent phosphorylation of Lgl protein.

Apical junctional complex and gene expression

In addition to their role in establishing and maintaining a correct epithelial phenotype, several components of the apical junctional complex have also been found able to actively influence gene expression. In fact, accumulating evidence indicated that some nontransmembrane proteins involved in the formation of the apical junctional complex can shuttle between plasma membrane and nucleus where they participate in the formation of chromatin-associated complexes and hence in the control of gene transcription.

Initially reported for β-catenin, concerning to its role in Wingless (Wnt) signaling pathway[65], this shuttling activity has then been broadened to other TJs proteins (principally ZO-1 and ZO-2)[66, 67] and some cell polarity complex components including Par3, Par6 and Dlg1[68–70] suggesting for these apical polarity proteins a powerful role as epigenetic factors[71, 72].

As recently proposed by Lelièvre[73], the impact of the nuclear localization of apical polarity proteins on gene transcription should depend on the integrity of cell-cell junctions. In fact, if the apical junctional complex is intact, some apical proteins move into the nucleus and participate in the transcription repression of the genes that have to be silenced in order to maintain a differentiated phenotype. Conversely, when apical junctional complex is disrupted certain transcription regulators, normally compartmentalized at cell-cell junctions by apical polarity proteins, are free to move into the nucleus where they induce apical proteins to switch from nuclear repressors to nuclear promoters. Such an hypothesis has recently been supported by the finding that nuclear overexpression of symplekin, a transcriptional regulation normally localized at TJs, promotes tumorigenesis in the human colon and that the regulation of claudin-2 expression is instrumental in this effect[74].

Disassembly of junctional complex and cancer

Disruption of intercellular junctions and alterations in cell polarity are specific hallmarks of epithelial cancer cells. In fact, most human tumors arising in epithelial tissues, gradually lose their polarized morphology and acquire a more peculiar mesenchymal phenotype according to a process termed epithelial-mesenchymal transition (EMT)[75].

Physiologically associated with embryogenesis and wound healing in the adult, EMT is a process characterized by the loss of cell-cell adhesion and apicobasal cell polarity and the concomitant acquisition of a fibroblastoid motile phenotype. When pathologically activated during tumor development, EMT provides cells with ability to escape from the primary tumor mass and to migrate to distant region where they metastasize[76].

Disruption of cell-cell adhesion is principally due to the disassembly of the junctional complex that may be induced by a direct modification of the any junctional components (transmembrane and cytoplasmic proteins) or by indirect effects through the actin cytoskeleton that controls the integrity of TJs and AJs. In particular, alterations in the structure and function of TJs have been reported in adenocarcinomas of various organs, including colon and breast[77, 78], whereas absent or defective TJs have also been associated with the development of the neoplastic phenotype in endometrial cells[79]. TJs dysfunction has also been described in inflamma-

tory processes that end up in cancerous transformation. For example, Crohn's disease and ulcerative colitis are inflammatory illnesses involving the gastrointestinal tract in which an abnormal paracellular permeability defect, probably induced by cytokines and growth factors associated to inflammation including interleukin-1, interleukin-4, interleukin-13, transforming growth factor-α, insulin-like growth factor-I and II, interferon-γ, tumor necrosis factor-α and hepatocyte growth factor, appears to precede the development of both syndromes[80]. Interestingly, it has also been shown that the transforming potential of some oncoproteins, encoded by human adenovirus, papillomavirus (HPV), T-cell leukaemia virus type, depends in part on their ability to interact with TJ-associated proteins of epithelial cells[81].

As previously illustrated, alterations in some apical proteins and transcription regulators compartmentalization, due to TJs and AJs disassembly, may have a dramatic impact on gene transcription with the switch in the apical proteins activity from nuclear repressors to nuclear promoters as supported by the observation that ZO-1 protein is found at the plasma membrane in noninvasive cells whereas it is located in the nucleus of invasive cells[82]. Similarly, the dissociation of E-cadherin-catenin complex results in an increase of the cytosolic pool of β-catenin, the key regulator of Wnt signaling pathway, that drives cell proliferation once migrated to the nucleus[83]. It is important to note that, in addition to transforming growth factor-β (TGF-β), Wnt is one of the extracellular growth factors that have been shown to trigger epithelial dedifferentiation and EMT by the downregulation of epithelial genes and the upregulation of genes coding for fibroblastoid-associated features as N-cadherin, the typical mesenchymal marker[84-86]. That, according to a process known as "cadherin switch" during which cells shift to express different isoforms of this transmembrane component[87].

Also transmembrane and cytoplasmic proteins with at least a PDZ domain have been found target of some oncoproteins including HPV E6 protein, one of the major oncogenic determinants of the sexually transmitted HPV, the primary etiologic agent of cervical cancers. HPV E6 protein has a functional PDZ binding motif that interacts with the corresponding PDZ domain of the TJ proteins MUPP-1, MAGI-1, MAGI-2, MAGI-3, and PATJ[36, 88]. Through such a binding E6 targets these proteins as well as the Dlg and Scrib molecules to ubiquitin-mediated degradation in the proteosome[89–91]. In this way, expression of HPV E6 protein in epithelial cells destabilizes TJs, generates ZO-1 mislocalization, disrupts AJs and promotes carcinogenesis.

Cell polarity complexes dysregulation and cancer
The first hint that polarity proteins might contribute to cancer was provided by experiments in *Drosophila* which showed that knockout of any member of the Scribble complex results in the loss of apicobasal cell polarity, mislocalization of apical junctions and failure to form the zonula adherens, and neoplastic overgrowth of imaginal discs, the ectodermal structure from

which originate epithelia, that lead to death at the larval stage suggesting for these proteins an oncosuppressive key function[92, 93].

Also in mammals, several reports describe a strong correlation between decreased expression of mammalian homologues of Scrib, Lgl and Dlg and tumor progression. Mice lacking Lgl1, one of the two Lgl homologues, show severe brain dysplasia, accompanied by loss of cell polarity in neuroepithelial cells[94], whereas loss or aberrant localization of Lgl2 is associated with human gastric epithelial dysplasia and adenocarcinomas[95]. In addition, as already described, ubiquitin-mediated degradation of Dlg and Scrib proteins may contribute to the development of the HPV-induced cervical carcinoma[91, 96]. It should be noted that cancer promoting viruses, such as HPV also destabilize the CRB/PAR complexes interaction required for TJs formation and induce epithelial depolarization[97] suggesting for CBR components a role as tumor suppressors[98].

Recent findings also implicate the PAR complex in human carcinogenesis. Gene amplification and elevated activity of aPKC have been detected in ovarian, lung and colon cancer and correlated with a poor prognosis[99–101]. In addition, as SCRIB complex components are known to cooperate with those of PAR complex in the assembly of TJs, dysregulation of Scrib, Lgl and Dlg proteins affects also PAR complex activity. As the members of PAR complex play a pivotal role in signaling pathways that control polarity and proliferation, PAR complex implication in human carcinogenesis is not surprising[102]. An example of the link between growth factors signaling, cell polarity and cancer is provided by the ErbB2 receptor tyrosine kinase signaling pathway in breast cancer, in which an overexpression or amplification of the gene is found in 25%-30% of cases. It has recently been demonstrated that after activation, the ErbB2 receptor binds directly to Par6 protein, leading to the competitive recruitment of aPKC and the disruption of the apicobasal polarity[103]. Further recent insights into the regulation of cell polarity during EMT have converged on PAR complex. In fact, in rat intestinal epithelial cells, upon exposure to TGF-β, Par3 protein level has been found decreased, concomitantly to E-cadherin suppression and the induction of mesenchymal markers. The decrease in Par3 mediated by TGF-β resulted in a redistribution of Par3-aPKC complex from the membrane to the cytoplasm leading to the disorganization of PAR complex and loss of polarity[104].

Also mutations in tumor suppressor proteins, such as von Hippel-Lindau protein (VHL), may affect PAR complex efficiency and junctional complex assembly. In fact, as demonstrated by Okuda *et al*[105], VHL, a tumor suppressor involved in the von Hippel-Lindau syndrome which leads to the development of hemagioblastoma, clear-cell renal carcinoma and pheochromocytomas, mediates ubiquitination of a variety of proteins, including activated aPKC, and it regulates the assembly of intercellular junctions. Because VHL tumor suppressor simultaneously affects cell polarity and growth, inactivating mutations result in an abnormal AJs and TJs organization and cell proliferation as evident in VHL-negative cancer cells.

Cell polarity and cell-cell adhesion proteins in cancer diagnosis and prognosis

Due to their multiple links to cancer, many structural and regulatory components of the junctional complex may represent valuable tumor biomarkers. Even though the acquisition of new insights is increasing, at present the largest body of clinical evidence derived from studies on E-cadherin expression. Changes in the normal expression pattern of the E-cadherin/catenin complex have been found in various human cancers from epithelial origin where a partial or total loss of E-cadherin expression correlates with loss of differentiation characteristics, increased tumor grade and metastatic behavior, and poor prognosis. Such a downregulation of E-cadherin may occur as a consequence of gene mutation or epigenetic silencing. Thus, for example, mutations in CDH1, the gene encoding human E-cadherin, are found in more than 50% of stomach cancers[106] whereas, in lobular breast cancer, E-cadherin expression is irreversibly lost due to loss of heterozygosis (LOH) in more than 85% of cases; an LOH which is frequently associated with epigenetic silencing of the remaining CDH1 allele via promoter hypermethylation or transcriptional repression[12]. The prevalence of E-cadherin loss in non-invasive precursor lesions as lobular carcinomas *in situ* of the breast or pancreas adenomas[107] highlights the importance of E-cadherin as a tumor and invasion suppressor and it suggests E-cadherin loss as a critical step in the transition from adenoma to carcinoma.

Also the expression of occludin, one of the major transmembrane components of TJs, has been found decreased with disease progression. For example, moderately and poorly differentiated gastric carcinomas show a reduced occludin mRNA and corresponding protein level when compared to well differentiated ones[108]. Similarly, loss of occludin has been found in human breast cancer[109], in unpolarized prostate cancer cells of Gleason grades 4 and 5[110], and in grades 2 and 3 endometrioid carcinoma with respect to grade 1[79].

More debated is the diagnostic/prognostic role of claudins. In fact, because of their tissue-specific pattern of expression, a causal relationship between claudins expression/localization and cancer has not been established. In some cancers, including prostate, breast, melanocytic neoplasia, esophageal squamous cell carcinoma and lung[111-115], a decreased expression of some claudins, especially claudin-1, has been associated with cancer progression, recurrence and a shorter disease-free survival, suggesting a cancer invasion/metastasis suppressive role. Conversely, in other cancers such as papillary thyroid, oral squamous cell carcinoma, ovarian, colon, melanoma and gastric[116-121], overexpression of claudins has been associated with a more aggressive phenotype.

With regards to the clinical relevance of cytoplasmic proteins, such as ZOs and JAMs proteins, several studies have reported that their reduced expression correlates with dedifferentiation in tumors arising from various compartments of the biliary tract and progression of clear cell renal carcinoma or endometrial cancer[122-124]. However, ZO-1, which is generally considered as a tumor suppressor, has unexpectedly been found overexpressed and associated with N-cadherin in melanoma[125], overexpressed and aberrantly localized in primary and metastatic pancreatic cancer[126], whereas JAM-A has been found overexpressed and positively correlated with poor prognosis in breast cancer patients[127].

About cell polarity complex components recent data provide evidence that aPKC is overexpressed in gastric cancer and associated with unfavorable prognosis[128]. In addition, in a very recent study, aPKC overexpression has been found associated with the loss of Lgl2, a component of the SCRIB polarity complex, in foveolar-type gastric dysplasia suggesting their combined evaluation useful to refine dysplasia diagnosis[129]. The immunohistochemical determination of Lgl2 expression has also provided to be useful in separating pancreatic intraepithelial neoplasia-3 and pancreatic ductal adenocarcinoma from lower-grade pancreatic intraepithelial neoplasias; in fact, while loss or abnormal Lgl2 expression is seen in pancreatic intraepithelial neoplasia-3 and adenocarcinoma, pancreatic intraepithelial neoplasia-1 and pancreatic intraepithelial neoplasia-2 express the protein in a normal-like basolateral fashion[130].

Similarly, the loss of Lgl1 has been associated with several solid tumors including melanoma, prostate, breast, colon, liver and lung cancer[131-134]. In these cancers Lgl1 loss is generally associated with higher tumor grade, and is more pronounced in lymph node or distant metastases.

Also Scrib and Dlg, the other two members of the SCRIB complex, have been found of clinical relevance. In fact, an emerging finding is the association of Dlg1 with HPV-induced gynecological malignancies: in later-stage and poorly differentiated tumors, cytoplasmic Dlg1 protein level increases while it decreases at the membrane sites of cell-cell adhesion[135, 136]. A similar trend of early-stage overexpression and mislocalization has been described in colon carcinogenesis: in adenomatous polyps and well- and moderately differentiated adenocarcinomas, Dlg1 protein level increased but become more diffuse with an increase cytoplasmic staining[137] suggesting its potential use as selective biomarker. Similarly even though preliminary, the evidence that alterations in Scrib protein expression and localization are associated with some cancer of epithelial origin including endometrial, cervical and colorectal neoplasias[138, 139]. In particular in the former, Scrib protein alterations have been found associated with clinical stage, histopathological differentiation, and lymph node metastasis[140] whereas in cervical carcinoma the histochemical analysis showed a dramatic decrease in the expression of Scrib with the progression of disease from normal uterine cervical tissues to invasive cervical cancers through the precursor lesions[139]. Finally, in colorectal carcinoma the overexpression and distribution of Scrib were observed to extensively overlap with the cytoplasmic accumulation of β-catenin and an intense immunoreactivity of Scrib was often observed in small adenomas suggesting that Scrib could be involved in an early step of colon carcinogenesis and supporting the experimental finding of a link between cell polarity disruption and EMT[140].

While no clear evidence of a direct link between CRB complex components and tumor features and clinical outcome, it

has now emerged, Par6 protein, a PAR complex component, has recently been found overexpressed in breast cancer-derived cell lines and in both precancerous breast lesions and advanced primary human breast cancers, especially in estrogen receptor-positive ones[141].

Although, as reported above, several polarity and junctional complex components have been found singly associated with initiation or progression in many cancers of epithelial origin, an integrated picture of the mechanisms controlling their expression and activity during cancer development is lacking. To this aim, novel approaches such as gene expression profile analysis are needed to investigate the associations between the expression of genes coding for cell polarity and cell-cell adhesion determinants and the biologic features of preneoplastic and neoplastic lesions. In such a perspective, for example, we have investigated whether, with respect to normal tissue, epithelial or mixed malignant pleural mesothelioma (MPM) were associated with specific patterns of expression of a selected set of genes related to EMT and cell polarity and adhesion[142]. Using active and passive Principal Components Analysis-based biplots, to visualize specific patterns of expression for epithelial and mixed MPMs, we found that epithelial MPMs, mixed MPMs and normal tissues were characterized by different patterns of expression of genes contributing to a better characterization of MPM histologies, thus suggesting the possibility of using gene expression profile analysis in refining the morphological diagnosis also in other controversial pathological situations as for example preneoplastic lesions.

Cell polarity and cell-cell adhesion proteins as therapeutic targets

Blocking cell proliferation in neoplasias and preventing EMT in preneoplastic lesions eventually restoring normal epithelial morphology represent the main goal of differentiation therapy. Several attempts, targeting cell polarity and adhesion components, have been made at experimental level with interesting and promising results. For example, it has been observed that, in suspension 3D breast tumor spheroids, the retrovirally-induced reexpression of claudin-1, downregulated or completely lost in breast cancer cells *in vitro*, resulted in plasma membrane homing of the protein and reconstitution of paracellular flux[143]. Similarly, in several cancer cell lines, the treatment with demethylators and histone deacetylase inhibitors or retinoids was able to reexpress occludin (silenced by CpG island hypermethylation on its promoter region) with a decreased cellular invasiveness and motility, thereby abrogating the metastatic potency of cancer cells[144].

Conversely, as regard to claudins which appear overexpressed in tumors, the use of siRNA to silence gene expression has provided a significant reduction in cell proliferation, reduction in tumor growth and a significant increase in the number of apoptotic cells[145]. A negative control of claudins overexpression has also been achieved using monoclonal antibody against specific members of the family and promising results have been obtained in pancreatic and ovarian cancers[146, 147]. The use of monoclonal antibodies has also been applied to inhibit the activity of JAM proteins and in particular to block the proangiogenic activity of JAM-3, another component of TJs that in tumor cells mediates the homophilic interaction with endothelial cells. In a murine model of lung carcinoma, monoclonal antibody against JAM-3 was able to inhibit the growth of lung pulmonary tumor grafts by reducing tumor vasculature[148].

In addition to the immunotherapeutic strategy, the potential of claudins as targets for cancer therapy has been highlighted by the observation that treatment with *Clostridium perfringens* enterotoxin (CPE) elicits a rapid and specific cytolysis of breast, ovarian, pancreatic and prostate carcinoma cells. This toxin, responsible for the gastrointestinal symptoms associated with *Clostridium perfringens* food poisoning, is released into the intestinal lumen where it binds specifically to claudin-3 and -4 present in the intestinal epithelial. This triggers the formation of a large multiprotein membrane pore that ultimately results in cell lysis. Since claudin-3 and -4 are overexpressed in numerous carcinomas, this condition represents a unique opportunity for innovative therapy using CPE[149, 150].

As regard polarity complex components, preliminary data on the ternary Par6/Par3/aPKC complex as a novel target for therapeutic intervention are emerging. In particular, Par6 protein appears a promising target both in early and late stage of breast cancers[141] whereas aPKC, as well as being a new prognostic indicator, has been proposed as a novel therapeutic target for the treatment of gastric cancer[128].

Conclusion and future perspectives

Increasing evidence clearly shows that the loss of apico-basal polarity and changes in cellular junctions can be initiating events in tumor formation and that they are hallmark of malignant transformation. Although in recent years there has been a significant advance regarding our understanding of the physiologic mechanisms governing cell polarity, the exact sequence of events leading to cell polarity dysregulation are still being uncovered whereas it is clear that the expression of genes coding for core polarity and junctional adhesion components can be directly or indirectly transcriptionally regulated by several factors including growth factors, oncogene products, tumor suppressors and EMT inducers.

Of particular interest, the emerging relationship among EMT, cell polarity and stem cell phenotype based on the observation that the proteins regulating cell polarity also have an important function in asymmetric cell division, a critical event that guarantees the two essential properties of stem cells: self-renewal and differentiation[151]. In fact, studies in *Drosophila* have shown that the asymmetric localization of cell-fate determinants is controlled by PAR and SCRIB complexes and that mutations in their components provoke defects in asymmetric stem cell division which finally results in tumor development[93, 94].

Also in adult somatic stem cells, which play a central role in epithelial homeostasis, it is thought that polarity is particularly important with respect to fate decisions on stem cell division and that the failure in establishing or regulating stem

cell polarity might result in neoplastic transformation[152]. The recent demonstration that Par3 influences the progenitor cell compartment during mammary gland morphogenesis[153] supports this hypothesis and strengthens the urgency to thoroughly investigate the relationship between apico-basal polarity and progenitor/stem cells. That taking into consideration also the recently proposed link between EMT activation and the acquisition by tumor cells of a stem-like phenotype[154].

Interfering with the signaling pathways that promote the loss of epithelial integrity may be one of the most promising avenues for the development of new therapeutic strategies to impair tumor progression and to revert preneoplastic lesion toward a more differentiated phenotype.

References

1 Jemal A, Siegel R, Ward E, Hao Y, Xu J, Murray T, *et al*. Cancer Statistics, 2008. CA Cancer J Clin 2008; 58: 71–96.
2 Thiery JP. Epithelial-mesenchymal transitions in tumour progression. Nat Rev Cancer 2002; 2: 442–4.
3 Thompson EW, Newgreen DF. Carcinoma invasion and metastasis: a role for epithelial-mesenchymal transition? Cancer Res 2005; 65: 5991–5.
4 Thiery JP, Acloque H, Huang RY, Nieto MA. Epithelial-mesenchymal transitions in development and disease. Cell 2009; 139: 871–90.
5 Micalizzi DS, Ford HL. Epithelial-mesenchymal transition in development and cancer. Future Oncol 2009; 5: 1129–43.
6 Radisky DC. Epithelial-mesenchymal transition. J Cell Sci 2005; 118: 4325–6.
7 Zavadil J, Haley J, Kalluri R, Muthuswamy SK, Thompson E. Epithelial-mesenchymal transition. Cancer Res 2008; 68: 9574–7.
8 Lee M, Vasioukhin V. Cell polarity and cancer-cell and tissue polarity as a non-canonical tumor suppressor. J Cell Sci 2008; 121: 1141–50.
9 Hugo H, Ackland ML, Blick T, Lawrence MG, Clemens JA, Williams ED, *et al*. Epithelial-mesenchymal and mesenchymal-epithelial transitions in carcinoma progression. J Cell Physiol 2007; 213: 374–83.
10 Moreno-Buono G, Portillo F, Cano A. Transcriptional regulation of cell polarity in EMT and cancer. Oncogene 2008; 27: 6958–69.
11 Cavallaro U, Christofori G. Cell adhesion and signalling by cadherins and Ig-CAMs in cancer. Nat Rev Cancer 2004; 4: 118–32.
12 Cowin P, Rowlands TM, Hatsell SJ. Cadherins and catenins in breast cancer. Curr Opin Cell Biol 2005; 17: 499–5.
13 Dow LE, Humbert PO. Polarity regulators and the control of epithelial architecture, cell migration, and tumorigenesis. Int Rev Cytol 2007; 262: 253–302.
14 Tanos B, Rodriguez-Boulan E. The epithelial polarity program: machineries involved and their hijacking by cancer. Oncogene 2008; 27: 6939–57.
15 Niessen CM. Tight junctions/adherens junctions: basic structure and function. J Invest Dermatol 2007; 127: 2525–32.
16 Hartsock A, Nelson WJ. Adherens and tight junctions: structure, function and connections to the actin cytoskeleton. Biochim Biophys Acta 2008; 1778: 660–9.
17 Matter K, Balda MS. Epithelial tight junctions, gene expression and nucleojunctional interplay. J Cell Sci 2007; 120: 1505–11.
18 Matter K, Aijaz S, Tsapara A, Balda MS. Mammalian tight junctions in the regulation of epithelial differentiation and proliferation. Curr Opin Cell Biol 2005; 17: 453–8.
19 Schneeberger EE, Lynch RD. The tight junction: a multifunctional complex. Am J Physiol Cell Physiol 2004; 286: C1213–28.
20 Harris TJC, Tepass U. Adherens junctions: from molecules to morphogenesis. Nature Rev Mol Cell Biol 2010; 11: 502–4.
21 Morita K, Furuse M, Fujimoto K, Tsukita S. Claudin multigene family encoding four-transmembrane domain protein components of tight junction strands. Proc Natl Acad Sci U S A 1999; 96: 511–6.
22 Furuse M, Hirase T, Itoh M, Nagafuchi A, Yonemura S, Tsukita S, *et al*. Occludin: a novel integral membrane protein localizing at tight junctions. J Cell Biol 1993; 123: 1777–88.
23 Ikenouchi M, Furuse K, Furuse H, Sasaki S, Tsukita S. Tricellulin constitutes a novel barrier at tricellular contacts of epithelial cells. J Cell Biol 2005; 171: 939–45.
24 Liu Y, Nusrat A, Schnell FJ, Reaves TA, Walsh S, Pochet M, *et al*. Human junction adhesion molecule regulates tight junction resealing in epithelia. J Cell Sci 2000; 113: 2363–74.
25 Krause G, Winkler L, Mueller SL, Haseloff RF, Piontek J, Blasig IE. Structure and function of claudins. Biochim Biophys Acta 2008; 1778: 631–45.
26 Furuse M, Hata M, Furuse K, Yoshida Y, Haratake A, Sugitani Y, *et al*. Claudin-based tight junctions are crucial for the mammalian epidermal barrier: a lesson from claudin-1–deficient mice. J Cell Biol 2002; 156: 1099–111.
27 Sasaki H, Matsui C, Furuse K, Mimori-Kiyosue Y, Furuse M, Tsukita S. Dymanic behaviour of paired claudin strands within opposing plasma membranes. Proc Natl Acad Sci U S A 2003; 100; 3971–76.
28 Rehder D, Iden S, Nasdala I, Wegener J, Brickwedde MK, Vestweber D, *et al*. Junctional adhesion molecule-A participates in the formation of apico-basal polarity through different domains. Exp Cell Res 2006; 312: 3389–403.
29 Citi S, Amorosi A, Franconi F, Giotti A, Zampi G. Cingulin, a specific protein component of tight junctions, is expressed in normal and neoplastic human epithelial tissues. Am J Pathol 1991; 138: 781–9.
30 Keon BH, Schifer S, Kuhn C, Grund C, Franke WW. Symplekin, a novel type of tight junction plaque protein. J Cell Biol 1996; 134: 1003–18.
31 Nishimura M, Kakizaki M, Ono Y, Morimoto K, Takeuchi M, Inoue Y, *et al*. JEAP, a novel component of tight junctions in exocrine cells. J Biol Chem 2002; 277: 5583–7.
32 Fanning AS, Anderson JM. Zonula occludens-1 and -2 are cytosolic scaffolds that regulate the assembly of cellular junctions. Ann NY Acad Sci 2009; 1165: 113–20.
33 Straight SW, Shin K, Fogg VC, Fan S, Liu C-J, Roh M, *et al*. Loss of PALS1 expression leads to tight junction and polarity defects. Mol Biol Cell 2004; 15: 1981–90.
34 Itoh M, Furuse M, Morita K, Kubota K, Saitou M, Tsukita S. Direct binding of three tight junction-associated MAGUKs, ZO-1, ZO-2, and ZO-3, with the COOH termini of claudins. J Cell Biol 1999; 147: 1351–63.
35 Ide N, Hata Y, Nishioka H, Hirao K, Yao I, Deguchi M, *et al*. Localization of membrane-associated guanylate kinase (MAGI)-1/BAI-associated protein (BAP) 1 at tight junctions of epithelial cells. Oncogene 1999; 18: 7810–5.
36 Thomas M, Laura R, Hepner K, Guccione E, Sawyers C, Lasky L, *et al*. Oncogenic human papillomavirus E6 proteins target the MAGI-2 and MAGI-3 proteins for degradation. Oncogene 2002; 21: 5088–96.
37 Wu Y, Dowbenko D, Spencer S, Laura R, Lee J, Gu Q, *et al*. Interaction of the tumor suppressor PTEN/MMAC with a PDZ Domain of MAGI3, a novel membrane-associated guanylate kinase. J Biol Chem 2000; 275: 21477–85.
38 Wu X, Hepner K, Castelino-Prabhu S, Do D, Kaye MB, Yuan XJ, *et*

al. Evidence for regulation of the PTEN tumor suppressor by a membrane-localized multi-PDZ domain containing scaffold protein MAGI-2. Proc Natl Acad Sci U S A 2000; 97: 4233–8.

39 Shin K, Straight S, Margolis B. PATJ regulates tight junction formation and polarity in mammalian epithelial cells. J Cell Biol 2005; 168: 705–11.

40 Adachi M, Hamazaki Y, Kobayashi Y, Itoh M, Tsukita S, Furuse M, *et al*. Similar and distinct properties of MUPP1 and Patj, two homologous PDZ domain-containing tight-junction proteins. Mol Cell Biol 2009; 29: 2372–89.

41 Goodwin M, Yap AS. Classical cadherin adhesion molecules: coordinating cell adhesion, signaling and the cytoskeleton. J Mol Histol 2004; 35: 839–44.

42 Kobielak A, Fuchs E. α-Catenin: at the junction of intercellular adhesion and actin dynamics. Nat Rev Mol Cell Biol 2004; 5: 614–25.

43 Xu W, Kimelman D. Mechanistic insights from structural studies of β-catenin and its binding partners. J Cell Sci 2007; 120: 3337–44.

44 Reynolds AB. p120-catenin: Past and present. Biochim Biophys Acta 2007; 1773: 2–7.

45 Chen YT, Stewart DB, Nelson WJ. Coupling Assembly of the E-cadherin/β-catenin complex to efficient endoplasmic reticulum exit and basal-lateral membrane targeting of E-cadherin in polarized MDCK cells. J Cell Biol 1999; 144: 687–99.

46 Bajpai S, Correia J, Feng Y, Figueiredo J, Sun SX, Longmore GD, *et al*. α-Catenin mediates initial E-cadherin-dependent cell–cell recognition and subsequent bond strengthening. Proc Natl Acad Sci U S A 2008; 105: 18331–6.

47 Ireton RC, Davis MA, van Hengel J, Mariner DJ, Barnes K, Thoreson MA, *et al*. A novel role for p120 catenin in E-cadherin function. J Cell Biol 2002; 159: 465–76.

48 Tachibana K, Nakanishi H, Mandai K, Ozaki K, Ikeda W, Yamamoto Y, *et al*. Two cell adhesion molecules, nectin and cadherin, interact through their cytoplasmic domain-associated proteins. J Cell Biol 2000; 150: 1161–76.

49 Takai Y, Ikeda W, Ogita H, Rikitake Y. The immunoglobulin-like cell adhesion molecule nectin and its associated protein afadin. Annu Rev Cell Dev Biol 2008; 24: 309–42.

50 Takai Y, Irie K, Shimizu K, Sakisaka T, Ikeda W. Nectins and nectin-like molecules: roles in cell adhesion, migration, and polarization. Cancer Sci 2003; 94: 655–67.

51 Irie K, Shimizu K, Sakisaka T, Ikeda W, Takai Y. Roles and modes of action of nectins in cell–cell adhesion. Semin Cell Dev Biol 2004; 15: 643–56.

52 Cereijido M, Contreras RG, Shoshani L, Flores-Benitez D, Larre I. Tight junction and polarity interaction in the transporting epithelial phenotype. Biochim Biophys Acta 2008; 1778: 770–93.

53 Humbert PO, Down LE, Russell SM. The scribble and Par complexes in polarity and migration: friends or foes? Trends Cell Biol 2006; 16: 622–30.

54 Assemat E, Bazellieres E, Pallesi-Pocachard E, Le Bivic A, Massey-Harroche D. Polarity complex proteins. Biochim Biophys Acta 2008; 1778: 614–30.

55 Suzuki A, Ohno S. The PAR-aPKC system: lessons in polarity. J Cell Sci 2006; 119: 979–87.

56 Kemphues KJ, Priess JR, Mortn DG, Cheng NS. Identification of genes required for cytoplasmic localization in early *C elegans* embryos. Cell 1988; 52: 311–20.

57 Goldstein B, Macara IG. The PAR proteins: fundamental players in animal cell polarization. Dev Cell 2007; 13: 609–22.

58 Lemmers C, Medina E, Delgrossi MH, Michel D, Arsanto JP, Le Bivic A. hINADL/PATJ, a homolog of discs lost, interacts with crumbs and localizes to tight junctions in human epithelial cells. J Biol Chem 2002; 277: 25408–15.

59 Michel D, Arsanto JP, Massey-Harroche D, Béclin C, Wijnholds J, Le Bivic A. PATJ connects and stabilizes apical and lateral components of tight junctions in human intestinal cells. J Cell Sci 2005; 118: 4049–57.

60 Dow LE, Brumby AM, Muratore R, Coombe ML, Sedelies KA, Trapani JA, *et al*. hScrib is a functional homologue of the Drosophila tumour suppressor Scribble. Oncogene 2003; 22: 9225–30.

61 Yamanaka T, Ohno S. Role of Lgl/Dlg/Scribble in the regulation of epithelial junction, polarity and growth. Front Biosci 2008; 13: 6693–6707.

62 Itoh M, Sasaki H, Furuse M, Ozaki H, Kita T, Tsukita S. Junctional adhesion molecule (JAM) binds to PAR-3: a possible mechanism for the recruitment of PAR-3 to tight junctions. J Cell Biol 2001; 154: 491–7.

63 Schock F, Perrimon N. Molecular mechanisms of epithelial morphogenesis. Annu Rev Cell Dev Biol 2002; 18: 463–93.

64 Gibson MC, Perrimon N. Apicobasal polarization: epithelial form and function. Curr Opin Cell Biol 2003; 15: 747–52.

65 Clevers H. Wnt/β-catenin signaling in development and disease. Cell 2007; 127: 469–80.

66 Gottardi CJ, Arpin M, Fanning AS, Louvard D. The junction-associated protein, zonula occludens-1, localizes to the nucleus before the maturation and during the remodeling of cell-cell contacts. Proc Natl Acad Sci U S A 1996; 93: 10779–84.

67 Traweger A, Fuchs R, Krizbai IA, Weiger TM, Bauer HC, Bauer H. The tight junction protein zo-2 localizes to the nucleus and interacts with the heterogeneous nuclear ribonucleoprotein scaffold attachment factor-B. J Biol Chem 2003; 278: 2692–700.

68 Fang L, Wang Y, Du D, Yang G, Tak Kwok T, Kai Kong S, *et al*. Cell polarity protein Par3 complexes with DNA-PK via Ku70 and regulates DNA double-strand break repair. Cell Res 2007; 17: 100–16.

69 Cline EG, Nelson WJ. Characterization of mammalian Par 6 as a dual-location protein. Mol Cell Biol 2007; 27: 4431–43.

70 Garcia-Mata R, Dubash AD, Sharek L, Carr HS, Frost JA, Burridge K. The nuclear RhoA exchange factor Net1 interacts with proteins of the Dlg family, affects their localization and influences their tumor suppressor activity. Mol Cell Biol 2007; 27: 8683–97.

71 Chandramouly G, Abad PC, Knowles DW, Lelièvre SA. The control of tissue architecture over nuclear organization is crucial for epithelial cell fate. J Cell Sci 2007; 120: 1596–1606.

72 Traweger A, Lehner C, Farkas A, Krizbai IA, Tempfer H, Klement E, *et al*. Nuclear Zonula occludens-2 alters gene expression and junctional stability in epithelial and endothelial cells. Differentiation 2008; 76: 99–106.

73 Lelièvre SA. Tissue polarity-dependent control of mammary epithelial homeostasis and cancer development: an epigenetic perspective. J Mammary Gland Biol Neoplasia 2010; 15: 49–63.

74 Buchert M, Papin M, Bonnans C, Darido C, Raye WS, Garambois V, *et al*. Symplekin promotes tumorigenicity by up-regulating claudin-2 expression. Proc Natl Acad Sci U S A 2010; 107: 2628–33.

75 Thiery J. Epithelial-mesenchymal transitions in development and pathologies. Curr Opin Cell Biol 2003; 15: 740–6.

76 Gupta A, Massaguè J. Cancer metastasis: building a framework. Cell 2006; 127: 679–95.

77 Hoover KB, Liao S-Y, Bryant PJ. Loss of the tight junction MAGUK ZO-1 in breast cancer: relationship to glandular differentiation and loss of heterozygosity. Am J Pathol 1998; 153: 1767–73.

78 Soler AP, Miller RD, Laughlin KV, Carp NZ, Klurfed DM, Mullin

JM. Increased tight junctional permeability is associated with the development of colon cancer. Carcinogenesis 1999; 20: 1425–31.

79 Tobioka H, Isomura H, Kokai Y, Tokunaga Y, Yamaguchi J, Sawada N. Occludin expression decreases with the progression of human endometrial carcinoma. Hum Pathol 2004; 35: 159–64.

80 Macarthur M, Hold GL, El-Omar EM. Inflammation and Cancer II. Role of chronic inflammation and cytokine gene polymorphisms in the pathogenesis of gastrointestinal malignancy. Am J Physiol Gastrointest Liver Physiol 2004; 286: G515–20.

81 Javier RT. Cell polarity proteins: common targets for tumorigenic human viruses. Oncogene 2008; 27: 7031–46.

82 Polette M, Gilles C, Nawrocki-Raby B, Lohi J, Hunziker W, Foidart JM, *et al*. Membrane-type 1 matrix metalloproteinase expression is regulated by zonula occludens-1 in human breast cancer cells. Cancer Res 2005; 65: 7691–8.

83 Brembeck FH, Rosario M, BirchmeierW. Balancing cell adhesion and Wnt signaling, the key role of β-catenin. Curr Opin Genet Dev 2006; 16: 51–9.

84 Huber M, Kraut N, Beug H. Molecular requirements for epithelial-mesenchymal transition during tumor progression. Curr Opin Cell Biol 2005; 17: 548–58.

85 Thiery J, Sleeman J. Complex networks orchestrate epithelial-mesenchymal transitions. Nat Rev Mol Cell Biol 2006; 7: 131–42.

86 Peinado H, Olmeda D, Cano A. Snail, Zeb and bHLH factors in tumour progression: an alliance against the epithelial phenotype? Nature Rev Cancer 2007; 7: 415–28.

87 Wheelock MJ, Shintani Y, Maeda M, Fukumoto Y, Johnson KR. Cadherin switching. J Cell Sci 2008; 121: 727–35.

88 Storrs CH, Silverstein SJ. PATJ, a tight junction-associated PDZ protein, is a novel degradation target of high-risk human papillomavirus E6 and the alternatively spliced isoform 18 E6. J Virol 2007; 81: 4080–90.

89 Thomas M, Glaunsinger B, Pim D, Javier R, Banks L. HPV E6 and MAGUK protein interactions: determination of the molecular basis for specific protein recognition and degradation. Oncogene 2001; 20: 5431–9.

90 Nakagawa S, Huibregtse JM. Human scribble (vartul) is targeted for ubiquitin-mediated degradation by the high-risk papillomavirus e6 proteins and the e6ap ubiquitin-protein ligase. Mol Cell Biol 2000; 20: 8244–53.

91 Gardiol D, Kuhne C, Glaunsinger B, Lee SS, Javier R, Banks L. Oncogenic human papillomavirus E6 proteins target the discs large tumour suppressor for proteasome-mediated degradation. Oncogene 1999; 18: 5487–96.

92 Gateff E. Malignant neoplasms of genetic origin in *Drosophila melanogaster*. Science 1978; 200: 1448–59.

93 Bilder D. Epithelial polarity and proliferation control: links from Drosophila neoplastic tumor suppressors. Genes Dev 2004; 18: 1909–25.

94 Klezovitch O, Fernandez TE, Tapscott SJ, Vasioukhin V. Loss of cell polarity causes severe brain dysplasia in Lgl1 knockout mice. Genes Dev 2004; 18: 559–71.

95 Lisovsky M, Dresser K, Baker S, Fisher A, Woda B, Banner B, *et al*. Cell polarity protein Lgl2 is lost or aberrantly localized in gastric dysplasia and adenocarcinoma: an immunohistochemical study. Mod Pathol 2009; 22: 977–84.

96 Massimi P, Narayan N, Cuenda A, Banks L. Phosphorylation of the disc large tumor suppressor protein controls its membrane localization and enhances its susceptibility to HPV E6-induced degradation. Oncogene 2006; 25: 4276–85.

97 Latorre IJ, Roh MH, Frese KK, Weiss RS, Margolis B, Javier RT. Viral oncoprotein-induced mislocalization of select PDZ proteins disrupts tight junctions and causes polarity defects in epithelial cells. J Cell Sci 2005; 118: 4283–93.

98 Karp CM, Tan TT, Mathew R, Nelson D, Mukherjee C, Degenhardt K, *et al*. Role of the polarity determinant crumbs in suppressing mammalian epithelial tumor progression. Cancer Res 2008; 68: 4105–15.

99 Eder AM, Sui X, Rosen DG, Nolden LK, Cheng KW, Lahad JP, *et al*. Atypical PKCi contributes to poor prognosis through loss of apical–basal polarity and Cyclin E overexpression in ovarian cancer. Proc Natl Acad Sci U S A 2005; 102: 12519–24.

100 Murray NR, Jamieson L, Yu W, Zhang J, Gokmen-Polar Y, Sier D. Protein kinase Ciota is required for Ras transformation and colon carcinogenesis *in vivo*. J Cell Biol 2004; 164: 797–802.

101 Regala RP, Weems C, Jamieson L, Copland JA, Thompson EA, Fields AP. Atypical protein kinase Ciota plays a critical role in human lung cancer cell growth and tumorigenicity. J Biol Chem 2005; 280: 31109–15.

102 Aranda V, Nolan ME, Muthuswamy SK. Par complex in cancer: a regulator of normal polarity joins the dark side. Oncogene 2008; 27: 6878–87.

103 Aranda V, Haire T, Nolan ME, Calarco JP, Rosenberg AZ, Fawcett JP, *et al*. Par6–aPKC uncouples ErbB2 induced disruption of polarized epithelial organization from proliferation control. Nature Cell Biol 2006; 8: 1235–48.

104 Wang X, Nie J, Zhou Q, Liu W, Zhu F, Chen W, *et al*. Downregulation of Par-3 expression and disruption of Par complex integrity by TGF-beta during the process of epithelial to mesenchymal transition in rat proximal epithelial cells. Biochim Biophys Acta 2008; 1782: 51–9.

105 Okuda H, Saitoh K, Hirai S, Iwai K, Takaki Y, Baba M, *et al*. The von Hippel-Lindau tumor suppressor protein mediates ubiquitination of activated atypical protein kinase C. J Biol Chem 2001; 276: 43611–7.

106 Graziano F, Humar B, Guilford P. The role of E-cadherin gene (CDH1) in diffuse gastric cancer susceptibility: from the laboratory to clinical practice. Ann Oncol 2003; 14: 1705–13.

107 Perl AK, Wilgenbus P, Dahl U, Semb H, Christofori G. A causal role for E-cadherin in the transition from adenoma to carcinoma. Nature 1998; 392: 190–3.

108 Ohtani S, Terashima M, Satoh J, Soeta N, Saze Z, Kashimura S, *et al*. Expression of tight-junction-associated proteins in human gastric cancer: down-regulation of claudin-4 correlates with tumor aggressiveness and survival. Gastric Cancer 2009; 12: 43–51.

109 Martin TA, Mansel RE, Jiang WG. Loss of occludin leads to the progression of human breast cancer. Int J Mol Med 2010; 26: 723–34.

110 Busch C, Hanssen TA, Wagener C, O'Brink B. Down-regulation of CEACAM1 in human prostate cancer: correlation with loss of cell polarity, increased proliferation rate, and Gleason grade 3 to 4 transition. Hum Pathol 2002; 33: 290–8.

111 Sheehan GM, Kallakury BVS, Sheehan CE, Fisher HAG, Kaufman RP, Ross JS. Loss of claudins-1 and -7 and expression of claudins-3 and -4 correlate with prognostic variables in prostatic adenocarcinomas. Hum Pathol 2007; 38: 564–9.

112 Tokés AM, Kulka J, Paku S, Szik A, Páska C, Novák PK, *et al*. Claudin-1, -3 and -4 proteins and mRNA expression in benign and malignant breast lesions: a research study. Breast Cancer Res 2005; 7: R296–305.

113 Cohn ML, Goncharuk VN, Diwan AH, Zhang PS, Shen SS, Prieto VG. Loss of claudin-1 expression in tumor-associated vessels correlates with acquisition of metastatic phenotype in melanocytic neoplasms. J Cutaneous Pathol 2005; 32: 533–6.

114 Miyamoto K, Kusumi T, Sato F, Kawasaki H, Shibata S, Ohashi M, *et al*. Decreased expression of claudin-1 is correlated with recurrence status in esophageal squamous cell carcinoma. Biomed Res 2008; 29: 71–6.

115 Chao YC, Pan SH, Yang SC, Yu SL, Che TF, Lin CW, *et al*. Claudin-1 is a metastatic suppressor and correlates with clinical outcome in lung adenocarcinoma. Am J Resp Crit Care Med 2009; 179: 123–33.

116 Nemeth J, Nemeth Z, Tatrai P, Peter I, Somoracz A, Szasz AM, *et al*. High expression of claudin-1 protein in papillary thyroid tumor and its regional lymph node metastasis. Pathol Oncol Res 2010;16: 19–27.

117 Oku N, Sasabe E, Ueta E, Yamamoto T, Osaki T. Tight junction protein claudin-1 enhances the invasive activity of oral squamous cell carcinoma cells by promoting cleavage of laminin-5 gamma2 chain via matrix metalloproteinase (MMP)-2 and membrane-type MMP-1. Cancer Res 2006; 66: 5251–7.

118 Kleinberg L, Holth A, Trope CG, Reich R, Davidson B. Claudin upregulation in ovarian carcinoma effusions is associated with poor survival. Hum Pathol 2008; 39: 747–57.

119 Kinugasa T, Huo Q, Higashi D, Shibaguchi H, Kuroki M, Tanaka T, *et al*. Selective up-regulation of claudin-1 and claudin-2 in colorectal cancer. Anticancer Res 2007; 27: 3729–34.

120 Leotlela PD, Wade MS, Duray PH, Rhode MJ, Brown HF, Rosenthal DT, *et al*. Claudin-1 overexpression in melanoma is regulated by PKC and contributes to melanoma cell motility. Oncogene 2007; 26: 3846–56.

121 Wu YL, Zhang S, Wang GR, Chen YP. Expression transformation of claudin-1 in the process of gastric adenocarcinoma invasion. World J Gastroenterol 2008; 14: 4943–8.

122 Nemeth Z, Szasz AM, Somoracz A, Tatrai P, Nemeth J, Gyorffy H, *et al*. Zonula occludens-1, occludin, and E-cadherin protein expression in biliary tract cancers. Pathol Oncol Res 2009; 15: 533–9.

123 Gutwein P, Schramme A, Voss B, Abdel-Bakky MS, Doberstein K, Ludwig A, *et al*. Downregulation of junctional adhesion molecule-A is involved in the progression of clear cell renal cell carcinoma. Biochem Biophys Res Commun 2009; 380: 387–91.

124 Koshiba H, Hosokawa K, Kubo A, Tokumitsu N, Watanabe A, Honjo H. Junctional adhesion molecule A expression in human endometrial carcinoma. Int J Gynecol Cancer 2009; 19: 208–13.

125 Smalley KS, Brafford P, Haass NK, Brandner JM, Brown E, Herlyn M. Up-regulated expression of zonula occludens protein-1 in human melanoma associates with N-cadherin and contributes to invasion and adhesion. Am J Pathol 2005; 166: 1541–54.

126 Kleeff J, Shi X, Bode HP, Hoover K, Shrikhande S, Bryant PJ, *et al*. Altered expression and localization of the tight junction protein ZO-1 in primary and metastatic pancreatic cancer. Pancreas 2001; 23: 259–65.

127 McSherry EA, McGee SF, Jirstrom K, Doyle EM, Brennan DJ, Landberg G, *et al*. JAM-A expression positively correlates with poor prognosis in breast cancer patients. Int J Cancer 2009; 125: 1343–51.

128 Takagawa R, Akimoto K, Ichikawa Y, Akiyama H, Kojima Y, Ishiguro H, *et al*. High expression of atypical protein kinase C lambda/iota in gastric cancer as a prognostic factor for recurrence. Ann Surg Oncol 2010; 17: 81–8.

129 Lisovsky M, Ogawa F, Dresser K, Woda B, Lauwers GY. Loss of cell polarity protein Lgl2 in foveolar-type gastric dysplasia: correlation with expression of the apical marker aPKC-zeta. Virchows Arch 2010; 457: 635–42.

130 Lisovsky M, Dresser K, Woda B, Mino-Kenudson M. Immunohistochemistry for cell polarity protein lethal giant larvae 2 differentiates pancreatic intraepithelial neoplasia-3 and ductal adenocarcinoma of the pancreas from lower-grade pancreatic intraepithelial neoplasias.

Hum Pathol 2010; 41: 902–9.

131 Grifoni D, Garoia F, Schimanski CC, Schmitz G, Laurenti E, Galle PR, *et al*. The human protein Hugl-1 substitutes for Drosophila Lethal giant larvae tumour suppressor function *in vivo*. Oncogene 2004; 23: 8688–94.

132 Kuphal S, Wallner S, Schimanski CC, Bataille F, Hofer P, Strand S, *et al*. Expression of Hugl-1 is strongly reduced in malignant melanoma. Oncogene 2006; 25: 103–10.

133 Schimanski CC, Schmitz G, Kashyap A, Bosserhoff AK, Bataille F, Schafer SC, *et al*. Reduced expression of Hugl-1, the human homologue of *Drosophila* tumour suppressor gene lgl, contributes to progression of colorectal cancer. Oncogene 2005; 24: 3100–9.

134 Lu X, Feng X, Man X, Yang G, Tang L, Du D, *et al*. Splicing of Hugl-1 is associated with hepatocellular carcinoma progression. Clin Cancer Res 2009; 15: 3287–96.

135 Lin HT, Steller MA, Aish L, Hanada T, Chishti AH. Differential expression of human Dlg in cervical intraepithelial neoplasias. Gynecol Oncol 2004; 93: 422–8.

136 Cavatorta AL, Fumero G, Choihy D, Aguirre R, Nocito AL, Giri AA, *et al*. Differential expression of the human homologue of *Drosophila* discs large oncosuppressor in histologic samples from human papillomavirus-associated lesions as a marker for progression to malignancy. Int J Cancer 2004; 111: 373–80.

137 Gardiol D, Zacchi A, Petrera F, Stanta G, Banks L. Human discs large and scrib are localized at the same regions in colon mucosa and changes in their expression patterns are correlated with loss of tissue architecture during malignant progression. Int J Cancer 2006; 119: 1285–90.

138 Ouyang Z, Zhan W, Dan L. hScrib, a human homolog of *Drosophila* neoplastic tumor suppressor, is involved in the progress of endometrial cancer. Oncol Res 2010; 18: 593–9.

139 Nakagawa S, Yano T, Nakagawa K, Takizawa S, Suzuki Y, Yasugi T, *et al*. Analysis of the expression and localisation of a LAP protein, human scribble, in the normal and neoplastic epithelium of uterine cervix. Br J Cancer 2004; 90: 194–9.

140 Kamei Y, Kito K, Takeuchi T, Imai Y, Murase R, Ueda N, *et al*. Human scribble accumulates in colorectal neoplasia in association with an altered distribution of beta-catenin. Hum Pathol 2007; 38: 1273–81.

141 Nolan ME, Aranda V, Lee S, Lakshmi B, Basu S, Allred DC, *et al*. The polarity protein par6 induces cell proliferation and is overexpressed in breast cancer. Cancer Res 2008; 68: 8201–9.

142 Casarsa C, Bassani N, Ambrogi F, Zabucchi G, Boracchi P, Biganzoli E, *et al*. Epithelial-mesenchymal transition, cell polarity and stemness-associated features in malignant pleural mesothelioma. Cancer Lett 2011; 302; 136-43.

143 Hoevel T, Macek R, Swisshelm K, Kubbies M. Re-expression of the TJ protein CLDN1 induces apoptosis in breast tumor spheroids. Int J Cancer 2004; 108: 374–83.

144 Osanai M, Murata M, Nishikiori N, Chiba H, Kojima T, Sawad N. Epigenetic silencing of occludin promotes tumorigenic and metastatic properties of cancer cells via modulations of unique sets of apoptosis-associated genes. Cancer Res 2006; 66: 9125–33.

145 Huang YH, Bao Y, Peng W, Goldberg M, Love K, Bumcrot DA, *et al*. Claudin-3 gene silencing with siRNA suppresses ovarian tumor growth and metastasis. Proc Natl Acad Sci U S A 2009; 106: 3426–30.

146 Kato-Nakano M, Suzuki M, Kawamoto S, Furuya A, Ohta S, Nakamura K, *et al*. Characterization and evaluation of the antitumour activity of a dual-targeting monoclonal antibody against claudin-3 and claudin-4. Anticancer Res 2010; 30: 4555–62.

147 Suzuki M, Kato-Nakano M, Kawamoto S, Furuya A, Abe Y, Misaka H, *et al*. Therapeutic antitumor efficacy of monoclonal antibody against Claudin-4 for pancreatic and ovarian cancers. Cancer Sci 2009; 100: 1623–30.

148 Lamagna C, Hodivala-Dilke KM, Imhof BA, Aurrand-Lions M. Antibody against junctional adhesion molecule-c inhibits angiogenesis and tumor growth. Cancer Res 2005; 65: 5703–10.

149 Saeki R, Kondoh M, Kakutani H, Matsuhisa K, Takahashi A, Suzuki H, *et al*. A claudin-targeting molecule as an inhibitor of tumor metastasis. J Pharmacol Exp Ther 2010; 334: 576–82.

150 Cocco E, Casagrande F, Bellone S, Richter CE, Bellone M, Todeschini P, *et al*. Clostridium perfringens enterotoxin carboxy-terminal fragment is a novel tumor-homing peptide for human ovarian cancer. BMC Cancer 2010; 10: 349.

151 Wodarz A, Näthke I. Cell polarity in development and cancer. Nat Cell Biol 2007; 9: 1016–24.

152 Florian MC, Geiger H. Concise review: polarity in stem cells, disease, and aging. Stem Cells 2010; 28: 1623–9.

153 McCaffrey LM, Macara IG. The Par3/aPKC interaction is essential for end bud remodelling and progenitor differentiation during mammary gland morphogenesis. Genes Dev 2009; 23: 1450–60.

154 Mani SA, Guo W, Liao MJ, Eaton EN, Ayyanan A, Zhou AY, *et al*. The Epithelial-mesenchymal transition generates cells with properties of stem cells. Cell 2008; 133: 704–15.

npg

Original Article

Toll-like receptor 7/8 agonist resiquimod induces late preconditioning in neonatal cardiac myocytes

Yong-yi WANG, Sha LIU, Feng LIAN, Wen-gang YANG, Song XUE*

Department of Cardiovascular Surgery, RenJi Hospital of Shanghai Jiaotong University, Shanghai 200127, China

Aim: To investigate whether R-848 (resiquimod, toll-like receptor 7/8 agonist) can induce late preconditioning in neonatal cardiac myocytes.
Methods: The protective effects of R-848 on neonatal myocytes against anoxia-reoxygenation-induced injury were tested, and intracellular reactive oxygen species (ROS) were determined. The protein synthesis inhibitor cyclohexamide (CH) and the ROS scavenger *N*-acetylcysteine (NAC) were used in this model to test if new protein synthesis and oxidative stress were necessary for their cardioprotective effects. The activation of nuclear factor kappa B (NFκB) and hypoxia inducible factor 1 (HIF1) was investigated by electrophoretic mobility shift assays (EMSA), and inducible nitric oxide synthase (iNOS) was assessed by immunoblotting. After iNOS was downregulated by small interfering RNA (siRNA) transfection, the cardioprotective effect was reassessed.
Results: ROS were triggered soon after R-848 (0.01–1.0 µg/L) administration, however, the cardioprotective effect of which was induced 24 h later. This protection was abolished by CH or NAC pretreatment. NFκB and HIF1 activation and iNOS up-regulation were involved in this protective mechanism. The cardioprotective effect was also attenuated after iNOS was knocked down.
Conclusion: R-848 provided a cardioprotective effect through a late preconditioning mechanism via a ROS/NFκB-HIF1/iNOS-dependent pathway.

Keywords: toll like receptor; resiquimod; late preconditioning; anoxia-reoxygenation; reactive oxygen species; cardioprotection

Introduction

TLRs (Toll-like receptors) are part of the innate immune system. They detect infections by highly conserved components of pathogens, such as some protein, lipid and nucleic structures. The stimulation of TLRs initiates the activation of an intracellular signaling network that promotes an inflammatory response via the release of proinflammatory cytokines[1]. Among the 10 TLRs identified in humans, TLR2 and TLR4, in addition to their critical role in mediating cardiac dysfunction in septic conditions, can also recognize endogenous ligands and may play an important role in modulating cardiomyocyte survival[2–4]. LPS-induced preconditioning via TLR4 has been explored in heart, lung and brain[5]. Recently, it was reported that preconditioning by the TLR2 agonist Pam3CSK4 reduces CXCL1-dependent leukocyte recruitment in murine myocardial ischemia/reperfusion injury[6]. The TLR9 ligand CpG oligodeoxynucleotide (ODN) can serve as a potent preconditioning stimulus and provide protection against ischemic brain injury[7]. These recent studies indicate that multiple TLRs offer

promise as novel therapeutic targets for cell survival during ischemia/reperfusion injury in the heart.

TLR7 and TLR8, which are expressed intracellularly within one or more endosomal compartments, have been shown to mediate anti-viral responses by means of recognizing single-stranded RNA (ssRNA). Before ssRNA was identified as the natural ligand for TLR7 and TLR8, adenosine analogs such as imidazoquinolines were already used as agonists of TLR7 and TLR8. The imidazoquinoline imiquimod activates transcription factors like nuclear factor kappa B (NFκB) and results in a T helper (Th) 1-polarized immune response by the secretion of proinflammatory cytokines in human blood cells[8]. Therefore, imiquimod has been used as an anti-cancer treatment because of its ability to activate several immune pathways simultaneously, resulting in effective anti-tumor immunity. Resiquimod (R-848) is another imidazoquinoline that binds to both TLR7 and TLR8, resulting in an enhanced activity profile compared to imiquimod, and the use of R-848 is a promising strategy in TLR-based immunotherapy for acute myeloid leukemia[9]. Coxsackierus group B type 3 (CVB3) is considered the most common cause of viral myocarditis in humans, which triggers a cardiac inflammatory response mainly through a TLR7/TLR8-dependent pathway[10]. Therefore, we deduced that

R-848 could also initiate an inflammatory response and oxidative stress in cardiomyocytes. In this study, we demonstrate that R-848 can induce late preconditioning in cardiomyocytes.

NFκB is a redox-sensitive transcription factor. NFκB activation is involved in TLR7/8 downstream signaling through a MyD88-dependent pathway and is necessary in late preconditioning[11]. Recently, it was reported that both TLR4 and TLR7/8 induce accumulation/activation of HIF1α protein through a redox-dependent mechanism[12, 13], and activation of HIF1α is also involved in ischemic late preconditioning[14]. Therefore, the activation of NFκB and HIF1α in R-848-induced late preconditioning was determined, and the role of ROS in this activation and the down-regulated protein of these two transcription factors, inducible nitric oxide synthase (iNOS), were determined.

Materials and methods

Neonatal cardiomyocytes culture and anoxia-reoxygenation

Principles of laboratory animal care were followed. Neonatal cardiac myocytes were prepared from the hearts of 1-3 day-old Wistar rats (from Shanghai Laboratory Animal Center of the Chinese Academy of Sciences, Shanghai, China) as described previously[15]. Cells were plated at M199 (Invitrogen, Carlsbad, CA, USA) containing 10% fetal bovine serum (FBS, Invitrogen, Carlsbad, CA, USA) for 48 h. Cells were incubated at 37 °C in an atmosphere with 5% CO_2, 20% O_2 and 75% Ar (standard gas mixture). Anoxia was attained with an airtight jar from which the O_2 was flushed with a gas mixture containing 5% CO_2 and 95% Ar for 30 min. Reoxygenation was realized by exchanging fresh medium and by its aeration with the standard gas mixture for 60 min. R-848 (0.01 to 1.0 µg/mL, Invivogen, San Diego, CA, USA) was dissolved in media and incubated with the cells for 24 h before anoxia-reoxygenation. The cells were incubated with cyclohexamide (CH, 1.0 µmol/L) for 10 min or *N*-acetylcysteine (NAC, the ROS scavenger, 1 mmol/L) for 1 h before the addition of R-848 (0.1 µg/mL) to the cultures.

Cell viability determination

Cell survival was evaluated by the ability to reduce MTT, an indication of metabolic activity. This viability assay was conducted in 96-well plates and read by spectrophotometry with a microplate reader (Bio-Tek Instruments, USA).

Measurement of lactate dehydrogenase (LDH), superoxide dismutase (SOD) activity and malondialdehyde (MDA) content in cells

Twenty-four hours after anoxia-reoxygenation, LDH was detected by a chromatometry assay kit, and SOD was measured by spectrophotometry using a commercially available detection kit (both kits were from Nanjing Jiancheng Biochemical Reagent CO, Nanjing, China) according to the manufacturer's instructions. The MDA content was determined using the thiobarbituric acid method with a commercial kit. The absorbance of each supernatant was measured at 532 nm.

Measurement of the rate of protein synthesis (incorporation of [³H]leucine)

Cells in the presence of [³H]leucine were collected 2 h after stimulation with R-848 (or/and CH), washed with PBS and precipitated with 10% trichloroacetic acid (TCA) at 4 °C for 1 h. The precipitate was solubilized in NaOH 0.15 mol/L. The cell lysate was vacuum-filtrated onto the glass-fiber filter. The filter was dried after being washed with 10% TCA and 100% ethanol. The radioactivity of the incorporated [³H]leucine was measured with a scintillation counter.

Measurement of intracellular ROS

Equal numbers of cells (10 000/well in 96-well plates in Hanks Balanced Salt Solution) were treated with 10 µmol/L 2,7-dichlorofluoroscein diacetate (DCF-DA) for 3 h. Cells were washed with phosphate-buffered saline and treated with 0.1 µg/mL R-848 during different time intervals. DCF-DA penetrates into viable cells, and inside the cells, it is converted to DCF, which later reacts with ROS and fluorescence. At the indicated time intervals, the intensity of the fluorescence was measured at an excitation wavelength of 485 nm and an emission wavelength of 527 nm and is expressed as percent of control fluorescence.

Transfer of iNOS siRNA to cardiomyocytes and R-848 treatment

iNOS siRNA was chemically synthesized by Shanghai GeneChem Co, Ltd. The targeted sequence resides within the open reading frame of the rat iNOS gene (accession: NM_012611), 898 nucleotides downstream of the start codon. The double strands of siRNA for rat iNOS were taken from published sequences[16]. Cells were transfected with a siRNA targeted for rat iNOS using Lipofectamine 2000 (Invitrogen). A siRNA consisting of a scrambled sequence of similar length was transfected as a control siRNA. Cells that experienced the same transfection procedure without any siRNA transfection were considered to be the sham-treated group. One day before transfection, cells were plated in 500 µL of growth medium without antibiotics such that they were 25%–45% confluent at the time of transfection. The transfected cells were cultured in M199 containing 10% fetal calf serum for 72 h after transfection. After 72 h of siRNA transfection, both the transfected and non-transfected (sham) cells were cultured for 1 d in serum-free M199 media to arrest growth before R-848 treatment. R-848 was added at a concentration of 0.1 µg/mL. Cells were collected for NFκB, HIF1α, and iNOS examination 24 h after R-848 treatment.

RNA extraction and reverse transcription real time PCR

Total RNA was isolated from cell pellets using a Qiagen RNeasy minikit (Qiagen, Valencia, CA, USA). First-strand cDNA synthesis was performed for each RNA sample using Superscript II RT Kit (GIBCO BRL, Life Technologies). iNOS mRNA expression was determined by real time PCR using SYBR Premix Ex TaqTM (Takara, Tokyo, Japan). Nucleotide sequences of specific primers for iNOS were designed as described previously[16]. A two-step PCR program was per-

formed. Data were collected and quantitatively analyzed on an ABI PRISM 7900HT sequence detection system (Applied Biosystems, Warrington, Cheshire, UK). The 18S rRNA gene was used as an endogenous control to normalize the differences in the amount of total RNA in each sample. All values were expressed as fold increase or decrease relative to the expression of 18S rRNA. The mean value of the replicates for each sample was calculated and expressed as cycle threshold (Ct: cycle number at which each PCR reaction reaches a predetermined fluorescence threshold, set within the linear range of all reactions). The amount of gene expression was then calculated as the difference (ΔCt) between the Ct value of the sample for the target gene and the mean Ct value of that sample for the endogenous control (18S rRNA). Relative expression was calculated as the difference ($\Delta\Delta$Ct) between the ΔCt values of the test sample and of the control sample. Relative expressions of genes of interest were calculated and expressed as $2^{-\Delta\Delta Ct}$ [17].

Preparation of protein extracts

The method by Andrews and Faller[18] was adopted to get the nuclear extracts. Briefly, the cells were washed with cold PBS and homogenized with a cell scraper. The pellets were collected after centrifugation. The cell pellets were then resuspended in buffer B (10 mmol/L HEPES-KOH pH 7.9, 1.5 mmol/L $MgCl_2$, 10 mmol/L KCl, 1 mmol/L DTT, 1 mmol/L PMSF, 10 µg/mL apotinin, 10 µg/mL pepstatin, 10 µg/mL leupeptin and 0.1% NP-40) and vortexed at 4 °C for 10 s. The tube was centrifuged to re-obtain the pellet. The pellets were resuspended in buffer C (20 mmol/L HEPES-KOH pH 7.9, 1.5 mmol/L $MgCl_2$, 400 mmol/L NaCl, 0.2 mmol/L EDTA, 25% glycerol, 1 mmol/L DTT, 1 mmol/L PMSF, 2 µg/mL aprotinin and 10 µg/mL leupeptin) and gently shaken at 4 °C for 30 min. Nuclear protein extracts were obtained by centrifugation at 12 000 revolutions per minute for 15 min. All the extracts were stored at -80 °C.

Electrophoretic mobility shift assay (EMSA)

Nuclear extracts (20 µg) were pre-incubated for 10 min in binding buffer (1 µg poly dI-dC, 10 mmol/L Tris-HCl pH 7.5, 50 mmol/L NaCl, 1 mmol/L EDTA, 5% Glycerol, 1 mmol/L DTT, 1 µg/µL BSA) on ice, followed by 30 min of incubation at room temperature with 1×10^5 dpm (about 0.5 ng) of a γ-^{32}P-labeled probe (Amersham Biosciences, Sunnyvale, CA, USA) containing the NFκB binding site 5'-AGTTGAGGGGACTTTC-CCAGGC-3' or the HIF1α binding site 5'-AGCGTAATGCGT-

GCCTCAGGA-3' (both from Santa Cruz Biotechnology, Santa Cruz, CA, USA). DNA-protein complexes were run on a 6% polyacrylamide gel. For supershift analysis, anti-p65, anti-p50 or anti HIF1α was incubated in the binding buffer for 15 min prior to adding the radiolabeled probe. Unlabeled probes for NFκB and HIF1α, both in 50× excess, were used as competition assays.

Western blotting analysis

The cytoplasmic extracts (20 µg) were mixed with buffer and boiled for 5 min. Proteins were electrophoresed followed by transfer to precoated nitrocellulose membranes. Membranes were blocked with 3% bovine serum albumin for 2 h, then incubated overnight with primary mouse antibodies against iNOS (Santa Cruz Biotechnology, Santa Cruz, CA, USA) or β-actin. Membranes were incubated with a primary antibody and were then exposed to peroxidase-conjugated anti-mouse IgG for 2 h. Proteins were visualized by enhanced chemiluminescence. Bands were scanned into Adobe Photoshop 5.0 and relative absorbency was calculated in Tina 2.0 software as a semi-quantitative method. The iNOS quantitative relative expression (RE) was calculated by comparison to β-actin.

Statistical analysis

The software SPSS13.0 was used to analyze the experimental data. Values are presented as mean±SD. All data were analyzed by one-way ANOVA. Statistical significance was defined as a P value less than 0.05.

Results

Effect of R-848 on neonatal cardiomyocyte viability, LDH, SOD activity and MDA content

We first assessed the effect of R-848 on cardiomyocytes. Cardiomyocytes were examined by testing their viability, LDH, SOD activity and MDA content. As shown in Table 1, the cell viability increased after being treated with R-848 ($P<0.05$), compared to the control group. In addition, pretreatment of cell cultures with R-848 (0.01 to 1.0 µg/mL) for 24 h before exposure to the anoxia-reoxygenation process significantly reduced cell death. The effect of R-848 was maximally protective at 0.1 µg/mL.

Further, the integrity of cell membranes or necrosis is estimated by LDH release into the media in response to oxidant burden. The toxicity caused by ROS was normally accompanied by an increase of lipid peroxides and was determined by MDA content and SOD activity. As shown in Table 1, there

Table 1. Cardioprotective effects of R-848 24 h after anoxia-reoxygenation injury assessed by cell viability, LDH activity, MDA content, and SOD activity. Mean±SD. $^bP<0.05$, $^cP<0.01$ vs control group.

	Cell viability (%)	LDH activity (U/L)	MDA content (nmol/L)	SOD activity (U/L)
Control	42.22±10.15	1477.80±148.91	15.71±3.58	14.44±1.35
R-848 (0.01 µg/mL)	56.11±11.13[b]	935.36±109.17[b]	11.21±3.74[b]	18.24±1.33[b]
R-848 (0.1 µg/mL)	87.57±14.89[c]	535.03±80.43[c]	6.98±1.62[c]	28.64±3.63[c]
R-848 (1.0 µg/mL)	61.41±12.11[b]	696.14±83.29[b]	9.02±2.54[b]	19.53±2.48[b]

was an increase in SOD activity, a decrease in LDH leakage and MDA production after R-848 pretreatment. There was a maximally protective effect of R-848 at the concentration of 0.1 μg/mL. Based on these dose response results, all further studies were performed with 0.1 μg/mL R-848. Collectively, these results indicate that pretreatment of cells with R-848 24 h before anoxia-reoxygenation provides marked protection.

R-848 induced ROS expression

As shown in Figure 1, 0.1 μg/mL R-848 increased ROS in a time-dependent manner. The increase in ROS after 30 min was followed by a slow increase until 4 h. ROS decreased almost to their original levels by 24 h.
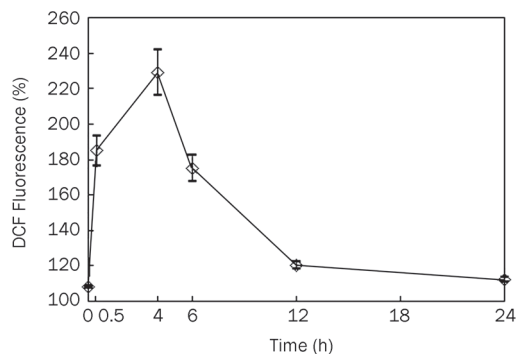
Figure 1. Measurement of intracellular ROS. Time course of induction of ROS by R-848 in cardiac myocytes. Cells were incubated with 0.1 μg/mL R-848. Fluorescence was measured at different time intervals as described in Materials and methods. The values expressed as percent of control fluorescence mean±SD of 8 wells and the figure is a representative from three experiments performed independently.

Effect of CH or NAC pretreatment in cell viability, LDH, SOD activity and MDA content after R-848 administration

As shown in Table 2, the toxic action of CH can be ignored because the anoxia-reoxygenation injury determined by cell viability, LDH activity, MDA content and SOD activity was similar between the control and CH groups. The NAC group did not present better results compared to the control group. NAC was administered 24 h before anoxia-reoxygenation, and

it is possible that its activity as a ROS scavenger was abolished 24 h later. Otherwise, the concentration used in this study was minor compared to the intense oxidative stress induced by anoxia-reoxygenation. The cardioprotective effect of R-848 was completely blocked after simultaneous CH pretreatment. Compared to the R-848 group, protein synthesis and the cardioprotective effect were also completely blocked after simultaneous NAC pretreatment. A ROS-dependent pathway was apparent in protein synthesis.

Activation of NFκB and HIF1α after R-848 administration, which was abolished after NAC pretreatment

We have demonstrated that the R-848-induced cardioprotective effect was completely blocked after NAC administration. Here, we have examined the activation of NFκB and HIF1. As shown in Figure 2A, we found that NFκB was activated by R-848, as evidenced by the retardation in the mobility of the DNA probe containing the NFκB motif R-848 groups. Conversely, low activation of NFκB was noted in the R-848+NAC group. The same status was seen in EMSA of HIF1 (Figure 2B). Therefore, we deduced that R-848 can activate these two transcription factors in a redox-dependent manner. The identity of the proteins bound to the probe was determined by supershift analysis. The antibody specific for the p65 subunit, the p50 subunit, or both subunits of the NFκB heterodimer in particular caused retardation of the mobility of the DNA probe (Figure 2C). The antibody specific for HIF1α also slowed probe mobility (Figure 2D). The supershift assay demonstrated the bands as NFκB and HIF1, respectively. Competitive inhibition with the cold probe for NFκB and HIF1α extinguished the bands. The competition assay further identified the bands as NFκB and HIF1, respectively.

iNOS protein was elevated after R-848 administration, and this elevation was attenuated after NAC pretreatment
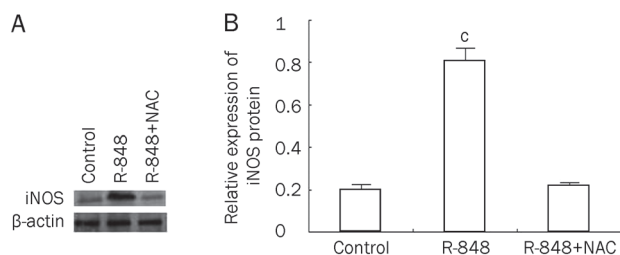
Detection of iNOS in cytoplasmic extracts by Western blotting showed that iNOS protein expression was robustly elevated after R-848 treatment; however, this elevation was abolished after NAC pretreatment. As shown in Figure 3, the RE in the R-848 group (0.810±0.057) was higher than the control group (0.204±0.019) and the R-848+NAC group (0.221±0.013), $P<0.01$. This agrees with the above result that protein synthesis was ROS-dependent.

Table 2. Effect of CH or NAC pretreatment in cell viability, LDH, SOD activity and MDA content after R-848 administration. $^c P<0.01$ *vs* control group.

	[^{3}H]leu incorporation (cpm/well)	Cell viability (%)	LDH activity (U/L)	MDA content (nmol/L)	SOD activity (U/L)
Control	2070±114	39.13±8.14	1601.23±147.86	17.26±3.97	14.14±1.39
CH	2101±116	39.07±7.76	1589.65±163.85	16.82±3.89	14.58±1.37
R-848	3191±249^c	82.32±16.45^c	540.21±71.17^c	5.38±1.78^c	24.69±3.61^c
CH+R-848	1946±97	40.40±8.68	1592.32±156.87	15.89±3.27	15.89±2.49
NAC	2053±105	38.79±9.92	1623.24±141.93	17.02±3.79	14.71±1.72
NAC+R-848	2119±123	43.63±10.27	1603.07±155.98	16.76±3.63	16.23±1.92
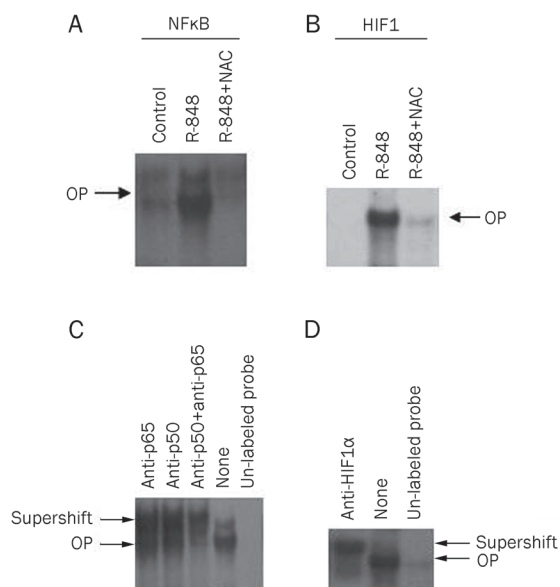
Figure 2. Identification of NFκB and HIF1 complexes in nuclear extracts by electrophoretic mobility shift assay (EMSA), supershift assay and competitive assay. Nuclear protein was extracted and analyzed by EMSA. Arrows denote oligonucleotide/protein complex. (A) Activation of NFκB. (B) Activation of HIF1. (C) To test the specificity of NFκB detection, nuclear extracts without preincubated with any antibody or competitive probe (none), or nuclear extracts were preincubated with an antibody against p65 subunit, an antibody against p50 subunit, antibodies against p65 plus p50 subunit, or 50 fold excess of un-labeled NFκB probe. (D) To test the specificity of HIF1 detection, nuclear extracts without preincubated with any antibody or competitive probe (none), or nuclear extracts were preincubated with an antibody against HIF1α subunit, or 50 fold excess of un-labeled HIF1 probe. EMSAs are representative of one experiment done in triplicate. OP, oligonucleotide/protein complex.


Figure 3. Immunoblotting analysis of iNOS after R-848 or R-848+NAC disposal. Detection of iNOS in cytoplasmic extracts was conducted 24 h after R-848 treatment. iNOS quantitative relative expression (RE) was calculated by comparing to β-actin. (A) iNOS protein in cytoplasmic extracts among groups. (B) Relative expression (RE) level of iNOS protein among groups. Results are expressed as mean±SD; Data are the mean of three separate experiments. $^{c}P<0.01$ *vs* control.

RNAi knocked down iNOS mRNA and protein expression in R-848-treated cells and abolished the cardioprotective effects

To investigate the effect of iNOS RNAi in R-848 treated cells,

all groups were treated with R-848 after RNAi. As shown in Figure 4, iNOS siRNA produced significant reductions in iNOS mRNA compared to the sham-treated and control groups. The relative iNOS mRNA expression in the control siRNA group (1.0±0.03) and the sham transfection group (0.97±0.04) was higher than the iNOS RNAi group (0.023±0.003), $P<0.01$. This indicates that RNAi knocked down the mRNA expression of iNOS effectively. Data are expressed as fold increase or decrease relative to the rRNA expression of the housekeeping gene 18S.
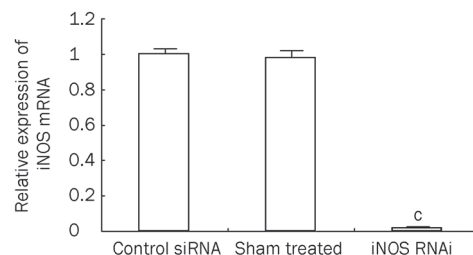
Figure 4. RNAi knocks down the mRNA expression of iNOS in R-848 treated cells. Detection of iNOS mRNA expression was conducted by real time PCR 24 h after R-848 treatment. The amount of gene expression was calculated as the difference (ΔCt) between the Ct value of the sample for the target gene and the mean Ct value of that sample for the endogenous control (18S rRNA). Relative expression was calculated as the difference ($\Delta\Delta$Ct) between the ΔCt values of the test sample and of the control sample. Relative expression of genes of interest was calculated and expressed as $2^{-\Delta\Delta Ct}$. $^{c}P<0.01$.

In comparison to the result of real time PCR, Western blotting for iNOS confirmed a similar pattern of expression of the protein, such that the level of iNOS was decreased with RNAi treatment. As shown in Figure 5, the RE in the sham transfection (0.77±0.047) and control siRNA groups (0.79±0.051) was higher than the iNOS RNAi group (0.33±0.013), $P<0.01$. This demonstrates that RNAi knocked down the expression of
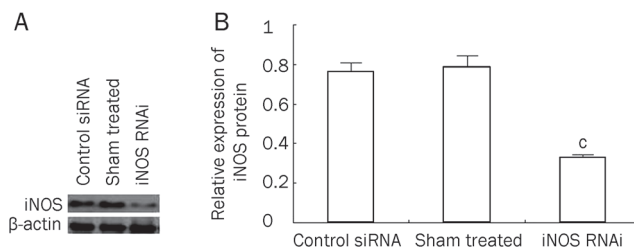
Figure 5. Immunoblotting analysis of iNOS after RNAi treatments. After 72 h of siRNA transfection, all cells were cultured for 24 h in serum-free media to arrest growth. Then, detection of iNOS in cytoplasmic extracts was conducted 24 h after R-848 treatment. iNOS quantitative relative expression (RE) was calculated by comparing to β-actin. (A) iNOS protein in cytoplasmic extracts among groups. (B) Relative expression (RE) level of iNOS protein among groups. Results are expressed as mean±SD; data are the mean of three separate experiments. $^{c}P<0.01$.

iNOS protein in R-848-treated cells.

After iNOS down-regulation by siRNA, we next examined its cardioprotective effect following anoxia-reoxygenation. As shown in Table 3, we found that the cardioprotective effect was completely lost in the iNOS siRNA group compared to the other two groups.

Discussion

Experimentally preconditioning with various TLR agonists has been proven to successfully attenuate ischemic damage through various protective mechanisms[19]. In this study, an endogenous protective mechanism called late preconditioning was explored in TLR7/8 agonist, R-848-induced cardioprotection. Late preconditioning induced ischemically or pharmacologically becomes apparent 12–24 h later and lasts 3–4 d. Nonlethal cellular stress causes the release of chemical signals such as nitric oxide (NO), ROS and adenosine, which serve as triggers for late preconditioning. Many pharmacological agents including proinflammatory cytokines and nitric oxide donors can also induce late preconditioning. This preconditioning is followed by a complex signal transduction cascade involving protein kinase Cε (PKCε), protein tyrosine kinase (PTK), mitogen-activated protein kinase (MAPKs) and as of yet unknown kinases. The recruitment of these kinases leads to the activation of NFκB and AP-1 and other transcription factors, which results in the synthesis of multiple cardioprotective proteins that serve as effectors 24 h after the preconditioning stimulus. The effector proteins include inducible nitric oxide synthase (iNOS), manganese superoxide dismutase (MnSOD), heat shock proteins (HSPs) and activated ion channels[20]. In summary, late preconditioning depends on genomic reprogramming, and effector protein synthesis is necessary for the development of late preconditioning[21]. Effector protein synthesis is required for the late preconditioning effects observed *in vitro* after pretreatment of rats with norepinephrine[22] or cells with osteopontin[23] and *in vivo* after six short ischemia-reperfusion cycles in rabbits[21]. In our study, the cardioprotective effect of R-848 was blocked after CH intervention.

Cardiomyocytes exposed to anoxia-reoxygenation *in vitro* experience a pathophysiological process similar to myocardial ischemia-reperfusion injury *in vivo*, and this is a well-established model. Pretreatment of cell cultures with R-848 for 24 h before exposure to anoxia-reoxygenation significantly increased cell survival and reduced LDH, SOD activity and MDA content. This demonstrates a prolonged cardioprotective effect that becomes apparent 24 h later, after pharmaco-

logic disposal.

As mentioned above, the R-848-induced protective effect was obvious 24 h after drug administration, and this effect was completely abolished after CH intervention. Therefore, we conclude that R-848-induced protection is achieved through a late preconditioning mechanism.

ROS plays a crucial role in the pathogenesis of myocardial ischemia-reperfusion injury giving rise to the "death signal" resulting in apoptotic cell death, leading to an infarcted heart. However, the cardioprotective abilities of preconditioning are completely abolished when the heart is perfused with NAC to scavenge ROS, suggesting that redox signaling plays a crucial role in generating survival signals during myocardial adaptation to ischemia. Therefore, ROS can function as signaling molecules in mediating survival signals[24]. The transduction signature of ischemic preconditioning is comprised of the activation of PKC via G-protein-coupled receptors and endogenously released oxygen radicals. Protection and PKC activation can be mimicked by extracellular generation or application of ROS[25]. Limited oxidative stress can actually induce preconditioning[26]. Recently, it was reported that when TLR4 is activated, ROS are produced and inflammatory cytokines and nitric oxide are released[27]. The universal adaptor MyD88 is also associated with TLR7/8, and is known to promote the generation of ROS. A signaling pathway including Burton's tyrosine kinase (Btk), PLC-1γ, DAG, PI, intracellular Ca^{2+}, PKCα/β and Nox was demonstrated to generate subsequent ROS after R-848 administration in THP-1 human myeloid marophages[13]. In our study, the generation of ROS after R-848 administration in cardiomyocytes was demonstrated directly by ROS measurement and indirectly by NAC administration. Because NAC pretreatment blocked protein synthesis and abolished the delayed protective effect completely, we deduce that generated ROS play important roles in transmitting survival signals in R-848-induced late preconditioning.

MyD88 is a universal adaptor that activates the inflammatory pathway in TLR7/8 signaling. In the MyD88-dependent pathway, transforming growth factor β-activated kinase 1 (TAK1), a mitogen-activated protein kinase (MAPK) kinase kinase (MAPKKK), activates two downstream pathways involving the inhibitor of NFκB kinase (IKK) complex and the MAPK family, p38 and c-Jun NH_2-terminal kinase. The IKK complex catalyzes the phosphorylation and proteolytic degradation of IκB proteins, which leads to the translocation of NFκB to the nucleus and its subsequent binding to its cognate DNA sequence on responsive genes[1]. Activated NFκB is

Table 3. Cardioprotective effects 24 h after anoxia-reoxygenation injury assessed by cell viability, LDH activity, MDA content, SOD activity after iNOS siRNA transfection disposal. $^c P<0.01$ *vs* control siRNA group.

	Cell viability (%)	LDH activity (U/L)	MDA content (nmol/L)	SOD activity (U/L)
Control siRNA	83.51±13.09	516.13±83.85	6.68±1.47	28.80±3.72
Sham treated	90.53±14.91	527.04±85.69	6.55±1.71	27.76±3.57
iNOS RNAi	46.60±11.19^c	1502.85±139.89^c	15.37±3.10^c	15.58±1.68^c

essential for ischemia late preconditioning. Recently, Nicholas SA et al demonstrated that ligand-induced activation of TLR7/8 results in the accumulation of HIF1α protein in THP-1 human myeloid macrophages via redox- and reactive nitrogen species-dependent mechanisms[12]. This activation is important for the support of cell survival as it protects the effector cells against the depletion of ATP and thus contributes to the production of proinflammatory cytokines[13, 14]. In our study, activated HIF1 was also demonstrated. Briefly, receptor tyrosine kinases play an important role in redox signaling via autophosphorylation of tyrosines along their own intracellular tails. We conclude that the mitogenic signals were mediated through the generation of ROS activate transcription factors including NFκB and HIF1α because the activation of NFκB and HIF1α was abolished after NAC pretreatment before R-848 administration.

Expression of HIF1α mRNA and protein is induced in the brains of neonatal rats following hypoxia, intraperitoneal injection of cobalt chloride or desferrioxamine, and this up-regulation is associated with protection against cerebral infarction following hypoxia and ischemia[28]. HIF1α expression is also likely to be involved in cardiac preconditioning because NOS2 expression is essential for late preconditioning, and an intact HIF1 DNA binding site in the NOS2 promoter is required for its transcriptional induction in hypoxic myocardial cells[29]. Previous reports demonstrated that HIF1 interacts with the iNOS promoter directly in myocardial extracts after intermittent hypoxic preconditioning by using chromatin immunoprecipitation assay (CHIP) analysis[30]. Moreover, other studies have indirectly observed the regulation of the iNOS by HIF1 in the heart with the use of knockout iNOS mice[31]. Besides HIF1 regulation, NFκB regulation of iNOS expression was also involved in anisomycin-elicited late preconditioning in the heart[32]. NFκB and HIF1α are the major modulators of iNOS gene expression. Therefore, iNOS protein expression in R-848-treated myocytes was determined. We demonstrated that iNOS protein expression elevated. However, this elevation was attenuated after NAC pretreatment. Because ROS-dependent activation of NFκB and HIF1α was proven in a previous experiment, we conclude that iNOS gene expression occurs through a ROS/ NFκB-HIF1α-dependent pathway.

There is substantial evidence that iNOS plays an obligatory role in NO generation in late preconditioning by acting as a mediator or an effector protein of preconditioning[20, 33]. NO generated from iNOS may open mitochondrial ATP-sensitive K$^+$ channels, which have been considered to be end-effectors for myocardial protection[34]. In our study, R-848-induced protection was also abolished after iNOS knocked down.

In summary, a ROS/ NFκB-HIF1α/ iNOS-dependent pathway was demonstrated in R-848-induced late preconditioning, and this result offers promise for the application of R-848 as a cardioprotectant in anoxia-reoxygenation (ischemia-reperfusion) injury. Recently, two classes of single-stranded TLR7/8 and TLR8 RNA agonists with diverse target cell and species specificities and immune response profiles were reported[35]. Goodchild et al demonstrated a model of TLR7/8 activation

by siRNAs, in which the two strands are denatured in the endosome, and single-stranded, U-rich RNA species activate TLR7/8[36]. A follow-up study is warranted to determine whether these highly specific RNA species already identified are also useful in the development of pharmacological agents with cardioprotective applications.

Author contribution

Yong-yi WANG and Song XUE designed the research; Yong-yi WANG and Wen-gang YANG performed the research; Sha LIU and Feng LIAN analyzed the data; Yong-yi WANG and Song XUE wrote the paper.

References

1 Kawai T, Akira S. TLR signaling. Semin Immunol 2007; 19: 24–32.

2 Chao W. Toll-like receptor signaling: a critical modulator of cell survival and ischemic injury in the heart. Am J Physiol Heart Circ Physiol 2009; 296: H1–12.

3 Timmers L, Sluijter JP, van Keulen JK, Hoefer IE, Nederhoff MG, Goumans MJ, et al. Toll-like receptor 4 mediates maladaptive left ventricular remodeling and impairs cardiac function after myocardial infarction. Circ Res 2008; 102: 257–64.

4 Zhu X, Bagchi A, Zhao H, Kirschning CJ, Hajjar RJ, Chao W, et al. Toll-like receptor 2 activation by bacterial peptidoglycan-associated lipoprotein activates cardiomyocyte inflammation and contractile dysfunction. Crit Care Med 2007; 35: 886–92.

5 Zhu X, Zhao H, Graveline AR, Buys ES, Schmidt U, Bloch KD, et al. MyD88 and NOS2 are essential for toll-like receptor 4-mediated survival effect in cardiomyocytes. Am J Physiol Heart Circ Physiol 2006; 291: H1900–9.

6 Mersmann J, Berkels R, Zacharowski P, Tran N, Koch A, Iekushi K, et al. Preconditioning by toll-like receptor 2 agonist Pam3CSK4 reduces CXCL1-dependent leukocyte recruitment in murine myocardial ischemia/reperfusion injury. Crit Care Med 2010; 38: 903–9.

7 Stevens SL, Ciesielski TM, Marsh BJ, Yang T, Homen DS, Boule JL, et al. Toll-like receptor 9: a new target of ischemic preconditioning in the brain. J Cereb Blood Flow Metab 2008; 28: 1040–7.

8 Wagner TL, Ahonen CL, Couture AM, Gibson SJ, Miller RL, Smith RM, et al. Modulation of TH1 and TH2 cytokine production with the immune response modifiers, 8-848 and imiquimod. Cell Immunol 1999; 191: 10–9.

9 Smits EL, Cools N, Lion E, Van Camp K, Ponsaerts P, Berneman ZN, et al. The Toll-like receptor 7/8 agonist resiquimod greatly increases the immunostimulatory capacity of human acute myeloid leukemia cells. Cancer Immunol Immunother 2010; 59: 35–46.

10. Triantafilou K, Orthopoulos G, Vakakis E, Ahmed MA, Golenbock DT, Lepper PM, et al. Human cardiac inflammatory responses triggered by Coxsackie B viruses are mainly Toll-like receptor (TLR) 8-dependent. Cell Microbiol 2005; 7: 1117-26.

11 Xuan YT, Tang XL, Banerjee S, Takano H, Li RC, Han H, et al. Nuclear factor B plays an essential role in the genesis of the late phase of ischemia preconditioning in conscious rabbits. Circ Res 1999; 84:

1095–109.

12 Nicholas SA, Sumbayev VV. The role of redox-dependent mechanisms in the downregulation of ligand-induced Toll-like receptors 7, 8 and 4-mediated HIF1 alpha prolyl hydroxylation. Immunol Cell Biol 2010; 88: 180–6.

13 Nicholas SA, Sumbayev VV. The involvement of hypoxia-inducible factor 1 alpha in Toll-like receptor 7/8-mediated inflammatory response. Cell Res 2009; 19: 973–83.

14 Natarajan R, Salloum FN, Fisher BJ, Kukreja RC, Fowler AA. Hypoxia inducible factor-1 activation by prolyl 4-hydroxylase-2 gene silencing attenuates myocardial ischemia reperfusion injury. Circ Res 2006; 98: 133–40.

15 Reinecke H, Zhang M, Bartosek T, Charles E. Survival, integration, and differentiation of cardiomyocyte grafts. Circulation 1999; 100: 193–202.

16 Li F, Mahato RI. iNOS gene silencing prevents inflammatory cytokine induced β-cell apoptosis. Mol Pharm 2008; 5: 407–17.

17 Kenneth JK, Thomas DS. Analysis of relative gene expression data using real-time quantitative PCR and the $2^{-\Delta\Delta Ct}$ method. Methods 2001; 25: 402–8.

18 Andrews NC, Faller DV. A rapid micropreparation technique for extraction of DNA-binding proteins from limiting numbers of mammalian cells. Nucleic Acid Res 1991; 19: 2499.

19 Leung PY, Packard AE, Stenzel-Poore MP. It's all in the family: multiple Toll-like receptors offer promise as novel therapeutic targets for stroke neuroprotection. Future Neurol 2009; 4: 201–8.

20 Bolli R. Preconditioning: a paradigm shift in the biology of myocardial ischemia. Am J Physiol Heart Circ Physiol 2007; 292: H19–27.

21 Rizvi A, Tang XL, Qiu Y, Xuan YT, Takano H, Jadoon AK, *et al*. Increased protein synthesis is necessary for the development of late preconditioning against myocardial stunning. Am J Physiol 1999; 277: H874–84.

22 Meng X, Cleveland JC Jr, Rowland RT, Mitchell MB, Brown JM, Banerjee A, *et al*. Norepinephrine-induced sustained myocardial adaptation to ischemia is dependent on alpha 1-adrenoceptors and protein synthesis. J Mol Cell Cardiol 1996; 28: 2017–25.

23 Wang YY, Chen BF, Shen DF, Xue S. Osteopontin protects against cardiac ischemia-reperfusion injury through late preconditioning. Heart Vessels 2009; 24: 116–23.

24 Das DK, Maulik N. Preconditioning protentiates redox signaling and converts death signal into survival signal. Arch Biochem Biophys 2003; 420: 305–11.

25 Baines CP, Goto M, Downey JM. Oxygen radicals released during ischemic preconditioning contribute to cardioprotection in the rabbit myocardium. J Mol Cell Cardiol 1997; 29: 207–16.

26 Dendorfer A, Heidbreder M, Hellwig-Burgel T, Johren O, Qadri F, Dominiak P. Deferoxamine induces prolonged cardiac preconditioning via accumulation of oxygen radicals. Free Radic Biol Med 2005; 38: 117–24.

27 Frantz S, Ertl G, Bauersachs J. Mechanisms of disease: Toll-like receptors in cardiovascular disease. Nat Clin Pract Cardiovasc Med 2007; 4: 444–54.

28 Bergeron M, Gidday JM, Yu AY, Semenza GL, Ferriero DM, Sharp FR. Hypoxia-inducible factor 1 (HIF-1) role in hypoxia-induced ischemic tolerance in neonatal rat brain. Ann Neurol 2000; 48: 285–96.

29 Jung F, Palmer LA, Zhou N, Johns RA. Hypoxic regulation of inducible nitric oxide synthase via hypoxia inducible factor-1 in cardiac myocytes. Circ Res 2000; 86: 319–25.

30 Belaidi E, Beguin PC, Levy P, Ribuot C, Godin-Ribuot D. Prevention of HIF-1 activation and iNOS gene targeting by low-dose cadmium results in loss of myocardial hypoxic preconditioning in the rat. Am J Physiol Heart Circ Physiol 2008; 294: H901–8.

31 Xi L, Taher M, Yin C, Salloum F, Kukreja RC. Cobalt chloride induces delayed cardiac preconditioning in mice through selective activation of HIF1α and AP-1 and iNOS signaling. Am J Physiol Heart Circ Physiol 2004; 287: H2369–75.

32 Zhao TC, Taher MM, Valerie KC, Kukreja RC. P38 triggers late preconditioning elicited by anisomycin in heart: involvement of NFκB and iNOS. Circ Res 2001; 89: 915–22.

33 Jones SP, Bolli R. The ubiquitous role of nitric oxide in cardioprotection. J Mol Cell Cardiol 2006; 40: 16–23.

34 West MB, Rokosh G, Obal D, Velayutham M, Xuan YT, Hill BG, *et al*. Cardiac myocyte-specific expression of inducible nitric oxide synthase protects against ischemia/reperfusion injury by preventing mitochondrial permeability transition. Circulation 2008; 118: 1970–8.

35 Forsbach A, Nemorin JG, Montino C, Müller C, Samulowitz U, Vicari AP, *et al*. Identification of RNA sequence motifs stimulating sequence-specific TLR8-dependent immune responses. J Immunol 2008; 180: 3729–38.

36 Goodchild A, Nopper N, King A, Doan T, Tanudji M, Arndt GM, *et al*. Sequence determinants of innate immune activation by short interfering RNAs. BMC Immunol 2009; 10: 40.

npg

Original Article

Chemerin/ChemR23 signaling axis is involved in the endothelial protection by K_{ATP} channel opener iptakalim

Rui-jun ZHAO[1], Hai WANG[1, 2, *]

[1]Department of Environmental Medicine, Institute of Health and Environmental Medicine, Academy of Military Medical Sciences, Beijing 100850, China; [2]Thadweik Academy of Medicine, Beijing 100039, China

Aim: To elucidate the modulation of the chemerin/ChemR23 axis by iptakalim-induced opening of K_{ATP} channels and to determine the role of the chemerin/ChemR23 axis in the iptakalim-mediated endothelial protection.
Methods: Cultured rat aortic endothelial cells (RAECs) were used. Chemerin secretion and ChemR23 protein expression were investigated using Western blot analysis. The gene expression level of ChemR23 was examined with RT-PCR. In addition, the release of nitric oxide (NO) was measured with a nitric oxide assay.
Results: Homocysteine, uric acid, high glucose, or oxidized low-density lipoprotein (ox-LDL) down-regulated the chemerin secretion and ChemR23 gene/protein expression in RAECs as a function of concentration and time, which was reversed by pretreatment with iptakalim (1-10 µmol/L). Moreover, these effects of iptakalim were abolished in the presence of the K_{ATP} channel antagonist glibenclamide (1 µmol/L). Both iptakalim and recombinant chemerin restored the impaired NO production in RAECs induced by uric acid, and the effects were abolished by anti-ChemR23 antibodies.
Conclusion: Iptakalim via opening K_{ATP} channels enhanced the endothelial chemerin/ChemR23 axis and NO production, thus improving endothelial function.

Keywords: ATP-sensitive potassium channel; iptakalim; endothelial cells; ChemR23; chemerin; NO

Introduction

Endothelial dysfunction, which induces disequilibrium in vascular tension, coagulation, and fibrinolysis, contributes to the pathological progression of cardiovascular diseases. It is a common initial risk factor for cardiovascular diseases, such as hypertension and coronary artery diseases[1]. Recent clinical trials have demonstrated that endothelial dysfunction is a predictor of the development of cardiovascular events[2]. Targeting endothelial dysfunction is an important therapeutic strategy for cardiovascular diseases. Iptakalim is a promising endothelial protective drug that opens K_{ATP} channels by preferentially activating the SUR2B/Kir6.1 subtype of K_{ATP} channels. Iptakalim protects endothelial function by enhancing the endothelial nitric oxide (NO) system[3]. It inhibits the endothelin-1 (ET-1) system by opening K_{ATP} channels, and it prevents the overexpression of adhesive molecules, such as intracellular adhesive molecule-1 (ICAM-1), vascular cell adhesion molecule-1 (VCAM-1), and monocyte chemoattractant protein-1

(MCP-1)[3]. Iptakalim also improves endothelial function by the activation of K_{ATP} channels, thereby preventing the progression of cardiac hypertrophy to congestive heart failure induced by pressure overload[4]. Improved endothelial function plays a critical role in the iptakalim-mediated prevention of the pathogenetic progression in cardiovascular diseases. The pathophysiology of endothelial dysfunction is complex and involves multiple mechanisms. However, the mechanism whereby iptakalim activates K_{ATP} channels to protect against endothelial dysfunction is not completely understood.

ChemR23, a G protein-coupled receptor, when activated by the fish oil derivative, resolving E1 (RvE1), reduced inflammation by inhibiting the transcriptional activation of NF-κB in neutrophils and by selectively counter-regulating leukocytes and platelets, which may correlate with peripheral atherosclerosis[5–7]. Chemerin, the endogenous ligand of ChemR23, is a newly discovered adipokine that regulates adipocyte differentiation and modulates chemotaxis and recruitment of NK cells, dendritic cells, and macrophages[8–10]. Chemerin is strongly associated with markers of inflammation, metabolic syndrome components, and atherosclerosis[11], for which endothelial dysfunction is a fundamental etiological factor. The chemerin/

ChemR23 system also plays an important role in endothelial cells[12, 13]. ChemR23 is reported to be a multifunctional receptor, but little is known about the relationship between the chemerin/ChemR23 axis and endothelial dysfunction[14]. We investigated the regulatory mechanisms of the chemerin/ChemR23 axis in dysfunctional endothelial cells induced by homocysteine, uric acid, glucose, and oxidized low-density lipoprotein (ox-LDL) and found that the chemerin/ChemR23 axis restores the impaired NO production and is upregulated by the K_{ATP} channel opener, iptakalim, in endothelial cells. Our data suggest that augmentation of the chemerin/ChemR23 axis may be a pivotal mechanism for protecting endothelial function by opening K_{ATP} channels.

Materials and methods
Chemicals
Iptakalim was synthesized by Nhwa Thad Pharmaceutical Co Ltd (Xuzhou, China). All other chemicals and materials were obtained from local commercial sources.

Cell culture
Rat aortic endothelial cells (RAECs) were isolated from normal Sprague-Dawley rat aortas as described previously[3]. The aorta was dissected out, sliced open, and rinsed with phosphate-buffered saline. It was cut into pieces and placed lumen surface-down in 100-mm culture dishes with 6 mL of M199 medium containing 20% fetal bovine serum (FBS) without growth supplements. On the third day, the aorta pieces were rinsed, and the collected cells were cultured in M199 medium containing 10% FBS, 100 mg/mL streptomycin, and 100 U/mL penicillin. The RAECs were grown to confluency at 37 °C in a humidified atmosphere of 95% air and 5% CO_2. A cobblestone morphology and positive immunofluorescence with antibodies against von Willebrand factor, factor VII-related antigen, or both confirmed that the cells were endothelial in nature. The culture medium was replaced every other day, and the cells were subcultured until they were approximately 90% to 95% confluent. Cells were seeded in 100-mm culture dishes or 6- or 24-well plates and used after three to five passages.

Experimental treatment
Prior to the experimental procedures, cell growth was arrested by culture in phenol red-free M199 supplemented with 1% FBS and 1% penicillin–streptomycin for 6 h. RAECs were treated with homocysteine at two different concentrations (0.5 or 0.1 mmol/L) for various time periods (6, 32, or 40 h) to determine the effect of iptakalim on chemerin secretion and ChemR23 gene/protein expression. RAECs were pretreated with iptakalim (0.1, 1, or 10 µmol/L) for 8 h before treatment with homocysteine, uric acid, glucose or ox-LDL; 1 µmol/L of glibenclamide was applied 1 h before iptakalim. RAECs were treated with 1 µg/mL of ChemR23 antibody for 1 h, iptakalim and recombinant chemerin for 6 or 8 h, and then with 7.5 mg/L of uric acid for 16 h, to determine NO production.

Western blot analysis
Protein expression of ChemR23
After the treatments, RAECs were lysed with a denaturing lysis buffer, and the protein content of the supernatant was determined. The protein extract was then boiled with sample buffer (Tris 100 mmol/L, pH 6.8, 20% glycerol, 4% sodium dodecyl sulfate (SDS) and 0.2% bromophenol blue) at a protein extract to buffer ratio of 4:1. Protein samples were separated using 8% SDS polyacrylamide gel electrophoresis (SDS-PAGE) and electrophoretically transferred to 0.45 µm polyvinylidene fluoride (PVDF) membranes (Millipore, Bedford, MA, USA) in a Tris−glycine transfer buffer. The membranes were washed in Tris-buffered saline with Tween 20 (TBS-T, 10 mmol/L Tris, pH 7.5, 0.1 mmol/L NaCl, 1 mmol/L EDTA, 0.1% Tween 20) three times for 5 min, incubated in TBS-T with 5% skimmed milk for 2 h and then incubated overnight at 4 °C with a ChemR23-specific antibody (42 kDa, goat, 1:500, Santa Cruz, CA, USA) and an α-tubulin-specific antibody as a loading control (55 kDa, mouse, 1:500, Santa Cruz) in TBS-T with 5% skimmed milk. The blot was then incubated with a secondary antibody (1:1000, R & D Systems, Abingdon, Oxon, UK) for 2 h. Immunoblots were developed with an ECL Plus substrate (PerkinElmer, LAS GmbH, Rodgau, Germany). The fluorograph film was developed with a Kodak GBX developer after the optimum exposure time and fixed with Kodak GBX (Kodak, Rochester, New York, USA). Protein expression was quantified by scanning the films and analyzing the densitometric volume of bands using a Personal Densitometer and Bio-Rad Quantity One software. The relative protein levels of ChemR23 were normalized to α-tubulin for each lane.

Secretion of chemerin
RAECs were cultured in 6-well plates for Western blot analysis of chemerin secretion. The cell culture supernatant and the total cell lysate were collected after treatment. The cell culture supernatant was mixed with an equal volume of sample buffer and subjected to SDS-PAGE before transfer to polyvinylidene fluoride (PVDF) membranes (0.22 µm). Primary antibodies for chemerin (18 kDa, mouse, 1:2000, Alexis Biochemicals, San Diego, CA, USA) in the cell culture supernatant and the control β-actin (43 kDa, mouse, 1:500, Santa Cruz, CA, USA) in the cell lysates were incubated overnight with the membranes in TBS-T with 5% skimmed milk at 4 °C. Membranes were subsequently washed with TBS-T and incubated with a secondary antibody (1:1000, R & D Systems, Abingdon, Oxon, UK) for 2 h at room temperature. The procedures for immunodetection and development of the fluorograph film were the same as mentioned above. Relative levels of chemerin secretion were normalized to β-actin in the corresponding samples of total cell lysates.

Reverse transcriptase-PCR (RT-PCR)
Total RNA was extracted from RAECs and reverse transcribed to cDNA using reverse transcriptase with random hexamer priming. PCR was performed using primers selected for

ChemR23 and β-actin. As a control, β-actin mRNA was amplified from the same RNA preparation. The primer sequences for ChemR23 were as follows: sense, 5'-ACCTATGCCGC-TATGGAC-3'; and antisense, 5'-GACAGTGAGCAGGAA-GACG-3', 108 bp. The primer sequences for β-actin were as follows: sense, 5'-GTGTTGTCCCTGTATGCCTCTGG-3'; and antisense, 5'-GCTGTGGTGGTGAAGCTGTAGCC-3', 197 bp. The PCR was conducted for 35 cycles of 95 °C for 30 s, 56 °C for 30 s, and 72 °C for 40 s. The final cycle included an extension at 72 °C for 10 min. The PCR products were analyzed on a 2% agarose gel, and the intensity of the bands was measured with densitometry. Results were expressed as the density of ChemR23 normalized to β-actin in the same sample.

NO measurement
To assess the effects of iptakalim and recombinant chemerin on NO release, the cultured RAECs were seeded on 24-well culture plates and grown to full confluence. Because of the instability of NO in physiological solutions, most of the NO is typically rapidly converted to nitrite (NO_2^-), which is further broken down to nitrate (NO_3^-). Therefore, the level of the NO_2^-/NO_3^- ratio in the culture medium was measured with a Nitric Oxide Assay Kit (Nanjing Jiancheng Bioengineering Institute, Nanjing, China) according to the manufacturer's instructions. Briefly, nitrate was converted to nitrite with aspergillus nitrite reductase, and the total nitrite was measured using the colorimetric method of the Griess assay as previously described[15].

Statistical analysis
The Student's *t*-test and one-way ANOVA for paired values were used. Data are expressed as mean ± SD. $P<0.05$ was considered to be statistically significant.

Results
Chemerin secretion and ChemR23 protein/gene expression are upregulated by the iptakalim-mediated opening of K_{ATP} channels in homocysteine-induced dysfunctional RAECs
ChemR23 plays an important role in the prevention of cardiovascular events, so we hypothesized that the chemerin/ChemR23 axis was involved in the endothelial protective effect of iptakalim via the opening of K_{ATP} channels. We investigated the effect of iptakalim on chemerin secretion (Figure 1A) and ChemR23 protein/gene expression (Figure 1B, 1C) to explore the effects of modulating K_{ATP} channel activation on the chemerin/ChemR23 axis in endothelial cells. Homocysteine treatment of RAECs resulted in decreased chemerin secretion and decreased levels of ChemR23 gene/protein expression. A concentration of 0.1–10 µmol/L of iptakalim reversed these decreases in a dose-dependent manner, which was antagonized by the K_{ATP} channel antagonist glibenclamide (Figure 1). The opening of K_{ATP} channels by iptakalim upregulated chemerin secretion and ChemR23 gene/protein expression in RAECs (Figure 1).

ChemR23 gene expression is downregulated by homocysteine, uric acid, glucose, and ox-LDL as a function of concentration and time
Endothelial dysfunction is independently induced by hyperhomocysteinemia, hyperuricemia, hyperglycemia, and hyperlipemia. ChemR23 protein/gene expression was downregulated in homocysteine-induced dysfunctional endothelial cells, so we investigated whether ChemR23 expression was also downregulated by uric acid, glucose, and ox-LDL. RAEC treatment with homocysteine, uric acid, glucose, and ox-LDL resulted in decreased ChemR23 gene expression levels as a function of concentration and time. Increased homocysteine, uric acid, glucose, and ox-LDL levels represent risk factors for cardiovascular diseases associated with endothelial dysfunction. Gene expression levels of ChemR23 are decreased in dysfunctional endothelium (Figure 2).

Iptakalim opens K_{ATP} channels to reverse the downregulation of ChemR23 gene expression induced by uric acid, glucose, and ox-LDL
Iptakalim upregulated the chemerin/ChemR23 axis in homocysteine-induced dysfunctional endothelial cells, so we hypothesized that iptakalim would have the same effect on the chemerin/ChemR23 axis in dysfunctional endothelial cells induced by hyperuricemia, hyperglycemia, and hyperlipemia. A concentration of 0.1–10 µmol/L of iptakalim restored ChemR23 gene expression in a dose-dependent manner in endothelial cells treated with uric acid, glucose, and ox-LDL, and this restoration was antagonized by glibenclamide (Figure 3). Chemerin secretion and ChemR23 protein expression were correlated with ChemR23 gene expression, so they may also be upregulated by iptakalim via the opening of K_{ATP} channels when endothelial dysfunction is induced by hyperuricemia, hyperglycemia, and hyperlipemia. Thus, the chemerin/ChemR23 axis may be upregulated by iptakalim via the activation of endothelial K_{ATP} channels in dysfunctional endothelial cells.

Iptakalim and recombinant chemerin promote NO production, which is involved in the activation of ChemR23 in dysfunctional endothelial cells
A ChemR23 antibody was used to block the effects of iptakalim and recombinant chemerin on endothelial NO production, which helped clarify the role of the chemerin/ChemR23 axis in iptakalim protection against endothelial dysfunction. NO production was decreased when the RAECs were treated with uric acid. Iptakalim (10 µmol/L) upregulated the NO production impaired by uric acid and the effect of iptakalim was blocked by the ChemR23 antibody (Figure 4A). Recombinant chemerin (10, 100, and 300 ng/L) increased NO production compared to uric acid (Figure 4B). The effects of 10 µmol/L of iptakalim and 100 ng/L of chemerin were blocked in the presence of the ChemR23 antibody (1 µg/mL; Figure 4B). Thus, ChemR23 activation directly participates in enhancing the endothelial NO production and is correlated with the opening
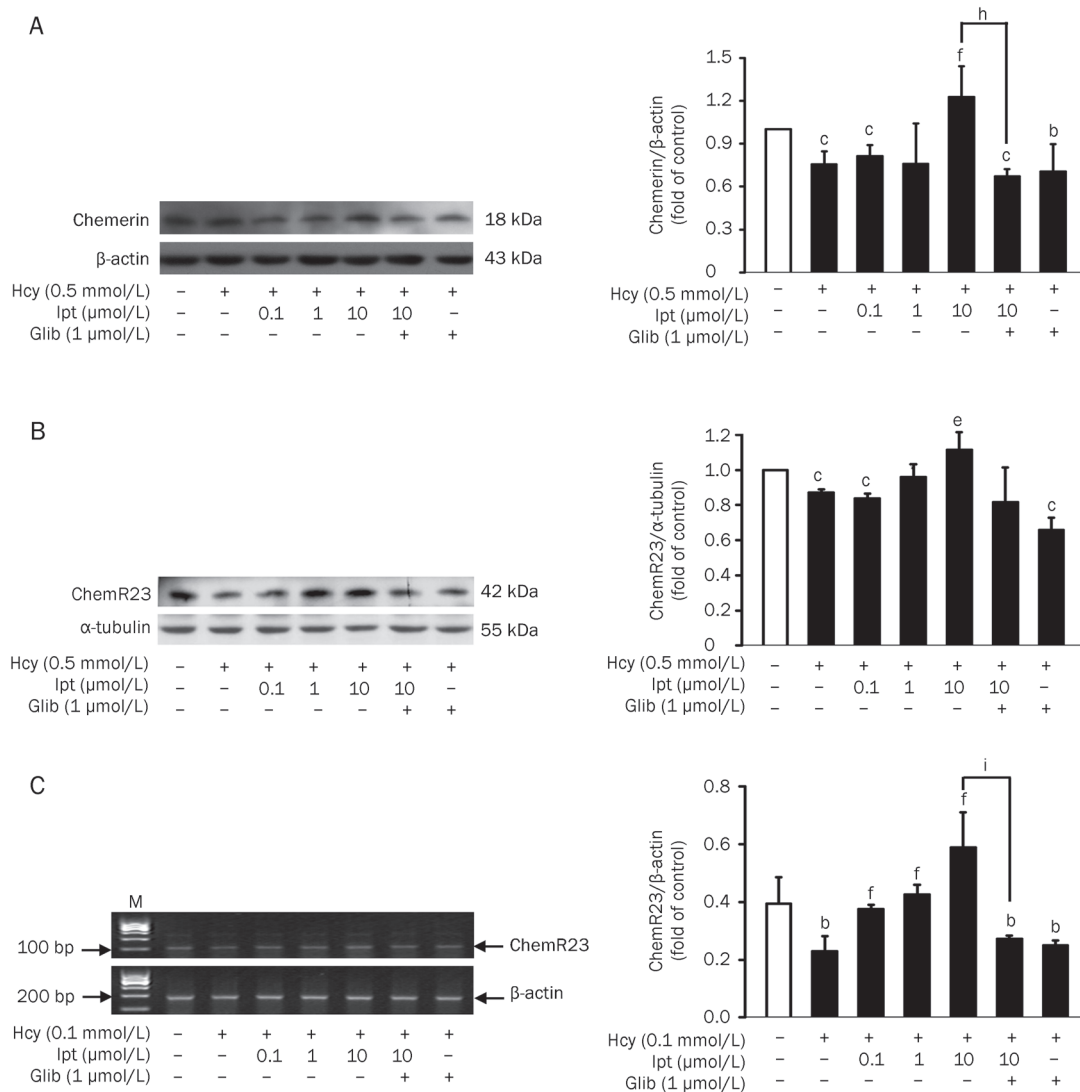
Figure 1. Iptakalim upregulates the chemerin secretion and ChemR23 protein/gene expression in dysfunctional RAECs induced by homocysteine. (A) Representative Western blots and statistical analysis showing the changes in the effect of iptakalim (Ipt) (0.1–10 μmol/L) on chemerin secretion when cells were treated/untreated with 0.5 mmol/L of homocysteine (Hcy) for 40 h. Values are the mean of three separate experiments, and the data represent chemerin normalized to the β-actin. (B) Representative Western blots and statistical analysis showing the changes in the effect of iptakalim (Ipt) (0.1–10 μmol/L) on ChemR23 protein expression when cells were treated/untreated with 0.5 mmol/L of homocysteine for 32 h. Values are the mean of three separate experiments, and the data represent ChemR23 normalized to the α-tubulin. (C) Representative RT-PCR and statistical analysis showing changes in the effect of iptakalim (Ipt) (0.1–10 μmol/L) on ChemR23 gene expression when cells were treated/untreated with 0.1 mmol/L of homocysteine for 6 h (n=4). PCR primers against rat ChemR23 and β-actin amplified a single band of the expected size (108 and 197 bp) in all samples. DNA markers (M) ranging from 100 to 600 bp were used for electrophoresis. Glibenclamide (Glib, 1 μmol/L) was used as a K_{ATP} channel antagonist. Data are expressed as mean±SD. The ANOVA test was used. [b]$P<0.05$, [c]$P<0.01$ *vs* corresponding control; [e]$P<0.05$, [f]$P<0.01$ *vs* homocysteine stimuli; [h]$P<0.05$, [i]$P<0.01$ *vs* iptakalim pretreatment, respectively.

of K_{ATP} channels in endothelial cells.

Discussion

In this study, we showed that iptakalim may regulate the chemerin/ChemR23 axis via the opening of K_{ATP} channels in the protection against endothelial dysfunction. Iptakalim restored the impaired chemerin secretion and ChemR23 gene/protein expression induced by homocysteine, uric acid, glucose, and ox-LDL in RAECs. The effects of iptakalim were

mediated via K_{ATP} channel opening, which was antagonized by glibenclamide. Furthermore, iptakalim and recombinant chemerin restored the NO production that was decreased by uric acid, and this effect was abrogated by anti-ChemR23 antibodies. Our data suggest that the chemerin/ChemR23 axis is a novel molecular pathway that is involved in iptakalim-mediated protection against endothelial dysfunction and cardiovascular pathology.

ChemR23 can be activated by its endogenous ligand
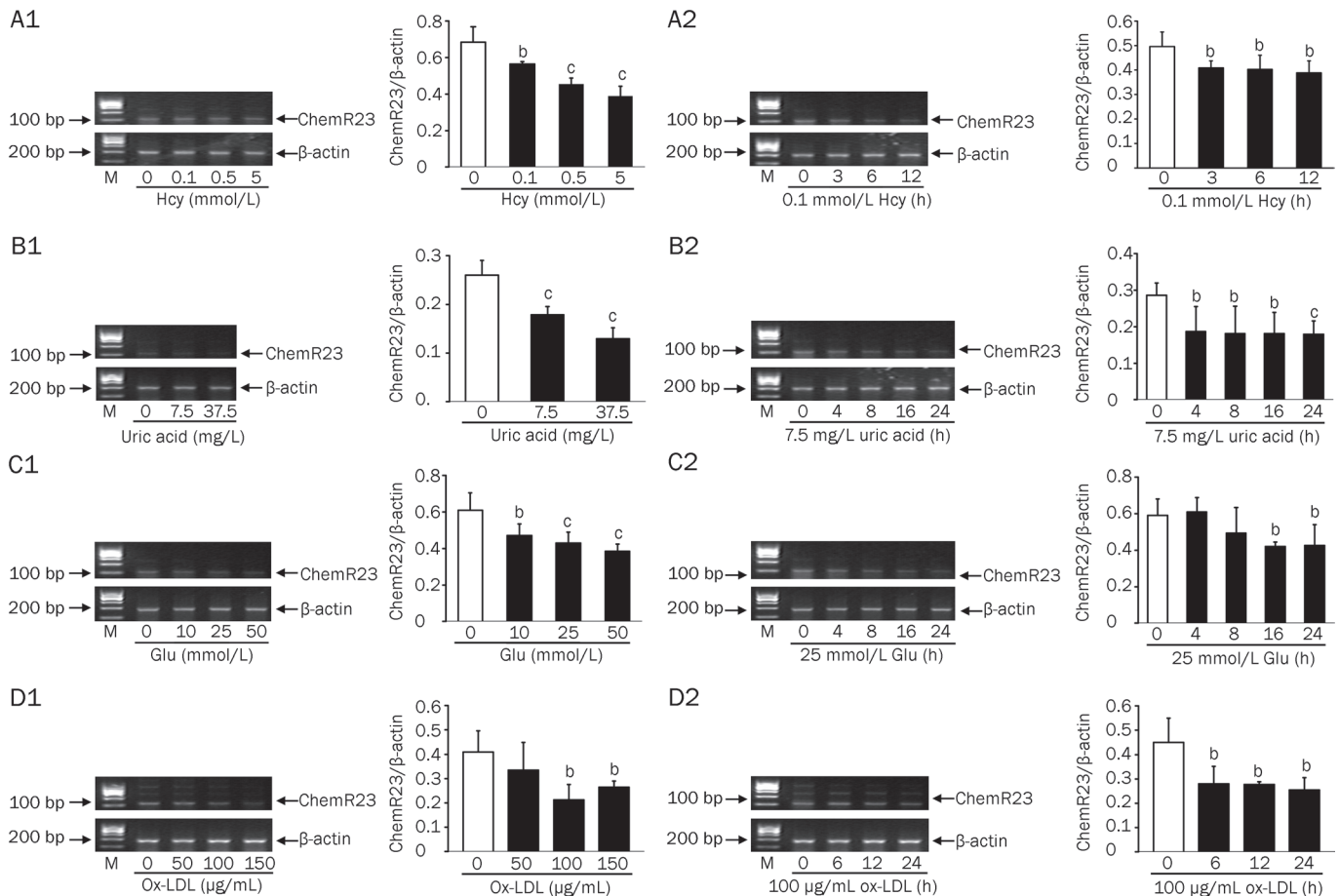
Figure 2. Downregulation of ChemR23 gene expression as a function of concentration and time by homocysteine (A), uric acid (B), glucose (C), and ox-LDL (D) in RAECs. RAECs were treated for various time periods and various concentrations of homocysteine (Hcy), uric acid, glucose (Glu), and ox-LDL. Data are expressed as mean±SD. $n=4$. The t-test was used. [b]$P<0.05$, [c]$P<0.01$ *vs* the corresponding vehicle control.

chemerin and its exogenous ligand RvE1, which is an endogenous anti-inflammatory mediator derived from eicosapentaenoic acid. ChemR23, when activated by RvE1, induces the phosphorylation of the ribosomal protein S6 of the PI3K-Akt pathway, which may contribute to the resolution of vascular inflammation and ADP-dependent platelet activation in pathological cardiovascular events[16, 17]. The chemerin/ChemR23 axis may become weaker in pathological conditions, which may not only impair endothelial function, but may also accelerate cardiovascular inflammation[18]. We demonstrated that the expression of the chemerin/ChemR23 axis fluctuates with endothelial function. We found that homocysteine, uric acid, glucose, and ox-LDL all decreased ChemR23 mRNA levels as a function of concentration and time. Iptakalim protected endothelial function by opening endothelial K_{ATP} channels, and it restored the impaired chemerin secretion and ChemR23 gene/protein expression caused by homocysteine, uric acid, glucose, and ox-LDL in endothelial cells. Glibenclamide antagonized the effects of iptakalim, which indicates that the effects of iptakalim are mediated by K_{ATP} channel opening. In aortic endothelial cells, K_{ATP} channels consist of a heteromultimeric complex of Kir6.1, Kir6.2, and SUR2B subunits[19]. Glibenclamide and iptakalim bind with different sites on the regulatory subunit, the sulfonylurea receptor[20]. However, some investigators reported that chemerin expression and secretion were enhanced in lupus erythematosus dermal endothelial cells and in interleukin-1β-stimulated adipocytes[13, 21]. This paradox can be reconciled because these cell types differ in their distinctive physiological functions. ChemR23 expression was downregulated by cardiovascular risk factors, which is consistent with other reports, that showed ChemR23 is downregulated by interleukin-2 or interleukin-15 in NK cells and by proinflammatory cytokines and Toll-like receptor ligands in macrophages[9, 22]. The downregulation of ChemR23 expression was correlated with the inhibition of cell migration in response to chemerin in NK cells, which may indicate that the receptor function of ChemR23 is decreased along with its downregulation[9]. Our data suggest that K_{ATP} channel opening upregulates the chemerin/ChemR23 axis in dysfunctional endothelial cells, but the mechanism remains unclear.

NO is one of the most important vasodilating substances released by the endothelium, and it inhibits growth and
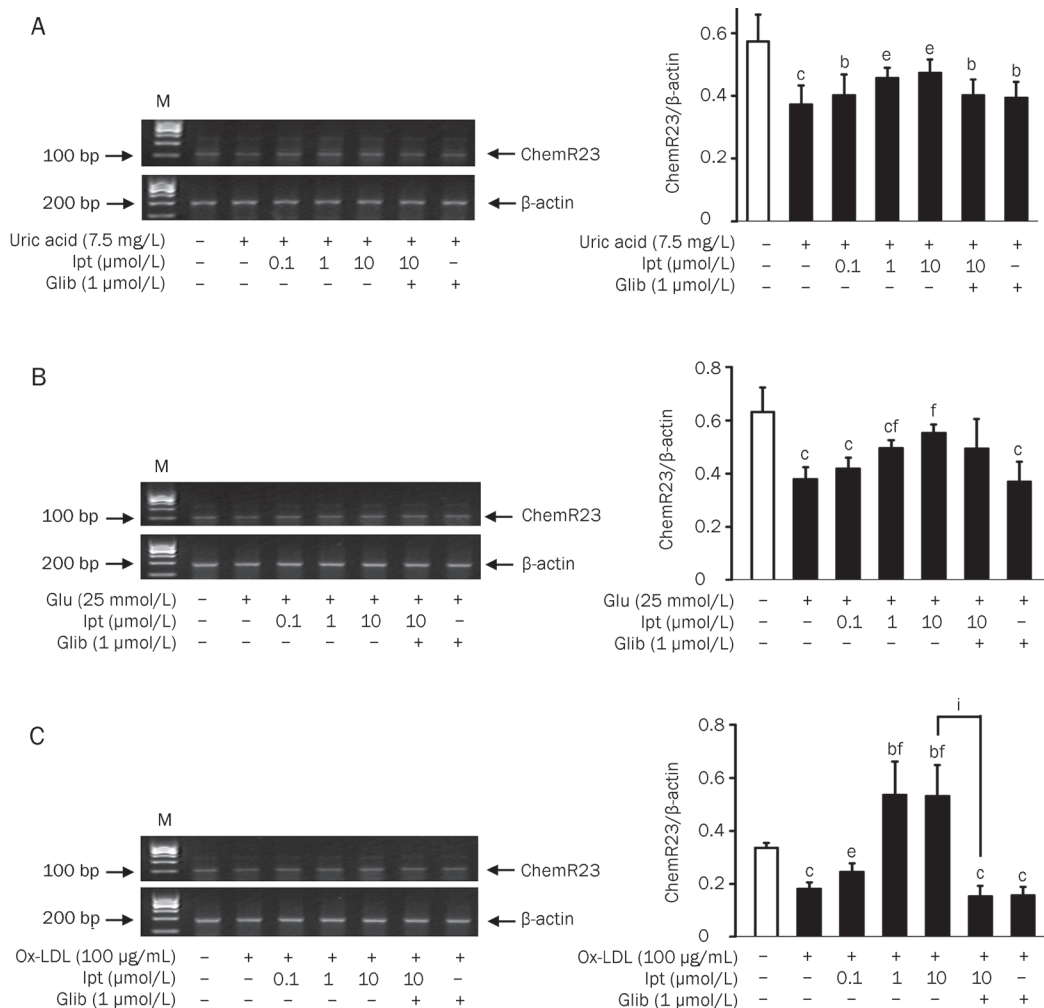
Figure 3. Iptakalim restores ChemR23 gene expression decreased by uric acid (A), high glucose (B), and ox-LDL (C) in RAECs. RAECs were pretreated with/without iptakalim (Ipt) for 8 h and then stimulated with 7.5 mg/L uric acid for 24 h, 25 mmol/L glucose (Glu) for 16 h, and 100 µg/mL ox-LDL for 12 h. Glibenclamide (Glib, 1 µmol/L) was applied 1 h before iptakalim. Data are expressed as mean±SD. $n=4$. The ANOVA test was used. [b]$P<0.05$, [c]$P<0.01$ vs the corresponding control; [e]$P<0.05$, [f]$P<0.01$ vs uric acid, glucose, or ox-LDL stimuli; [i]$P<0.01$ vs iptakalim pretreatment, respectively.

inflammation, has anti-aggregant effects on platelets and plays an important role in cardiovascular diseases. The ability to synthesize NO reflects the functional status of endothelial cells. The endothelial NO system can be downregulated by a number of cardiovascular risk factors, such as hyperhomocysteinemia, hyperuricemia, hyperglycemia, and hyperlipemia[3, 15]. We detected effects of the chemerin/ChemR23 axis on NO-related endothelial function. We found that iptakalim and chemerin restored NO production; this was decreased by uric acid in RAECs, and this decrease was abolished by anti-ChemR23 antibodies. This suggests that the activation of ChemR23 is necessary for iptakalim and chemerin improvements in endothelial function. Endothelial NO is mainly produced by eNOS, the enzymatic activity of which is regulated at several levels, including Ca^{2+}/calmodulin binding and the interaction of eNOS with associated proteins[23]. ChemR23 activation resulted in intracellular calcium release promoted by recombinant chemerin in ChemR23-expressing

CHO-K1 cells[24]. Calcium enhanced the phosphorylation of eNOS and NO release by binding to calmodulin[25]. Although several studies have reported that the chemerin/ChemR23 axis is strongly associated with cardiovascular disease and aspects of metabolic syndrome[11, 26, 27], there was no direct evidence for the role of the chemerin/ChemR23 axis in maintaining endothelial function. The chemerin/ChemR23 axis enhances the NO system, so it is likely that the chemerin/ChemR23 axis contributes to the maintenance of endothelial function.

A previous study demonstrated that iptakalim upregulated the NO system and downregulated the endothelin system and the production of adhesion molecules ICAM-1/VCAM-1/MCP-1 in endothelial cells to protect against the progression of cardiac hypertrophy to congestive heart failure[3, 4]. Endothelial dysfunction is characterized by the reduced bioavailability of NO, an alteration in the production of prostanoids, impairment of endothelium-dependent hyperpolarization, and an increased release of endothelin-1, all of which separately or in
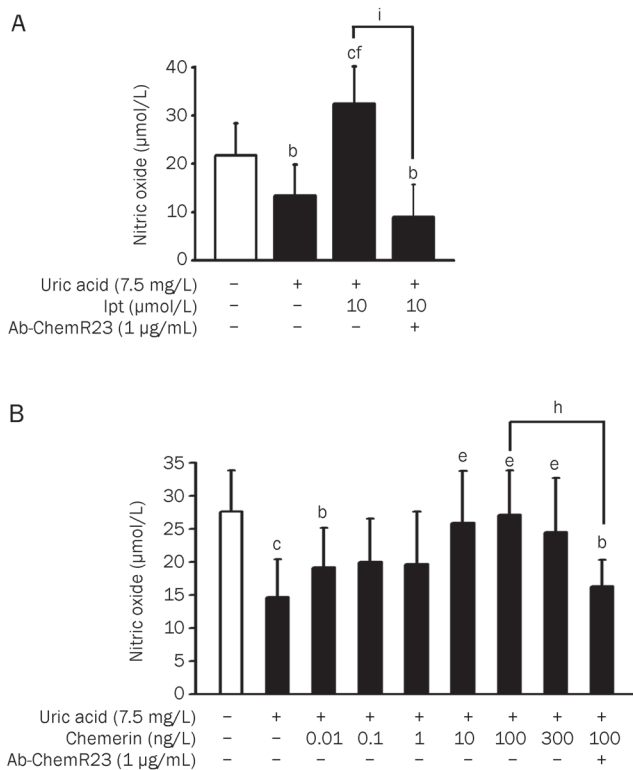
Figure 4. Iptakalim (A) and chemerin (B) restored NO production decreased by uric acid in RAECs. RAECs were preincubated with/without 1 μg/mL Ab-ChemR23 for 1 h and then treated with iptakalim (Ipt) or recombinant chemerin for 6 or 8 h, respectively, followed by incubation with 7.5 mg/L uric acid for 16 h. NO production in the cell culture supernatant was determined with an nitrate reductase assay at the end of incubation. Data are expressed as mean±SD. $n=7$. The ANOVA test was used. [b]$P<0.05$, [c]$P<0.01$ vs corresponding control; [e]$P<0.05$, [f]$P<0.01$ vs uric acid stimuli; [h]$P<0.05$, [i]$P<0.01$ vs iptakalim or chemerin pretreatment, respectively.

association contribute to endothelial dysfunction[1]. Elevated NO contributes to the equilibrium of vasoactive mediators involved in the regulation of endothelial function and vascular homeostasis. We suggest that the chemerin/ChemR23 axis may attenuate the endothelin system and the overexpression of adhesion molecules in dysfunctional endothelial cells because the chemerin/ChemR23 axis enhances the NO system. Upregulation of the chemerin/ChemR23 axis is a well-supported explanation for how iptakalim improves endothelial function. The chemerin/ChemR23 axis is connected with endothelial function by two lines of evidence. The first is that the chemerin/ChemR23 axis is an endogenous pathway that improves endothelial function. The second is that the chemerin/ChemR23 axis can be modulated by pharmacological intervention via the opening of K_{ATP} channels. The chemerin/ChemR23 axis may potentially be a new drug target in endothelial function improvement and cardiovascular disease.

The present study demonstrates that the opening of K_{ATP} channels by iptakalim enhances the chemerin/ChemR23 axis

in dysfunctional cultured RAECs. ChemR23 activation may be the mechanism by which iptakalim and chemerin increase NO production. This may be a new molecular pathway by which iptakalim upregulates the chemerin/ChemR23 axis to improve endothelial function. A detailed molecular and functional analysis of the role of the chemerin/ChemR23 axis in endothelial function should provide further understanding of the relationship between the chemerin/ChemR23 axis and endothelial function.

Acknowledgements

Author contribution

Hai WANG designed the study, and Rui-jun ZHAO performed the research, analyzed data, and wrote the paper.

References

1   Feletou M, Vanhoutte PM. Endothelial dysfunction: a multifaceted disorder. Am J Physiol Heart Circ Physiol 2006; 291: H985–1002.

2   Minamino T, Hori M. Protecting endothelial function: A novel therapeutic target of ATP-sensitive potassium channel openers. Cardiovasc Res 2007; 73: 448–9.

3   Wang H, Long C, Duan Z, Shi C, Jia G, Zhang Y. A new ATP-sensitive potassium channel opener protects endothelial function in cultured aortic endothelial cells. Cardiovasc Res 2007; 73: 497–503.

4   Gao S, Long CL, Wang RH, Wang H. K(ATP) activation prevents progression of cardiac hypertrophy to failure induced by pressure overload via protecting endothelial function. Cardiovasc Res 2009; 83: 444–56.

5   Ho KJ, Spite M, Owens CD, Lancero H, Kroemer AH, Pande R, *et al*. Aspirin-triggered lipoxin and resolvin E1 modulate vascular smooth muscle phenotype and correlate with peripheral atherosclerosis. Am J Pathol 2010; 177: 2116–23.

6   Arita M, Ohira T, Sun YP, Elangovan S, Chiang N, Serhan CN. Resolvin E1 selectively interacts with leukotriene B4 receptor BLT1 and ChemR23 to regulate inflammation. J Immunol 2007; 178: 3912–7.

7   Dona M, Fredman G, Schwab JM, Chiang N, Arita M, Goodarzi A, *et al*. Resolvin E1, an EPA-derived mediator in whole blood, selectively counterregulates leukocytes and platelets. Blood 2008; 112: 848–55.

8   Albanesi C, Scarponi C, Pallotta S, Daniele R, Bosisio D, Madonna S, *et al*. Chemerin expression marks early psoriatic skin lesions and correlates with plasmacytoid dendritic cell recruitment. J Exp Med 2009; 206: 249–58.

9   Parolini S, Santoro A, Marcenaro E, Luini W, Massardi L, Facchetti F, *et al*. The role of chemerin in the colocalization of NK and dendritic cell subsets into inflamed tissues. Blood 2007; 109: 3625–32.

10 Maheshwari A, Kurundkar AR, Shaik SS, Kelly DR, Hartman Y, Zhang W, *et al*. Epithelial cells in fetal intestine produce chemerin to recruit macrophages. Am J Physiol Gastrointest Liver Physiol 2009; 297: G1–G10.

11 Lehrke M, Becker A, Greif M, Stark R, Laubender RP, von Ziegler F, *et al*. Chemerin is associated with markers of inflammation and components of the metabolic syndrome but does not predict coronary atherosclerosis. Eur J Endocrinol 2009; 161: 339–44.

12 Kaur J, Adya R, Tan BK, Chen J, Randeva HS. Identification of

chemerin receptor (ChemR23) in human endothelial cells: chemerin-induced endothelial angiogenesis. Biochem Biophys Res Commun 2010; 391: 1762–8.

13 Vermi W, Riboldi E, Wittamer V, Gentili F, Luini W, Marrelli S, *et al*. Role of ChemR23 in directing the migration of myeloid and plasmacytoid dendritic cells to lymphoid organs and inflamed skin. J Exp Med 2005; 201: 509–15.

14 Yoshimura T, Oppenheim JJ. Chemokine-like receptor 1 (CMKLR1) and chemokine (C-C motif) receptor-like 2 (CCRL2); Two multifunctional receptors with unusual properties. Exp Cell Res 2011; 317: 674-84.

15 Long CL, Qin XC, Pan ZY, Chen K, Zhang YF, Cui WY, *et al*. Activation of ATP-sensitive potassium channels protects vascular endothelial cells from hypertension and renal injury induced by hyperuricemia. J Hypertens 2008; 26: 2326–38.

16 Fredman G, Van Dyke TE, Serhan CN. Resolvin e1 regulates adenosine diphosphate activation of human platelets. Arterioscler Thromb Vasc Biol 2010; 30: 2005–13.

17 Ohira T, Arita M, Omori K, Recchiuti A, Van Dyke TE, Serhan CN. Resolvin E1 receptor activation signals phosphorylation and phagocytosis. J Biol Chem 2010; 285: 3451–61.

18 Merched AJ, Ko K, Gotlinger KH, Serhan CN, Chan L. Atherosclerosis: evidence for impairment of resolution of vascular inflammation governed by specific lipid mediators. FASEB J 2008; 22: 3595–606.

19 Yoshida H, Feig JE, Morrissey A, Ghiu IA, Artman M, Coetzee WA. K_{ATP} channels of primary human coronary artery endothelial cells consist of a heteromultimeric complex of Kir6.1, Kir6.2, and SUR2B subunits. J Mol Cell Cardiol 2004; 37: 857–69.

20 Pan Z, Huang J, Cui W, Long C, Zhang Y, Wang H. Targeting hyper-tension with a new adenosine triphosphate-sensitive potassium channel opener iptakalim. J Cardiovasc Pharmacol 2010; 56: 215–28.

21 Kralisch S, Weise S, Sommer G, Lipfert J, Lossner U, Bluher M, *et al*. Interleukin-1beta induces the novel adipokine chemerin in adipocytes *in vitro*. Regul Pept 2009; 154: 102–6.

22 Zabel BA, Ohyama T, Zuniga L, Kim JY, Johnston B, Allen SJ, *et al*. Chemokine-like receptor 1 expression by macrophages *in vivo*: regulation by TGF-beta and TLR ligands. Exp Hematol 2006; 34: 1106–14.

23 Holton M, Mohamed TM, Oceandy D, Wang W, Lamas S, Emerson M, *et al*. Endothelial nitric oxide synthase activity is inhibited by the plasma membrane calcium ATPase in human endothelial cells. Cardiovasc Res 2010; 87: 440–8.

24 Wittamer V, Franssen JD, Vulcano M, Mirjolet JF, Le Poul E, Migeotte I, *et al*. Specific recruitment of antigen-presenting cells by chemerin, a novel processed ligand from human inflammatory fluids. J Exp Med 2003; 198: 977–85.

25 Butt E, Bernhardt M, Smolenski A, Kotsonis P, Frohlich LG, Sickmann A, *et al*. Endothelial nitric-oxide synthase (type III) is activated and becomes calcium independent upon phosphorylation by cyclic nucleotide-dependent protein kinases. J Biol Chem 2000; 275: 5179–87.

26 Spiroglou SG, Kostopoulos CG, Varakis JN, Papadaki HH. Adipokines in periaortic and epicardial adipose tissue: differential expression and relation to atherosclerosis. J Atheroscler Thromb 2010; 17: 115–30.

27 Ernst MC, Issa M, Goralski KB, Sinal CJ. Chemerin exacerbates glucose intolerance in mouse models of obesity and diabetes. Endocrinology 2010; 151: 1998–2007.

npg

Original Article

Intrapleural delivery of mesenchymal stem cells: a novel potential treatment for pleural diseases

Zhao-hui QIN[1, #], Jie-ming QU[1, *], Jin-fu XU[2], Jing ZHANG[3], Hanssa SUMMAH[1], He-xi Ge SAI-YIN[4], Chun-mei CHEN[4], Long YU[4]

[1]Department of Pulmonary Medicine, Huadong Hospital, Shanghai Medical College, Fudan University, Shanghai 200040, China;
[2]Department of Pulmonary Medicine, Shanghai Pulmonary Hospital, Tongji University, Shanghai 200433, China; [3]Department of Pulmonary Medicine, Zhongshan Hospital, Shanghai Medical College, Fudan University, Shanghai 200032, China; [4]State Key Laboratory of Genetic Engineering, Institute of Genetics, School of Life Sciences, Fudan University, Shanghai 200433, China

Aim: To develop a method to deliver mesenchymal stem cells (MSCs) into the pleural cavity for the treatment of pleural diseases.
Methods: MSCs were isolated from rat bone marrow of rats and labeled with 4′,6-diamidino-2-phenylindole dihydrochloride (DAPI) or green fluorescent protein (GFP) using a lentiviral vector. Eighteen Sprague-Dawley (SD) rats were inoculated intrapleurally with 1×10^6 MSCs-DAPI. The distribution of the fluorescent cells was observed using fluorescent microscopy for the following 30 d. Another 12 rats inoculated intrapleurally with 1×10^6 MSCs-GFP were observed for 14 d.
Results: The isolated cells were typical MSC phenotypes and could differentiate into adipocytes, osteoblasts, and chondroblasts *in vitro*. Microscopic analysis revealed that the labeled cells adhered to the surface of the pleural cavity. The highest number of the labeled cells was found to be adhered to all specimens from the mediastinal pleura, but no labeled cells were detected in the lung parenchyma or other tissues/organs, such as the liver, kidney, spleen, and mesenterium. Incidentally, stomas were found in the mediastinal pleura. The recovered MSCs-GFP from the pleural cavity retained their ability to adhere and proliferate.
Conclusion: We have established a novel method for intrapleural delivery of MSCs. The distribution of intrapleurally delivered MSCs was found to be limited to the pleurae and the pleural cavity, thereby providing us with a new approach to further investigation of the therapeutic roles of MSCs in pleural diseases.

Keywords: mesenchymal stem cells (MSCs); stem cells transplantation; pleural cavity; pleural diseases; lung

Introduction

Primary and secondary pleural diseases such as malignant pleural mesothelioma, pleural metastasis of lung cancer, pneumothorax, pleurisy and pleural effusions are common chest diseases involving the pleura. Despite advancement in different diagnostic tools and in the array of treatment options available today, effective treatment of pleural diseases such as malignant pleural mesothelioma, malignant pleural effusion and recurrent pneumothorax still remains challenging[1–4].

Recent studies, including one of our previous studies, have demonstrated that intravenous (iv) or intratracheal (it) delivery of bone marrow-derived mesenchymal stem cells (MSCs) participates in the improvement of various experimental

models of lung injury, thus demonstrating that MSCs play an important role in the treatment of animals with acute lung injury[5–12].

Because the pleural cavity is a tightly closed compartment, we hypothesized whether intrapleurally delivered MSCs could survive and adhere to the host pleura, and whether these cells could help to modulate the repair process of the injured pleura, thus intrapleural MSCs could become a new cell-based therapeutic strategy for pleural diseases. In the current study, we observed the dynamic distribution of intrapleurally delivered MSCs with the aim of validating this new route for the delivery of MSCs as a potential treatment method for pleural diseases.

[#] Now in *Department of Pulmonary Medicine, Longhua Hospital, Shanghai University of Traditional Chinese Medicine, Shanghai 200032, China.*
[*] To whom correspondence should be addressed.
E-mail jmqu64@yahoo.com.cn

Materials and methods
Animal care
The animals used in this study were specific-pathogen-free male Sprague-Dawley rats (6–8 weeks old; Slac Laboratory

Animal Co Ltd, Shanghai, China). The rats received humane care in compliance with the NIH principles of laboratory animal care and the Chinese national regulations for experimental animal care. All protocols were approved by the Animal Care and Use Committee of Fudan University.

Isolation, purification, and expansion of MSCs

MSCs were isolated from rat bone marrow as described in previous studies[8]. In brief, whole marrow was flushed from the tibias and femurs of Sprague-Dawley rats (4-weeks old, male) with ice-cold Dulbecco's modified Eagle's medium/F12 (DMEM/F12; Gibco, Carlsbad, CA, USA). The cells were washed and plated in plastic flasks at 2×10^6 cells/mL in DMEM/F12 containing 10% fetal bovine serum (FBS), 100 units/mL penicillin, and 100 µg/mL streptomycin (Gibco, Carlsbad, CA, USA). The cell suspension was incubated at 37 °C with 5% CO_2; nonadherent cells were discarded 48 h later. For routine maintenance, the medium was replaced twice weekly and cells were subcultured at a one-to-three split ratio by trypsinization (0.25% trypsin/1 mmol/L EDTA; Gibco, Carlsbad, CA, USA). Cells were further purified by passages.

FACS analysis of MSCs

MSCs were analyzed by FACS using antibodies for cell surface markers CD11b, CD45, CD29, CD73, and CD90, as described previously[13]. Briefly, MSCs from passage 3 were trypsinized and counted after rinsing in PBS (pH 7.2). Aliquots of 5×10^5 cells were incubated for 30 min with PE/FITC labeled monoclonal antibodies against rat CD11b, rat CD45, rat CD29, rat CD90 (BioLegend, San Diego, CA, USA), purified mouse anti-CD73 (BD Pharmingen™, San Diego, CA, USA), donkey anti-mouse IgG-FITC (Santa Cruz Biotechnology, Santa Cruz, CA, USA), and isotype-matched FITC- and PE-conjugated negative controls (IgG1-FITC/IgG1-PE, IQ products, CA, USA) according to the manufacturer's recommendations. After being washed with PBS, the stained cells were analyzed on a flow cytometer (Beckman Coulter Epics XL, USA) to identify the phenotypes of MSCs.

Differentiation assays

Passage 2 MSCs cultured with DMEM/F12 containing 10% FBS were used for the differentiation assay[6]. Adipogenic differentiation was induced by seeding the MSCs for 21 d in DMEM/F12 containing 10% FBS supplemented with 1 µmol/L dexamethasone (Sigma-Aldrich, USA), 10 µg/mL insulin (Sigma-Aldrich, USA), 200 µmol/L indomethacin, and 0.5 mmol/L IBMX. The cells containing droplets of fat were identified by staining the culture with 3.75% Oil Red. Osteogenic differentiation was induced by cultivating the MSCs in DMEM/F12 containing 10% FBS and supplemented with 10 mmol/L β-glycerol phosphate, 50 µmol/L ascorbic acid, and 0.1 µmol/L dexamethasone for 14 to 21 d. Alkaline phosphatase (AKP) levels were investigated by staining cells using AKP kits at d 14. The calcium-containing precipitates were visualized after staining with 2% Alizarin Red S

(Sigma-Aldrich, USA) adjusted to a pH of 4.2 with ammonium hydroxide at d 21. Chondroblast differentiation was induced by cultivation of the MSC in DMEM/F12 containing 0.25% FBS supplemented with 0.1 µmol/L dexamethasone, 50 µg/mL ascorbic acid, 10 ng/mL transforming growth factor beta 1 (TGF-β1), and 1% ITS (Sigma-Aldrich, USA). Toluidine blue staining was used to demonstrate chondroblast differentiation.

DAPI labeling of MSCs and growth characteristics assays

MSCs were labeled with 4',6-diamidino-2-phenylindole dihydrochloride (DAPI; cell culture tested by Sigma, St Louis, MO, USA) *in vitro* prior to *in vivo* inoculation into the pleural cavity. For labeling, MSCs were incubated for 4 h in DMEM/F12 medium containing 50 µg/mL DAPI. Cells were washed 6 times with PBS and then dissociated into a single cell suspension with 0.25% trypsin/1 mmol/L EDTA for further analysis[8].

Growth curves were generated to ascertain whether DAPI labeling would affect the growth characteristics of MSCs. Passage 2 MSCs labeled or not labeled with DAPI were typsinized, counted, seeded in 6-well plates, and cultured with DMEM/F12 containing 10% FBS. MSCs or MSCs-DAPI were seeded at the same cell density (3×10^4/well) in a total of 12 cell culture plates. For the next 12 d, the cells were counted using a microscope and a hemocytometer on a daily basis. The average cell number of three wells for each time point was calculated to plot the cell growth curve.

Green fluorescent protein (GFP) labeling of MSCs

Because GFP is expressed by the labeled cell itself, its fluorescent signal does not attenuate with cell division, and its fluorescent signal is more stable than that of DAPI. To compare with and validate the experimental results of the DAPI labeling method, GFP labeling of MSCs was also used in this study. MSCs (1×10^5) were incubated for 8 h with pGC FU-GFP-Lentivirus (Shanghai GeneChem Co, Ltd, China) at a multiplicity of infection (MOI) of 10 and 5 µg/mL of polybrene. The supernatant was then discarded, and the transfected cells were cultured and passaged in DMEM/F12 medium containing 10% FBS by trypsinization followed by splitting at a 1:3 ratio. The presence of MSCs-GFP cells and the intensity of GFP fluorescence were observed by fluorescent microscopy. MSCs labeled with GFP were dissociated into a single cell suspension using 0.25% trypsin/1 mmol/L EDTA for further intrapleural administration.

Inoculation of MSCs-DAPI or MSCs-GFP into the pleural cavity

Six-to-eight week-old rats were anesthetized using diethyl ether inhalation. A 5-mm incision was made on the right chest through the skin and the subcutaneous soft tissues. MSCs-DAPI (1×10^6 cells in 750 µL DMEM/F12) were injected into the pleural cavity using a 20 µL plastic pipette tip, instead of a needle, connected to a 1 mL syringe so as to avoid possible pneumothorax or lung injury that could have been caused by a needle. After cell transplantation, the skin incision was closed

with sutures.

A total of 20 naive rats were inoculated into the right pleural cavity with MSCs-DAPI; fluorescent cells were traced in 16 rats at four different time points over a period of 30 d (*n*=4; d 1, 4, 14, and 30). The remaining 4 rats (1 rat for each time point) were used to recover the viable MSCs-DAPI *in vivo* from their pleural cavity to see whether the normal features of these cells had been changed when cultured *in vitro* again. Fifteen rats were used for MSC-GFP inoculation, 12 of which were used to trace the fluorescent cells over a period of 14 d (*n*=3; d 1, 4, 7, and 14), and 3 rats were used to recover the viable MSCs-GFP *in vivo* from the pleural cavity at d 1 only. The d 7 time point was added and d 30 was omitted to better trace the fluorescent cells in the early days.

Sample collection

Rats were anesthetized using diethyl ether inhalation and the peritoneal cavity was opened. Animals were then sacrificed by incision of the abdominal aorta. After collection of the liver, kidney, spleen and mesenterium samples, both the right and the left pleural cavities were fixed for 15 min by injection of 2 mL 4% paraformaldehyde into each side through the diaphragm. Specimens from both the right and the left thorax were collected for further analysis, including pleural fixative fluid; whole lungs; mediastinal pleura, including the pleura on the left and right sides of the right lung accessory lobe; pericardium located at the left and right sides of heart; whole diaphragms; parts of chest walls; the thymuses; and the heart.

It is necessary to point out that, different from humans, rats have an additional lobe in the right lung, the right accessory lobe. Located either at its left or right side is a free membrane that belongs to the mediastinal pleura. The term "visceral pleura" only refers to the pleura on the surface of the lung, while "parietal pleura" refers to the pleura on the surface of the pleural cavity, except the visceral pleura. The mediastinal pleura, including the pericardium, the pleurae on the surfaces of the diaphragms, and the inner side of chest walls and thymuses, are all parietal pleurae. However, the epicardium, which is located on the surface of heart, does not belong to either the visceral or the parietal pleura.

Histological analysis

The mediastinal pleura, mesenterium and translucent diaphragms collected from the animals were mounted on glass slides and visualized under a florescence microscope. Paraformaldehyde-fixed pleural cavity fluid and translucent thymus were also examined directly under a fluorescence microscope. Other solid organs or tissues, including the lungs, heart, liver, kidney, spleen, and chest wall, could not be observed directly under a microscope, so the surfaces of these organs and the inner sides of the chest wall were carefully sliced into very thin sections with a sharp razor blade. With the upper sides of the sections attached closely to the surfaces of slides, the presence of fluorescence was visualized under a fluorescence microscope.

Harvest of cells from the pleural cavity

Into each pleural cavity 0.25% trypsin/1 mmol/L EDTA (3 mL) was injected through the diaphragm. After 6 min, digested cells were collected with a needle connected to a 10 mL syringe inserted into the cavity through the lower part of the diaphragm. Using this method, more than 90% of the digestive solution was recovered. Then trypsinization was terminated with DMEM/F12 medium containing 10% FBS, and the recovered cell suspension was centrifuged. Cells were resuspended and cultured in DMEM/F12 containing 10% FBS for further analysis.

Exchange of fluids and cells between the left and right pleural cavities

Any diffusion of pleural fluid and injected MSCs between the left and right pleural cavity was determined by injection of methylene blue dye and DAPI-labeled MSCs, respectively. Briefly, five animals were anesthetized by diethyl ether inhalation and exsanguinated by incision of the abdominal aorta. A small opening was made on the right chest wall, and the left pleural cavity was carefully exposed, without damaging the mediastinal pleura. Methylene blue dye (3 mL, 10 mg/mL) or DAPI-labeled MSCs (1×10^6 cells in 3 mL PBS) were then injected into the right pleural cavity through the small opening. At the same time, we observed whether the injected fluids and cells penetrated through the mediastinal pleura to the left side.

Microscopic observation for channels between the left and right pleural cavities

Both normal and DAPI-stained mediastinal pleurae were visualized under light and fluorescence microscopes to investigate the presence of channels that could be responsible for the exchange of fluid and cells. Rats were anesthetized by diethyl ether inhalation, and mediastinal pleurae were stained for 4 h by injecting 2 mL DMEM/F12 medium containing 50 μg/mL DAPI into the right pleural cavity. The rats were then reanesthetized and the pleural cavities were fixed with 4% paraformaldehyde for 15 min. The rats were finally sacrificed, and the DAPI-stained mediastinal pleurae were collected for further microscopic observation. In addition, normal mediastinal pleurae were also collected in a similar way and observed under a light microscope.

Statistical analysis

Statistical analysis was done using chi-square test. A *P* value of <0.05 was considered statistically significant.

Results

Identification of MSC phenotypes

Various cell-specific markers of MSCs were analyzed by FACS to determine the cell phenotypes present in our experiments. Consistent with previous studies[13, 14], our results revealed that the majority of MSCs were CD29, CD73, and CD90 positive. However, only a small proportion of isolated cells were

positive for hemopoietic cell surface makers CD11b/c and CD45 (Figure 1). The results of isotype-matched FITC- and PE-conjugated negative controls are shown in Figure S1. A differentiation assay demonstrated that the cells could differentiate into adipocytes, osteoblasts, and chondroblasts under standard *in vitro* differentiating conditions, which means that the cells have multipotent differentiation potential (Figure 2).
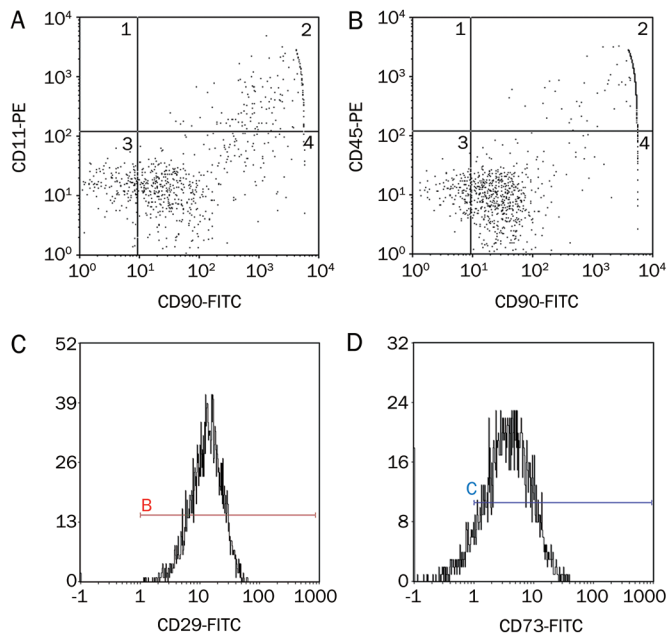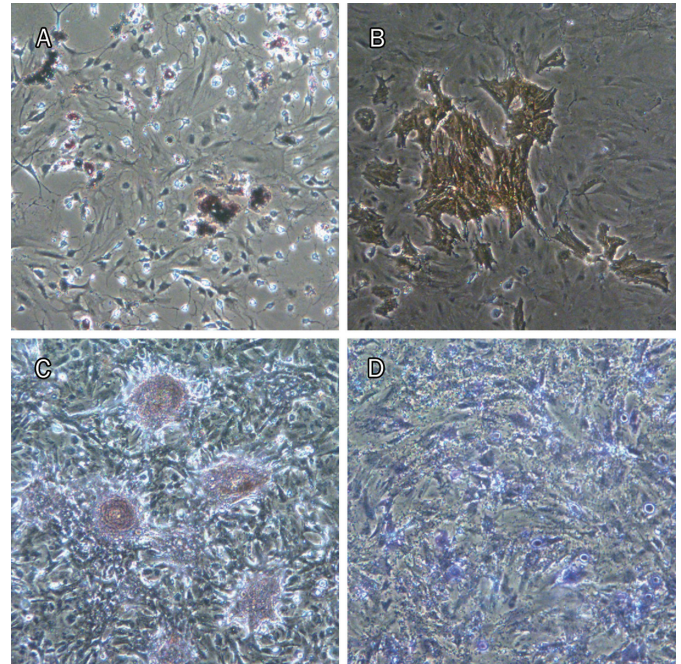

Figure 1. Characterization of MSC phenotype. Flow cytometry of MSCs demonstrated that majority of MSCs were CD90 (A, 95.84%; B, 98.31%), CD29 (C, 99.7%) and CD73 (D, 89.5%) positive. In contrast, only a small portion of isolated cells were positive for hemopoietic cell surface makers, CD11b/c (A, 1.86%) and CD45 (B, 1.59%).

Figure 2. MSCs demonstrated multipotent property under standard *in vitro* differentiating condition. Differentiation into adipocytes (Oil Red staining, red) (A), osteoblasts (AKP staining, orange) (B) and (Alizarin staining, red) (C), and chondroblasts (Toluidin blue staining, blue) (D) was seen.

Influence of DAPI labeling on growth of MSCs and stability of GFP expression

After incubation in DAPI (50 μg/mL) for 4 h, an intensive fluorescent signal was found in the nuclei of the MSCs (Figure 3A–3C). In addition, strong fluorescent signal was present in the labeled cells even after 10 d (Figure 3D–3F), indicating that DAPI can be used to label MSCs effectively for at least 10 d. Growth curves of unlabeled MSCs *vs* DAPI-labeled MSCs showed that the DAPI-labeling method decreased the proliferation rate of MSCs by a longer lag phase and longer population doubling time (Figure S2). This result confirmed that DAPI was toxic to MSCs. After transfection with pGC FU-GFP-Lentivirus, MSCs were found to be expressing GFP even after 29 d (Figure 3I). The efficiency of MSCs-GFP transfection was nearly 100% (Figure 3G–3I).

Distribution of MSCs in the plurae of rats

Microscopic analysis revealed the presence of DAPI-labeled MSCs in various tissues, including the visceral pleura and the parietal pleura, as well as on the surface of epicardium (Figure 4, 5). While DAPI-labeled cells were found in all 64 mediastinal pleura specimens, including the cardiac pericardium (100%), and in all 32 pleural fixative solutions (100%), they were found less frequently in tissues such as the epicardium, the parietal pleura of both the left and the right chest wall, and both the left and the right diaphragm (Figure 4). Here, the mediastinal pleura specimens included the pleura located in both the left and the right sides of the right lung accessory lobe and the pericardium located in both the left and the right sides of the heart. Therefore, 4 mediastinal pleura specimens were collected for each rat. A total of 16 rats were used in the DAPI-labeling method, so the total specimen number was 64. No labeled cells were detected in the other tissues/organs, including the liver, kidney, spleen and the mesenterium (only the kidney is shown in Figure 5L). The labeled cells formed aggregates on the tissue surface and could be removed by scraping with a needle under a fluorescence microscope. Therefore, it seemed that inoculated MSCs adhered only to surfaces of these tissues. Overall, the number of adhered MSCs appeared to decrease with time because they could be less easily visualized in the same area of the microscopic field. A large number of labeled MSCs was also found in all 32 pleural fixative fluid specimens retrieved from each side of the pleural cavities, indicating that a significant portion of injected MSCs were in suspension rather than adhered to different surfaces during the observed period (Figure 5K). Interestingly, MSCs inoculated into the right pleural cavity were found to
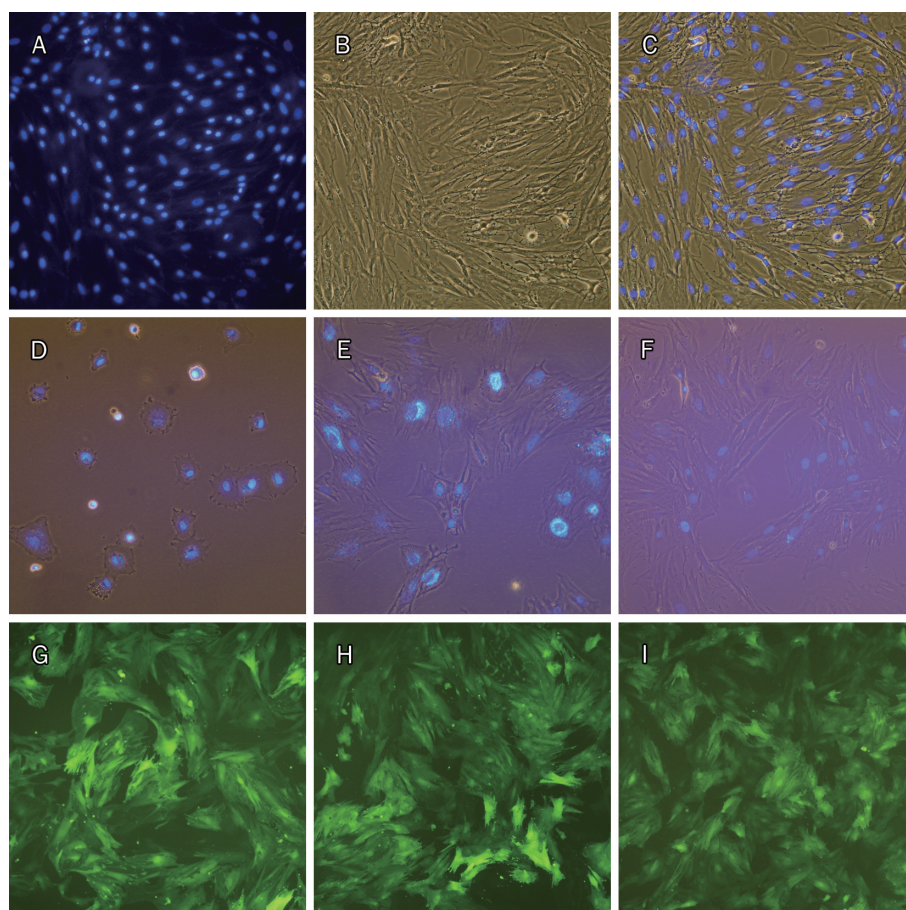
Figure 3. MSCs labeled with DAPI and GFP. MSCs stained with DAPI for 4 h, fluorescence microscopy (A), phase contrast (B) and merge (C). MSCs nuclei were stained and the fluorescent signal was high. MSCs harvested from above cells were cultured *in vitro* for 4 h (D, merge), 4 d (E, merge), and 10 d (F, merge, 2 d after passaged once). Relatively strong fluorescent signal was present in the cells even after 10 d post-labeling. Fluorescence microscopy of MSCs after transfection with pGC FU-GFP-Lentivirus for 7 d (G), 19 d (H, 9 d after passaged once), and 29 d (I, 2 d after passaged twice). (A–F), ×200; (G–I), ×100.
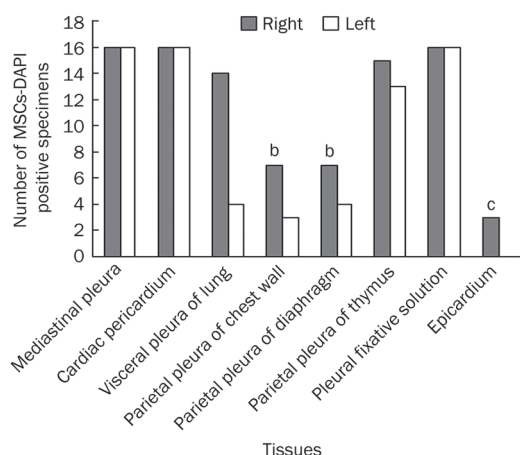

Figure 4. The MSCs-DAPI positive number of different tissues within two pleural cavities and pleural fixative solutions collected from total 16 experimental rats. For each bar, the maximum number was 16, since the tissue it represents was collected from 16 rats. While DAPI-labeled cells were found in all 64 mediastinal pleura specimens including the cardiac pericardium (100%) and in all 32 pleural fixative solutions (100%), they were found less frequently in other tissues like the epicardium (3/16=19%), the parietal pleura of both left and right chest wall (10/32=31%) and both left and right diaphragm (11/32=34%). In this figure, the column of mediastinal pleura represents only pleura located at both sides of right lung accessory lobe, while pericardium, which also belongs to the mediastinal pleura, was shown in a separate column. Right or Left, specimens collected from the right or left side of pleural cavities. [b]$P<0.05$, [c]$P<0.01$, compared with the mediastinal pleura including the pericardium.

be present in the left pleural cavity (Figure 4, 5), although the number of positive samples was less when compared to the right side (Figure 4). Figure 5 shows that MSCs adhered in the form of either cell aggregates or scattered cells. In the early phase (d 1, 4), cell aggregates were more common than scattered cells. MSCs also showed a trend to adhere near small blood vessels (Figure 5A, 5C, 5D, Figure 6L).

It was also noted that the DAPI fluorescent signal of MSCs, although becoming weaker, was still strong enough to be detected even 30 d after MSC inoculation into the pleural cavity (Figure 5I–5K), implying that the fluorescent signal of DAPI in MSCs can be traced *in vivo* for a long time.

Tracking of MSCs-GFP showed similar results as DAPI labeling. MSCs-GFP were easily found in mediastinal pleura specimens at all four time points and in the translucent thymus at d 1 (Figure 6). As GFP is expressed in the cytoplasm, the shape of the cells is clearly shown (Figure 6K). "Halos" around MSCs-GFP and MSCs-DAPI aggregates on the medi-
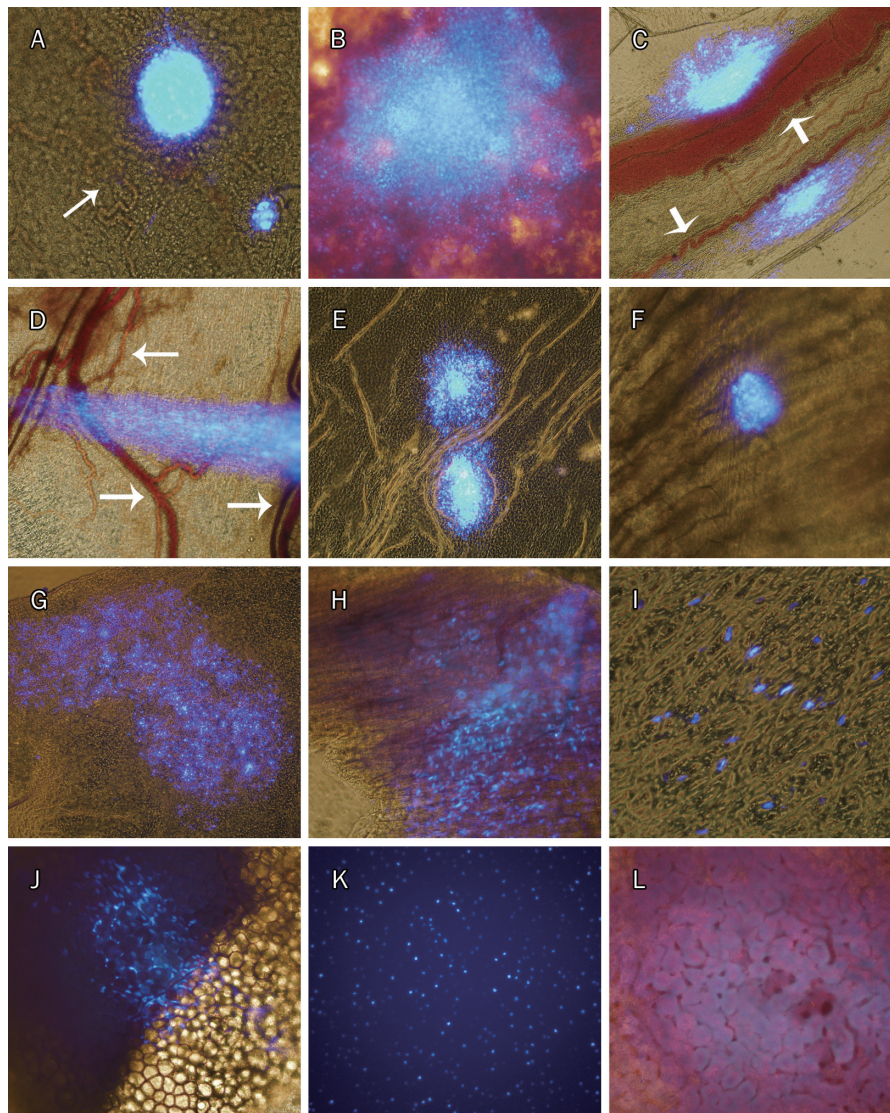
Figure 5. Destination of MSCs-DAPI after being inoculated into right pleural cavity in healthy rats. All were merged images. Images from d 1: the right cardiac pericardium (A) and the surface of right lung (B). Images from d 4: the mediastinal pleura located at the right side of the right lung accessory lobe (C), the membranous part of right diaphragm (D), the left cardiac pericardium (E), and inner surface of the right chest wall (F). Images from d 14: the mediastinal pleura located at the right side of the right lung accessory lobe (G), and the surface of epicardium (H). Images from d 30: the mediastinal pleura located at the left side of the right lung accessory lobe (I), the surface of the left thymus (J), the pleural fixative solution from the left thorax (K), and the surface of kidney (L). Of all microphotographs, (B–E) and (G), ×100; (A), (F), (H), and (J–L), ×200; and (I), ×400. This figure showed that the cells can adhere only to the surfaces of two pleural cavities (*ie* left and right), including on the surface of the epicardium. MSCs adhered in the form of either cell mass of different shape or scattered cells, and found to be proned to adhere near small blood vessels (white arrows in A, C, D). No DAPI labeled cell was found on the surface of kidney.

astinal pleurae were often visualized (Figure 6C, Figure S3) on d 1 but not at any of the following time points. MSCs-GFP were rarely found in pleural fixative fluids. Furthermore, no MSCs-GFP were found in the remaining specimens, including surfaces of the lungs, the heart, the chest wall, and the diaphragm.

Channels exist for MSCs to traverse between the right and left pleural cavities

An unexpected finding from our study was the migration of MSCs from the right pleural cavity to the left one and adherence to the surface in the left pleural cavity (Figure 4, 5). This observation suggests that a channel exists in the mediastinal pleura that allows MSCs to penetrate to the other side. To further confirm this possibility, we injected methylene blue dye or a DAPI-labeled MSC suspension into the right pleural cavity and observed whether the dye or labeled cells could be found in the left pleural cavity. We found that the methylene blue dye was present in the non-injected left cavity just a few
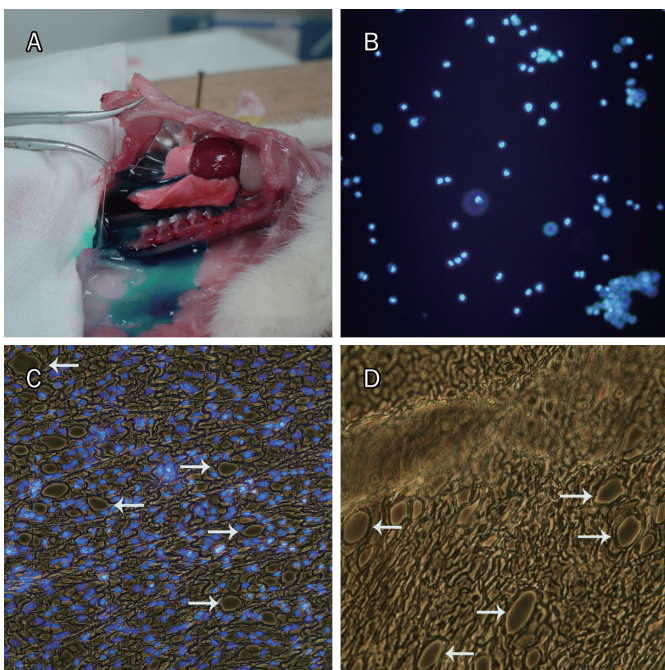
seconds after dye injection into the right pleural cavity (Figure 7A). Importantly, labeled MSCs inoculated into the right pleural cavity quickly migrated into the left pleural cavity along with the fluid (Figure 7B). Further microscopic observation of normal and DAPI-stained mediastinal pleura revealed that there were many oval stomas of different sizes in the cell monolayer of the mediastinal pleura (Figure 7C–7D), indicating that these stomas may be the channels mentioned above.

**Growth characteristics of inoculated MSCs recovered from the pleural cavity**

Mixed with many non-fluorescent native cells from the pleural cavity, a large number of viable MSCs-DAPI were visualized by fluorescence microscopy in the digestive solution recovered from the pleural cavity, even 30 d after inoculation (Figure 8D–8F). When cultured *in vitro* again, the recovered MSCs-DAPI from all four time points still exhibited a capacity to adhere to plastic (Figure 8A–8F; only d 14 and d 30 are shown here). However, especially when passaged, the recovered
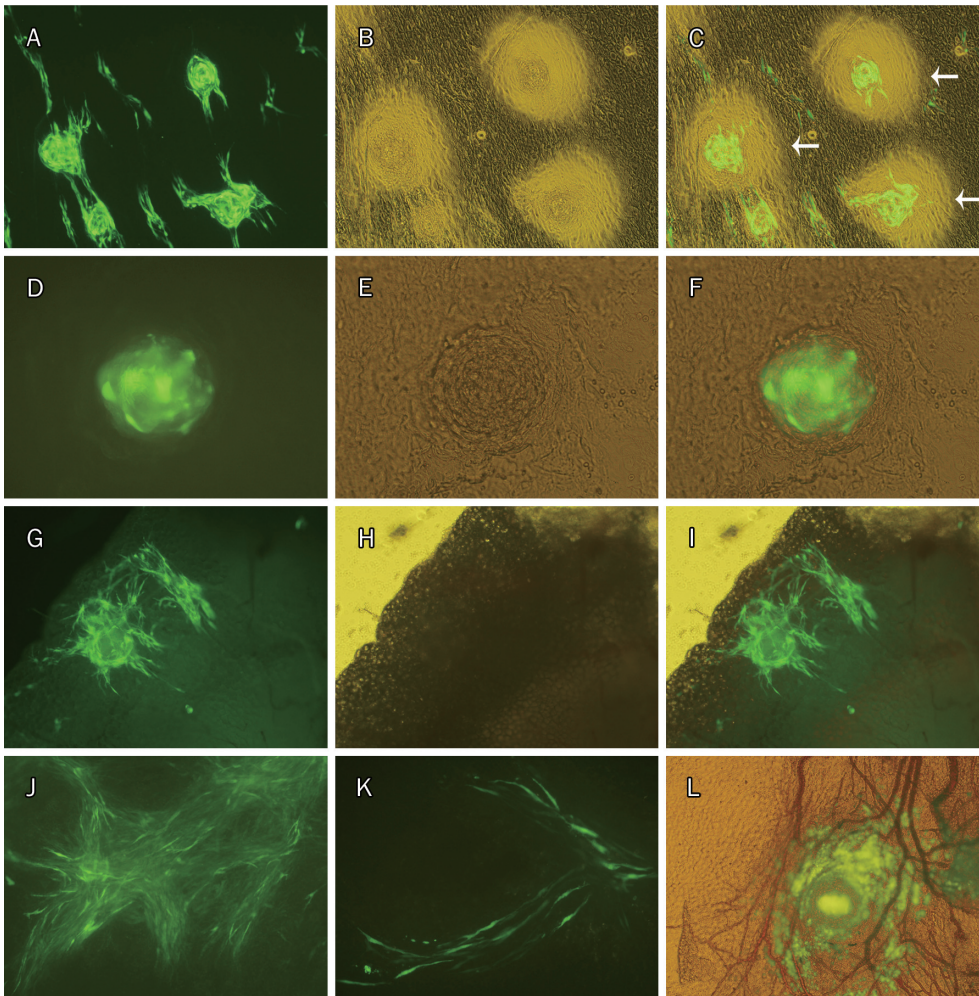
Figure 6. Destination of MSCs-GFP after being inoculated into right pleural cavity in healthy rats. Images from d 1: the mediastinal pleura (A–F), the right thymus (G–I); d 4: the mediastinal pleura (J); d 7: the mediastinal pleura (K); d 14: the mediastinal pleura (L). "Halo" around MSCs-GFP aggregate was seen in image C (white arrows), indicating that interactions between MSCs and the pleural constituent cells occurred during adhesion. MSCs-GFP aggregate localized in a net of small blood vessels was shown in image (L). (A, D, G), fluorescence. (B, E, H), phase contrast. (C, F, I), merge. (J, K), fluorescence microscopy. (L), merge. (A–C, G–I, J, L), ×100; (K), ×200; (D–F), ×400.

Figure 7. Channels exist for MSCs and fluid to traverse between the right and left pleural cavities. Only a few seconds after methylene blue injection into the right side pleural cavity, blue fluid was found flowing into the left thorax (A), indicating that there were quick fluid channels that permitted fluid to pass through the mediastinum. Likewise, DAPI-labeled MSCs suspension was also injected into the right side pleural cavity, fluorescence cells were easily visualized in the fluid flowing into left thorax under fluorescence microscopy (B). Both images of DAPI-stained (C) and normal mediastinal pleura (D) demonstrated that there were many oval stomas of different sizes in the cell monolayer part of mediastinal pleura (white arrows), indicating that these may be the unidentified anatomical channels by which fluid and cells traverse between the two pleural cavities freely. (B–D), ×100.
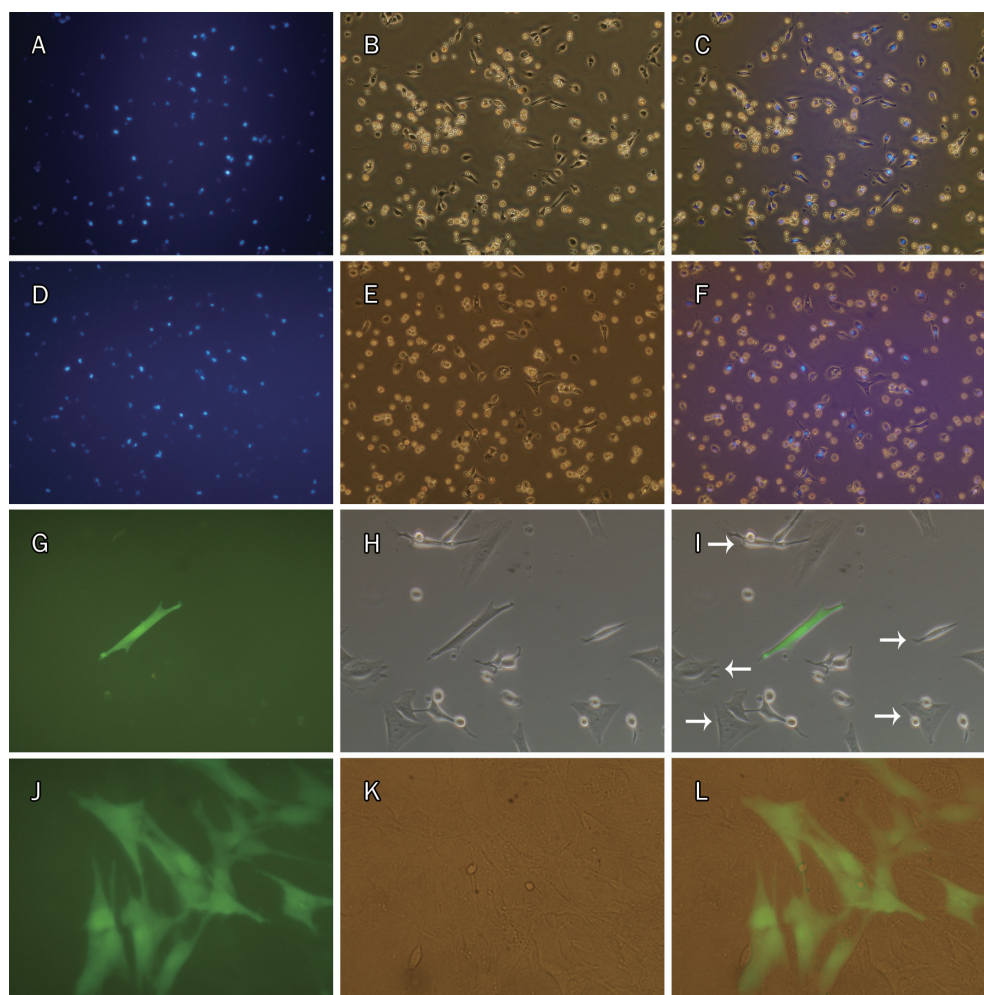
Figure 8. MSCs-DAPI and MSCs-GFP recovered from the pleural cavity and cultured *in vitro* again. MSCs-DAPI recovered were cultured *in vitro* for 1 d after being inoculated for 14 d (A–C) and for 30 d (D–F). MSCs-GFP recovered were cultured *in vitro* for 3 d (G–H) and 17 d (J–L, 7 d after passaged once) after being inoculated for 1 d. Both recovered MSCs-DAPI and MSCs-GFP have the capability to adhere. However, only MSCs-GFP can proliferate. Beside MSCs-GFP, native cells from the pleural cavity also have property to adhere and proliferate (white arrows in I). (A, D, G, J), fluorescence microscopy. (B, E, H, K), phase contrast. (C, F, I, L), merge. (A–F), ×200; (G–L), ×400.

MSCs-DAPI from all time points died quickly, while some of the native cells with the capacity to adhere proliferated and gradually became the predominating cells, the indentity of which still need to be determined. Compared with MSCs-DAPI, inoculated MSCs-GFP could also be recovered from the pleural cavity on d 1. When cultured and passaged *in vitro* again, both colonies of MSCs-GFP and those of native cells formed at the same time, and the total cell number increased, indicating that MSCs-GFP had capacity not only to adhere but also to proliferate (Figure 8G–8L).

Discussion

In this study, we have established and characterized a novel intrapleural method to deliver MSCs *in vivo* for the future treatment of pleural diseases. Unlike classical intravenous or intratracheal delivery methods[5-9], intrapleurally delivered MSCs were found to be distributed only to the pleurae and the pleural cavity, providing a promising cell-based therapeutic strategy for primary and secondary pleural diseases.

As recommended in the workshop report written by Weiss *et al* that published in 2008[12], development of methods for culture systems that mimic *in vivo* niches was one of the strategies for a better understanding of the repair mechanisms of stem cells and their microenvironmental niche. The air-liquid interface, three-dimensional scaffolding/artificial matrices, the application of multiple cell types and mechanical forces (stretch, strain, *etc*) are four important factors suggested in this report for *in vitro* MSCs culture systems. Inspired by this, we initially thought that the pleural cavity might be an ideal target for MSC inoculation. As far as we are concerned, the pleural cavity is a tightly closed three-dimensional and potential compartment with negative pressure and multiple cell types and is like a "complex culture flask" *in vivo*; it satisfies most of the criteria. Most importantly, if inoculated MSCs can survive, proliferate, and be recovered viably by trypsinization like they can in an *in vitro* culture system, it would be an excellent model for MSC culture *in vivo*. At the same time, we hypothesized that this novel delivery method might have the potential to provide a new cell-based therapeutic strategy for pleural diseases.

Different pleural diseases may preferentially involve different parts of the pleura. For example, pleural mesothelioma has a tendency to affect the parietal pleura; in contrast, recurrent pneumothorax has a tendency to affect the visceral pleura. Therefore, we consider it necessary to ascertain if there is any difference in MSCs with regard to adherence to different parts

of the pleurae. Results of this study showed that MSCs only adhered to the surfaces of the two pleural cavities (i.e. left and right), except for a small number of MSCs in several animals that were able to penetrate the cardiac pericardium and adhere to the surface of the epicardium in the pericardial cavity. No labeled MSCs were found in the lung parenchyma or in other tissues/organs distal to lung, such as the liver, the kidney, the spleen and the mesenterium. In addition to the adherence to the surfaces of the pleural cavities, a considerable number of MSCs were found in a suspended state in the two pleural cavities, indicating that a significant proportion of injected MSCs did not adhere to any surface. Although it is hard to ascertain the total number of suspended and adhered MSCs at the different time points, the number of adhered MSCs appeared to decrease over time. This likely reflects toxicity or another effect of DAPI rather than any inherent property of the MSCs or the pleural environment, as indicated by the growth curve analysis in the study. Further studies using Ki67 staining or some other marker of proliferation would be helpful to clarify this point. Unlike DAPI, a nuclear dye with intense fluorescence, GFP is expressed by the labeled cell itself, so its fluorescent signal is not attenuated by cell division and is more stable than that of DAPI. As it is expressed in the cytoplasm, GFP is better for showing the whole cell shape. Both DAPI- and GFP-labeling methods were used in this study to compare and validate the experimental results. MSCs-GFP were easily found in the mediastinal pleurae and translucent thymus as were MSCs-DAPI, but they were not found in other thick tissues like the surface of the diaphragm or the lungs. This could be explained by the fact that both the fluorescent signal of MSCs-GFP and the contrast between them and their background due to autofluorescence were much weaker when compared with that of MSCs-DAPI. The fact that a large number of MSCs-DAPI but not MSCs-GFP was found in pleural fixative fluid also suggests toxicity of DAPI. The formation of a "Halo" around MSCs-GFP or MSCs-DAPI aggregate on d 1 indicated that complex interactions had occurred between the MSCs and the pleural constituent cells during adhesion. This process may have included the production of adhesion molecules and the secretion of extracellular matrix. Furthermore, this phenomenon disappeared after d 1, indicating that the process of adhesion might have been completed. Our results confirm the hypothesis that inoculated MSCs can survive and be limited to the pleural cavities. Because most of the cell adherence that occurred was confined to the visceral and the parietal pleura, it can reasonably be deduced that the administration of MSCs within the pleural cavity may have potential direct and indirect beneficial effects for the treatment of primary and secondary pleural diseases.

Most of the adhered MSCs were found on the mediastinal pleurae. This phenomenon indicated that the mediastinal pleura was the most favorable tissue for MSC adhesion. This may be due to the specific structure of the mediastinal pleura, a thin and relatively free membrane that separates the two pleural cavities. MSCs were prone to adhere near small blood vessels, implying that it might be a more convenient location

for them to acquire nutrition from blood. Unlike cells cultured *in vitro* that grew as monolayers, MSCs that adhered *in vivo* were found to grow in a three-dimensional style, showing patterns of cell aggregates of different forms and scattered cells. We hypothesized that this may be mainly related to the tightly sealed and three-dimensional construction features of the pleural cavity or that it might result from interactions between MSCs and the pleural mesothelium cell microenvironment.

Interestingly, we found that MSCs could migrate into the left pleural cavity after inoculation into the right side. Subsequent experiments confirmed that there were indeed physical channels existing in the mediastinal pleura of rats, implying that the anatomy of rat mediastinal pleura is different from that of human beings. Although stomas on the costal pleura and the diaphragm have been identified and confirmed previously[15, 16], there was previously no report on stomas on the mediastinal pleura, which is a thin membrane. Through light microscopy, we could observe stomas on the mediastinal pleura, as shown in Figure 7C–7D. Future studies using electron microscopy would be needed to further confirm this finding. The functions of these channels also need to be clarified in the future. This interesting result also indicates that injecting MSCs into one side of pleural cavity could have merit for the treatment of bilateral pleural diseases in an experimental rat model.

We also found that viable MSCs administered *in vivo* could be retrieved even 30 d post-inoculation. When cultured *in vitro* again, both MSCs-DAPI from all four time points and MSCs-GFP from d 1 have the capability to adhere. However, only MSCs-GFP proliferate, while MSCs-DAPI do not. This is not necessarily surprising since it was confirmed that the proliferation rate of MSCs decreased due to DAPI-labeling in this study. In addition, whether the recovered MSCs still retain characteristics exhibited prior to administration or whether these cells differentiated into host cells such as the mesothelium still needs to be characterized in future studies. Isolation of the inoculated MSCs from native cells trypsinized and recovered simultaneously should be done first, followed by flow cytometry and differentiation assays.

In summary, we have established and characterized a novel intrapleural method to deliver MSCs *in vivo* for the future treatment of pleural diseases. The distribution of intrapleurally delivered MSCs was limited to the pleurae and the pleural cavity, which may provide a novel way to further investigate the therapeutic roles of MSC-based therapy in pleural diseases.

Acknowledgements

tion (No 20090460588), and the Shanghai Leading Talent Projects (No 036, 2010).

Author contribution

Supplementary information

Supplementary figures are available at Acta Pharmacologica Sinica website of NPG.

References

1 Vorobiof DA, Mafafo K. Malignant pleural mesothelioma: medical treatment update. Clin Lung Cancer 2009; 10: 112–7.

2 Heffner JE, Klein JS. Recent advances in the diagnosis and management of malignant pleural effusions. Mayo Clin Proc 2008; 83: 235–50.

3 Kass SM, Williams PM, Reamy BV. Pleurisy. Am Fam Physician 2007; 75: 1357–64.

4 Gupta A, Patel B, Almoosa K, McKelvy BJ. Recurrent spontaneous pneumothorax. Cleve Clin J Med 2010; 77: 345–7.

5 Xu J, Qu J, Cao L, Sai Y, Chen C, He L, *et al*. Mesenchymal stem cell-based angiopoietin-1 gene therapy for acute lung injury induced by lipopolysaccharide in mice. J Pathol 2008; 214: 472–81.

6 Gupta N, Su X, Popov B, Lee JW, Serikov V, Matthay MA. Intrapulmonary delivery of bone marrow-derived mesenchymal stem cells improves survival and attenuates endotoxin-induced acute lung injury in mice. J Immunol 2007; 179: 1855–63.

7 Xu J, Woods CR, Mora AL, Joodi R, Brigham KL, Iyer S, *et al*. Prevention of endotoxin-induced systemic response by bone marrow-derived mesenchymal stem cells in mice. Am J Physiol Lung Cell Mol Physiol 2007; 293: L131–41.

8 Zhao F, Zhang YF, Liu YG, Zhou JJ, Li ZK, Wu CG, *et al*. Therapeutic effects of bone marrow-derived mesenchymal stem cells engraftment on bleomycin-induced lung injury in rats. Transplant Proc 2008; 40: 1700–5.

9 Rojas M, Xu J, Woods CR, Mora AL, Spears W, Roman J, *et al*. Bone marrow-derived mesenchymal stem cells in repair of the injured lung. Am J Respir Cell Mol Biol 2005; 33: 145–52.

10 Horwitz EM, Prather WR. Cytokines as the major mechanism of mesenchymal stem cell clinical activity: expanding the spectrum of cell therapy. Isr Med Assoc J 2009; 11: 209–11.

11 Caplan AI. Why are MSCs therapeutic? New data: new insight. J Pathol 2009; 217: 318–24.

12 Weiss DJ, Kolls JK, Ortiz LA, Panoskaltsis-Mortari A, Prockop DJ. Stem cells and cell therapies in lung biology and lung diseases. Proc Am Thorac Soc 2008; 5: 637–67.

13 Harting M, Jimenez F, Pati S, Baumgartner J, Cox C Jr. Immunophenotype characterization of rat mesenchymal stromal cells. Cytotherapy 2008; 10: 243–53.

14 Dominici M, Le Blanc K, Mueller I, Slaper-Cortenbach I, Marini F, Krause D, *et al*. Minimal criteria for defining multipotent mesenchymal stromal cells. The International Society for Cellular Therapy position statement. Cytotherapy 2006; 8: 315–7.

15 Negrini D, Mukenge S, Del Fabbro M, Gonano C, Miserocchi G. Distribution of diaphragmatic lymphatic stomata. J Appl Physiol 1991; 70: 1544–9.

16 Wang NS. Anatomy of the pleura. Clin Chest Med 1998; 19: 229–40.

npg

Original Article

Bezafibrate enhances proliferation and differentiation of osteoblastic MC3T3-E1 cells via AMPK and eNOS activation

Xing ZHONG[#], Ling-ling XIU[#], Guo-hong WEI, Yuan-yuan LIU, Lei SU, Xiao-pei CAO, Yan-bing LI, Hai-peng XIAO[*]

Department of Endocrinology, First Affiliated Hospital, Sun Yat-sen University, Guangzhou 510080, China

Aim: To investigate the effects of bezafibrate on the proliferation and differentiation of osteoblastic MC3T3-E1 cells, and to determine the signaling pathway underlying the effects.
Methods: MC3T3-E1 cells, a mouse osteoblastic cell line, were used. Cell viability and proliferation were examined using MTT assay and colorimetric BrdU incorporation assay, respectively. NO production was evaluated using the Griess reagent. The mRNA expression of ALP, collagen I, osteocalcin, BMP-2, and Runx-2 was measured using real-time PCR. Western blot analysis was used to detect the expression of AMPK and eNOS proteins.
Results: Bezafibrate increased the viability and proliferation of MC3T3-E1 cells in a dose- and time-dependent manner. Bezafibrate (100 µmol/L) significantly enhanced osteoblastic mineralization and expression of the differentiation markers ALP, collagen I and osteocalcin. Bezafibrate (100 µmol/L) increased phosphorylation of AMPK and eNOS, which led to an increase of NO production by 4.08-fold, and upregulating BMP-2 and Runx-2 mRNA expression. These effects could be blocked by AMPK inhibitor compound C (5 µmol/L), or the PPARβ inhibitor GSK0660 (0.5 µmol/L), but not by the PPARα inhibitor MK886 (10 µmol/L). Furthermore, GSK0660, compound C, or N[G]-nitro-*L*-arginine methyl ester hydrochloride (*L*-NAME, 1 mmol/L) could reverse the stimulatory effects of bezafibrate (100 µmol/L) on osteoblast proliferation and differentiation, whereas MK886 only inhibited bezafibrate-induced osteoblast proliferation.
Conclusion: Bezafibrate stimulates proliferation and differentiation of MC3T3-E1 cells, mainly via a PPARβ-dependent mechanism. The drug might be beneficial for osteoporosis by promoting bone formation.

Keywords: bezafibrate; osteoblast; MC3T3-E1 cell; AMPK; eNOS; PPARα; PPARβ

Introduction

Osteoporosis is a major public health problem, characterized by low bone mass and micro-architectural deterioration of bone tissue with a consequent increase in bone fragility and susceptibility to fracture due to imbalance between bone resorption by osteoclasts and bone formation by osteoblasts. Bone formation is likely to be affected by reductions of osteoblast proliferation, differentiation and lifespan[1]. Hypercholesterolemia was reported to be associated with lower bone mineral density (BMD)[2, 3]. An animal model study has also demonstrated some detrimental effects of dyslipidemia on bone metabolism[4]. Fibrate use, including bezafibrate, was associated with a reduced odds of vertebral fractures in men

and women[5]. Bezafibrate was shown to increase bone mass in intact male rats principally through increasing periosteal bone formation[6]. A growing body of evidence suggests that bezafibrate plays an important role in bone metabolism. However, it is not clear whether these changes result from the direct effects of bezafibrate on bone or from changes in lipid levels.

Bezafibrate, a dual ligand for peroxisome proliferator-activated receptors α (PPARα) and PPARβ[7], is a lipid-lowering drug widely used to treat hypertriglyceridemia. In addition, fibrates, including bezafibrate, were reported in both clinical and basic research to reduce the progression of atherosclerotic lesions[8] and improve endothelial function[9]. Fenofibrate, a PPARα agonist, stimulates eNOS phosphorylation and nitric oxide (NO) production through AMP-activated protein kinase (AMPK) activation[10, 11]. GW501516, a PPARβ agonist, also activates AMPK and stimulates glucose uptake in skeletal muscle cells[12].

AMPK is a heterotrimeric enzyme complex consisting of one catalytic α subunit, two regulatory β subunits and a γ subunit. AMPK is recognized as a regulator of energy homeostasis and is known to be expressed ubiquitously, including in bone. Pharmacological AMPK activators, 5-aminoimidazole-4-carboxamide-β-*D*-ribonucleoside (AICAR) or metformin, could promote the differentiation and mineralization of osteoblastic MC3T3-E1 cells[13, 14]. It has recently been shown that AMPK activity regulates bone formation *in vitro* and the maintenance of bone mass *in vivo*[15]. These previous findings together suggested that AMPK could affect bone metabolism. AMPK has been shown to increase eNOS activity and contribute to NO production in endothelial cells[16]. NO is also a signaling molecule constitutively produced in bone cells. The source of NO production in bone cells is largely due to eNOS, which was constitutively expressed in bone. The eNOS isoform seems to play a key role in regulating osteoblast activity and bone formation since eNOS knockout mice have osteoporosis due to defective bone formation[17, 18].

Because these data have been obtained from non-osteoblastic cells, it is still unclear whether bezafibrate could activate AMPK and eNOS in osteoblasts. A model commonly used to study osteogenic development is the MC3T3-E1 osteoblast-like cell line because in culture, these cells are characterized by distinct proliferative and differentiated stages, thereby reproducing a temporal program consistent with osteoblast differentiation as it occurs during *in vivo* bone formation[19].

Thus, the objective of the present study was to investigate whether bezafibrate promotes the proliferation and differentiation of osteoblastic MC3T3-E1 cells. In addition, we also investigated possible mechanisms of action of bezafibrate, such as the AMPK-eNOS signaling pathway, and the effect of PPARα or PPARβ.

Materials and methods
Reagents
Chemicals including bezafibrate, GSK0660, N^G-nitro-*L*-arginine methyl ester hydrochloride (*L*-NAME), glycerol 2-phosphate disodium salt hydrate (β-GP), ascorbic acid, ρ-nitrophenol (ρ-NP), and ρ-nitrophenylphosphate (ρ-NPP) were purchased from Sigma (St Louis, MO, USA). Compound C and MK886 were purchased from Calbiochem (Darmstadt, Germany). Fetal bovine serum (FBS), *L*-glutamine, penicillin/streptomycin, and α-minimal essential medium (α-MEM) were obtained from Gibco-BRL (Grand island, NY, USA). For Western blot analysis, total and phospho (p)-AMPKα (Thr-172), total and p-eNOS (Ser-1177), and total and p-acetyl-CoA carboxylase (ACC) (Ser-79) antibodies were purchased from Cell Signaling Technology (Danvers, MA, USA). All other chemicals were of the highest grade available commercially.

Cell culture
MC3T3-E1 cells, a mouse osteoblastic cell line, were obtained from American Type Culture Collection. MC3T3-E1 cells were cultured in α-MEM supplemented with 10% FBS and 1%

penicillin-streptomycin in 5% CO_2 at 37 °C. The medium was changed three times a week. When cells reached 80% confluence two or three days after plating, they were subsequently cultured for 7-28 d in differentiation medium consisting of 90% α-MEM, 10% FBS, 50 mg/L ascorbic acid, and 10 mmol/L β-GP. Cultured cells were analyzed on d 0, 7, 14, 21, 28 after reaching 80% confluence.

Measurement of cell viability and proliferation
Cell viability was determined by the 3-(4,5-dimethylthiazol-2-yl) 2,5-diphenyl-tetrazolium bromide (MTT) dye. MC3T3-E1 cells were incubated with bezafibrate (1–1000 µmol/L) for 24, 48, or 72 h, and were pretreated with the AMPK inhibitor compound C (5 µmol/L), PPARβ inhibitor GSK0660 (0.5 µmol/L), PPARα inhibitor MK886 (10 µmol/L), or NOS inhibitor *L*-NAME (1000 µmol/L) followed by bezafibrate (100 µmol/L) incubation for 48 h. After the incubations, 10 µL of MTT (Sigma-Aldrich) was added to each well of a 96-well microplate, and the microplates were placed in an incubator at 37°C for 4 h. One hundred fifty microliters of dimethyl sulfoxide (DMSO) was added to all wells and mixed thoroughly to lyse the cells and dissolve the dark blue crystals. After 10 min, the absorbance was measured at 570 nm using a microplate reader (Bio-Rad iMARK, Japan).

Cell proliferation was determined by the colorimetric bromodexyuridine (BrdU) incorporation assay (Millipore, USA). A quantity of 3×10^3 cells were seeded in triplicate into a 96 well plate. BrdU solution (20 µL) was added to the cells and incubated for 4 h at 37 °C in a humidified atmosphere containing 5% CO_2 in air. After removing the culture medium, the cells were fixed, and the DNA was denatured in one step by using the Fixing solution. Incorporated BrdU was detected by an anti-BrdU monoclonal antibody. The immune complex was detected by a subsequent TMB Peroxidase Substrate reaction and the absorbance was measured at 450/540 nm using a microplate reader.

RNA isolation and real-time PCR
To investigate the expression of alkaline phosphatase (ALP), collagen I (Col-I), osteocalcin, bone morphogenetic protein-2 (BMP-2), and runt related transcription factor 2 (Runx-2) mRNA in MC3T3-E1 cells incubated with bezafibrate (100 µmol/L) for 0, 7, 14, 21, or 28 d in differentiation medium, SYBR green chemistry was used to perform quantitative determinations of the mRNAs. Total RNA was extracted from cultured MC3T3-E1 cells using the TRIzol reagent (Invitrogen, San Diego, CA, USA) according to the manufacturer's recommended protocol. The concentration and purity of total RNA were calculated with the absorbance at 260 and 280 nm. Total RNA (1 µg) was employed for the synthesis of first strand cDNA (cDNA synthesis kit; Toyobo, Japan). PCR primers (Table 1) were designed using the Primer 5.0 software. Real-time PCR was performed using 1 µL of cDNA in a 25 µL reaction volume with the ABI PRISM 7500 (Applied Biosystems, USA). The double-stranded DNA-specific dye SYBR Green I was incorporated into the PCR buffer provided in the SYBR

Table 1. Primers used for real-time quantitative PCR.

Name	Primer sequence	Size (bp)	Accession No
β-actin	5′-TCTTGGGTATGGAATCCTGTG-3′ 5′-AGGTCTTTACGGATGTCAACG-3′	82	NM_007393.2
Osteocalcin	5′-TGCTTGTGACGAGCTATCAG-3′ 5′-GAGGACAGGGAGGATCAAGT-3′	149	NM_001032298.2
BMP-2	5′-GGTCACAGATAAGGCCATTGC-3′ 5′-GCTTCCGCTGTTTGTGTTTG-3′	102	NM_007553.2
Runx-2	5′-AAGTGCGGTGCAAACTTTCT-3′ 5′-TCTCGGTGGCTGGTAGTGA-3′	90	NM_009820.2
ALP	5′-AACCCAGACACAAGCATTCC-3′ 5′-GAGAGCGAAGGGTCAGTCAG-3′	151	NM_007431.1
Col-I	5′-AGAGCATGACCGATGGATTC-3′ 5′-CCTTCTTGAGGTTGCCAGTC-3′	177	NM_007742.3

PCR kit (Toyobo, Japan) to allow for quantitative detection of the PCR product. The PCR reactions were carried out under the following conditions: 95 °C for 60 s, 40 cycles at 95 °C for 15 s, 60 °C for 15 s, and 72 °C for 45 s. All reactions were run in triplicate and analyzed by the $2^{-\Delta\Delta CT}$ method[20]. β-Actin was used as the internal control gene.

Assay of mineralization
To examine the mineralization of the MC3T3-E1 cells, the cells were seeded at 5×10^4 per well in 24-well plates with differentiation medium containing vehicle (DMSO) or bezafibrate (100 µmol/L). After 21 d, the formation of mineralizing plaques was visualized by Alizarin red staining. Cells were washed with PBS 3 times and fixed in 10% formaldehyde for 1 h at 4 °C. After 3 washes with distilled water, the cells were stained in 1% Alizarin red solution (pH 4.3) for 30 min. The remaining dye was washed out by several washes with distilled water. To quantify matrix mineralization, Alizarin red stained cultures were incubated in 100 mmol/L cetylpyridinium chloride for 1 h to solubilize and release calcium-bound Alizarin red into solution. The absorbance of the released Alizarin red was measured at 550 nm.

Assay of alkaline phosphatase activity
The MC3T3-E1 cells were pretreated with compound C (5 µmol/L), GSK0660 (0.5 µmol/L), MK886 (10 µmol/L), or *L*-NAME (1000 µmol/L) for 1 h, followed by incubation with bezafibrate (100 µmol/L) for 7 d in differentiation medium. ALP enzyme activity was determined by measuring the hydrolysis of ρ-NPP according to the manufacturer's instructions (Sigma, St Louis, MO, USA). In brief, cells in 24-well plates were rinsed three times with PBS and then sonicated in 0.1% Triton X-100. The protein assays were performed with the bicinchoninic acid (BCA) protein assay reagent. Cell lysates containing 2 µg of total protein were added to 200 µL of the ρ-NPP solution. The plate was incubated in the dark for approximately 30 min at room temperature. The reaction was stopped by 3 mol/L NaOH, and the absorbance was measured

at 405 nm using the Bio-Rad microplate reader. A standard curve was prepared with ρ-NP.

Western blot analyses
For Western blotting, the MC3T3-E1 cells were plated in 6 cm dishes. Cells were treated with bezafibrate (100 µmol/L) for 0, 15, 30, 60, 120, or 240 min and were pretreated with compound C (5 µmol/L), GSK0660 (0.5 µmol/L), or MK886 (10 µmol/L), followed by incubation with bezafibrate (100 µmol/L) for 120 min. MC3T3-E1 cells were washed twice with ice-cold PBS and then resuspended in lysis buffer (RIPA, Beyone, China) containing 1% NP-40, 0.1% SDS, 5 mmol/L EDTA, 0.5% sodium deoxycholate, 1 mmol/L sodium orthovanadate, and 1 mmol/L phenylmethylsulfonyl fluoride. The cell lysates were then sonicated for 30 s. For each sample, 30 µg of protein, assessed by a BCA protein assay (Bio-Rad, Mississauga, Ontario, Canada), was run on a 7% polyacrylamide gel and transferred to a polyvinylidene difluoride (PVDF) membrane (Millipore). After being blocked with 5% non-fat milk/TBST, the membrane was incubated overnight at 4 °C with p-AMPKα, total-AMPKα, p-ACC, total-ACC, p-Akt, total-Akt, p-eNOS, and total-eNOS antibodies at a 1:1000 dilution. Specific antibody binding was detected by a 1:2000 dilution of corresponding horseradish peroxidase-conjugated secondary antibodies (Cell Signaling Technology) for 1 h at room temperature. The blots were then washed, and the signal was visualized by an HRP chemiluminescent substrate reagent kit (Invitrogen, San Diego, CA, USA) according to the manufacture's protocol. After stripping of p-AMPKα, p-eNOS or p-ACC, total-AMPKα, total-eNOS or total-ACC, immunoreactivity was determined in the same membrane. The band intensity was quantified by densitometric analysis using IMAGE J software (National Institutes of Health, USA).

Assessment of NO production
Cells were grown in 24-well plates to measure NO production, which was assessed by the measurement of the stable end-product of NO oxidation, nitrite. MC3T3-E1 cells were incubated with bezafibrate (100 µmol/L) for 0, 30, 60, 120, or 240 min and were pretreated with compound C (5 µmol/L) followed by bezafibrate for 240 min. Nitrite was measured using a total nitric oxide assay kit (Beyotime, Haimen, China). Briefly, a standard curve was prepared with standard nitrite solutions in α-MEM medium, covering a concentration range of 2–50 µmol/L. The standard solutions or cell supernatants were reacted with nitrate reductase for 40 min in a 96-well plate, and Griess reagent I and Griess reagent II were then added. After a 10 min incubation at room temperature, the absorbance was measured at 540 nm, and nitrite concentrations were determined from the standard curve made using a solution of KNO_2 dissolved in medium.

Statistical analysis
Data were expressed as mean±SEM and analyzed by SPSS 16.0 software. Statistical evaluations for the differences between groups were performed by two-tailed independent Student's

t-tests or a one-way analysis of variance (ANOVA) followed by Fisher's protected least significant difference (PLSD). $P<0.05$ was considered statistically significant.
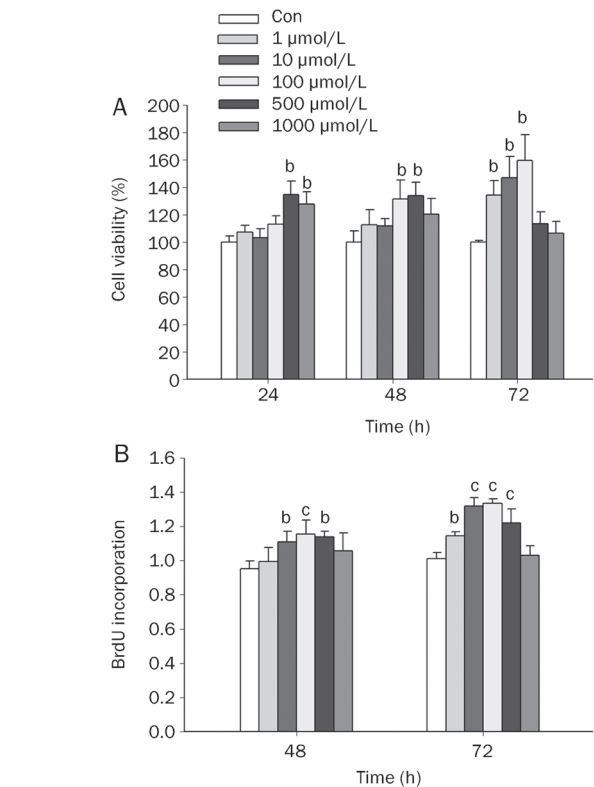
Results

Effect of bezafibrate on the viability and proliferation of MC3T3-E1 cells

To investigate the effect of bezafibrate on osteoblastic MC3T3-E1 cell growth, cell viability was assessed using the MTT assay and cell proliferation was assessed using the BrdU assay after treating cells with bezafibrate (1–1000 μmol/L) for 24–72 h. We found that treating the cells with bezafibrate led to a dose- and time-dependent increase in cell viability (Figure 1A) and cell proliferation (Figure 1B). The maximal effect on cell viability was reached at the concentrations of 500 (134% of basal) and 100 (159% of basal) μmol/L at 24 and 72 h, respectively. The maximal effect on cell proliferation was reached at a concentration of 100 μmol/L at 48 (121% of basal) and 72 (132% of basal) h.

Effect of bezafibrate on the differentiation and mineralization of MC3T3-E1 cells

To investigate the effect of bezafibrate on osteoblast differentiation, the mRNA expression levels of ALP, Col-I and osteocalcin on d 0, 7, 14, 21, and 28 were evaluated by real-time PCR (Figure 2A, 2B, and 2C). Bezafibrate (100 μmol/L) increased the mRNA expression levels of ALP on d 7 and 14 by 1.89- and 1.46-fold, respectively ($P<0.05$). Bezafibrate also increased the mRNA expression levels of Col-I on d 7, 14, and 21 by 1.88-, 1.40-, and 1.5-fold, respectively ($P<0.05$), as well as the mRNA expression levels of osteocalcin on d 14 and 21 by 2.04- and 1.65-fold, respectively ($P<0.05$).

In contrast, after 21 d of exposure to the osteogenic induction medium, bezafibrate (100 μmol/L) showed marked and diffuse mineralization nodules (Figure 2D). A 1.25-fold

Figure 1. Effects of bezafibrate on viability and proliferation differentiation of MC3T3-E1 cells. MC3T3-E1 cells were treated with bezafibrate (1–1000 μmol/L) at 24, 48, or 72 h. (A) Cell viability was determined using the MTT assays. Results represent as the percentage of cell viability with the control (*n*=4). (B) Cell proliferation was determined using the colorimetric BrdU incorporation assays. Results represent as arbitrary units by optical absorption (*n*=3). [b]$P<0.05$, [c]$P<0.01$ compared to the control group

increase in the extent of mineralization was also observed by spectrophotometric readings (Figure 2E).
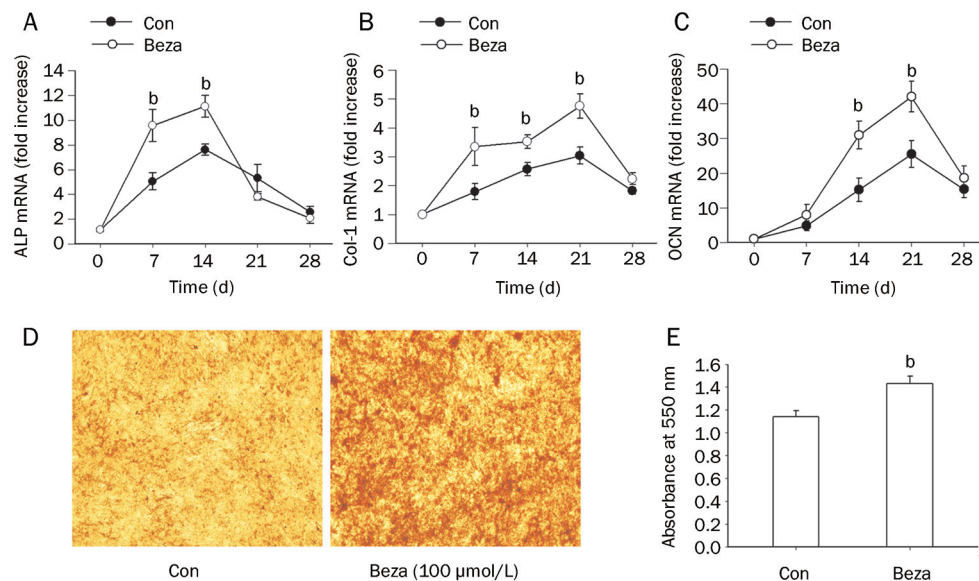
Figure 2. Effects of bezafibrate on differentiation and mineralization of MC3T3-E1 cells. (A, B, C) Cells were treated with vehicle (con) or bezafibrate (beza) (100 μmol/L) for the time periods indicated after the cells reached 80% confluence. Total RNA was collected on d 0, 7, 14, 21, and 28. ALP, Col-1, and osteocalcin (OCN) mRNA expression were evaluated by real-time PCR. Results were expressed as fold increase over the control values. (D) Photomicrograph of mineralized nodules stained by Alizarin red staining at the differentiation d 21 (Original magnification: ×100). (E) Quantification of Alizarin red staining with cetylpyridinium chloride. The absorbance of the released Alizarin red was measured at 550 nm. [b]$P<0.05$ compared to the control group (*n*=3).

Effect of bezafibrate on eNOS phosphorylation and NO production in MC3T3-E1 cells

To investigate whether bezafibrate can induce eNOS phosphorylation and NO production in osteoblastic MC3T3-E1 cells, bezafibrate was added after the cells reached 80% confluence with different time points and dosages. Western blot analysis was performed to determine the expression of p-eNOS and eNOS. Treatment of MC3T3-E1 cells with bezafibrate resulted in a time- and dose-dependent activation of eNOS phosphorylation, reaching approximately 1.58-fold that of the control at 100 µmol/L (Figure 3A) and 2.05-fold that of the baseline level at 60 min (Figure 3B). The total amount of eNOS was unchanged throughout this experiment. Furthermore, bezafibrate-induced NO production increased markedly in osteoblasts in a time-dependent manner (Figure 3C).

Effects of bezafibrate on the AMPK and Akt signaling pathway in MC3T3-E1 cells

To investigate whether bezafibrate can activate phosphorylation of AMPK and Akt, the upstream kinases for eNOS, bezafibrate (100 µmol/L), was added to osteoblastic MC3T3-E1 cells at various time points (0, 15, 30, 60, 120, and 240 min). Western blot analysis revealed that the phosphorylation levels of AMPK and ACC, which is a well-established downstream target of AMPK[21], rose gradually in a time-dependent manner. The maximum effect of bezafibrate on AMPK and ACC appeared after a 2-h incubation, which was 1.34- and 1.75-fold, respectively, that of the baseline level (Figure 4A and 4B), whereas the phosphorylation level of Akt remained unchanged throughout the time course (Figure 4A and 4C). These results indicate that treatment with bezafibrate can activate the AMPK signaling pathway.

To further address whether the AMPK signaling pathway is involved in bezafibrate-induced upregulation of eNOS phosphorylation and NO production, we pretreated MC3T3-E1 cells with the AMPK inhibitor compound C (5 µmol/L). Compared to the control group, bezafibrate (100 µmol/L) enhanced the phosphorylation level of eNOS by 1.46-fold, which was suppressed by 37.68% when pretreated with compound C, compared to the group treated with bezafibrate alone (*P*<0.01, Figure 5A). Compared to the control group, bezafibrate (100 µmol/L) enhanced NO production by 4.08-fold, which was suppressed by 60.8% when pretreated with compound C, compared to the group treated with bezafibrate alone (*P*<0.01, Figure 5B). These results indicate that AMPK activation is essential for bezafibrate-induced upregulation of eNOS phosphorylation and NO production.

Effects of bezafibrate on PPARα and PPARβ signal transduction pathways

To investigate whether PPARα and PPARβ signaling pathways are involved in bezafibrate-induced upregulation of AMPK and eNOS phosphorylation, the MC3T3-E1 cells were pretreated with the PPARα inhibitor MK886 (10 µmol/L) and PPARβ inhibitor GSK0660 (0.5 µmol/L), and the level of AMPK and eNOS phosphorylation was then evaluated
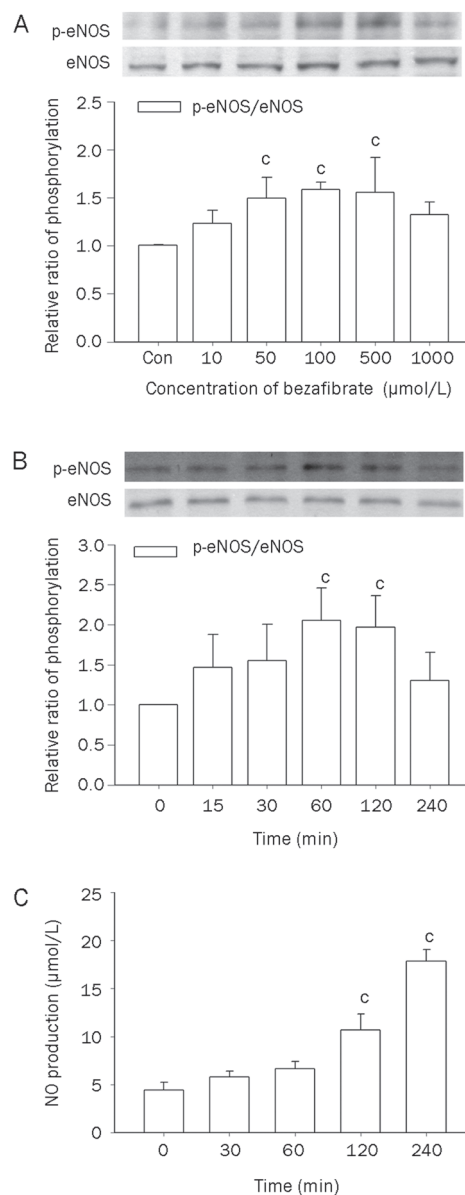
Figure 3. Effect of bezafibrate on eNOS phosphorylation levels and NO production in MC3T3-E1 cells. (A) MC3T3-E1 cells were treated with indicated concentration of bezafibrate for 2 h and immunobloted with anti-phosphorylated eNOS (Ser-1177) and anti-eNOS antibodies. (B) MC3T3-E1 cells were treated with bezafibrate (100 µmol/L) for indicated duration and immunobloted with anti-phosphorylated eNOS (Ser-1177) and anti-eNOS antibodies. Bar graph showing semi-quantitative results by ratio of phosphorylated eNOS to total eNOS scanning density values and were normalized by setting the control as 1. (C) MC3T3-E1 cells were treated with bezafibrate (100 µmol/L) for indicated duration and NO production was evaluated using the Griess reagent. ^{c}*P*<0.01 compared to the control group (*n*=3).

by Western blotting (Figure 6). Pretreatment with GSK0660 reduced the levels of AMPK and eNOS phosphorylation by 34.86% (*P*<0.05) and 48.18% (*P*<0.01) respectively, compared to the group treated with bezafibrate alone. Pretreatment with MK886 slightly reduced the level of AMPK and eNOS phos-
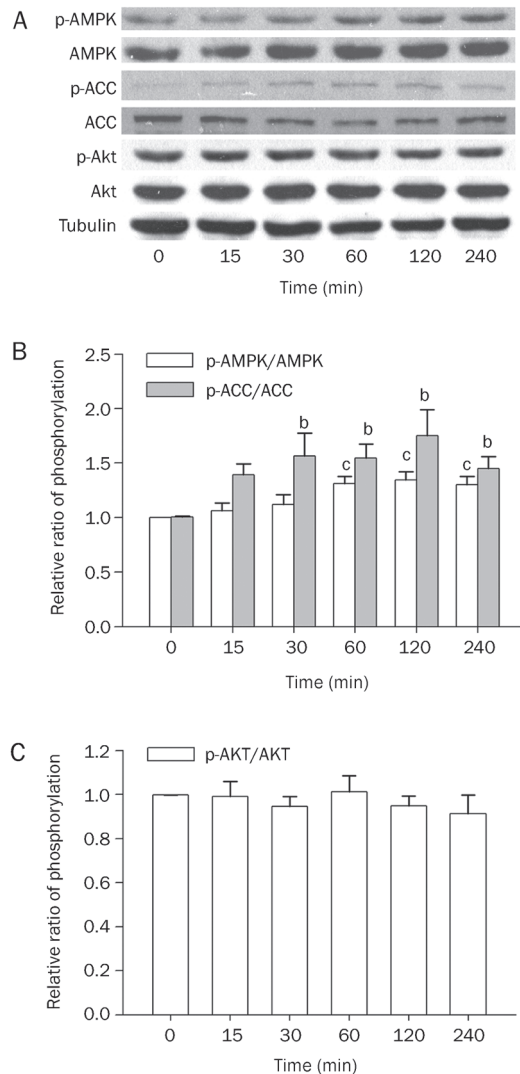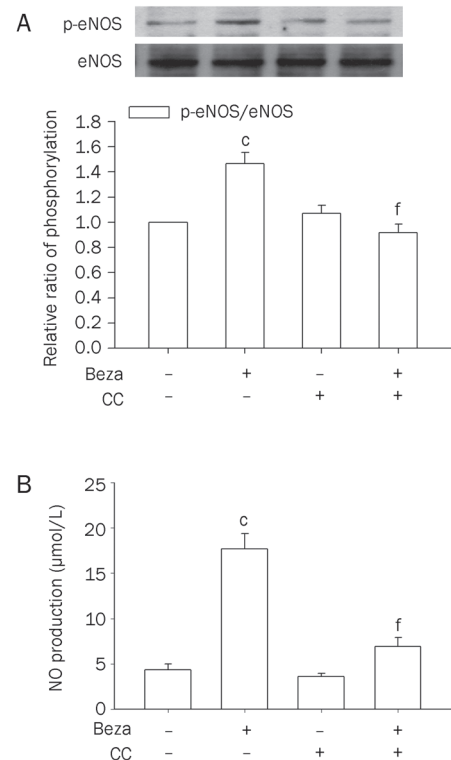
Figure 4. Effects of bezafibrate on AMPK, ACC, and Akt phosphorylation levels in MC3T3-E1 cells. (A) MC3T3-E1 cells were treated with bezafibrate (100 µmol/L) for indicated duration and immunoblotted with anti-phosphorylated AMPK, ACC, or Akt antibodies. (B and C) Bar graph showing semi-quantitative results by ratio of phosphorylated antibody to total antibody scanning density values and were normalized by setting the control group as 1. [b]$P<0.05$, [c]$P<0.01$ compared to the control group ($n=3$).


Figure 5. Effects of AMPK inhibitor compound C on bezafibrate-induced upregulation of eNOS phosphorylation and NO production. (A) MC3T3-E1 cells were pretreated with 5 µmol/L compound C (CC) 1 h, followed by incubation with or without 100 µmol/L bezafibrate for 2 h, and then immunobloted with anti-phosphorylated eNOS antibody. Data were normalized by setting the untreated control group as 1. (B) MC3T3-E1 cells were treated with or without 100 µmol/L bezafibrate in the presence or absence of 5 µmol/L compound C for 4 h and NO production was evaluated using the Griess reagent. [c]$P<0.01$ compared to the control group; [f]$P<0.01$ compared to the group treated with bezafibrate alone ($n=3$).

phorylation by 12.58% ($P>0.05$) and 15.25% ($P>0.05$) respectively. These results indicate that bezafibrate-induced up-regulation of AMPK and eNOS phosphorylation is partially dependent on PPARβ.

Effects of bezafibrate on BMP-2 and Runx-2 expression in MC3T3-E1 cells

Next, we investigated the effect of bezafibrate on BMP-2 and Runx-2 mRNA expression by real-time PCR. After addition of bezafibrate, BMP-2 mRNA expression was increased to 1.80- and 1.74-fold ($P<0.05$) of the control group by bezafibrate at d 7 and 14, respectively (Figure 7A), whereas Runx-2 mRNA expression was increased to 1.51-, 1.55-, and 1.64-fold ($P<0.05$)

at d 7, 14, and 21, respectively (Figure 7B). Compared to the group treated with bezafibrate alone, pretreatment with the PPARβ inhibitor GSK0660 reduced BMP-2 and Runx-2 mRNA expression by 40.76% ($P<0.01$) and 35.22% ($P<0.01$), respectively. Pretreatment with the AMPK inhibitor compound C reduced BMP-2 and Runx-2 mRNA expression by 37.82% ($P<0.01$) and 40.15% ($P<0.01$), respectively (Figure 7C and 7D). However, pretreatment with the PPARα inhibitor MK886 only slightly reduced BMP-2 and Runx-2 mRNA expression by 6.40% ($P>0.05$) and 8.85% ($P>0.05$), respectively (Figure 7C and 7D). These results indicate that the expression of BMP-2 and Runx-2 is affected largely by PPARβ and AMPK activity.

Effects of blocking different signaling molecules on bezafibrate-induced MC3T3-E1 cell proliferation and differentiation

To further investigate whether the PPARα, PPARβ, AMPK, or eNOS signaling pathways participate in the bezafibrate-induced enhancement of osteoblast proliferation and differentiation, the MC3T3-E1 cells were pretreated with the PPARα inhibitor MK886, PPARβ inhibitor GSK0660, AMPK inhibitor
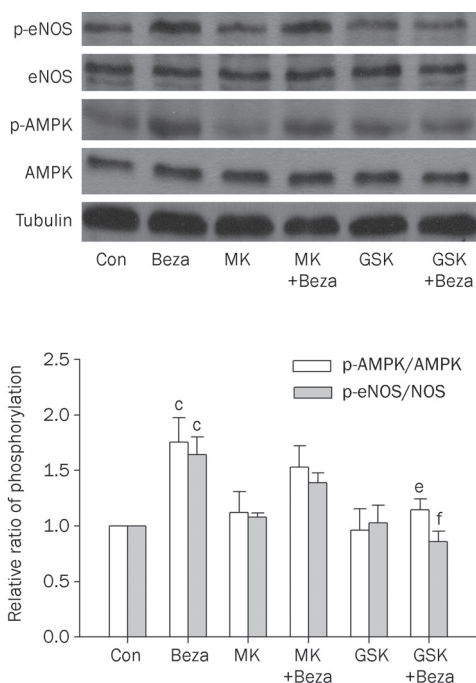
Figure 6. Effects of bezafibrate on PPARα and PPARβ signal transduction pathways. MC3T3-E1 cells were pretreated with 10 µmol/L MK886 (MK) or 0.5 µmol/L GSK0660 (GSK) 1 h, followed by incubation with or without 100 µmol/L bezafibrate (beza) for 2 h, and then immunobloted with anti-phosphorylated AMPK or eNOS antibody. Bar graph showing semi-quantitative results by ratio of phosphorylated antibody to total antibody scanning density values and were normalized by setting the control group as 1. $^{c}P<0.01$ compared to the control group; $^{e}P<0.05$, $^{f}P<0.01$ compared to the group treated with bezafibrate alone (n=3).

Compound C, or NOS inhibitor *L*-NAME. Pretreatment with compound C, MK886, GSK0660, or *L*-NAME inhibited bezafibrate-induced cell viability by 28.3%, 43.8%, 40.5%, or 41.8% (Figure 8A), respectively, and cell proliferation by 15.5%,

38.2%, 28.1%, or 36.4% (Figure 8B), respectively ($P<0.01$), compared to the group treated with bezafibrate alone for 48 h. ALP activity and ALP mRNA expression in response to MK886, compound C, GSK0660, or *L*-NAME were also examined (Figure 8C and 8D). Pretreatment with compound C (2 and 5 µmol/L), *L*-NAME (100 and 1000 µmol/L), or GSK0660 (0.1 and 0.5 µmol/L) reversed the bezafibrate-induced enhancement of ALP activity on d 7 ($P<0.05$), whereas MK886 (5 or 10 µmol/L) slightly reversed it ($P>0.05$). In addition, pretreatment with compound C (5 µmol/L), GSK0660 (0.5 µmol/L), or *L*-NAME (1000 µmol/L) partly reversed the bezafibrate-induced enhancement of ALP mRNA expression on d 7 ($P<0.05$), whereas MK886 (10 µmol/L) had no significant effect ($P>0.05$).

Discussion

Results from this study suggest that bezafibrate can induce the proliferation and differentiation of osteoblastic MC3T3-E1 cells and augment the expression of BMP-2 and Runx-2 in the cells. Moreover, bezafibrate could enhance NO production as well as the phosphorylation of AMPK and eNOS, which can be reversed by the PPARβ inhibitor GSK0660, but not the PPARα inhibitor MK886. Thus, bezafibrate seems to promote the proliferation and differentiation of MC3T3-E1 cells partly through the PPARβ-AMPK-eNOS signaling pathway.

Fibrates, including fenofibrate and bezafibrate, are a group of drugs widely used for the treatment of hypertriglyceridemia and hypercholesterolemia. Recently published data have shown that bezafibrate was able to increase the number of osteoblastic colonies formed from rat bone marrow stromal cells (BMSCs)[6]. It has been reported that the inhibition of NO synthesis by NMMA markedly decreases the proliferation of the osteoblast-like cell line MG63[22] and primary fetal calvarial osteoblasts[23]. Furthermore, the addition of NO through donor compounds stimulates osteoblastic MC3T3-E1 cell proliferation[24]. Our results are consistent with their reports and
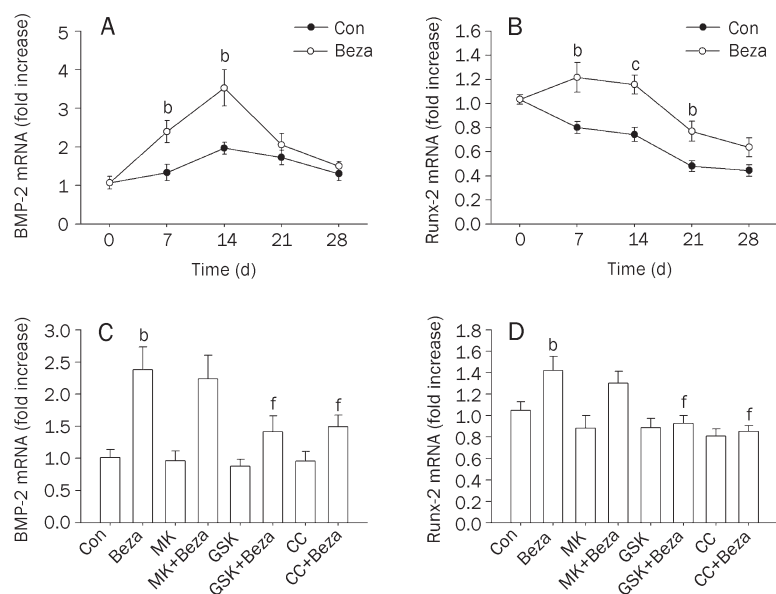
Figure 7. Effects of bezafibrate on BMP-2 and Runx-2 mRNA expression in MC3T3-E1 cells. (A and B) MC3T3-E1 cells were treated with vehicle (con) or bezafibrate (beza) (100 µmol/L) for indicated time period. Total RNA was collected on d 0, 7, 14, 21, and 28. BMP-2 and Runx-2 mRNA expression was evaluated by real-time PCR. (C and D) MC3T3-E1 cells were pretreated with 10 µmol/L MK886 (MK), 0.5 µmol/L GSK0660 (GSK), or 5 µmol/L compound C (CC) 1 h, followed by incubation with or without 100 µmol/L bezafibrate (beza) for 7 d, and were then collected to determine the mRNA levels of BMP-2 and Runx-2. Results were expressed as fold increase over the control group values. $^{b}P<0.05$, $^{c}P<0.01$ compared to the control group; $^{f}P<0.01$ compared to the group treated with bezafibrate alone (n=3).
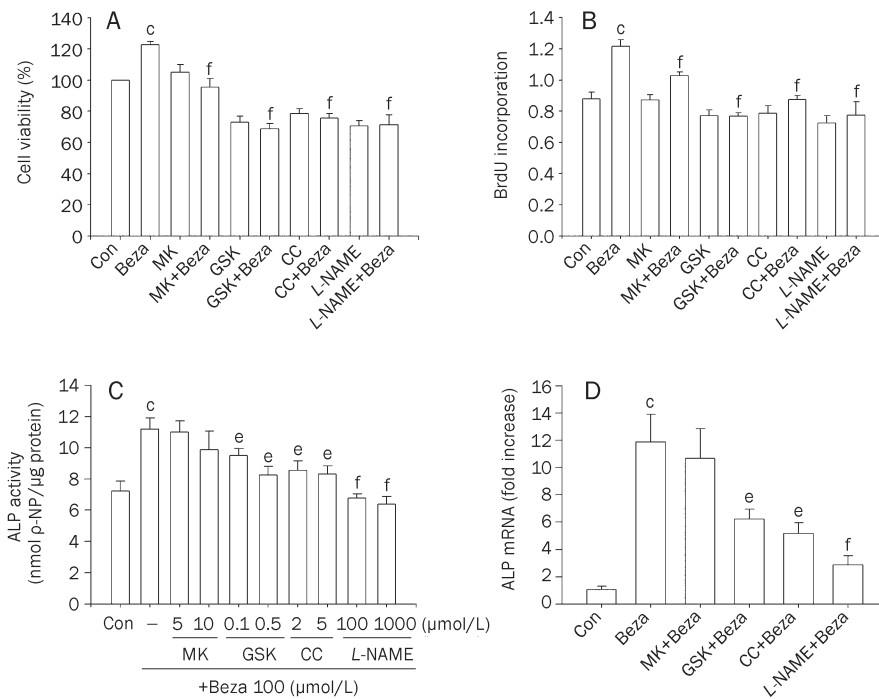
Figure 8. Effects of inhibitors of different signaling molecules on bezafibrate-induced proliferation and differentiation in MC3T3-E1 cells. (A and B) MC3T3-E1 cells were pretreated with 10 μmol/L MK886 (MK), 0.5 μmol/L GSK0660 (GSK), 5 μmol/L compound C (CC) or 1000 μmol/L *L*-NAME for 1 h, followed by treatment with or without 100 μmol/L bezafibrate (beza) for 48 h. Cell viability was determined using the MTT assays. Results represent as the percentage of cell viability compared with the untreated control group (n=4). Cell proliferation was determined using the colorimetric BrdU incorporation assays. Results represent as arbitrary units by optical absorption (n=3). (C and D) MC3T3-E1 cells were pretreated with MK, GSK, or CC with 1 h, followed by treated with 100 μmol/L bezafibrate for 7 d. ALP activity of MC3T3-E1 cells were measured using the ρ-NPP assay. ALP mRNA expression was evaluated by real-time PCR. Results were expressed as fold increase over the control group values (n=3). [c]P<0.01 compared to the control group; [e]P<0.05, [f]P<0.01 compared to the group treated with bezafibrate alone.

indicate that bezafibrate significantly stimulated osteoblastic MC3T3-E1 cell proliferation. Both PPARα and PPARβ could be involved in bezafibrate-induced osteoblastic proliferation, and this action could be associated with eNOS activity and NO production. However, the mechanisms by which PPARα may be involved in cell proliferation need to be investigated in future experiments.

In this study, we demonstrated that bezafibrate can promote mineralization and the expression of osteobastic differentiation markers in MC3T3-E1 cells, including ALP, Col-I and osteocalcin, which was consistent with previous finding that fenofibrate stimulated osteoblast differentiation[25]. These results further confirmed the role of fibrates in stimulating bone formation. It has been demonstrated that both PPARα and PPARβ can be activated by bezafibrate[26]. In our study, we found that the PPARβ inhibitor GSK0660, not the PPARα inhibitor MK886, could partly but significantly reverse the bezafibrate-induced osteoblast differentiation. Thus, our study suggests that the effects of bezafibrate are in part dependent on PPARβ and are not dependent on PPARα, in MC3T3-E1 cells.

We next examined the mechanisms involved in bezafibrate-induced osteoblast proliferation and differentiation. Previous studies have shown that bezafibrate can enhance phosphorylation of eNOS (Ser1177), which increases eNOS activity and then contributes to increased NO production in endothelial cells[27]. NO has pleiotropic effects on bone cells *in vitro*. In osteoblast and osteoblast-like cells, NO promotes differentiation[28] and increases proliferation[29]. Long-term therapy with NO will not only increase BMD but may also decrease fracture rates[17]. Estrogen is known to enhance proliferation and differentiation of osteoblastic cells by stimulating eNOS

activity[17]. These findings indicate that eNOS and NO play an important role in osteoblast differentiation and function. In the present study, bezafibrate was found to significantly enhance eNOS phosphorylation and NO production in osteoblastic MC3T3-E1 cells.

The phosphorylation of eNOS is known to be regulated by various kinases. In endothelial cells, AMPK has been shown to phosphorylate and activate eNOS[16, 30]. Another study showed that the PI3K/Akt signal pathway was involved in bezafibrate-mediated upregulation of eNOS phosphorylation[31]. To investigate whether the AMPK or Akt pathway is involved in bezafibrate-induced eNOS phosphorylation in osteoblasts, we examined the effects of bezafibrate on AMPK and Akt phosphorylation. In this study, we found that treatment of MC3T3-E1 cells with bezafibrate led to an increase in the phosphorylation of AMPK and ACC, a well-characterized substrate of AMPK[21], whereas no changes were observed in the level of Akt phosphorylation. Additionally, the AMPK inhibitor compound C was found to suppress bezafibrate-induced eNOS phosphorylation and NO production. These data suggest a possible role of AMPK as an upstream kinase of bezafibrate-induced eNOS phosphorylation and NO production in osteoblasts.

However, the mechanisms involved in bezafibrate-activated AMPK are still unknown. Bezafibrate was reported to reduce circulating cholesterol and affect hepatic cholesterol metabolism through a PPARα-independent mechanism in mice[32]. In addition, PPARα is also not required for bezafibrate-mediated lipid metabolism since the PPARβ isoform is predominant in the small intestine[33]. However, Wang *et al*[31]showed that bezafibrate-induced up-regulation of eNOS phosphorylation was fully inhibited by the PPARα inhibitor MK886 in

bovine endothelial cells. In the present study, we indicated that bezafibrate activated AMPK and eNOS partly via PPARβ, not PPARα. It is presumable that these inconsistent results might be due to the differences in the expression of PPARα and PPARβ in various cells. The mRNA expression level of PPARβ is much higher than that of PPARα mRNA in MC3T3-E1 cells[34]. Additionally, the potency of bezafibrate at the murine PPARα and PPARβ is remarkably similar because the EC_{50} for bezafibrate is 90 and 110 μmol/L, respectively[26]. Therefore, the bezafibrate-induced activation of PPARβ may contribute to its beneficial effects in osteoblastic MC3T3-E1 cells.

BMP-2, a member of the transforming growth factor-β superfamily, regulates the differentiation of various cells involved in cartilage and bone formation during fracture repair[35]. Runx-2 has been widely recognized as the master osteogenic transcription factor because Runx-2-knockout mice display complete absence of bone due to arrested osteoblast maturation; it also plays a critical role in osteoblast marker gene expression, including Col-1, BSP, and osteocalcin[36]. The activation of AMPK promotes the differentiation of osteoblastic cells via increasing eNOS and BMP-2 expression[37]. The activation of eNOS and NO activity might lead to BMP-2 protein increases[38]. The present study found that bezafibrate enhanced BMP-2 and Runx-2 expression in the early stages of osteoblast differentiation in osteoblastic MC3T3-E1 cells, which was reversed by the PPARβ inhibitor GSK0660 or the AMPK inhibitor compound C, but not the PPARα inhibitor MK886. Thus, it is possible that bezafibrate enhances BMP-2 and Runx-2 expression at least partly via activation of PPARβ and AMPK.

Osteoporosis is associated with atherosclerosis and vascular calcification[39]. Dyslipidemia appears to participate in the pathogenesis of bone and vascular diseases[40]. A number of studies have suggested a positive relationship between BMD and triglyceride levels[3, 41]. Hormone replacement therapy has beneficial effects in the prevention of both atherosclerosis and osteoporosis[42]. Bisphosphonates, which inhibit bone resorption, are used for the treatment of osteoporosis, whereas the statins, which inhibit cholesterol biosynthesis, are used for the treatment of atherosclerosis. Some clinical data suggest that statins can increase bone density[38], whereas bisphosphonates may have a beneficial effect on plasma lipid levels and on the atherosclerotic process[43]. Previous studies suggested that agents modulating AMPK can not only cure dyslipidemia and atherosclerosis[30] but also promote bone formation[37]. In this study, we also found that bezafibrate might be a candidate drug promoting bone formation.

In summary, these results show that bezafibrate can enhance the proliferation and differentiation of MC3T3-E1 cells, partly via the activation of PPARβ, but not PPARα, which could be mediated by the activation of AMPK and eNOS, leading to increased BMP-2 and Runx-2 expression. This study provides evidence that bezafibrate might be beneficial for osteoporosis by promoting bone formation.

Author contribution

Xing ZHONG and Guo-hong WEI performed the research and wrote the paper; Xing ZHONG, Ling-ling XIU, Guo-hong WEI, Yuan-yuan LIU, Yan-bing LI, and Lei SU analyzed the data; Ling-ling XIU, Xiao-pei CAO, and Hai-peng XIAO designed the study and wrote the paper.

References

1 Chan GK, Duque G. Age-related bone loss: old bone, new facts. Gerontology 2002; 48: 62–71.

2 Dennison EM, Syddall HE, Aihie Sayer A, Martin HJ, Cooper C. Lipid profile, obesity and bone mineral density: the Hertfordshire Cohort Study. QJM 2007; 100: 297–303.

3 Cui LH, Shin MH, Chung EK, Lee YH, Kweon SS, Park KS, *et al*. Association between bone mineral densities and serum lipid profiles of pre- and post-menopausal rural women in South Korea. Osteoporos Int 2005; 16: 1975–81.

4 Lorincz C, Reimer RA, Boyd SK, Zernicke RF. High-fat, sucrose diet impairs geometrical and mechanical properties of cortical bone in mice. Br J Nutr 2010; 103: 1302–8.

5 Meier CR, Schlienger RG, Kraenzlin ME, Schlegel B, Jick H. HMG-CoA reductase inhibitors and the risk of fractures. JAMA 2000; 283: 3205–10.

6 Still K, Grabowski P, Mackie I, Perry M, Bishop N. The peroxisome proliferator activator receptor alpha/delta agonists linoleic acid and bezafibrate upregulate osteoblast differentiation and induce periosteal bone formation *in vivo*. Calcif Tissue Int 2008; 83: 285–92.

7 Peters JM, Aoyama T, Burns AM, Gonzalez FJ. Bezafibrate is a dual ligand for PPARalpha and PPARbeta: studies using null mice. Biochim Biophys Acta 2003; 1632: 80–9.

8 Effect of fenofibrate on progression of coronary-artery disease in type 2 diabetes: the Diabetes Atherosclerosis Intervention Study, a randomised study. Lancet 2001; 357: 905–10.

9 Malik J, Melenovsky V, Wichterle D, Haas T, Simek J, Ceska R, *et al*. Both fenofibrate and atorvastatin improve vascular reactivity in combined hyperlipidaemia (fenofibrate versus atorvastatin trial–FAT). Cardiovasc Res 2001; 52: 290–8.

10 Okayasu T, Tomizawa A, Suzuki K, Manaka K, Hattori Y. PPARalpha activators upregulate eNOS activity and inhibit cytokine-induced NF-kappaB activation through AMP-activated protein kinase activation. Life Sci 2008; 82: 884–91.

11 Murakami H, Murakami R, Kambe F, Cao X, Takahashi R, Asai T, *et al*. Fenofibrate activates AMPK and increases eNOS phosphorylation in HUVEC. Biochem Biophys Res Commun 2006; 341: 973–8.

12 Kramer DK, Al-Khalili L, Guigas B, Leng Y, Garcia-Roves PM, Krook A. Role of AMP kinase and PPARdelta in the regulation of lipid and glucose metabolism in human skeletal muscle. J Biol Chem 2007; 282: 19313–20.

13 Kanazawa I, Yamaguchi T, Yano S, Yamauchi M, Yamamoto M, Sugimoto T. Adiponectin and AMP kinase activator stimulate proli-

feration, differentiation, and mineralization of osteoblastic MC3T3-E1 cells. BMC Cell Biol 2007; 8: 51–62.

14 Kanazawa I, Yamaguchi T, Yano S, Yamauchi M, Sugimoto T. Metformin enhances the differentiation and mineralization of osteoblastic MC3T3-E1 cells via AMP kinase activation as well as eNOS and BMP-2 expression. Biochem Biophys Res Commun 2008; 375: 414–9.

15 Shah M, Kola B, Bataveljic A, Arnett TR, Viollet B, Saxon L, *et al.* AMP-activated protein kinase (AMPK) activation regulates *in vitro* bone formation and bone mass. Bone 2010; 47: 309–19.

16 Morrow VA, Foufelle F, Connell JM, Petrie JR, Gould GW, Salt IP. Direct activation of AMP-activated protein kinase stimulates nitric-oxide synthesis in human aortic endothelial cells. J Biol Chem 2003; 278: 31629–39.

17 Wimalawansa SJ. Nitric oxide and bone. Ann N Y Acad Sci 2010; 1192: 391–403.

18 Grassi F, Fan X, Rahnert J, Weitzmann MN, Pacifici R, Nanes MS, *et al.* Bone re/modeling is more dynamic in the endothelial nitric oxide synthase(–/–) mouse. Endocrinology 2006; 147: 4392–9.

19 Quarles LD, Yohay DA, Lever LW, Caton R, Wenstrup RJ. Distinct proliferative and differentiated stages of murine MC3T3-E1 cells in culture: an *in vitro* model of osteoblast development. J Bone Miner Res 1992; 7: 683–92.

20 Livak KJ, Schmittgen TD. Analysis of relative gene expression data using real-time quantitative PCR and the 2(-Delta Delta C(T)) Method. Methods 2001; 25: 402–8.

21 Hardie DG, Carling D, Carlson M. The AMP-activated/SNF1 protein kinase subfamily: metabolic sensors of the eukaryotic cell? Annu Rev Biochem 1998; 67: 821–55.

22 Riancho JA, Salas E, Zarrabeitia MT, Olmos JM, Amado JA, Fernandez-Luna JL, *et al.* Expression and functional role of nitric oxide synthase in osteoblast-like cells. J Bone Miner Res 1995; 10: 439–46.

23 Lin IC, Smartt JM Jr, Nah HD, Ischiropoulos H, Kirschner RE. Nitric oxide stimulates proliferation and differentiation of fetal calvarial osteoblasts and dural cells. Plast Reconstr Surg 2008; 121: 1554–66.

24 Kanamaru Y, Takada T, Saura R, Mizuno K. Effect of nitric oxide on mouse clonal osteogenic cell, MC3T3-E1, proliferation *in vitro*. Kobe J Med Sci 2001; 47: 1–11.

25 Syversen U, Stunes AK, Gustafsson BI, Obrant KJ, Nordsletten L, Berge R, *et al.* Different skeletal effects of the peroxisome proliferator activated receptor (PPAR)alpha agonist fenofibrate and the PPARgamma agonist pioglitazone. BMC Endocr Disord 2009; 9: 10–22.

26 Willson TM, Brown PJ, Sternbach DD, Henke BR. The PPARs: from orphan receptors to drug discovery. J Med Chem 2000; 43: 527–50.

27 Boo YC, Sorescu G, Boyd N, Shiojima I, Walsh K, Du J, *et al.* Shear stress stimulates phosphorylation of endothelial nitric-oxide synthase at Ser1179 by Akt-independent mechanisms: role of protein kinase A. J Biol Chem 2002; 277: 3388–96.

28 Fan X, Rahnert JA, Murphy TC, Nanes MS, Greenfield EM, Rubin J. Response to mechanical strain in an immortalized pre-osteoblast cell is dependent on ERK1/2. J Cell Physiol 2006; 207: 454–60.

29 Koyama A, Otsuka E, Inoue A, Hirose S, Hagiwara H. Nitric oxide accelerates the ascorbic acid-induced osteoblastic differentiation of mouse stromal ST2 cells by stimulating the production of prostaglandin E$_2$. Eur J Pharmacol 2000; 391: 225–31.

30 Shirwany NA, Zou MH. AMPK in cardiovascular health and disease. Acta Pharmacol Sin 2010; 31: 1075–84.

31 Wang Y, Yang Q, Yan JT, Zhao C, Cianflone K, Wang DW. Effects of bezafibrate on the expression of endothelial nitric oxide synthase gene and its mechanisms in cultured bovine endothelial cells. Atherosclerosis 2006; 187: 265–73.

32 Nakajima T, Tanaka N, Sugiyama E, Kamijo Y, Hara A, Hu R, *et al.* Cholesterol-lowering effect of bezafibrate is independent of peroxisome proliferator-activated receptor activation in mice. Biochem Pharmacol 2008; 76: 108–19.

33 Poirier H, Niot I, Monnot MC, Braissant O, Meunier-Durmort C, Costet P, *et al.* Differential involvement of peroxisome-proliferator-activated receptors alpha and delta in fibrate and fatty-acid-mediated inductions of the gene encoding liver fatty-acid-binding protein in the liver and the small intestine. Biochem J 2001; 355: 481–8.

34 Jackson SM, Demer LL. Peroxisome proliferator-activated receptor activators modulate the osteoblastic maturation of MC3T3–E1 preosteoblasts. FEBS Lett 2000; 471: 119–24.

35 Rosen V. BMP2 signaling in bone development and repair. Cytokine Growth Factor Rev 2009; 20: 475–80.

36 Komori T. Regulation of skeletal development by the Runx family of transcription factors. J Cell Biochem 2005; 95: 445–53.

37 Kanazawa I, Yamaguchi T, Yano S, Yamauchi M, Sugimoto T. Activation of AMP kinase and inhibition of Rho kinase induce the mineralization of osteoblastic MC3T3-E1 cells through endothelial NOS and BMP-2 expression. Am J Physiol Endocrinol Metab 2009; 296: E139–46.

38 Jadhav SB, Jain GK. Statins and osteoporosis: new role for old drugs. J Pharm Pharmacol 2006; 58: 3–18.

39 Naves M, Rodriguez-Garcia M, Diaz-Lopez JB, Gomez-Alonso C, Cannata-Andia JB. Progression of vascular calcifications is associated with greater bone loss and increased bone fractures. Osteoporos Int 2008; 19: 1161–6.

40 Parhami F, Garfinkel A, Demer LL. Role of lipids in osteoporosis. Arterioscler Thromb Vasc Biol 2000; 20: 2346–8.

41 Adami S, Braga V, Gatti D. Association between bone mineral density and serum lipids in men. JAMA 2001; 286: 791–2.

42 Kanis JA. Assessment of fracture risk and its application to screening for postmenopausal osteoporosis: synopsis of a WHO report. WHO Study Group. Osteoporos Int 1994; 4: 368–81.

43 Fiore CE, Pennisi P, Pulvirenti I, Francucci CM. Bisphosphonates and atherosclerosis. J Endocrinol Invest 2009; 32: 38–43.

npg

Original Article

Characterization of Quin-C1 for its anti-inflammatory property in a mouse model of bleomycin-induced lung injury

Min HE[1], Ni CHENG[2], Wei-wei GAO[1], Meng ZHANG[1], Yue-yun ZHANG[1], Richard D YE[2], Ming-wei WANG[1, *]

[1]*The National Center for Drug Screening, the State Key Laboratory of Drug Research, Shanghai Institute of Materia Medica, Chinese Academy of Sciences, Shanghai 201203, China;* [2]*Department of Pharmacology, College of Medicine, University of Illinois, Chicago, IL 60612, USA*

Aim: To study the *in vivo* effects of Quin-C1, a highly specific agonist for formyl peptide receptor 2 (FPR2/ALX), in a mouse model of bleomycin (BLM)-induced lung injury.
Methods: Male ICR mice were injected intratracheally with BLM (d 0), and intraperitoneally with Quin-C1 (0.2 mg/d) or vehicle between d 1 and d 28, during which pulmonary inflammation was monitored. A similar regimen was carried out between d 5 and d 28 to differentiate anti-inflammatory from anti-fibrotic effects. During the treatment, leukocyte numbers in bronchoalveolar lavage fluid (BALF) were counted, and FPR2/ALX transcripts, tumor necrosis factor α (TNF-α), interleukin-1β (IL-1β), the mouse keratinocyte-derived chemokine (KC), transforming growth factor β1 (TGF-β1) and C-X-C motif chemokine 10 (CXCL10) expression levels in the lung tissue were also measured. Both hydroxyproline content and histological changes were examined on d 28 to assess the severity of lung fibrosis.
Results: BLM caused a significant increase in expression levels of all the selected cytokines and chemokines, as well as a thickening of the alveolar wall. Treatment with Quin-C1 significantly reduced the neutrophil and lymphocyte counts in BALF, diminished expression of TNF-α, IL-1β, KC, and TGF-β1, and decreased collagen deposition in lung tissue. The treatment also lowered the content of lung hydroxyproline. Quin-C1 did not ameliorate lung fibrosis when the treatment was started 5 d after the BLM challenge, suggesting that the protection may be attributed to its anti-inflammatory effects. Exposure to BLM or BLM plus Quin-C1 did not change the level of FPR2/ALX transcripts (mFpr1, mFpr2, and Lxa4r) in the lung tissue.
Conclusion: The results demonstrate an anti-inflammatory role for Quin-C1 in bleomycin-induced lung injury, which may be further explored for therapeutic applications.

Keywords: Quin-C1; anti-inflammation; bleomycin; lung injury; formyl peptide receptor; cytokines

Introduction

The G protein-coupled receptor (GPCR) formyl peptide receptor 2 (FPR2/ALX), also known as formyl peptide receptor-like 1 (FPRL1) and lipoxin A4 receptor (LXA4R), was initially identified as a structural homologue of human FPR1[1]. FPR2/ALX prefers mitochondrial formyl peptides[2] and is known for its promiscuous ligand recognition. More than 20 agonists have been identified for FPR2/ALX[1, 3], including many endogenous peptides and the eicosanoid LXA4[4]. These ligands produce different effects on neutrophils, macrophages and epithelial cells that express FPR2/ALX. While most FPR2/

ALX agonists stimulate proinflammatory activities, others (including LXA4, annexin A1 and its N-terminal peptides) exhibit anti-inflammatory properties. For example, when used *in vivo* in a model of zymosan-induced peritonitis, LXA4 reduces neutrophil infiltration and pro-inflammatory cytokine expression[5]. LXA4 also binds to other receptors, including a receptor shared with cysteinyl leukotriene receptor type 1 (CysLT1)[6] and the aryl hydrocarbon receptor (AhR)[7]. It was recently reported that mice lacking *mFpr2*, which codes for mouse Fpr2, exhibited enhanced inflammatory responses in several models, such as IL-1β-induced air pouch and zymosan-induced peritonitis[8], indicating that the receptor mediates anti-inflammatory actions upon stimulation.

To identify small synthetic molecules as potential FPR2/ALX-selective drug leads, we previously screened a com-

pound library and identified Quin-C1 (4-butoxy-*N*-[2-(4-methoxy-phenyl)-4-oxo-1,4-dihydro-2*H*-quinazolin-3-yl]-benzamide) as an FPR2/ALX agonist[9]. *In vitro* pharmacological characterization showed that Quin-C1 stimulated neutrophil calcium mobilization and chemotaxis but had a very low efficacy in the induction of superoxide production[9]. In binding assays, Quin-C1 was found to occupy a site on FPR2/ALX that partially overlaps with the binding site for the potent FPR2/ALX agonist WKYMVm[10]. These pharmacological properties indicate that Quin-C1 differs from most of the FPR2/ALX ligands identified to date and may selectively regulate biological functions in target cells.

In experimental animals, particularly rodents, bleomycin (BLM)-induced pulmonary fibrosis is a well-characterized model for investigating the pathogenesis of lung fibrosis[11-13]. BLM-induced pulmonary fibrosis results from an inflammatory response to lung injury, characterized by increased production of pro-inflammatory cytokines, including tumor necrosis factor α (TNF-α) and interleukin-1β (IL-1β), and chemokines such as macrophage inflammatory protein 1α (MIP-1α), the mouse keratinocyte-derived chemokine (KC) and monocyte chemotactic protein 1 (MCP-1)[14]. Pathological changes associated with the progression to fibrosis include increased production of TGF-β1, reactive oxygen species and C-X-C motif chemokine 10 (CXCL10) as well as decreased generation of adenosine triphosphate (ATP) and overproduction of mature collagen fibrils[15]. These changes eventually lead to thickening of the alveolar wall and reduction in blood oxygen exchange capacity.

In the present study, we investigated a potential anti-inflammatory function for Quin-C1 using a BLM-induced lung fibrosis model. Our data showed that mouse lung tissue expresses Quin-C1 receptors, and responds to Quin-C1 with reduced inflammatory cytokine expression and leukocyte infiltration leading to protection from BLM-induced lung injury. These results demonstrated an anti-inflammatory property for Quin-C1 *in vivo*.

Materials and methods
Animals and reagents
Male ICR mice (9–10 weeks old, 25–30 g, Shanghai SLAC Laboratory Animals Co, Shanghai, China), widely used for fibrosis studies, were housed at 22.7±0.8 °C with a 12/12-h light/dark cycle. They were fed and watered *ad libitum*. All animal experiments were conducted in accordance with regulations and protocols approved by the Animal Care and Use Committee, Shanghai Institute of Materia Medica, Chinese Academy of Sciences. Quin-C1 was synthesized as described previously[9].

Calcium mobilization assay
Mouse bone marrow polymorphonuclear (PMN) leukocytes (about 50 000 cells/sample with about 75% neutrophils) and a rat basophil leukemia cell line (RBL-2H3) expressing mouse Fpr1 (mFpr1) or mouse Fpr2 (mFpr2) cDNA (about 40 000

cells/sample) were placed in 96-well microtiter plates. The cells were incubated with FLIPR Calcium 5 reagent (Molecular Devices, Sunnyvale, CA, USA) at 37 °C for 1 h and were excited at 485 nm. Ca^{2+} fluorescence was detected at an emission wavelength of 525 nm, using a FlexStation II (Molecular Devices) with an auto emission cutoff set at 515 nm.

BLM-induced lung injury and Quin-C1 treatment
Lung injury was induced with BLM, as previously described, with minor modifications in dosage[16]. Briefly, bleomycin hydrochloride (Nippon Kayaku, Tokyo, Japan) was dissolved in 0.1 mL sterile saline and intratracheally injected into mouse lungs at a dose of 3 mg/kg body weight. Control animals received the same volume of saline. The day of BLM/saline administration was regarded as d 0. For intraperitoneal (ip) Quin-C1 treatment (daily from d 1 through d 28), mice were randomly assigned to one of three treatment groups with matching body weight: saline, BLM and BLM plus 0.2 mg Quin-C1 (1% DMSO, 19% PEG400 in saline, 0.5 mL, daily). A vehicle of equal volume was administered ip for comparison. Quin-C1 was also tested at 0.04 mg and 1.0 mg for dose-response information. In an additional group, Quin-C1 was given on d 5 at the fixed dose of 0.2 mg, and mice were sacrificed on d 9 for bronchoalveolar lavage fluid (BALF) analysis to measure leukocyte numbers. Lung tissue was also examined on d 9 for cytokine expression and on d 28 for signs of lung fibrosis, as detailed below.

Detection of the transcripts of formyl peptide receptors in mouse lung
Animals were sacrificed on d 0, 5, 7, 9, and 28 after BLM or saline administration and lungs were perfused with normal saline to remove blood cells. The lung tissue was then homogenized using TRIzol Reagent (Invitrogen, Carlsbad, CA, USA) for the preparation of total RNA. The total RNA (2 μg) was reverse transcribed, and 1 μL (1/20 of the reverse transcriptase product) of the resulting cDNA was subjected to polymerase chain reaction (PCR) in a 25-μL final reaction volume for analyzing levels of mouse *Fpr1*, *Lxa4r* and *Fpr2* mRNA transcripts. β-actin was used as an internal control. The amplification conditions were as follows: initial step at 94 °C for 5 min, followed by 30 cycles at 95 °C for 30 s, 55 °C for 1 min and 72 °C for 1 min. The primers and products for RT-PCR are presented in Table 1.

BALF analysis
On d 0, 5, 7, and 9 following BLM or saline injection, the animals were sacrificed, and the lungs were lavaged twice with 0.8 mL PBS containing 5 mmol/L EDTA by cannulating the trachea. The BALF was centrifuged at 1500 revolutions per minute for 10 min at 4 °C. To facilitate cell counting, the remaining red blood cells were eliminated with lysis buffer (Beyotime Institute of Biotechnology, Haimen, China). Total and differential cell counts (neutrophils, lymphocytes and macrophages) in the BALF were determined with the Diff-Quick Stain Kit (IMEB Inc, San Marcos, CA, USA).

Table 1. RT-PCR primers and products.

Mouse gene	Forward/ reverse	Primer sequence (5′ to 3′)	Product (bp)
Fpr1	Forward	GCACTGGACCGCTGTATTT	519
	Reverse	CAAGGGGCTTGTGATTTTC	
Fpr2	Forward	GCCTGGCTAGGAAGGTGGTT	352
	Reverse	CAAAAGGGCCACAAGCTGAA	
Lxa4r	Forward	CCTGGGGCAACTCTGTTGAG	381
	Reverse	AGTCCTGGCCCATGAAAACA	
β-actin	Forward	GGAAATTGTGCGTGACATCAAAG	213
	Reverse	ATGCCACAGGATTCCATACCC	

Abbreviations: RT-PCR, reverse transcription-polymerase chain reaction; Fpr1, formyl peptide receptor 1; Lxa4r, lipoxin A4 receptor; Fpr2, formyl peptide receptor 2.

Measurement of cytokines in lung tissue

Lung lobes were dissected from mice on d 0, 5, 7, and 9 and weighed. Samples were then homogenized on ice according to their respective weights (10% homogenate in saline). The homogenate supernatants were collected after centrifugation and assayed for levels of TNF-α, IL-1β, KC, TGF-β1, and CXCL10 using specific ELISA kits (R&D Systems Inc, Minneapolis, MN, USA). TGF-β1 (latent and active) was measured after pre-activation with acidification to pH 2–3 for 60 min, and corrected to pH 6.5–7.5 prior to ELISA assay.

Measurement of hydroxyproline contents

On d 28, all remaining animals were sacrificed, and the lung lobes were dissected and weighed. To measure the content of hydroxyproline in the lung, the tissue samples were homogenized and then hydrolyzed in 2 mol/L NaOH at 120 °C for 20 min. After the addition of chloramine T (0.056 mol/L; *eg*, 1.27 g of chloramine T was dissolved in 20 mL 50% n-propanol and brought to 100 mL with acetate-citrate buffer) and Ehrlich's reagent (1 mol/L; *eg*, 15 g of p-dimethylaminobenzaldehyde was dissolved in n-propanol/perchloric acid (2:1 *v/v*) and brought to 100 mL), the absorbance of the samples was read at 557 nm on a microplate reader (Molecular Devices)[17].

Histopathology

The right lung lobes removed from each mouse on d 28 were fixed in a 10% formalin solution and embedded in paraffin. Lung tissue sections (5-μm thickness) were cut and stained with Masson's trichrome (Sigma-Aldrich, St Louis, MO, USA) for histological examination under a light microscope (Olympus, Tokyo, Japan). Images were taken at 400×magnification. Alveolar wall thickness was determined by measuring the length of the lines drawn perpendicular to the narrowest segment of primary and secondary alveolar septa (60–80 lines per image at 100×magnification). The total number of septa counted for each group (3 mice) was 200–250, and the alveolar wall thickness was calculated using Image-Pro Plus 6.0 software (Media Cybernetics, Silver Spring, MD, USA)[18].

Statistical analysis

Statistical analysis was performed using GraphPad Prism software (GraphPad, San Diego, CA, USA) by one-way or two-way analysis of variance (ANOVA), followed by Bonferroni *post hoc* analysis. Data are presented as mean±SEM. The criterion for significance was a probability of less than 0.05.

Results

Agonistic effect of Quin-C1 in mouse cells

Quin-C1 was initially identified as an agonist for human FPR2/ALX[9]; however, its role in mice is yet to be established. We challenged mouse bone marrow-derived neutrophils with Quin-C1 in a calcium mobilization assay and compared the result with a WKYMVm-induced calcium response in the same cell population. As shown in Figure 1A, WKYMVm invoked dose-dependent calcium mobilization up to 100 nmol/L, and further increases in its concentration (up to 1 μmol/L) did not intensify the response. Quin-C1 at concentrations from 1 nmol/L to 10 μmol/L induced dose-dependent calcium mobilization in mouse neutrophils. When used at 10 μmol/L, Quin-C1 induced calcium mobilization levels similar to those produced by 10 nmol/L of WKYMVm (Figure 1B). These results are consistent with our previous finding, which demonstrated that Quin-C1 was approximately 1000-fold less potent as a ligand for FPR2/ALX than WKYMVm[9].

To determine whether mFpr1 or mFpr2 is responsible for mediating the pharmacological functions of Quin-C1, we measured Quin-C1-induced calcium response in RBL cells expressing the receptors. Both mFpr1 and mFpr2 were able to mediate Quin-C1-induced calcium mobilization (Figures 1C and 1D). A better EC_{50} value (35 nmol/L) was obtained with cells expressing mFpr1 than cells expressing mFpr2 (166 nmol/L).

Effect of Quin-C1 on formyl peptide receptor expression in the lung tissue following BLM challenge

In mice, the formyl peptide receptor family contains at least eight genes, three of which are expressed in leukocytes[19]. In neutrophils, mFpr1 and mFpr2 are most abundant at the transcript level, whereas the mouse Lxa4r transcript (encoded by *mFpr-rs1*) is found at a lower level[20]. The same expression pattern was seen in lung tissue devoid of circulating neutrophils. Our data showed that the expression of these three formyl peptide receptors did not change in response to BLM (or BLM plus Quin-C1 exposure) at the mRNA level (Figure 1E).

Effect of Quin-C1 on BLM-induced leukocyte accumulation in the BALF

To determine whether Quin-C1 affects the progression of BLM-induced chronic lung inflammation and fibrosis, mice were given intratracheal BLM (3 mg/kg) alone or together with Quin-C1 (0.2 mg, ip). As a negative control, normal saline was injected intratracheally in a separate group of mice. The outbred ICR strain used in this study is prone to fibrosis, such as *Schistosoma mansoni*-induced hepatic fibrosis[21] and cyclophosphamide-induced lung fibrosis[22]. On the indicated
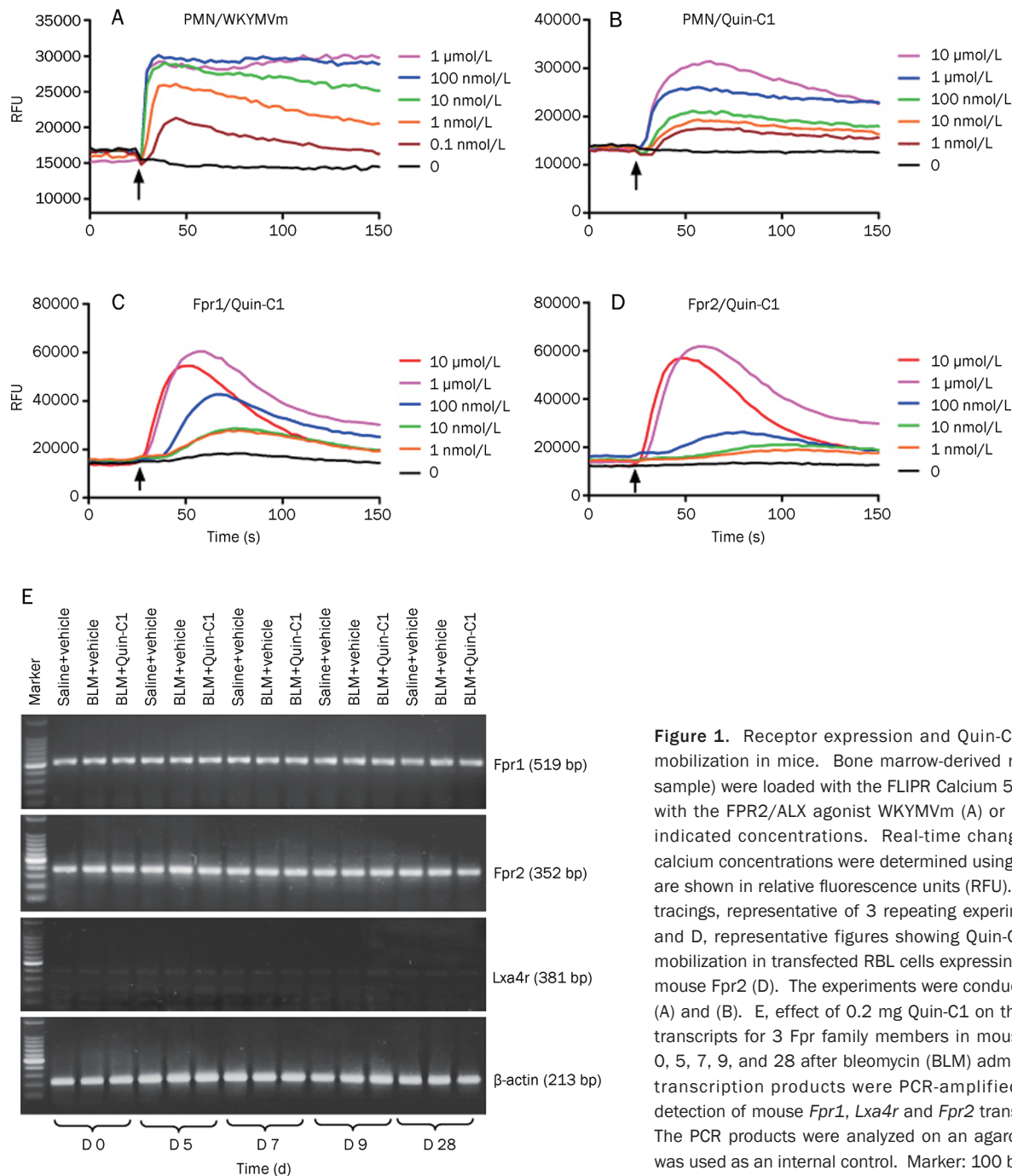
Figure 1. Receptor expression and Quin-C1-induced calcium mobilization in mice. Bone marrow-derived neutrophils (5×10^5/sample) were loaded with the FLIPR Calcium 5 dye and stimulated with the FPR2/ALX agonist WKYMVm (A) or with Quin-C1 (B) at indicated concentrations. Real-time changes in intracellular calcium concentrations were determined using a FlexStation II and are shown in relative fluorescence units (RFU). One set of calcium tracings, representative of 3 repeating experiments, is shown. C and D, representative figures showing Quin-C1 induced calcium mobilization in transfected RBL cells expressing mouse Fpr1 (C) or mouse Fpr2 (D). The experiments were conducted as described in (A) and (B). E, effect of 0.2 mg Quin-C1 on the expression of the transcripts for 3 Fpr family members in mouse lung tissue on d 0, 5, 7, 9, and 28 after bleomycin (BLM) administration. Reverse transcription products were PCR-amplified for 30 cycles for detection of mouse *Fpr1*, *Lxa4r* and *Fpr2* transcripts, respectively. The PCR products were analyzed on an agarose gel, and β-actin was used as an internal control. Marker: 100 bp DNA ladder.

days after BLM or saline injection, the mice were sacrificed, and their lungs were lavaged as described above for total and differential cell counts. Mice receiving BLM had markedly higher total cell counts on d 7 and 9 ($P<0.01$); however, the increase was abolished in mice receiving both BLM and Quin-C1 ($P<0.05$, Figure 2A). Differential leukocyte counts showed that the numbers of neutrophils and lymphocytes were increased in BALF from BLM-treated mice on d 5 and 9 after BLM induction ($P<0.01$, Figures 2C and 2D). Significantly fewer cells were found in BALF from mice receiving Quin-C1 for 7 or 9 d ($P<0.01$), indicating that Quin-C1 suppressed the infiltration of neutrophils and lymphocytes. The number of macrophages was also increased on d 7 and 9 in the BLM-treated group ($P<0.01$, Figure 2B); however, Quin-C1 did not reverse the increase in macrophage number ($P>0.05$).

Effect of Quin-C1 on the expression of cytokines and chemokines in the lung tissue of BLM-challenged mice

The expression levels of selected cytokines and chemokines were measured in lung tissue homogenates from mice sacrificed on d 5, 7, and 9 after BLM injection. As shown in Figure 3, the expression levels of TNF-α, IL-1β, and KC were sig-
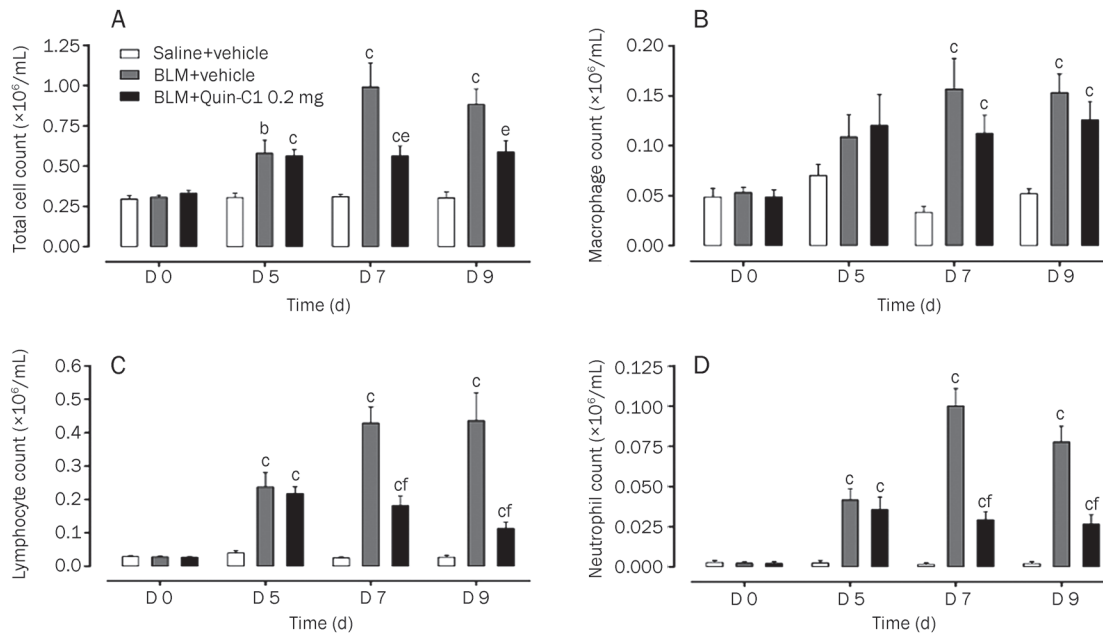
Figure 2. BLM induced changes in total and differential cell counts in the BALF and effects of Quin-C1. Mice were given intratracheal bleomycin (BLM) or saline injections (d 0), with or without daily Quin-C1 administration (0.2 mg or vehicle ip) starting on d 1. On d 0, 5, 7, and 9, mice from each group were sacrificed and the BALF was collected. Total cell count (A) was determined using a cell counter (Beckman Coulter, Fullerton CA, USA) and cell subset numbers were determined with Diff-quick staining (200 cells per animal were examined). Cell numbers for macrophages (B), lymphocytes (C) and neutrophils (D) in the BALF were calculated based on their respective percentage of the total cell count (A). Values are expressed as mean±SEM ($n \geq 6$ per group). [b]$P<0.05$, [c]$P<0.01$ compared to saline control; [e]$P<0.05$, [f]$P<0.01$ compared to BLM control.
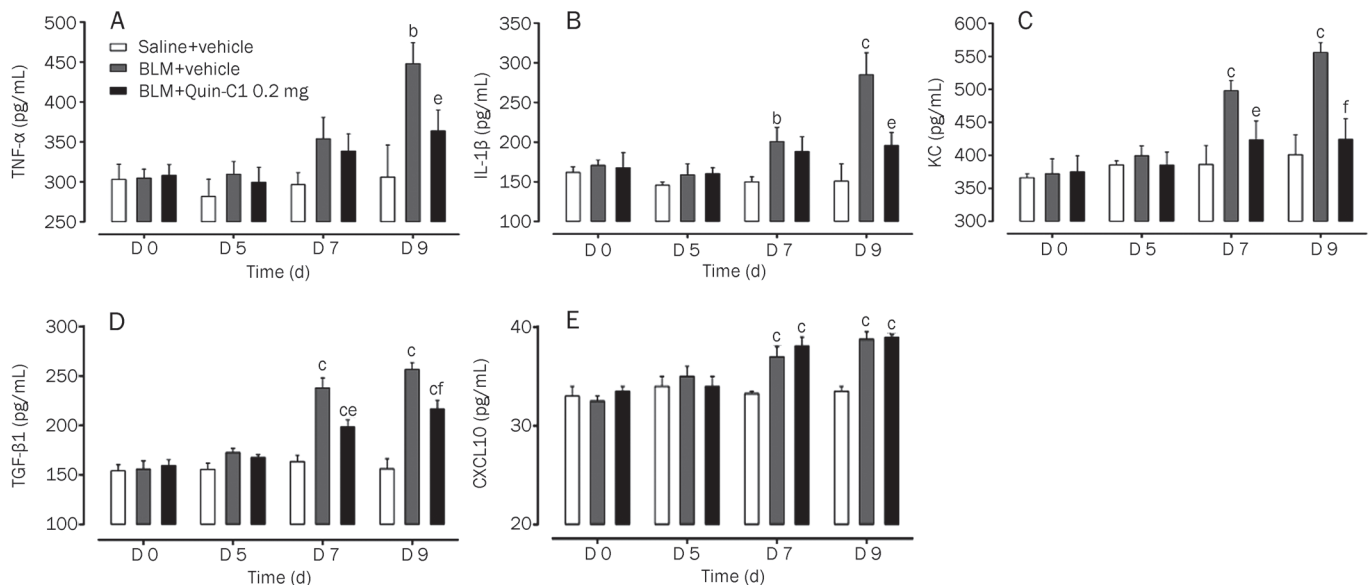
Figure 3. BLM induced expression of cytokines and chemokines in lung tissue and effects of Quin-C1. Bleomycin (BLM)-challenged mice were treated with Quin-C1 (0.2 mg) or vehicle as described above. On d 0, 5, 7, and 9, the mice were sacrificed, and lung tissue homogenates were examined by ELISA for levels of TNF-α (A), IL-1β (B), KC (C), TGF-β1 (D), and CXCL10 (E). Values are expressed as mean±SEM ($n \geq 5$ per group). [b]$P<0.05$, [c]$P<0.01$ compared to saline control; [e]$P<0.05$, [f]$P<0.01$ compared to BLM control.

nificantly elevated on d 9 after BLM administration ($P<0.05$, $P<0.01$ and $P<0.01$, respectively). In addition, considerably higher levels of KC and IL-1β were detected on d 7 ($P<0.01$ and $P<0.05$, respectively). Administration of Quin-C1 reduced the expression level of these cytokines in lung tissue on d 9 ($P<0.01$, $P<0.05$, and $P<0.05$ for KC, TNF-α, and IL-1β,
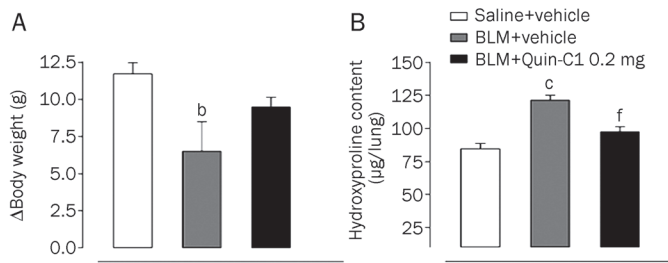
Figure 4. Effects of Quin-C1 on BLM induced body weight change and hydroxyproline content. The body weights of mice treated with saline, BLM and BLM plus Quin-C1 (0.2 mg) were monitored on d 0 and 28. The lung samples were homogenized and the contents of hydroxyproline measured on d 28 as described in the methods. Values are expressed as mean±SEM ($n \geq 10$ per group). [b]$P<0.05$, [c]$P<0.01$ compared to saline control; [f]$P<0.01$ compared to BLM control.

respectively) and for KC only on d 7 ($P<0.05$, Figure 3). These results suggest that Quin-C1 may partially offset the cytokine-mediated effects of BLM.

TGF-β1 plays a critical role in stimulating collagen synthesis by lung fibroblasts and contributes to the development of idiopathic pulmonary fibrosis[23, 24]. The level of TGF-β1 in lung tissue homogenates was determined by ELISA. Significantly higher levels of TGF-β1 were found in mice receiving BLM on d 7 and 9 ($P<0.01$, Figure 3D). In mice receiving Quin-C1, the BLM-induced TGF-β1 production was partially inhibited ($P<0.05$ on d 7 and $P<0.01$ on d 9, compared to the levels of TGF-β1 in mice treated with BLM alone, Figure 3D). The concentration of CXCL10 in lung tissue homogenates was markedly higher on d 7 and 9 in mice treated with BLM than those that received saline ($P<0.01$, Figure 3E). Quin-C1 administration did not alter this finding at any time point assessed.

Effect of Quin-C1 on BLM-induced weight loss and collagen deposition

BLM induction causes long-term consequences that include collagen deposition into the lung tissue resulting in thickening of the alveolar wall, which directly contributes to the

reduction in blood oxygen exchange[11]. BLM induction also leads to the eventual development of fibrosis, and these mice display weight loss. In the present study, mouse weight was monitored on d 0 and 28. As shown in Figure 4A, a significant ($P<0.05$) reduction in body weight was observed in mice receiving BLM compared to those receiving saline. In addition, mice receiving BLM injection showed a 47% increase in the content of hydroxyproline, which reflects collagen deposition in the lung tissue (Figure 4B). These deleterious effects were partially inhibited in mice that received both BLM and Quin-C1 ($P<0.01$ for the lung hydroxyproline content, Figure 4B) although the weight loss was not completely prevented ($P>0.05$, Figure 4A).

Histological examination of the lung tissue was conducted to evaluate the severity of BLM-induced lung fibrosis and the morphological alterations following Quin-C1 intervention. On d 28, the lung tissue from BLM-treated mice showed marked interstitial collagen deposition with a significant thickening of the alveolar septa (Figure 5B compared to 5A). In comparison, the mice that received Quin-C1 displayed a 75% reduction in BLM-induced thickening of alveolar walls (Figures 5C and 5D). Collectively, these results indicate that Quin-C1 is capable of mitigating BLM-induced pulmonary fibrotic lesions.

Dose-response characteristics of Quin-C1

We next determined what Quin-C1 dosage was most efficacious in preventing BLM-induced lung injury. Our therapeutic protocol described above was repeated with Quin-C1 at doses of 0.04 mg, 0.2 mg, and 1.0 mg. As shown in Figure 6, increasing the Quin-C1 dose from 0.04 mg to 0.2 mg enhanced protective effects by reducing leukocyte infiltration (primarily neutrophils, Figure 6A) and pro-inflammatory cytokine production in the BALF (Figure 6B). Interestingly, no protective effect was observed when the dose of Quin-C1 was further increased to 1.0 mg. However, no obvious detrimental effect on mouse body weight was observed with this dose (1.0 mg) compared to the 0.04-mg and 0.2-mg dose groups (Figure 6C).

Reduced lung fibrosis is secondary to the anti-inflammatory effects of Quin-C1

Because BLM-induced lung fibrosis is preceded by an inflam-
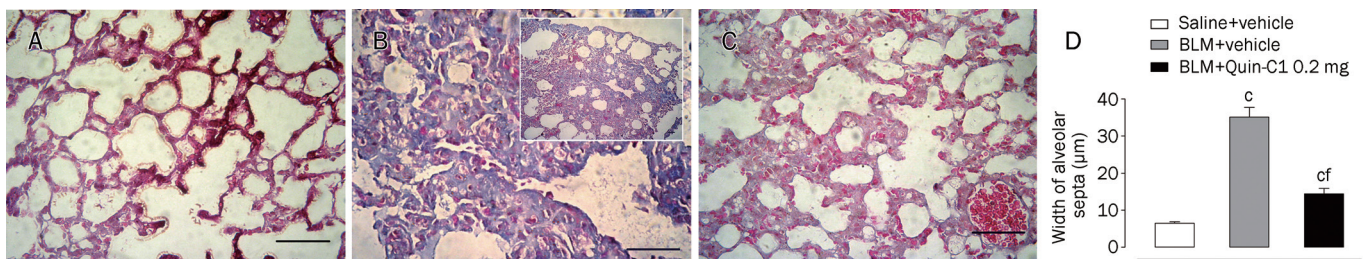
Figure 5. Histological analysis of BLM treated mouse lung tissue and effects of Quin-C1. Five-micrometer sections of lung tissue from mice receiving saline (A), BLM (B) and BLM plus Quin-C1 (0.2 mg) (C) were stained with Masson's trichrome for histological examination under a light microscope. (D) Alveolar wall thickness was determined using Image-Pro Plus 6.0 software and expressed as mean±SEM ($n=3$ mice from each experimental group). Images were taken at 400× except in insert (B), which was taken at 100× to show collagen deposition in a larger area of lung tissue. Bar=50 µm; [c]$P<0.01$ compared to saline control; [f]$P<0.01$ compared to BLM control.
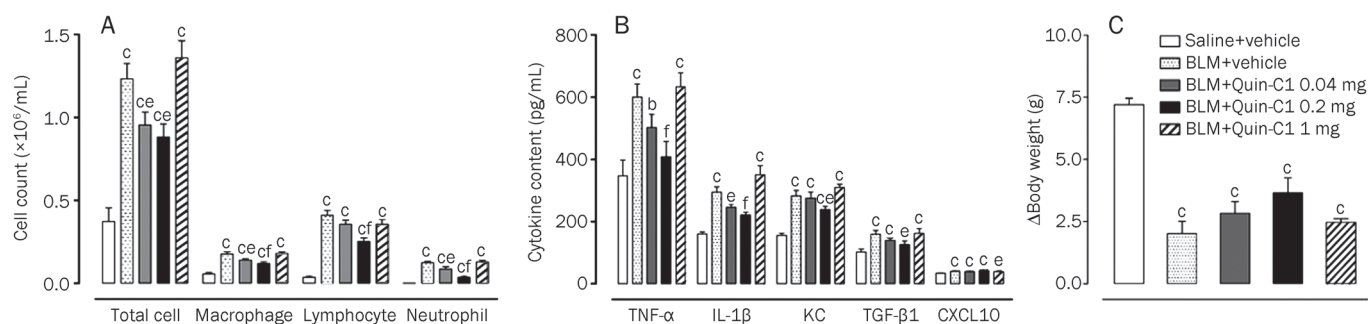
Figure 6. Effects of different doses of Quin-C1 on inflammatory cell counts in the BALF, expression of cytokines and chemokines in lung tissue and body weight change in BLM treated mice. Mice were challenged with BLM or saline on d 0, with or without daily Quin-C1 administration (0.04, 0.2, or 1 mg ip) starting on d 1. On d 9, mice were sacrificed to examine the total and differential cell counts in the BALF (A), TNF-α, IL-1β, KC, TGF-β1, and CXCL10 levels in lung homogenates (B) and body weight changes (C). Values are expressed as mean±SEM ($n \geq 8$ per group). [b]$P<0.05$, [c]$P<0.01$ compared to saline control; [e]$P<0.05$, [f]$P<0.01$ compared to BLM control.

matory response in the lung, we sought to determine whether the protective effect of Quin-C1 results from its anti-inflammatory property or from an additional anti-fibrotic function. For this experiment, Quin-C1 (0.2 mg) was given from d 5 through d 9 or 28 after intratracheal administration of BLM or saline. Groups of mice were sacrificed on d 9 for leukocyte counts and cytokine measurements in the BALF and on d 28 to examine alveolar septa thickness and hydroxyproline content. Our results (supplementary Figure S1) show that the administration of 0.2 mg Quin-C1 from d 5 through d 9 or 28 produced neither a protective effect against BLM-induced lung inflammation and fibrosis nor any detrimental impact on uninjured lungs from mice treated with saline.

Discussion

Results from the present study demonstrate an anti-inflammatory property for Quin-C1. Here, we describe this function *in vivo* in a mouse model of lung fibrosis, which is induced by an inflammatory response to BLM injury and is characterized by increased leukocyte infiltration, proinflammatory cytokine expression and deposition of collagen in alveolar septa. Published BLM-induced fibrosis studies showed a significant increase in TNF-α, IL-1β and TGF-β1 lung cytokine levels[14]. Inhibition of pro-inflammatory cytokine expression, such as by blocking nuclear factor κB (NF-κB) activation, reduces BLM-induced fibrosis[25, 26]. Suppression of other proinflammatory transcriptional pathways, including the p38 mitogen-activated protein kinase (p38 MAPK) pathway, also decreases lung fibrosis in response to BLM[27]. Therefore, the anti-inflammatory effects of Quin-C1 are likely responsible for the reduced pathological changes in lungs exposed to BLM. To determine further whether Quin-C1 has anti-fibrotic properties, we administered it on d 5 through d 28 following BLM challenge. Our data show that delayed administration of Quin-C1 abrogated its protective effect, indicating that Quin-C1 is incapable of reversing the fibrotic phenotype caused by the initial inflammatory response to BLM. These findings suggest that the protective effect of Quin-C1 results from its anti-inflammatory properties and that the observed anti-fibrotic

effect is secondary.

In addition to an increase in pro-inflammatory cytokine expression, BLM-induced lung fibrosis is preceded by increased local synthesis of chemokines, including MCP-1, MIP-2 and KC[28]. In this study, increases in KC expression are consistent with increased neutrophil and lymphocyte infiltration in the lung tissue. Local accumulation of leukocytes, particularly neutrophils, is a contributing factor to lung fibrosis, which develops in mice affected by BLM. Indeed, previous investigations indicate that decreased pulmonary fibrosis is associated with reduced accumulation of leukocytes, including neutrophils and lymphocytes[29]. However, although neutrophil infiltration and neutrophil-endothelial cell interactions are considered important to the development of lung fibrosis (as shown in studies using mice lacking both L-selectin and intercellular adhesion molecular-1 (ICAM-1)[29]), the role of T lymphocytes in BLM-induced lung fibrosis remains controversial. There is evidence in the literature to suggest that BLM-induced lung fibrosis does not require T cells[30]. However, another published study demonstrated that CD28 deficiency abolished BLM-induced lung fibrosis, whereas adoptive transfer of wild type T cells restored this capability[31]. Thus, it is possible that one of the anti-inflammatory functions of Quin-C1 mediates the suppression of leukocyte infiltration, thereby reducing local inflammation and neutrophil-mediated tissue injury.

The attenuation of BLM-induced lung fibrosis has been observed in several studies. For example, the suppression of interferon-γ (IFN-γ) signaling abrogates BLM-induced lung fibrosis[32] and neutralizing interleukin-13 (IL-13) produces similar effects, implying that IL-13 plays an important role in the progression of chronic lung inflammation[33]. We have shown that BLM stimulates TGF-β1 expression in mice, and Quin-C1 partially reverses this phenomenon. One established function of TGF-β1 is to stimulate collagen synthesis by fibroblasts, which directly contributes to tissue fibrosis[23, 24]. Fibroblasts also respond to TGF-β1 by stimulating c-Abl kinase activity. The inhibition of c-Abl by the drug imatinib prevents TGF-β1-induced extracellular membrane (ECM) gene

npg
608
www.nature.com/aps
He M *et al*

expression, morphologic transformation, and cell proliferation, and reduces BLM-induced lung fibrosis[34]. Quin-C1 may target these pathways to induce its anti-inflammatory effects; however, the exact target(s) and underlying mechanisms of action remain to be elucidated. The chemokine CXCL10, which is highly expressed in BLM-induced pulmonary fibrosis, has been shown to attenuate the development of fibrosis via inhibition of fibroblast recruitment or angiogenesis[35]. Up-regulating CXCL10 is associated with a reduction in fibroblast accumulation in the lung[36]. Our findings show a significant increase in CXCL10 levels on d 7 and 9 after BLM challenge. The observation that Quin-C1 has no direct effect on CXCL10 expression implies that it was unable to modulate the CXCL10 pathway in response to BLM exposure.

Quin-C1 is identified as an FPR2/ALX-selective agonist[9]. FPR2/ALX binds to LXA4, and this receptor contributes to the potent anti-inflammatory properties of LXA4 and annexin A1. It is believed that these functions are mediated through the suppression of neutrophil accumulation, inhibition of NF-κB activation, and enhancement of pro-resolving functions such as macrophage-mediated phagocytosis of apoptotic neutrophils[5, 37]. Our results show an abundant expression of both mFpr1 and mFpr2 transcripts in mouse lung tissue, and the latter is reported to be a receptor for LXA4[38]. Moreover, Quin-C1 induces calcium mobilization in mouse neutrophils, which express mFpr1 and mFpr2 transcripts[20]. Interestingly, our data indicate that both mFpr1 and mFpr2 are able to mediate Quin-C1-induced calcium mobilization and, based on the EC_{50} value, mFpr1 is more potent. Because mFpr1 shares high sequence homology and structural features with human FPR2/ALX, it is not surprising that this receptor also interacts with Quin-C1. Therefore, either one or both receptors may be responsible for the actions of Quin-C1 observed in this study. Recently, Dufton and colleagues reported that genetic deletion of mFpr2 gene led to an increase in inflammation in several mouse models, providing genetic evidence that mFpr2 is the equivalent of human FPR2/ALX, which mediates the anti-inflammatory functions of selected ligands[8]. However, Chen and colleagues[39] demonstrated a reduced allergic inflammation in the absence of this receptor using mFpr2 gene knockout mice. It is also notable that mFpr1 was not previously known as a functional homologue of FPR2/ALX in terms of its anti-inflammatory properties. Therefore, follow-up work is necessary to better characterize these two receptors using genetically altered animals.

It is intriguing that a G protein-coupled chemoattractant receptor, such as FPR2/ALX, mediates both neutrophil-activating and anti-inflammatory effects *in vivo*. Currently, there is not a clearly identified mechanism to explain these observations, but emerging evidence suggests several possibilities. First, all identified FPR2/ALX ligands that possess anti-inflammatory properties are agonists that elicit selected functions through the receptor. For example, LXA4 stimulates guanosine triphosphatase (GTPase) through FPR2/ALX[4]. In addition, annexin A1 and its N-terminal derived peptides activate the mitogen-activated protein kinase/extracellular

signal-regulated kinase (MAPK/ERK) pathways[8, 40]. However, these ligands are weak agonists compared to WKYMVm and serum amyloid A for stimulating other neutrophil actions. It is likely that the receptor is only partially activated when exposed to the ligands with anti-inflammatory properties. This introduces the second possibility, which relates to a dose effect. In our experiments, we observed protective effects of Quin-C1 in a narrow range of doses (between 0.04 to 0.2 mg). Further increasing the Quin-C1 dose to 1 mg completely abrogated the anti-inflammatory effect. Although the underlying mechanism remains unclear, it is of note that LXA4 produces anti-inflammatory effects at doses in the nanomolar range[5], whereas other properties of the ligand appear at higher concentrations[41]. Thus, it is necessary to further determine the dose-response characteristics of these ligands at the level of receptors and receptor-mediated signaling pathways. Finally, the FPR2/ALX-mediated agonistic activities of selected ligands appear to be indispensable for inducing anti-inflammatory proteins such as suppressor of cytokine signaling 2 (SOCS-2) as well as enhancing the pro-resolving functions of macrophages[42, 43]. Consistent with these findings, FPR2/ALX has been shown to mediate different functions of LXA4 in neutrophils and macrophages[44]. For example, LXA4 inhibits neutrophil infiltration and stimulates macrophage-mediated phagocytosis of apoptotic neutrophils. Complementary studies have also shown that small molecules serving as FPR2/ALX agonists possess anti-inflammatory functions *in vivo*[45]. The protective effect of Quin-C1 may also arise from its ability to inhibit TGF-β1 expression in BLM-treated lungs. In line with these observations, it is likely that the recently reported anti-fibrotic property of LXA4 may be due to its anti-inflammatory functions[46]. Although Quin-C1 has been pharmacologically characterized in greatest detail for its agonistic function at human FPR2/ALX[9], the identification of two mouse FPR family members as potential targets for this ligand suggests that the anti-inflammatory properties of these receptors are shared between species and can be useful for more in-depth analysis in mice. Collectively, the available experimental data suggest the feasibility for using FPR2/ALX agonists to treat certain inflammatory disorders. Additional investigations are required to determine the signaling mechanisms that underlie the observed anti-inflammatory functions of these agents.

Author contribution

Richard D YE and Ming-Wei WANG designed the research; Min HE, Ni CHENG, Wei-wei GAO, Meng ZHANG, and Yue-yun ZHANG performed the experiments; Min HE, Ni

CHENG, Richard D YE, and Ming-Wei WANG analyzed the data; and Richard D YE and Ming-Wei WANG wrote the paper.

Supplementary information

Supplementary figure is available at Acta Pharmacologica Sinica website of NPG.

References

1 Migeotte I, Communi D, Parmentier M. Formyl peptide receptors: a promiscuous subfamily of G protein-coupled receptors controlling immune responses. Cytokine Growth Factor Rev 2006; 17: 501–19.

2 Rabiet MJ, Huet E, Boulay F. Human mitochondria-derived N-formylated peptides are novel agonists equally active on FPR and FPRL1, while Listeria monocytogenes-derived peptides preferentially activate FPR. Eur J Immunol 2005; 35: 2486–95.

3 Ye RD, Boulay F, Wang JM, Dahlgren C, Gerard C, Parmentier M, et al. International Union of Basic and Clinical Pharmacology. LXXIII. Nomenclature for the formyl peptide receptor (FPR) family. Pharmacol Rev 2009; 61: 119–61.

4 Fiore S, Maddox JF, Perez HD, Serhan CN. Identification of a human cDNA encoding a functional high affinity lipoxin A4 receptor. J Exp Med 1994; 180: 253–60.

5 Serhan CN. Lipoxins and aspirin-triggered 15-epi-lipoxins are the first lipid mediators of endogenous anti-inflammation and resolution. Prostaglandins Leukot Essent Fatty Acids 2005; 73: 141–62.

6 Chiang N, Serhan CN, Dahlen SE, Drazen JM, Hay DW, Rovati GE, et al. The lipoxin receptor ALX: potent ligand-specific and stereoselective actions in vivo. Pharmacol Rev 2006; 58: 463–87.

7 Schaldach CM, Riby J, Bjeldanes LF. Lipoxin A4: a new class of ligand for the Ah receptor. Biochemistry 1999; 38: 7594–600.

8 Dufton N, Hannon R, Brancaleone V, Dalli J, Patel HB, Gray M, et al. Anti-inflammatory role of the murine formyl-peptide receptor 2: ligand-specific effects on leukocyte responses and experimental inflammation. J Immunol 2010; 184: 2611–9.

9 Nanamori M, Cheng X, Mei J, Sang H, Xuan Y, Zhou C, et al. A novel nonpeptide ligand for formyl peptide receptor-like 1. Mol Pharmacol 2004; 66: 1213–22.

10 Le Y, Gong W, Li B, Dunlop NM, Shen W, Su SB, et al. Utilization of two seven-transmembrane, G protein-coupled receptors, formyl peptide receptor-like 1 and formyl peptide receptor, by the synthetic hexapeptide WKYMVm for human phagocyte activation. J Immunol 1999; 163: 6777–84.

11 Adamson IY, Bowden DH. The pathogenesis of bloemycin-induced pulmonary fibrosis in mice. Am J Pathol 1974; 77: 185–97.

12 Chua F, Gauldie J, Laurent GJ. Pulmonary fibrosis: searching for model answers. Am J Respir Cell Mol Biol 2005; 33: 9–13.

13 Moore BB, Hogaboam CM. Murine models of pulmonary fibrosis. Am J Physiol Lung Cell Mol Physiol 2008; 294: L152–60.

14 Phan SH, Kunkel SL. Lung cytokine production in bleomycin-induced pulmonary fibrosis. Exp Lung Res 1992; 18: 29–43.

15 Keane MP. The role of chemokines and cytokines in lung fibrosis. Eur Respir Rev 2008; 17: 151–6.

16 Waseda Y, Yasui M, Nishizawa Y, Inuzuka K, Takato H, Ichikawa Y, et al. Angiotensin II type 2 receptor antagonist reduces bleomycin-induced pulmonary fibrosis in mice. Respir Res 2008; 9: 43.

17 Reddy GK, Enwemeka CS. A simplified method for the analysis of hydroxyproline in biological tissues. Clin Biochem 1996; 29: 225–9.

18 Pua ZJ, Stonestreet BS, Cullen A, Shahsafaei A, Sadowska GB, Sunday ME. Histochemical analyses of altered fetal lung development following single vs multiple courses of antenatal steroids. J Histochem Cytochem 2005; 53: 1469–79.

19 Wang ZG, Ye RD. Characterization of two new members of the formyl peptide receptor gene family from 129S6 mice. Gene 2002; 299: 57–63.

20 Southgate EL, He RL, Gao JL, Murphy PM, Nanamori M, Ye RD. Identification of formyl peptides from Listeria monocytogenes and Staphylococcus aureus as potent chemoattractants for mouse neutrophils. J Immunol 2008; 181: 1429–37.

21 Cheever AW, Dunn MA, Dean DA, Duvall RH. Differences in hepatic fibrosis in ICR, C3H, and C57BL/6 mice infected with Schistosoma mansoni. Am J Trop Med Hyg 1983; 32: 1364–9.

22 Kanekal S, Fraiser L, Kehrer JP. Pharmacokinetics, metabolic activation, and lung toxicity of cyclophosphamide in C57/B16 and ICR mice. Toxicol Appl Pharmacol 1992; 114: 1–8.

23 Branton MH, Kopp JB. TGF-beta and fibrosis. Microbes Infect 1999; 1: 1349–65.

24 Sheppard D. Transforming growth factor beta: a central modulator of pulmonary and airway inflammation and fibrosis. Proc Am Thorac Soc 2006; 3: 413–7.

25 Gurujeyalakshmi G, Wang Y, Giri SN. Taurine and niacin block lung injury and fibrosis by down-regulating bleomycin-induced activation of transcription nuclear factor-kappaB in mice. J Pharmacol Exp Ther 2000; 293: 82–90.

26 Inayama M, Nishioka Y, Azuma M, Muto S, Aono Y, Makino H, et al. A novel IkappaB kinase-beta inhibitor ameliorates bleomycin-induced pulmonary fibrosis in mice. Am J Respir Crit Care Med 2006; 173: 1016–22.

27 Matsuoka H, Arai T, Mori M, Goya S, Kida H, Morishita H, et al. A p38 MAPK inhibitor, FR-167653, ameliorates murine bleomycin-induced pulmonary fibrosis. Am J Physiol Lung Cell Mol Physiol 2002; 283: L103–12.

28 Yara S, Kawakami K, Kudeken N, Tohyama M, Teruya K, Chinen T, et al. FTS reduces bleomycin-induced cytokine and chemokine production and inhibits pulmonary fibrosis in mice. Clin Exp Immunol 2001; 124: 77–85.

29 Hamaguchi Y, Nishizawa Y, Yasui M, Hasegawa M, Kaburagi Y, Komura K, et al. Intercellular adhesion molecule-1 and L-selectin regulate bleomycin-induced lung fibrosis. Am J Pathol 2002; 161: 1607–18.

30 Helene M, Lake-Bullock V, Zhu J, Hao H, Cohen DA, Kaplan AM. T cell independence of bleomycin-induced pulmonary fibrosis. J Leukoc Biol 1999; 65: 187–95.

31 Okazaki T, Nakao A, Nakano H, Takahashi F, Takahashi K, Shimozato O, et al. Impairment of bleomycin-induced lung fibrosis in CD28-deficient mice. J Immunol 2001; 167: 1977–81.

32 Chen ES, Greenlee BM, Wills-Karp M, Moller DR. Attenuation of lung inflammation and fibrosis in interferon-gamma-deficient mice after intratracheal bleomycin. Am J Respir Cell Mol Biol 2001; 24: 545–55.

33 Belperio JA, Dy M, Burdick MD, Xue YY, Li K, Elias JA, et al. Interaction of IL-13 and C10 in the pathogenesis of bleomycin-induced pulmonary fibrosis. Am J Respir Cell Mol Biol 2002; 27: 419–27.

34 Daniels CE, Wilkes MC, Edens M, Kottom TJ, Murphy SJ, Limper AH, et al. Imatinib mesylate inhibits the profibrogenic activity of TGF-beta and prevents bleomycin-mediated lung fibrosis. J Clin Invest 2004; 114: 1308–16.

35 Strieter RM, Gomperts BN, Keane MP. The role of CXC chemokines in pulmonary fibrosis. J Clin Invest 2007; 117: 549–56.

36 Tager AM, Kradin RL, LaCamera P, Bercury SD, Campanella GS, Leary CP, et al. Inhibition of pulmonary fibrosis by the chemokine IP-10/CXCL10. Am J Respir Cell Mol Biol 2004; 31: 395–404.

37 O'Meara SJ, Rodgers K, Godson C. Lipoxins: update and impact of

endogenous pro-resolution lipid mediators. Rev Physiol Biochem Pharmacol 2008; 160: 47–70.

38 Vaughn MW, Proske RJ, Haviland DL. Identification, cloning, and functional characterization of a murine lipoxin A4 receptor homologue gene. J Immunol 2002; 169: 3363–9.

39 Chen K, Le Y, Liu Y, Gong W, Ying G, Huang J, *et al*. A critical role for the G protein-coupled receptor mFPR2 in airway inflammation and immune responses. J Immunol 2010; 184: 3331–5.

40 Walther A, Riehemann K, Gerke V. A novel ligand of the formyl peptide receptor: annexin I regulates neutrophil extravasation by interacting with the FPR. Mol Cell 2000; 5: 831–40.

41 Bae YS, Park JC, He R, Ye RD, Kwak JY, Suh PG, *et al*. Differential signaling of formyl peptide receptor-like 1 by Trp-Lys-Tyr-Met-Val-Met-CONH2 or lipoxin A4 in human neutrophils. Mol Pharmacol 2003; 64: 721–30.

42 Machado FS, Johndrow JE, Esper L, Dias A, Bafica A, Serhan CN, *et al*. Anti-inflammatory actions of lipoxin A4 and aspirin-triggered lipoxin are SOCS-2 dependent. Nat Med 2006; 12: 330–4.

43 Godson C, Mitchell S, Harvey K, Petasis NA, Hogg N, Brady HR. Cutting edge: lipoxins rapidly stimulate nonphlogistic phagocytosis of apoptotic neutrophils by monocyte-derived macrophages. J Immunol 2000; 164: 1663–7.

44 Romano M, Maddox JF, Serhan CN. Activation of human monocytes and the acute monocytic leukemia cell line (THP-1) by lipoxins involves unique signaling pathways for lipoxin A4 versus lipoxin B4: evidence for differential Ca^{2+} mobilization. J Immunol 1996; 157: 2149–54.

45 Burli RW, Xu H, Zou X, Muller K, Golden J, Frohn M, *et al*. Potent hFPRL1 (ALXR) agonists as potential anti-inflammatory agents. Bioorg Med Chem Lett 2006; 16: 3713–8.

46 Martins V, Valenca SS, Farias-Filho FA, Molinaro R, Simoes RL, Ferreira TP, *et al*. ATLa, an aspirin-triggered lipoxin A4 synthetic analog, prevents the inflammatory and fibrotic effects of bleomycin-induced pulmonary fibrosis. J Immunol 2009; 182: 5374–81.

npg

Original Article

Depletion of insulin receptor substrate 2 reverses oncogenic transformation induced by v-src

Hong-zhi SUN*, Lin XU#, Bo ZHOU#, Wei-jin ZANG, Shu-fang WU*

Key Laboratory of Environment and Genes Related to Diseases, Ministry of Education, Medical School of Xi'an Jiaotong University, Xi'an 710061, China

Aim: To investigate the role of insulin receptor substrate 2 (IRS-2) in oncogenic transformation induced by v-src.
Methods: IRS-2 gene was silenced using small interfering RNAs (siRNAs). Nuclear translocation and interaction of IRS-2 with v-src was determined using subcellular fractionation, confocal microscopy, and immunoprecipitation. The activity of the cyclin D1 promoter and r-DNA promoter was measured with a luciferase assay.
Results: Depletion of IRS-2 inhibited R-/v-src cell growth and reverse the oncogenic transformation. IRS-2 bound to src via its two PI3-K binding sites, which are critical for activities involved in the transformation. Nuclear IRS-2 occupied the cyclin D1 and rDNA promoters. The combination of IRS-2 and v-src increased the activity of the two promoters, especially the rDNA promoter.
Conclusion: Depletion of insulin receptor substrate 2 could reverse oncogenic transformation induced by v-src.

Keywords: insulin receptor substrate 2 (IRS-2); cellular transformation; nuclear translocation; v-src; cyclin D1 promoter; rDNA promoter; RNA interference

Introduction

The insulin-like growth factor-1 receptor (IGF-1R) mediates its functions through the activation of an intrinsic tyrosine kinase in its cytoplasmic domain. Upon activation, the receptor is autophosphorylated and recruits intracellular substrates, such as the insulin receptor substrate (IRS) proteins. IRS-1 and IRS-2 are two important adaptor molecules essential for IGF-1R intracellular signaling[1]. The IRS proteins have a common amino terminus that includes a pleckstrin homology (PH) domain and a phosphotyrosine-binding (PTB) domain. These two domains are comprised of roughly 300 amino acids and are followed by long tails that vary among the different IRS proteins. These domains contain a number of binding sites for different substrates (such as PI3-K, Grb2, and phosphatases)[2]. Despite extensive experimental studies over the past few years, the role of IRS proteins in oncogenic transformation remains elusive.

The IRS proteins are able to coordinate and amplify numerous signals that are critical during tumorigenesis. In par-

ticular, both IRS-1 and IRS-2 can similarly signal to induce proliferation and survival, two activities essential for cellular transformation[3]. In fibroblasts lacking IRS-1, IRS-2 can compensate for IRS-1's role in signal transduction but cannot stimulate cellular proliferation[4]. However, IRS-1 and IRS-2 may work differently in respect to certain phenotypes related to various oncogenes. Recently, it was shown that IRS-2 was an essential intermediate in the activation of PI3-K, promoting breast carcinoma through the α6β4-integrin receptor[5]. Signaling through the IRS-2 adaptor protein is important for promoting tumor cell invasion and survival (hallmarks of metastasis), and the relative IRS-2 expression level in tumors can significantly affect disease progression in patients with breast cancer[5]. Therefore, pathways that regulate IRS-2 expression, as well as downstream pathways activated through IRS-2, represent potential novel therapeutic targets.

The role of IGF-1R in malignant transformation is based on the observation that the targeted disruption of IGF-1R genes in mouse embryonic fibroblasts (MEFs) prevents their transformation[6]. MEFs that contain disrupted IGF-1R genes, referred to as R-cells, are resistant to transformation induced by numerous viral and cellular oncogenes, including the SV40 T antigen, the activated Ha-ras oncogene, the bovine papillomavirus E5 protein, the human papillomavirus E7 protein, the Ewing's sarcoma fusion protein, and activated src. To

date, the only oncogenes known to transform R-cells are v-src and a mutant of Gα13[7]. The observation that v-src is one of only two oncogenes to transform R-cells is quite remarkable because MEFs have a strong tendency to become transformed. Thus, understanding the actions of v-src in R-cells should be useful for elucidating IRS-dependent transformation.

The v-src oncogene of the Rous sarcoma virus is a 60 kDa tyrosine kinase capable of causing transformation in a variety of cell types. In v-src-transformed cells, both IGF-1R and IRS are constitutively phosphorylated. One of the most intriguing aspects of IRS signaling is that IRS proteins have noncanonical functions within the nucleus[8, 9]. In a similar fashion, IGF-1R and either SV40 T or v-src can cause the nuclear translocation of IRS proteins in MEFs. Once inside the nucleus, studies suggest that IRS-1 or IRS-2 binds the upstream binding factor 1 (UBF-1), playing a role in regulating RNA polymerase 1 activity and the subsequent synthesis of ribosomal RNA[10, 11].

In contrast to IRS-1, few studies have addressed the role of IRS-2 in oncogenic transformation. Our previous findings indicate the potential role of IRS-2 in cellular proliferation, but the functional significance of IRS-2 in transformation needs to be clarified[9, 11]. In the present study, we provide evidence for the role of IRS-2 nuclear translocation in R-/v-src and BT-20 cancer cells. Additionally, we demonstrate the role of IRS-2 in the proliferation and anchorage-independent growth in combination with v-src. These data support the hypothesis that IRS-2 plays a significant role in oncogenic transformation.

Materials and methods
Cell lines and plasmids
R-cells and R-derived cells are 3T3-like cells from mouse embryos with a targeted disruption of the IGF-1R genes[4]. BT-20 breast cancer cells and 32D-derived cells have been previously described[7]. Mutant IRS-2 plasmids have been previously described[6]. One IRS-2 mutant is essentially inactive because of the deletion of the PTB domain between residue 155 and residue 309 (delta PTB). The second mutant has a deletion of the pleckstrin domain (delta PH). A third mutant has decreased activity because of the mutation of the PI3-K-binding-site tyrosines 608 and 939 to phenylalanines.

Gene silencing of IRS-2 was performed by RNA interference using small interfering RNAs (siRNAs). R-/v-src cells were mock-transfected with vehicle (diethylpyrocarbonate-treated water), transfected with control siRNA (scrambled), or transfected with siRNA directed against IRS-2 (siRNA IRS-2: 5′-AAUAGCUGCAAGAGCGAUGAC-3′) in each well of a 12-well plate with the Gene Porter system (Gene Therapy System, San Diego, CA, USA). The second siRNA was directed against IRS-2 (Santa Cruz Biotechnology, Inc, Santa Cruz, CA, USA) using TransIT-siTKO reagents (Mirus Bio Corporation, Madison, WI, USA) according to the manufacturer's instructions. Generation of IRS-2-stably depleted R-/v-src cells was performed by antibiotic selection with G418 after they were transfected with a pcDNA3 vector containing an antisense cDNA against IRS-2, as previously described[6].

Colony formation in soft agar
Briefly, to compare the anchorage-independent growth of different cell lines, cells were plated in essential modified Eagle's medium containing 10% fetal bovine serum (with or without IGF-1) and 0.2% agarose (with a 0.4% agarose underlay). The numbers of colonies larger than 125 μm in diameter were determined 3 weeks after cells were plated.

Confocal microscopy
After fixation with 3% paraformaldehyde for 25 min, cells on coverslips were washed three times with PBS at room temperature, permeabilized with 0.2% Triton X-100 in PBS for 5 min, blocked with 10% normal donkey serum (sc-2044, Santa Cruz Biotechnology, Inc, Santa Cruz, CA, USA) for 20 min, and incubated for 1 h with appropriate primary and secondary antibodies. Confocal analysis was carried out according to the manufacturer's protocol.

Subcellular fractionation, Western blotting, and immunoprecipitation
For immunoprecipitation, 200 μg of nuclear or cytoplasmic lysate was incubated for 2 h at 4 °C with corresponding antibodies coupled to 20 μL of packed protein G-sepharose beads (Oncogene Science, Inc). Immunocomplexes were electrophoresed on a 4%–15% SDS-PAGE gel. Proteins were transferred onto a nitrocellulose membrane and were probed with the indicated antibodies[4, 6]. The blots were detected using enhanced chemiluminescence system (Amersham Biosciences, Piscataway, NJ, USA). The protein size was confirmed by molecular weight standards (Invitrogen, Carlsbad, CA, USA). The intensity of the bands on Western blots was analyzed by Image J (software from NCBI).

GST pull-down analysis
All GST-fusion proteins with various regions of IRS-2 were expressed in BL-21 bacterial cells (Invitrogen, Carlsbad, CA, USA) and purified with glutathione-agarose beads using standard techniques. Cells were lysed with 50 mmol/L HEPES (pH 7.5), 1% Nonidet P-40, 1 mmol/L EGTA, 10 mmol/L NaF, 20 mmol/L sodium pyrophosphate, 10 g/mL aproptinin, and 10 μg/mL leupeptin on ice for 30 min. The resulting supernatants were incubated with the immuno-immobilized GST proteins overnight. After extensive washing with 50 mmol/L HEPES (pH 7.5), 150 mmol/L NaCl, and 0.1% Triton X-100, the proteins bound to either IRS-2 or GST (control) were analyzed by SDS-PAGE, followed by immunoblotting with appropriate antibodies.

Chromatin immunoprecipitation assay (ChIP)
Chromatin immunoprecipitation assays were performed according to the manufacturer's instructions (Upstate, Lake Placid, NY, USA) and previously described methods[10]. An Epicentre Fail Safe PCR System (Epicentre, Madison, WI, USA) was used for PCR. The amplification products were analyzed in a 2% agarose gel and visualized by SYBR Gold (Molecular Probes, Eugene, OR, USA) staining. Gels stained with SYBR

Gold were scanned with a Typhoon Laser scanner (Typhoon 9400 Variable Mode Imager, Amersham Biosciences, Piscataway, NJ, USA).

Reporter genes

The cyclin D1 promoter and r-DNA promoter were used to transiently express luciferase. Determination of luciferase activity was performed with standard procedures. Transfection efficiency was monitored using previously described methods[10]. Each cell line was transfected in a single batch before being subdivided into aliquots that were measured at different time intervals after transfection and insulin stimulation. Mock-transfected cells were utilized to determine background.

Antibodies

The following antibodies were used: phospho-IRS-2 antibody against phosphorylated Tyr residues in IRS-2 (catalog No sc-17195-R, Santa Cruz Biotechnology, Inc, USA), mouse monoclonal anti-UBF (Santa Cruz Biotechnology, Inc, USA), anti-IRS-2 (Upstate, Inc, USA), v-src and mouse monoclonal anti-Grb2 (both from Transduction Laboratories, USA), goat anti-rabbit IgG-FITC (Santa Cruz Biotechnology, Inc, USA) and goat anti-mouse IgG2a-FITC (Santa Cruz Biotechnology, Inc, USA). The siRNA was from Santa Cruz Biotechnology, Inc or UBI Biotechnology, Inc.

Statistical analysis

Experiments were performed in triplicate and repeated at least three times. Results are expressed as mean±SD. All statistical analyses were performed with SigmaStat for Windows version 3.10 (Systat Software, Inc, Port Richmond, CA, USA). Differences were considered statistically significant when $P<0.05$.

Results

Depletion of IRS-2 inhibits growth and reverses transformation of R-/v-src cells

One of the distinctive features of transformed cell lines such as R-/v-src cells is the ability to proliferate in the absence of serum. Using siRNA, we effectively depleted endogenous IRS-2 when compared with vehicle-treated or control-treated cells. Additionally, this depletion had no effect on IRS-1 or Grb2, an unrelated internal control (Figure 1A). IRS-2 depletion considerably retarded the growth of R-/v-src cells in the absence of serum (Figure 1B), suggesting that endogenous IRS-2 contributes to the growth of R-/v-src cells in these conditions. To confirm the growth of identical cells that underwent treatment, we compared microscopic images of vehicle, control, and siRNA/IRS-2-transfected cells after 72 h (Figure 1C). Importantly, preliminary tests indicated that these siRNAs at this concentration had no toxic effect on R-/v-src cells with serum present (data not shown).

Based on these data, we sought to confirm the role of IRS-2
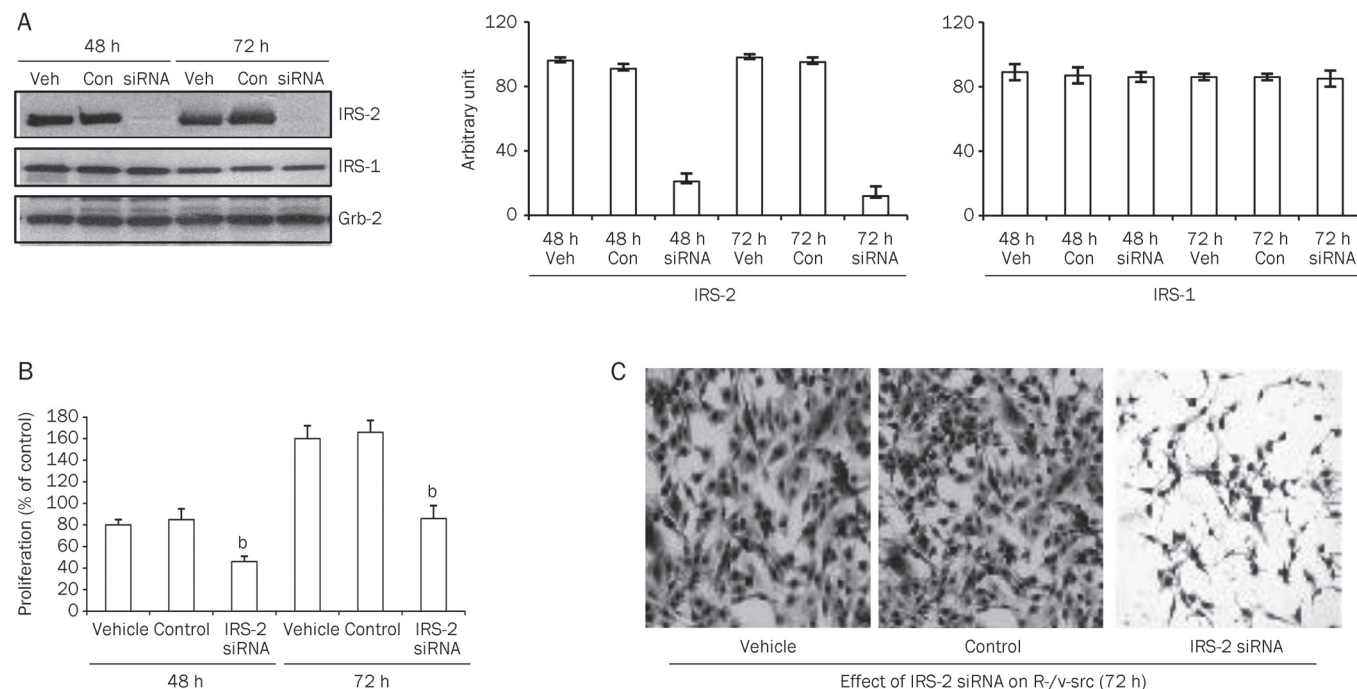
Figure 1. Depletion of endogenous IRS-2 proteins effectively reduces the proliferation of R-/v-src cells in serum-free conditions. (A) Gene knockdown of IRS-2 was achieved by siRNA. Densitometric analysis of endogenous IRS-2 and IRS-1 were quantified by Image J (software from NCBI) and normalized to the internal control Grb-2. Values in arbitrary units from three independent experiments are shown. (B) Cells at 48 and 72 h were processed and analyzed for growth. Values are expressed as percent increase over serum free medium (SFM). [b]$P<0.05$ compared with vehicle-treated control cells by ANOVA. (C) Microscopic images of R-/v-src cells treated with siRNA designed against IRS-2. Untreated cells and cells treated with siRNA were compared at 72 h. Veh, vehicle blank control; Con, scrambled control siRNA.

in the transformation of R-/v-src cells by stably depleting endogenous IRS-2. Antisense IRS-2 siRNAs dramatically reduced IRS-2 protein expression in R-/v-src cells (Figure 2A, top). Furthermore, the stable depletion of IRS-2 strongly decreased the growth of R-/v-src cells under conditions of serum starvation (Figure 2A, bottom), confirming our transient siRNA experimental findings.

Another critical measurement of cellular transformation is the ability of cancer cells to grow in an anchorage-independent manner. Therefore, we wanted to determine whether or not the stable depletion of IRS-2 in R-/v-src cells would affect their ability to form colonies in soft agar. We determined that only R-cells expressing wild-type IRS-2 and v-src formed colonies in soft agar (Figure 2B). Adding insulin increased the number of colonies on the plates. As expected, the number of colonies formed by R-/v-src cells lacking IRS-2 was significantly decreased in soft agar, confirming the fact that cellular transformation requires the activation of IRS-2 and is v-src independent.

Our findings indicate that IRS-2 is essential for the role of v-src to encourage serum-independent and anchorage-independent cellular growth, two key properties of aggressive tumorigenesis.

IRS-2 domains are required for interaction with v-src and PI3-K-binding tyrosine residues

To elucidate the role of IRS-2 in the growth inhibition of R-/v-src cells, we investigated the interaction between IRS-2 and v-src by immunoprecipitating (IP) lysates from R- and R-/v-src cells. When lysates were immunoprecipitated with IRS-2 antibodies, and Western blots were performed with antibodies against v-src, we detected an interaction between v-src and IRS-2 (Figure 3A). To further elucidate the domain required for this interaction, we performed a GST pull-down assay to determine the presence of proteins known to interact with IRS proteins and v-src, such as PI3-K and Grb2. The results shown in Figure 3B indicated that the p85 subunit of PI3-K could be pulled down with amino acids between resi-
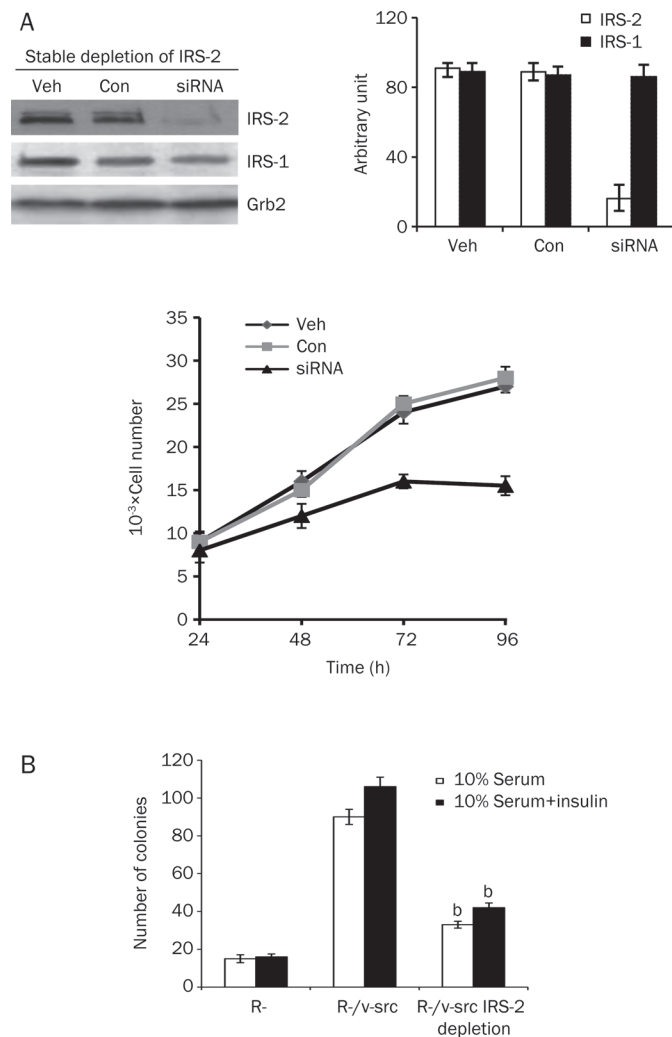
Figure 2. Depletion of IRS-2 inhibits growth and reverses the transformation of R-/v-src cells. (A) R-/v-src cells were transfected with a specific siRNA for IRS-2 and either DMSO (Veh) or control siRNA (Con) as described in the Materials and methods. IRS-2 expression in cell lysates was detected by immunoblotting at 48 h after transfection. Cells were washed, transferred to SFM, and counted at the indicated times. The level of endogenous IRS-2 and IRS-1 was detected by immunoblotting, and protein expression was quantified by Image J (software from NCBI) and normalized to the internal control Grb-2. Mean±SD. $^bP<0.05$ compared to control oligo-treated cells by ANOVA. (B) Colony formation of R-/v-src cells in soft agar after IRS-2 siRNA transfection. Cells were counted after 4 weeks. Colonies >125 µm were scored as positive. Mean±SD. *n*=3.
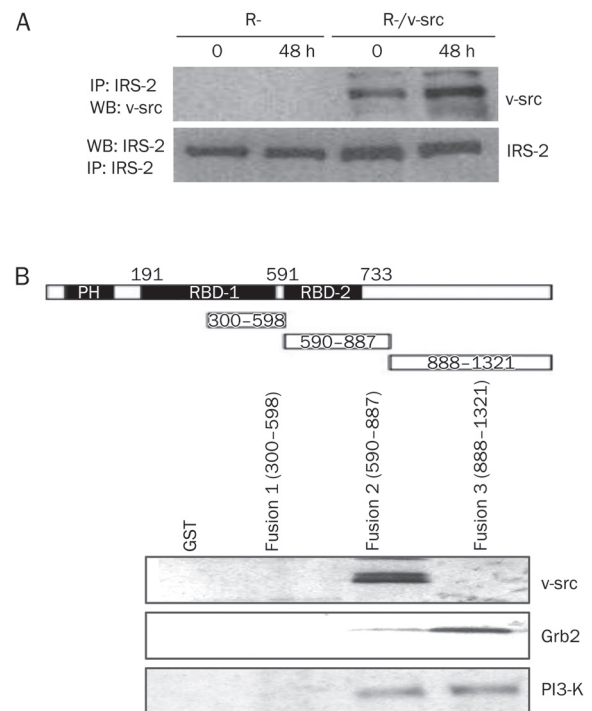

Figure 3. Interaction between IRS-2 and v-src. (A) IPs performed with an antibody against IRS-2, and Western blots performed with an anti-v-src antibody. (B) Diagram of IRS-2 GST constructs (RBD, receptor binding domain) and pull-down experiments for PI3-K, Grb2, and v-src.

dues 590 and 1321 of IRS-2. Additionally, the stretch of amino acids from residues 590 to 887 also pulled down v-src.

These data suggest that the sequences responsible for the binding of IRS-2 to v-src are required for IRS-2's involvement in transformation. To identify the importance of this PI3-K binding site, we stably expressed IRS-2 with a PI3-K binding site mutation in IRS-2 depleted R-/v-src cells. As shown in Figure 4, although IRS-2 still bound v-src (at one or several other sites other than the PI3-K site), the deletion of this essential PI3-K binding site abolished transformation, indicating that PI3-K is required in this process.
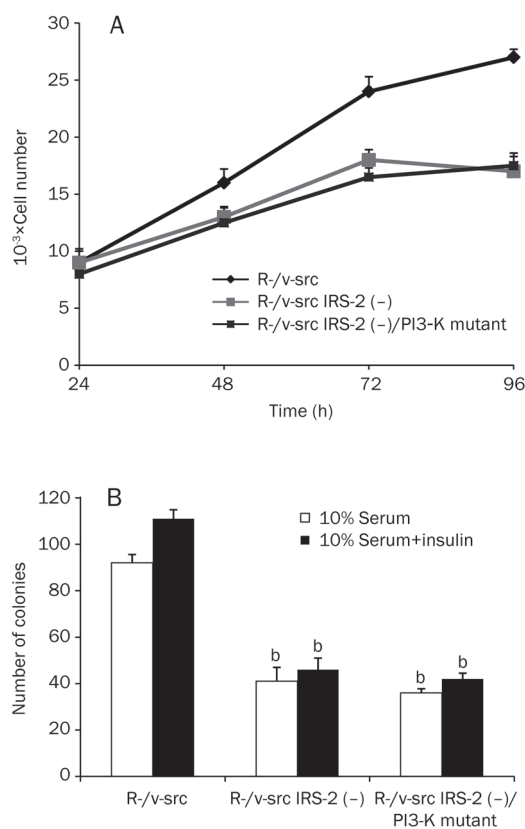
Figure 4. V-src co-precipitates Tyr-phosphorylated IRS-2. Cell lysates were immunoprecipitated with an antibody to v-src. Western blots with antibodies directed against anti-phospho-IRS-2 and v-src were performed. Mean±SD. *n*=3. [b]*P*<0.05 *vs* R-/v-src.

Nuclear translocation of IRS-2 in R-/v-src and BT-20 cells

Nuclear translocation is considered to be one of the most important steps in the process of cellular transformation[7]. Following subcellular fractionation, IRS-2 was present in the nuclear fraction of R-/v-src and BT-20 cells (Figure 5A). Grb2 and c-Jun antibodies were used to monitor the purity of these subcellular fractions[8]. Nuclear translocation of IRS-2 in R-/v-src and BT-20 cells was then confirmed by confocal microscopy. After stimulation with insulin for 16 h, merged images of R-/v-src and BT-20 cells stained with antibodies directed against IRS-2 (rhodamine, red) and nucleolin (FITC,
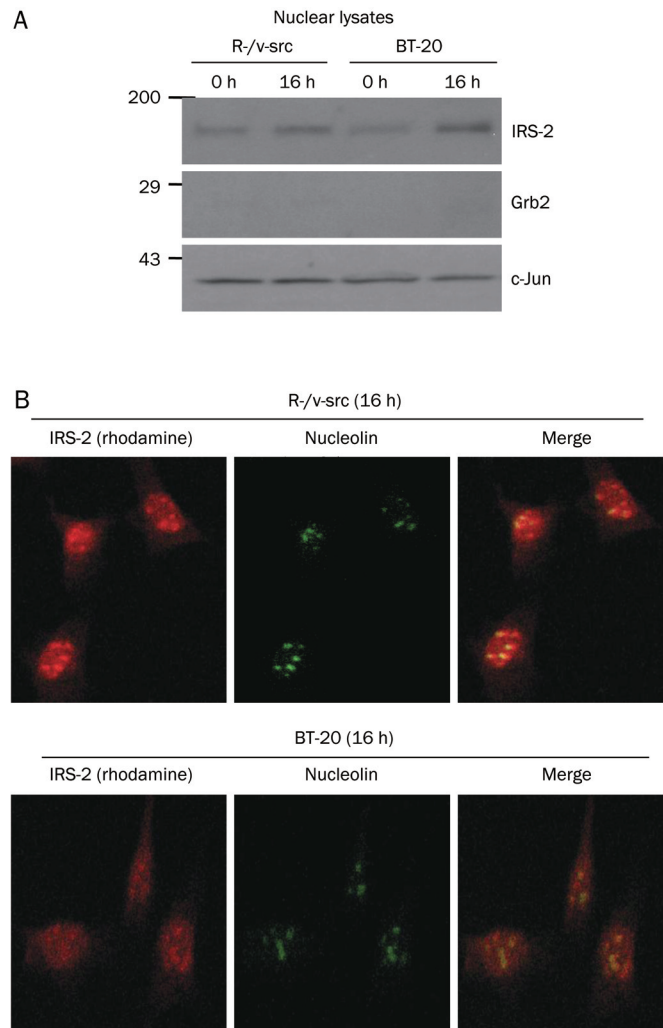
Figure 5. Nuclear translocation of IRS-2 in R-/v-src and BT-20 cells. (A) Subcellular localization of IRS-2 in R-/v-src and BT-20 cells. Nuclear fractions were prepared from cells in serum-free medium after insulin stimulation (0 and 16 h). To control for the purity of the subcellular fractions, we used antibodies to c-Jun (for nuclear purity) and antibodies to Grb2 (for cytosolic purity). (B) Confocal microscopy of BT-20 cells stained with antibodies directed against IRS-2 and nucleolin. IRS-2 was found in the nucleus as well as in the cytoplasm at the indicated times with insulin stimulation.

green) (Figure 5B, top) showed that a substantial fraction of IRS-2 was detectable in the nuclei of these cells, indicated by the co-expression of IRS-2 and nucleolin (greenish-yellow nucleolin).

Recruitment of nuclear IRS-2 to the rDNA and cyclin D1 promoters

The presence of IRS-2 in the nuclei of transformed cells suggested that IRS-2 might be associated with the regulatory sequences of target genes such as rDNA and cyclin D1, which are involved in cellular transformation and cell-cycle regulation. To determine whether IRS-2 was associated with the regulatory sequences of target genes, we investigated the recruit-

ment of IRS-2 to these promoters by ChIP. IRS-2 was detected with ChIP at the rDNA and cyclin D1 promoters. Because upstream binding factor (UBF) is always present at the rDNA and cyclin D1 promoters, this protein served as a positive control[10, 11]. Mouse and rabbit IgG served as the negative controls. These data are presented in Figure 6A and 6B, which shows ChIP results from untreated R-/v-src cells in serum-free medium (SFM) and cells stimulated with insulin for 24 and 48 h. In the R-/v-src cells, IRS-2 was detectable at both the cyclin D1 and rDNA promoters 24 and 48 h after insulin stimulation. A weak signal was already detectable at both promoters in unstimulated cells, but this signal became more clear after 24 h

Figure 6. Recruitment of IRS-2 to the rDNA and cyclin D1 promoter. The main panel shows the results of experiments in which sonicated chromatin from R-/v-src and BT-20 cells was immunoprecipitated with antibodies against IRS-2 and UBF (positive control). (A and B): the first lane is time 0 (no stimulation with insulin), followed by insulin stimulation for 24 and 48 h, respectively. (C) Activity of the cyclin D1 promoters in 32D-derived cell lines. Mean±SD. n=3. [b]P<0.05 *vs* 32D-IGF-IR.

of stimulation.

To further validate this result, we used ChIP assays to investigate whether or not IRS-2 was present at the rDNA and cyclin D1 promoters of BT-20 cells. IRS-2 was still detectable at both promoters. It seems that the mechanism by which IRS-2 promotes transformation is, at least in part, due to its participation in a complex of the rDNA promoter and UBF1, a protein that upregulates RNA polymerase I activity[12, 13].
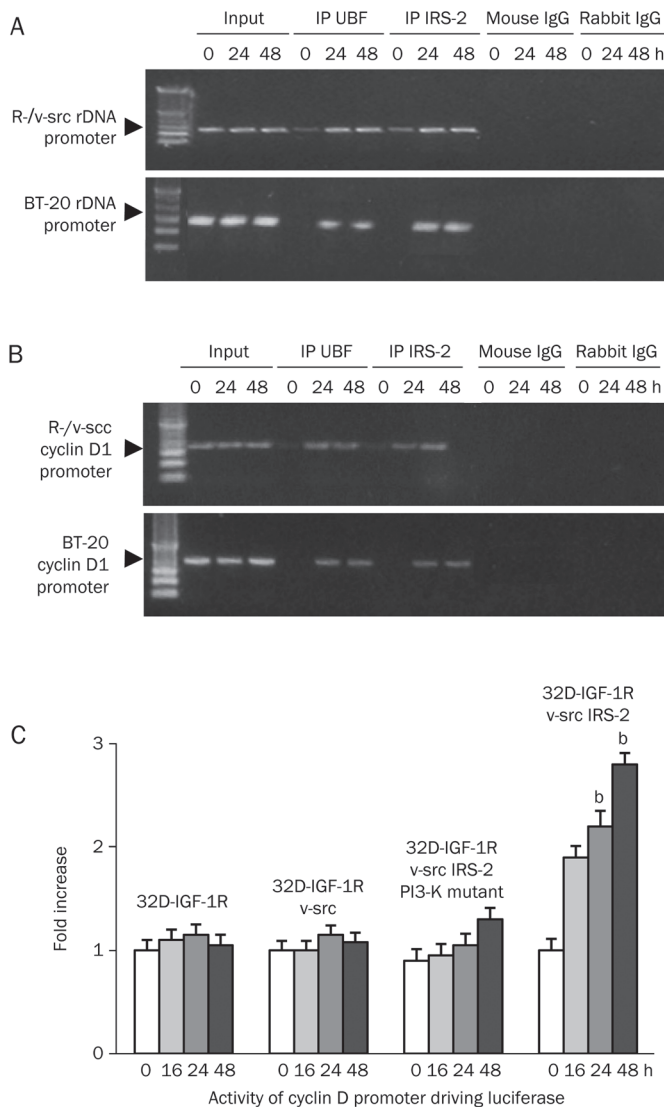
Activity of the cyclin D1 and rDNA promoters

The presence of IRS-2 at the rDNA and cyclin D1 promoters indicated that IRS-2 had a functional effect on rDNA and cyclin D1 activity during proliferation. The influence of this promoter occupancy was confirmed by determining the activities of the cyclin D1 and rDNA promoters in 32D-derived cell lines that were expressing v-src in addition to wild type or mutant IRS-2. For these experiments, the 32D-derived cell lines were transiently transfected with luciferase reporter genes. Then, luciferase activity was determined after insulin stimulation. Cyclin D1 promoter activity was slightly increased in parental 32D-IGF-1R cells and in 32D-IGF-1R cells expressing only v-src (Figure 6C). When IRS-2 and v-src were added combinatorially, the promoter activity was dramatically increased. However, when v-src was expressed with a PI3-K binding site deletion mutant of IRS-2, the promoter activity of cyclin D1 was comparable to the promoter's activity in parental 32D-IGF-1R cells. In conclusion, it seems as though IRS-2 contains distinct receptor binding domains that are different from IRS-1. Combined with the noncanonical functions of IRS-2 protein within the nucleus, IRS-2 may also be the principal cause of cellular transformation.

Discussion

In this study, we provide several lines of evidence that indicate the functional involvement of IRS-2 in oncogenic transformation. First, we demonstrated that the down-regulation of IRS-2 could inhibit growth and reverse transformation of R-/v-src cells. In addition, we determined that IRS-2 bound to v-src through its two PI3-K-binding tyrosine residues. Furthermore, it appears that these two residues are critical for cellular transformation. Moreover, we demonstrated that IRS-2 could translocate to the nuclei of R-/v-src and BT-20 breast cancer cells. Finally, IRS-2 occupied the cyclin D1 and rDNA promoters, and when combined with v-src, increased the activity of these two promoters (especially the rDNA promoter). These results indicate that IRS-2 plays a significant role in the activation of cell cycle progression and transformation by v-src.

The role of IGF-1R in cancer was previously established in MEFs from mice carrying a targeted disruption of the IGF-1R genes (R-cells), which are usually refractory to transformation by viral and cellular oncogenes (including the SV40 T antigen)[1]. However, the 60 kDa tyrosine kinase v-src oncogene is one of only two oncogenes able to bypass the requirement of IGF-1R to promote both proliferation and anchorage-independent growth in R-cells. This exception indicated that

IGF-1R and its downstream signaling pathways might be required for transformation[2].

We have recently reported the nuclear translocation of IRS-2 in R+ cells, but the functional consequence of this translocation remains unclear[6]. In this study, we confirmed that the nuclear translocation of IRS-2 in R-/v-src and BT-20 cells was involved in cell growth and transformation. Furthermore, we also demonstrated that the presence of IRS-2 at the rDNA and cyclin D1 promoters had a functional effect on their activity, and actually caused a marked activation of both promoters[14]. These findings are in agreement with the observation that IRS-2 interacts with src and that IGF-1R activates STAT proteins that are src-responsive[15].

Most transformation studies have focused on IRS-1, whereas the investigation of IRS-2's function in transformation has been limited[4]. However, recent studies indicate that the distinct biological actions of IRS-2 during cellular transformation have been underestimated. One such study indicated that IRS-2 exhibited the ability to initiate and promote mammary tumorigenesis[5]. The lengthy time required to form mammary tumors in IRS-2 transgenic animals suggests that other oncogenes act in concert with IRS-2, presumably by activating IRS-2. In addition, we have previously shown that unlike IRS-1, both wild-type IRS-2 and a truncated IRS-2 protein lacking the PH and PTB domains inhibit differentiation and sustain the IGF-1-dependent growth of 32D-IGF-1R cells[6].

The importance of IRS-2 in cellular proliferation may be due to its nuclear translocation. There have been reports that delta-PHPTB IRS-2 may have biological activity[16, 17]. The delta-PHPTB IRS-2 is fully capable (as is wild type IRS-2 and IRS-1) of both stimulating growth and inhibiting differentiation of 32D-IGF-1R cells. In contrast, IRS-1 proteins lacking the same PH and PTB domains are completely inactive in blocking differentiation and stimulating IL-3-independent growth of 32D-IGF-1R cells[6]. Down-regulation of IRS-2 may affect the protein's nuclear functions, bypassing its conventional signaling pathway[17, 18].

Our results show that in R-/v-src cells, transformation by v-src requires IRS-2, and that this mechanism seems to be based on an interaction between the two proteins. As shown in the GST pull-down assay, the sequence between the amino acid residues 590 and 887 in IRS-2 potentially interacts with v-src. Therefore, the phosphorylation status of IRS-2 and its effect on binding to v-src is of interest. To exclude interference from IRS-1, we performed the same experiments in the BT-20 cell line, which has no endogenous IRS-1, allowing an excellent model to verify the specific interaction between phospho-IRS-2 and v-src. This interaction was confirmed by Western blotting (with phospho-IRS-2 antibodies that specifically detect phosphorylated IRS-2 at Tyr612) an IP lysates of v-src (Figure S1). Results indicated that v-src co-precipitated phosphorylated IRS-2.

Wild type IRS-2 is detectable at both the rDNA and cyclin D1 promoters, and the PI3-K binding sites of IRS-2 are required for v-src binding[19, 20]. The importance of IRS-2 in v-src transformation was also demonstrated by the inability of IRS-2 protein with mutated PI3-K binding sites to activate the rDNA and cyclin D1 promoters. We propose that IRS-2 binds v-src, which leads to the phosphorylation of IRS-2 in the absence of IGF-1R signaling. This interaction requires the PI3-K binding sites of IRS-2, which causes the subsequent nuclear translocation of IRS-2 and its occupancy at the rDNA and cyclin D1 promoters that is observed during transformation[21, 22]. Oncogenes v-src not only directly associate with IRS-2, but also are dependent on IRS-2 tyrosine phosphorylation for their mitogenic and transforming activity.

Despite its nuclear localization, IRS-2 phosphorylates UBF, suggesting that its activation of cell proliferation and rRNA synthesis are regulated through conventional signal transduction pathways[23, 24]. The activity of UBF1 depends on its phosphorylation state and cellular levels[25]. It was reported that IRS-2 is more effective than IRS-1 in the InR-mediated phosphorylation of ERKs[26]. There is a possible contribution of ERKs to the overall activity of UBF1 because of the fact that ERKs phosphorylate UBF1 at two threonine residues (residues 117 and 201). Mutations at these residues inactivate UBF1[27], suggesting a possible link between these signaling pathways[28, 29]. Further studies are required to determine the relative roles of IRS-1 and IRS-2, as well as the upstream activators and downstream effectors of IRS-2 during oncogenic transformation.

Conclusion

We have shown that oncogenic transformation by v-src in MEFs requires the association of v-src with IRS-2. We have also shown that IRS-2 binds src through two tyrosine residues that also bind PI3-K. The interaction of v-src, coupled with the nuclear translocation of IRS-2, might be responsible for cell growth and transformation.

Abbreviations

IGF-1R, IGF-1 receptor; IRS, insulin receptor substrate; MEF, mouse embryo fibroblast; PH, pleckstrin homology; PI3-K, phosphatidylinositol 3-kinase; PTB, phosphotyrosine binding domain; UBF, upstream binding factor.

Acknowledgements

Author contribution

Hong-zhi SUN and Shu-fang WU designed and executed the experiments and drafted the manuscript. Bo ZHOU and Lin XU conducted most of the experiments and contributed to manuscript preparation. Wei-jin ZANG contributed to the

overall experimental design.

Supplementary information
Supplementary figure is available at Acta Pharmacologica Sinica website of NPG.

References

1   Nagle JA, Ma ZF, Byrne MA, White MF, Shaw LM. Involvement of insulin receptor substrate 2 in mammary tumor metastasis. Mol Cell Biol 2004; 24: 9726–35.

2   Baserga R, Peruzzi F, Reiss K. The IGF-I receptor in cancer biology. Int J Cancer 2003; 107: 873–7.

3   Baserga R. The insulin-like growth factor-1 receptor as a target for cancer therapy. Expert Opin Ther Targets 2005; 9: 753–68.

4   Sun H, Tu X, Prisco M, Wu A, Casiburi I, Baserga R. Insulin-like growth factor I receptor signaling and nuclear translocation of insulin receptor substrates 1 and 2. Mol Endocrinol 2003; 17: 472–86.

5   Dearth RK, Cui XJ, Kim HJ, Hadsell DL, Lee AV. Oncogenic transformation by the signaling adaptor proteins insulin receptor substrate (IRS)-1 and IRS-2. Cell Cycle 2007; 6: 705–13.

6   Sun H, Baserga R. Deletion of the pleckstrin and phosphotyrosine binding domains of insulin receptor substrate-2 does not impair its ability to regulate cell proliferation in myeloid cells. Endocrinology 2004; 145: 5332–43.

7   Dalmizrak O, Wu A, Chen J, Sun H, Utama FE, Zambelli D, *et al*. Insulin receptor substrate-1 regulates the transformed phenotype of BT-20 human mammary cancer cells. Cancer Res 2007; 67: 2124–30.

8   Reiss K, Wang JY, Romano G, Tu X, Peruzzi F, Baserga R. Mechanism of regulation of cell adhesion and motility by insulin receptor substrate-1 in prostate cancer cells. Oncogene 2001; 20: 490–500.

9   Sun H, Tu X, Baserga R. A mechanism for cell size regulation by the insulin and IGF-1 receptors. Cancer Res 2006; 66: 11106–9.

10   Drakas R, Tu X, Baserga R. Control of cell size through phosphorylation of upstream binding factor1 by nuclear phosphatidylinositol 3-kinase. Proc Natl Acad Sci U S A 2004; 101: 9272–6.

11   Baserga R. Customizing the targeting of IGF-1 receptor. Future Oncol 2009; 5: 43–50.

12   Voit R, Grummt I. Phosphorylation of UBF at serine 388 is required for interaction with RNA polymerase I and activation of rDNA transcription. Proc Natl Acad Sci U S A 2001; 98: 13631–6.

13   Comai L, Song Y, Tan C, Bui T. Inhibition of RNA polymerase I transcription in differentiated myeloid leukemia cells by inactivation of selectivity factor-1. Cell Growth Diff 2000; 11: 63–70.

14   Sun H, Baserga R. The role of insulin receptor substrate-1 in transformation by v-src. J Cell Physiol 2008; 215: 725–32.

15   White MF. The IRS-signalling system: a network of docking proteins that mediate insulin action. Mol Cell Biochem 1998; 182: 3–11.

16   Klippel A, Escobedo MA, Wachowicz MS, Apell G, Brown TW, Giedlin MA, *et al*. Activation of phosphatidylinositol 3-kinase is sufficient for cell cycle entry and promotes cellular changes characteristic of oncogenic transformation. Mol Cell Biol 1998; 18: 5699–711.

17   Byron SA, Horwitz KB, Richer JK, Lange CA, Zhang X, Byron SA, *et al*. Insulin receptor substrates mediate distinct biological responses to insulin-like growth factor receptor activation in breast cancer cells. Br J Cancer 2006; 95: 120–8.

18   DeAngelis T, Chen J, Wu A, Prisco M, Baserga R. Transformation by the Simian Virus 40 T antigen is regulated by IGF-1 receptor and IRS-1 signaling. Oncogene 2006; 25: 32–42.

19   Del Rincon SV, Guo Q, Morelli C, Shiu HY, Surmacz E, Miller WH. Retinoic acid mediates degradation of IRS-1 by the ubiquitin-proteasome pathway, via a PKC-dependent mechanism. Oncogene 2004; 23: 9269–79.

20   Peruzzi F, Prisco M, Dews M, Salomoni P, Grassilli E, Romano G, *et al*. Multiple signaling pathways of the IGF-I receptor in protection from apoptosis. Mol Cell Biol 1999; 19: 7203–15.

21   Yenush L, Fernandez R, Myers MG Jr, Grammer TC, Sun XJ, Blenis J, *et al*. The Drosophila insulin receptor activates multiple signaling pathways but requires insulin receptor substrate proteins for DNA synthesis. Mol Cell Biol 1996; 16: 2509–17.

22   Comai L, Song Y, Tan C, Bui T. Inhibition of RNA polymerase I transcription in differentiated myeloid leukemia cells by inactivation of selectivity factor-1. Cell Growth Diff 2000; 11: 63–70.

23   Baserga R. Customizing the targeting of IGF-1 receptor. Future Oncol 2009; 5: 43–50.

24   Sawka-Verhelle D, Tartare-Deckert S, White MF, van Obberghen E. Insulin receptor substrate-2 binds to the insulin receptor through its phosphotyrosine-binding domain and through a newly identified domain comprising amino acids 591–786. J Biol Chem 1996; 271: 5980–3.

25   Drakas R, Tu X, Baserga R. Control of cell size through phosphorylation of upstream binding factor1 by nuclear phosphatidylinositol 3-kinase. Proc Natl Acad Sci U S A 2004; 101: 9272–6.

26   Huang C, Thirone ACP, Huang X, Klip A. Differential contribution of insulin receptor substrate-1 *versus* 2 to insulin signaling and glucose uptake in L6 myotubes. J Biol Chem 2005; 280: 19426–35.

27   Stefanovsky VY, Pelletier G, Hannan R, Gagnon-Kugler T, Rothblum LI, Moss T. An immediate response of ribosomal transcription to growth factor stimulation in mammals is mediated by ERK phosphorylation of UBF. Mol Cell 2001; 8: 1063–73.

28   Klippel A, Escobedo MA, Wachowicz MS, Apell G, Brown TW, Giedlin MA, *et al*. Activation of phosphatidylinositol 3-kinase is sufficient for cell cycle entry and promotes cellular changes characteristic of oncogenic transformation. Mol Cell Biol 1998; 18: 5699–711.

29   Bader AG, Vogt PK. An essential role for protein synthesis in oncogenic cellular transformation. Oncogene 2004; 23: 3145–50.

npg

Original Article

Proteasome inhibitor MG-132 induces C6 glioma cell apoptosis via oxidative stress

Wen-hai FAN[1, #], Yi HOU[2, #], Fan-kai MENG[1], Xiao-fei WANG[3], Yi-nan LUO[1], Peng-fei GE[1, *]

[1]Department of Neurosurgery, 1st Bethune Hospital of Jilin University, Changchun 130021, China; [2]Tissue Engineering Laboratory, College of Pharmaceutical Sciences, Jilin University, Changchun 130021, China; [3]Division of Cancer Genetics, Department of Advanced Medical Science, Nihon University School of Medicine, Tokyo 102-8251, Japan

Aim: Proteasome inhibitors have been found to suppress glioma cell proliferation and induce apoptosis, but the mechanisms are not fully elucidated. In this study we investigated the mechanisms underlying the apoptosis induced by the proteasome inhibitor MG-132 in glioma cells.

Methods: C6 glioma cells were used. MTT assay was used to analyze cell proliferation. Proteasome activity was assayed using Succinyl-LLVY-AMC, and intracellular ROS level was evaluated with the redox-sensitive dye DCFH-DA. Apoptosis was detected using fluorescence and transmission electron microscopy as well as flow cytometry. The expression of apoptosis-related proteins was investigated using Western blot analysis.

Results: MG-132 inhibited C6 glioma cell proliferation in a time- and dose-dependent manner (the IC_{50} value at 24 h was 18.5 μmol/L). MG-132 (18.5 μmol/L) suppressed the proteasome activity by about 70% at 3 h. It induced apoptosis via down-regulation of antiapoptotic proteins Bcl-2 and XIAP, up-regulation of pro-apoptotic protein Bax and caspase-3, and production of cleaved C-terminal 85 kDa PARP). It also caused a more than 5-fold increase of reactive oxygen species. Tiron (1 mmol/L) effectively blocked oxidative stress induced by MG-132 (18.5 μmol/L), attenuated proliferation inhibition and apoptosis in C6 glioma cells, and reversed the expression pattern of apoptosis-related proteins.

Conclusion: MG-132 induced apoptosis of C6 glioma cells via the oxidative stress.

Keywords: C6 glioma cells; apoptosis; proteasome inhibitor; MG-132; tiron; oxidative stress; Bcl-2; Bax; caspase-3; PARP; X chromosome-linked inhibitor of apoptosis (XIAP)

Introduction

The proteasome is an evolutionarily conserved protease complex with multiple catalytic activities and is mainly responsible for selective degradation of abnormal intracellular proteins and many cellular regulatory proteins[1]. It is also involved in cellular differentiation, antigen presentation and cell cycle modulation[2]. Therefore, inhibition of proteasome activity has emerged as a new chemotherapy strategy for malignant tumors. Although studies have shown that inhibition of proteasome activity could inhibit cellular proliferation in several tumor cell lines including melanoma, prostate cancer and glioma cells[3–6], its underlying mechanism is not fully understood. The proteasome inhibitor bortezomib has

been authorized by the US Food and Drug Administration to enter clinical trials, but it is used mainly in the leukemia field. Thus, more studies are needed to investigate the effects of proteasome inhibition on solid cancers. MG-132 is an aldehyde peptide compound that has shown potent inhibitory effects on proteasome chymotrypsin-like activity and is chemically distinct from bortezomib (a boronic acid dipeptide)[7]. Although our previous studies *in vitro* showed that it could induce apoptosis in human glioma cells[8], its upstream events are largely unknown.

Oxidative stress is a complex and dynamic situation characterized by overproduction of reactive oxygen species (ROS) that cannot be cleared from cells[9]. Oxidative stress can damage macromolecules such as lipids, nucleic acids and proteins and trigger cell death through the effects of ROS on signal transduction pathways[10]. Therefore, oxidative stress could cause cell death via apoptotic pathways. Several studies have shown that oxidative stress is closely associated with

the proteasome, as the proteasome is involved in regulating anti-oxidants, including catalase, heme oxygenase-1 (HO-1), copper/zinc-superoxide dismutase and γ-GCS[11–14]. However, the relationship between proteasome dysfunction and oxidative stress is still a matter of dispute. In the central nervous system, proteasome dysfunction serves as an important switch for the induction of oxidative stress[15]. On the other hand, proteasome inhibition has protective effects on vascular cells undergoing oxidative stress[14]. Even for tumor cells, proteasome inhibition also has varied effects on the production of ROS in different thyroid cancer cell lines[16].

Therefore, in this study, we examined the effects of proteasome inhibition on rat C6 glioma cells and investigated the relationship between apoptosis and oxidative stress generated by inhibition of proteasome activity. Thus, tiron (4,5-dihydroxy-1,3-benzene disulfonic acid), a well-known and widely used antioxidant[17], was used in this study to attenuate the oxidative stress that proteasome inhibition might induce.

Materials and methods
Reagents
MG-132, obtained from Calbiochem (San Diego, CA, USA), was dissolved in PBS to a storage concentration of 50 μmol/L. DMEM medium was from Gibco (Rockville, MD, USA). Fetal bovine serum (FBS) was from Life Technologies (Grand Island, NY, USA). Antibodies against caspase-3, Bax, and Bcl-2 were from Santa Cruz Biotechnology (Santa Cruz, CA, USA). Anti-XIAP (X chromosome-linked inhibitor of apoptosis) was from R&D systems (Minneapolis, MN, USA). Anti-poly (ADPribose) polymerase (PARP) and PARP/85 were from BD Biosciences (San Jose, CA, USA). Protein concentration assay kits were from Bio-Rad (Hercules, CA, USA). ECL Western blotting detection reagents were from Amersham (Piscataway, NJ, USA). PVDF membranes were from Millipore Company (Billerica, MA, USA). Other reagents were from Sigma (St Louis, MO, USA).

Cell line and culture
Rat C6 glioma cells were obtained from Shanghai Institute of Cell Biology, Chinese Academy of Sciences (Shanghai, China). Cells were cultured in DMEM supplemented with 10% fetal bovine serum, 2 mmol/L glutamine (Gibco, Grand Island, NY, USA), penicillin (100 U/mL) and streptomycin (100 μg/mL) and maintained at 37 °C and 5% CO$_2$ in a humid environment. Cells in the mid-log phase were used for experiments.

Cell viability assay
C6 glioma cells were seeded onto 96-well microplates (3×10^4 cells/well) and cultured for 24 h. The cells were treated with PBS or MG-132 final concentrations of 10, 20, 30, and 40 μmol/L, respectively. Cell viability was assessed using an MTT assay at 3, 6, 12, and 24 h after MG-132 treatment. The absorbance value (*A*) at 570 nm was read using an automatic multi-well spectrophotometer (Bio-Rad, Richmond, CA, USA).

Hoechst 33342 staining
C6 glioma cells (3×10^5 cells/well) were allowed to grow on coverslips in 6-well culture plates (Nunc, Denmark) for 24 h. The cells were then treated with either PBS (control) or 18.5 μmol/L MG-132 at 37 °C for 24 h. Cells growing on glass coverslips were fixed in methanol for 5 min at room temperature. The fixed cells were washed twice with PBS and then incubated with Hoechst 33342 for 5 min at room temperature and observed under a fluorescence microscope. Fragmented or condensed nuclei were scored as apoptotic.

Transmission electron microscopy
C6 glioma cells were cultured and treated as described above and harvested using 0.25% trypsin and washed with PBS. Then the cells were collected by centrifugation at 800×*g* for 10 min and treated as described by Watkins and Cullen[18]. Briefly, the cells were fixed in ice-cold 2.5% glutaraldehyde in PBS (pH 7.3), rinsed with PBS and post-fixed in 1% osmium tetroxide with 0.1% potassium ferricyanide, dehydrated through a graded series of ethanol (30%–90%) and embedded in Epon (Energy Beam Sciences, Agawam, MA, USA). Semithin (300 nm) sections were cut using a Reichart Ultracut, stained with 0.5% toluidine blue and examined under a light microscope. Ultrathin sections (65 nm) were stained with 1% uranyl acetate and 0.1% lead citrate and examined on a JEM2000EX transmission electron microscope (JEOL, Pleasanton, CA, USA).

Proteasome activity assay
After growing on six-well plates (3×10^5 cells/well) for 24 h, C6 glioma cells were treated with either PBS (control) or 18.5 μmol/L MG-132 for 3, 6, 12, or 24 h at 37 °C. Cells were thoroughly scraped from the culture dishes with a cell scraper and washed with cold PBS. After centrifugation for 10 min at 800×*g*, the cell pellets were suspended in ice-cold buffer (50 mmol/L Tris-HCl, pH 7.5, 20 μmol/L ATP, 5 mmol/L MgCl$_2$, 1 mmol/L dithiothreitol, and 20% glycerol) and homogenized with a Pyrex glass microhomogenizer (20 strokes). The homogenate was centrifuged at 15 000×*g* for 10 min at 4 °C to obtain supernatant. Protein concentration was determined using protein assay kits (Bio-Rad Laboratories). A total of 10 μL (1 μg/μL) of each freshly made supernatant was incubated in a 96-well plate at 37 °C for 30 min with 10 μL of 300 μmol/L of Succinyl-LLVY-AMC (Calbiochem, San Diego, CA, USA) and 85 μL of assay buffer (20 mmol/L Tris-HCl, pH 7.5, and 20% glycerol). Release of fluorescent AMC was measured with a spectrofluorometer (Perkin-Elmer Life and Analytical Sciences, Inc, Wellesley, MA, USA) at 440 nm with an excitation wavelength of 380 nm.

Measurement of intracellular ROS levels
The average level of intracellular ROS in C6 glioma cells was evaluated in cells loaded with the redox-sensitive dye DCFH-DA (Molecular Probes, OR, USA). Cells treated with 18.5 μmol/L MG-132 alone were examined at 3, 6, 12, or 24 h; cells

pretreated with 1.0 mmol/L tiron before incubation with 18.5 µmol/L MG-132 were examined at 24 h. The cells treated with PBS were used as control. All experimental cells were washed twice in phosphate-buffered saline (PBS) and stained in the dark for 30 min with 20 µmol/L DCFH-DA and harvested. Cells were dissolved with 1% Triton X-100, and fluorescence was measured at an excitation wavelength of 485 nm and an emission wavelength 530 nm using a fluorescence spectrometer (HTS 7000, Perkin Elmer, Boston, MA, USA). ROS levels were expressed as arbitrary units/mg protein, then as a percentage of controls.

Detection of apoptosis and cell cycle

After 12 h of starvation in serum free DMEM/F12, C6 glioma cells were treated with 18.5 µmol/L MG-132 for 24 h or pretreated with 1.0 mmol/L tiron prior to 24 h incubation with 18.5 µmol/L MG-132. Cells treated with PBS were used as controls. Then, all the cells were washed with PBS, counted and adjusted to 1×10^6 cells/mL. The cells were fixed in 70% ethanol at 4 °C overnight, treated with 100 mg/L RNase at 37 °C for 30 min and stained with 50 mg/L propidium iodide (Sigma) for 30 min. The cells were analyzed using flow cytometry (FAC2Scan, Becton Dickinson, San Jose, CA, USA). The rate of apoptosis and cell cycle status were analyzed using CELLquest software (Becton Dickinson). Data were acquired by collecting 20 000 cells per tube; the numbers of viable and apoptotic cells were determined for each experimental condition.

Western blotting

C6 glioma cells were cultured, harvested and washed as described above. After centrifugation for 10 min at 1000×*g*, the cell pellets were suspended in ice-cold buffer (15 mmol/L Tris, pH 7.6, 250 mmol/L sucrose, 1 mmol/L MgCl₂, 2.5 mmol/L EDTA, 1 mmol/L EGTA (ethylene glycol-*bis* (b-amino ethyl-ether) tetraacetic acid), 1 mmol/L dithiothreitol, 1.25 mg/mL pepstatin A, 10 mg/mL leupeptin, 2.5 mg/mL aprotinin, 1.0 mmol/L phenylmethylsulfonyl fluoride (PMSF), 0.1 mmol/L Na₃VO₄, 50 mmol/L NaF, and 2.0 mmol/L Na₄P₂O₇) and homogenized with a Pyrex glass microhomogenizer (20 strokes). Homogenates were centrifuged at 10 000×*g* at 4 °C for 10 min to obtain supernatant. The protein content of the supernatant was determined using Bio-Rad protein assay kits.

Equal amounts of protein were electrophoresed on 10% sodium dodecyl sulfate-polyacrylamide gels and then transferred to PVDF membranes. The membranes were blocked with 3% bovine serum albumin in TBS for 30 min and then incubated overnight at 4 °C with the following primary antibodies: caspase-3, Bax, Bcl-2, XIAP, PARP, PARP/85, and β-actin. After being incubated with horseradish peroxidase-conjugated anti-rabbit IgG or anti-mouse IgG, the blots were washed, and immunoreactive proteins were visualized on Kodak X-omat LS film (Eastman Kodak Company, New Haven, CT, USA) with an enhanced chemiluminescence kit (Amersham Biosciences, Piscataway, NJ, USA). Densitometry was performed with Kodak ID image analysis software (East-

man Kodak Company).

Statistical analysis

All data represent at least 4 independent experiments and are expressed as the mean±SD. Statistical comparisons were made using Student's *t*-test. *P* values of less than 0.05 were considered significant.

Results

MG-132 inhibited C6 glioma cell proliferation and inhibited proteasome chymotrypsin-like activity

MG-132 significantly reduced the viability of C6 glioma cells beginning at 6 h in both time- and concentration-dependent manners (Figure 1A). At 24 h, the inhibitory effect reached a maximum, with inhibition rates of 23%, 45%, 73%, and 90% at concentrations of 10, 20, 30, and 40 µmol/L, respectively. The IC_{50} of MG-132 at 24 h was 18.5 µmol/L. Then, we assayed the inhibitory effect of 18.5 µmol/L MG-132 on proteasomal chymotrypsin-like activity using Succinyl-LLVY-AMC as a specific substrate[18]. MG-132 gradually inhibited enzymatic activity from 3 to 24 h (*P*<0.01, Figure 1B). This result suggested that 18.5 µmol/L MG-132 could effectively suppress proteasome activity and that proteasome inhibition occurred earlier (3 h) than that of viability reduction (6 h).
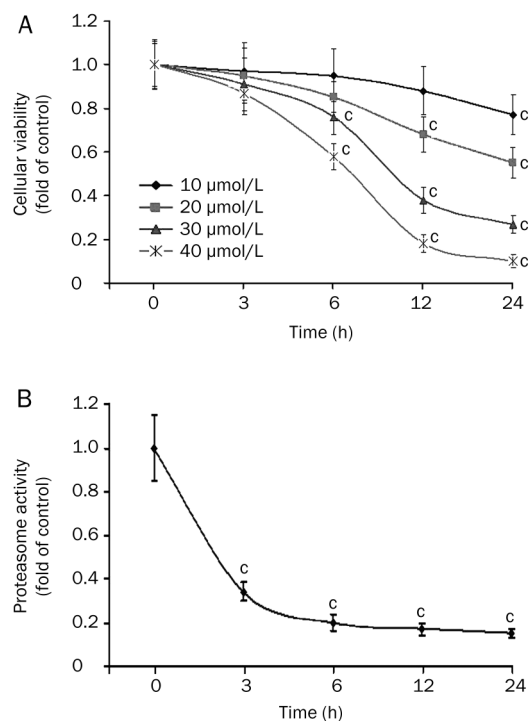
Figure 1. Cellular viability assay and proteasome activity assay. (A) MTT assay of cell viability. The proliferation of C6 glioma cells was inhibited after 3 h incubation with MG-132; at 24 h, the maximal inhibitory effect was reached. (B) Proteasome activity assay. Proteasome activity in C6 glioma cells was significantly inhibited at 3 h by 18.5 µmol/L MG-132. (*P*<0.01 *vs* control group).
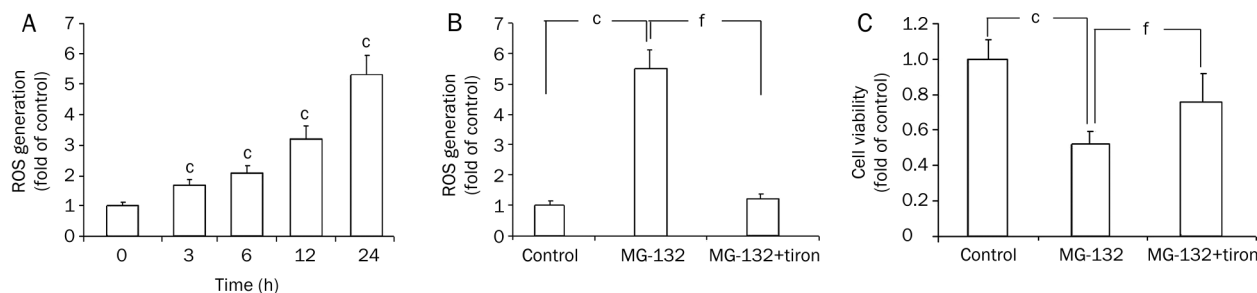
Figure 2. MG-132-induced oxidative stress. (A) ROS was generated in the MG-132-treated (18.5 µmol/L) C6 glioma cells at 3 h, increasing continuously to a peak at 24 h. When tiron (1 mmol/L) was used, ROS generation was blocked (B), and the viability of C6 glioma cells also increased significantly (C). Mean±SD. *n*=4. [c]*P*<0.01 *vs* control group, [f]*P*<0.01 *vs* MG-132 group.

Tiron blocked MG-132-induced oxidative stress

Compared with control cells, the ROS generated by MG-132 increased in a time-dependent manner in C6 glioma cells from 3 h to 24 h (*P*<0.01, Figure 2A). Then, tiron was used to investigate the relationship between oxidative stress and the viability reduction of C6 glioma cells after these cells were treated with 18.5 µmol/L MG-132 for 24 h. We found that 1.0 mmol/L tiron effectively blocked the generation of ROS (*P*<0.01 *versus* MG-132 group, Figure 2B), but it did not influence the viability of C6 glioma cells (data not shown). Furthermore, pretreatment with tiron significantly attenuated MG-132 (18.5 µmol/L)-induced cell viability reduction (*P*<0.01, Figure 2C), indicating that the effects of MG-132 in C6 glioma cells might be due partly to oxidative stress.

Tiron suppressed MG-132-induced apoptosis and cell cycle arrest

Chromatin accumulation under the nuclear membrane, nuclear condensation and DNA fragmentation were revealed by both fluorescence microscopy and transmission electron microscopy after C6 glioma cells were treated with 18.5 µmol/L MG-132 for 24 h (Figure 3). These morphological features were consistent with the characteristics of apoptosis reported previously[18], indicating that apoptosis was induced by MG-132 in C6 glioma cells. Subsequent examination by flow cytometry showed that tiron suppressed MG-132-induced apoptosis in C6 glioma cells. The apoptosis rate decreased from 30.46% to 20.79%, and the percentage of cells arrested in G_2/M phase was reduced from 17.31% to 12.77% (Figure 4). These results suggest that the apoptosis induced by MG-132 was closely associated with oxidative stress.

Tiron attenuated the expression of apoptosis-related proteins

Previous studies have shown that the expression of apoptotic machinery proteins such as Bcl-2, XIAP (X chromosome-linked inhibitor of apoptosis), Bax, caspase-3, and PARP is altered by oxidative stress[19]. In the present study, Western blot analysis revealed that the expressional level of pro-apoptotic proteins Bax and caspase-3 increased significantly, whereas the expressional level of anti-apoptotic proteins Bcl-2 and XIAP decreased markedly after C6 glioma cells were incubated with 18.5 µmol/L MG-132 for 24 h (Figure 5). However, tiron atten-
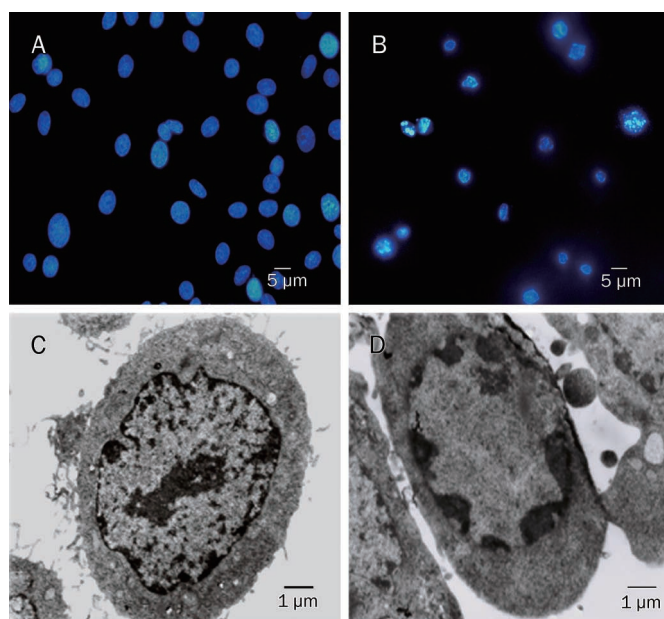
Figure 3. C6 glioma cells displayed apoptotic morphological features after incubation with MG-132. Fluorescence microscopy (A: control group and B: MG-132 group) and transmission electron microscopy (C: control group and D: MG-132 group) showed chromatin condensation, nuclear condensation and nuclear fragmentation in the nucleus of C6 glioma cells treated with MG-132.

uated the MG-132-induced expression patterns of the above-mentioned pro-apoptotic and anti-apoptotic proteins (Figure 5). Meanwhile, tiron significantly reduced the quantity of cleaved PARP as well (Figure 5). These results indicated that tiron rescues MG-132-induced apoptosis in C6 glioma cells by influencing the expression of apoptosis-related proteins.

Discussion

In this study, we found that MG-132, a competitive inhibitor of proteasome chymotrypsin-like activity, induces apoptosis of C6 glioma cells via oxidative stress. We found that proteasome activity is increased in malignant cells derived from different types of cancer as compared with normal cells[20], indi-
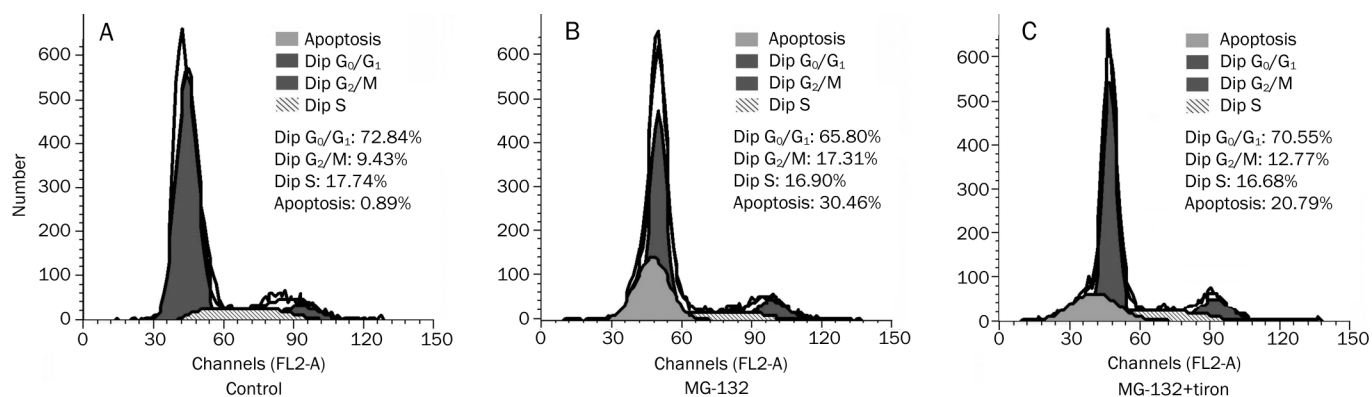
Figure 4. Tiron suppressed apoptosis and cell cycle arrest induced by MG-132. Flow cytometry analysis of apoptotic rate and cell cycle. In the control group (A), the apoptotic rate was 0.89%, and the percentage of the cells in G_2/M phase was 9.43%. Tiron effectively suppressed the increase of apoptosis rate (from 30.46% to 20.79%) and cell cycle arrest in G_2/M phase (from 17.31% to 12.77%) induced by MG-132 (B and C).

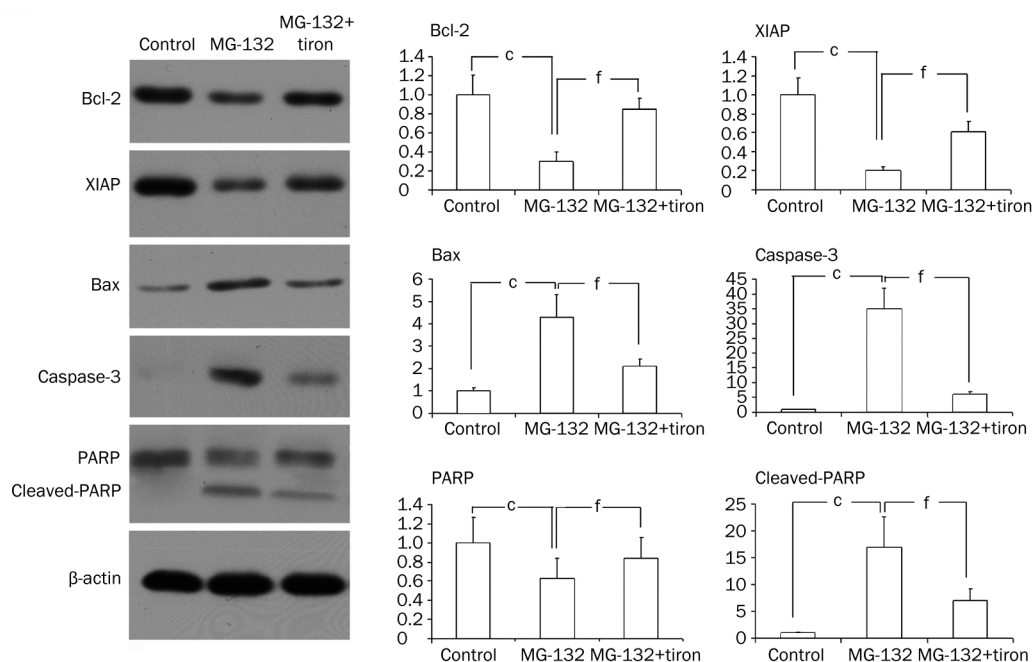**Figure 5.** Tiron altered the expression of apoptosis-related proteins. Western blot analysis revealed that MG-132 induced down-regulation of anti-apoptotic proteins Bcl-2 and XIAP, up-regulated expression of pro-apoptotic protein Bax and caspase-3, and produced cleaved C-terminal 85 kDa PARP. Additionally, tiron reversed these alterations. $^{c}P<0.01$ *vs* control; $^{f}P<0.01$ *vs* MG-132 group.

cating that malignant cells have a need for higher proteasome activity. Therefore, proteasome inhibition would theoretically exert fatal effects on malignant tumor cells, but not on normal cells.

Although it has been reported that nontoxic proteasome inhibition protected cells from oxidative stress[21], our results showed that proteasome inhibitor MG-132 at toxic concentrations could generate oxidative stress and induce apoptosis in glioma cells. Oxidative stress has been demonstrated to be closely associated with cellular death in various tumor cells[9, 16, 22]. Studies investigating the relationship between oxidative stress and apoptosis have indicated that oxidative stress may be a precursor to apoptosis in C6 glioma cells[23, 24]. In the present study, we found that selective inhibition of proteasome activity by MG-132 produced a cause-effect relationship

between oxidative stress and apoptosis in rat C6 glioma cells.

Although we did not further investigate the mechanism underlying the oxidative stress produced via the inhibition of proteasome activity, previous reports showed that abnormal or unfolded intracellular proteins would aggregate if they could not be degraded via the proteasome pathway, leading to the generation of reactive oxygen species, the most prominent marker of oxidative stress[25].

In addition, the present study showed that blocking oxidative stress with the anti-oxidant tiron attenuated the decreased expression of Bcl-2 and XIAP, both of which are not only anti-apoptotic factors but also function as regulators of anti-oxidants[26, 27]. Bcl-2 increases cellular resistance to H_2O_2 by increasing glutathione levels and Cu/Zn-superoxide dismutase (SOD1) activity[28]. XIAP induces up-regulation of at

least three antioxidants residing in mitochondria, including superoxide dismutase 2, thioredoxin 2 and lysine oxoglutarate reductase[29]. Therefore, decreased expression of Bcl-2 and XIAP would exacerbate the severity of oxidative stress caused by MG-132, forming a malignant feedback loop.

In addition to our findings on the alterations of anti-apoptotic and pro-apoptotic proteins in the present study, previous studies have revealed some typical features of apoptosis when glioma cells were treated with different proteasome inhibitors. It has been reported that MG-132 could trigger cytochrome *c* release and disruption of mitochondrial membrane potential, which were concurrent with DNA breaks and loss of membrane integrity. Further studies showed that proteasome inhibitor-induced apoptosis was dependent on caspases because multiple caspases such as caspase 2, 3, 7, 8, and 9 were activated and apoptosis was inhibited when glioma cells were exposed to the broad-spectrum caspase inhibitor zVAD-fmk (benzoyl-VAD-fluoromethyl ketone). Additionally, proteasome inhibitors could reduce the transcriptional activity and expression level of anti-apoptotic nuclear NF-kappaB[30]. These findings indicated that inhibition of proteasome activity is an effective strategy for inducing apoptosis in glioma cells.

Proteasome inhibitors could also activate intracellular signaling pathways. However, activation of the PI3K/AKT pathways impaired the response of tumor cells to proteasome inhibitor treatment, and inhibition of the PI3K/AKT pathways increased the antitumor effects of proteasome inhibitors[31]. By contrast, activation of the JNK/c-Jun pathway was closely associated with growth inhibition in human glioblastoma cells[5].

In addition to biochemical changes, morphological alteration is an important criterion for evaluating apoptosis. As described previously[18], apoptotic changes in morphology such as chromatin accumulation, nuclear condensation and DNA fragmentation were observed in the present study. Moreover, dilated rough endoplasmic reticulum (ER), dense mitochondrial deposits and cytoplasmic vacuolization could be found when proteasome activity was inhibited[30]. Interestingly, these non-apoptotic alterations could still exist even if zVAD-fmk was used to block apoptosis, indicating that proteasome inhibition might lead to cellular death via another mechanism.

In summary, we showed that inhibition of proteasome activity by MG-132 is an effective way to suppress the proliferation of C6 glioma cells via the induction of apoptosis. Tiron not only blocked the oxidative stress caused by MG-132 but also suppressed MG-132-induced apoptosis by decreasing the expression of Bax and caspase-3, rescuing the expression of Bcl-2 and XIAP and attenuating PARP cleavage. These results suggest that there is a cause and effect relationship between oxidative stress and apoptosis induced by MG-132. Although the present study demonstrated that the inhibition of proteasome activity induced apoptosis in C6 glioma cells via oxidative stress, further research is needed to evaluate this phenomenon on solid gliomas *in vivo*.

Author contribution

Prof Yi-nan LUO and Dr Peng-fei GE designed the research; Wen-hai FAN, Yi HOU, and Fan-kai MENG performed the research; Xiao-fei WANG analyzed data; and Peng-fei GE wrote the paper.

References

1 Rubinsztein DC. The roles of intracellular protein-degradation pathways in neurodegeneration. Nature 2006; 443: 780–6.

2 Hershko A. The ubiquitin system for protein degradation and some of its roles in the control of the cell division cycle. Cell Death Differ 2005; 12: 1191–7.

3 Sorolla A, Yeramian A, Dolcet X, de Santos AMPérez, Llobet D, Schoenenberger JA, *et al*. Effect of proteasome inhibitors on proliferation and apoptosis of human cutaneous melanoma-derived cell lines. Br J Dermatol 2008; 158: 496–504.

4 Momose I, Iijima M, Kawada M, Ikeda D. A new proteasome inhibitor, TP-110, induces apoptosis in human prostate cancer PC-3 cells. Biosci Biotechnol Biochem 2007; 71: 1036–43.

5 Yin D, Zhou H, Kumagai T, Liu G, Ong JM, Black KL, *et al*. Proteasome inhibitor PS-341 causes cell growth arrest and apoptosis in human glioblastoma multiforme (GBM). Oncogene 2005; 24: 344–54.

6 Legnani FG, Pradilla G, Thai QA, Fiorindi A, Recinos PF, Tyler BM, *et al*. Lactacystin exhibits potent anti-tumor activity in an animal model of malignant glioma when administered via controlled-release polymers. J Neurooncol 2006; 77: 225–32.

7 Yuan BZ, Chapman J, Reynolds SH. Proteasome inhibitors induce apoptosis in human lung cancer cells through a positive feedback mechanism and the subsequent Mcl-1 protein cleavage. Oncogene 2009; 28: 3775–86.

8 Ge PF, Zhang JZ, Wang XF, Meng FK, Li WC, Luan YX, *et al*. Inhibition of autophagy induced by proteasome inhibition increases cell death in human SHG-44 glioma cells. Acta Pharmacol Sin 2009; 30: 1046–52.

9 Cvorovic J, Tramer F, Granzotto M, Candussio L, Decorti G, Passamonti S. Oxidative stress-based cytotoxicity of delphinidin and cyanidin in colon cancer cells. Arch Biochem Biophys 2010; 501: 151–7.

10 Yu JW, Yang R, Kim YS. Differential cytoprotective effect of copper- and iron-containing chlorophyllins against oxidative stress-mediated cell death. Free Radic Res 2010; 44: 655–67.

11 Wu WT, Chi KH, Ho FM, Tsao WC, Lin WW. Proteasome inhibitors up-regulate haem oxygenase-1 gene expression: requirement of p38 MAPK (mitogen-activated protein kinase) activation but not of NF-kappaB (nuclear factor kappaB) inhibition. Biochem J 2004; 379: 587–93.

12 Cao C, Leng Y, Liu X, Yi Y, Li P, Kufe D. Catalase is regulated by ubiquitination and proteosomal degradation. Role of the c-Abl and Arg tyrosine kinases. Biochemistry 2003; 42: 10348–53.

13 Hoffman EK, Wilcox HM, Scott RW, Siman R. Proteasome inhibition enhances the stability of mouse Cu/Zn superoxide dismutase with mutations linked to familial amyotrophic lateral sclerosis. J Neurol Sci

1996; 139: 15–20.

14 Yamamoto N, Sawada H, Izumi Y, Kume T, Katsuki H, Shimohama S, *et al*. Proteasome inhibition induces glutathione synthesis and protects cells from oxidative stress: relevance to Parkinson disease. J Biol Chem 2007; 282: 4364–72.

15 Ding Q, Dimayuga E, Keller JN. Proteasome regulation of oxidative stress in aging and age-related diseases of the CNS. Antioxid Redox Signal 2006; 8: 163–72.

16 Du ZX, Zhang HY, Meng X, Guan Y, Wang HQ. Role of oxidative stress and intracellular glutathione in the sensitivity to apoptosis induced by proteasome inhibitor in thyroid cancer cells. BMC Cancer 2009; 9: 56.

17 Kim JS, Cho EW, Chung HW, Kim IG. Effects of Tiron, 4, 5-dihydroxy-1, 3-benzene disulfonic acid, on human promyelotic HL-60 leukemia cell differentiation and death. Toxicology 2006; 223: 36–45.

18 Watkins SC, Cullen MJ. A qualitative and quantitative study of the ultrastructure of regenerating muscle fibres in Duchenne muscular dystrophy and polymyositis. J Neurol Sci 1987; 82: 181–92.

19 Jungas T, Motta I, Duffieux F, Fanen P, Stoven V, Ojcius DM. Glutathione levels and BAX activation during apoptosis due to oxidative stress in cells expressing wild-type and mutant cystic fibrosis transmembrane conductance regulator. J Biol Chem 2002, 277: 27912–8.

20 Chen L, Madura K. Increased proteasome activity, ubiquitinconjugating enzymes, and eEF1A translation factor detected in breast cancer tissue. Cancer Res 2005; 65: 5599–606.

21 Meiners S, Ludwig A, Lorenz M, Dreger H, Baumann G, Stangl V, *et al*. Nontoxic proteasome inhibition activates a protective antioxidant defense response in endothelial cells. Free Radic Biol Med 2006; 40: 2232–41.

22 Li GX, Chen YK, Hou Z, Xiao H, Jin H, Lu G, *et al*. Pro-oxidative activities and dose-response relationship of (–)-epigallocatechin-3-gallate in the inhibition of lung cancer cell growth: a comparative study *in vivo*

and *in vitro*. Carcinogenesis 2010; 31: 902–10.

23 Wätjen W, Beyersmann D. Cadmium-induced apoptosis in C6 glioma cells: influence of oxidative stress. Biometals 2004; 17: 65–78.

24 Chen TJ, Jeng JY, Lin CW, Wu CY, Chen YC. Quercetin inhibition of ROS-dependent and -independent apoptosis in rat glioma C6 cells. Toxicology 2006; 223: 113–26.

25 Tabner BJ, El-Agnaf OM, German MJ, Fullwood NJ, Allsop D. Protein aggregation, metals and oxidative stress in neurodegenerative diseases. Biochem Soc Trans 2005; 33: 1082–6.

26 Hockenbery DM, Oltvai ZN, Yin XM, Milliman CL, Korsmeyer SJ. Bcl-2 functions in an antioxidant pathway to prevent apoptosis. Cell 1993; 75: 241–51.

27 Zhu C, Xu F, Fukuda A, Wang X, Fukuda H, Korhonen L, *et al*. X chromosome-linked inhibitor of apoptosis protein reduces oxidative stress after cerebral irradiation or hypoxia-ischemia through up-regulation of mitochondrial antioxidants. Eur J Neurosci 2007; 26: 3402–10.

28 Lee M, Hyun DH, Marshall KA, Ellerby LM, Bredesen DE, Jenner P, *et al*. Effect of overexpression of BCL-2 on cellular oxidative damage, nitric oxide production, antioxidant defenses, and the proteasome. Free Radic Biol Med 2001; 31: 1550–9.

29 Resch U, Schichl YM, Sattler S, de Martin R. XIAP regulates intracellular ROS by enhancing antioxidant gene expression. Biochem Biophys Res Commun 2008; 375: 156–61.

30 Wagenknecht B, Hermisson M, Groscurth P, Liston P, Krammer PH, Weller M. Proteasome inhibitor-induced apoptosis of glioma cells involves the processing of multiple caspases and cytochrome c release. J Neurochem 2000; 75: 2288–97.

31 Sloss CM, Wang F, Liu R, Xia L, Houston M, Ljungman D, *et al*. Proteasome inhibition activates epidermal growth factor receptor (EGFR) and EGFR-independent mitogenic kinase signaling pathways in pancreatic cancer cells. Clin Cancer Res 2008; 14: 5116–23.

Original Article

Effective combination of aligned nanocomposite nanofibers and human unrestricted somatic stem cells for bone tissue engineering

Behnaz BAKHSHANDEH[1, 2], Masoud SOLEIMANI[3, *], Nasser GHAEMI[4], Iman SHABANI[2]

[1]Department of Biotechnology, College of Science, University of Tehran, Tehran, Iran; [2]Stem Cell Biology Department, Stem Cell Technology Research Center, Tehran, Iran; [3]Department of Hematology, Faculty of Medical Sciences, Tarbiat Modares University, Tehran, Iran; [4]School of Chemistry, College of Science, University of Tehran, Tehran, Iran

Aim: Bioartificial bone tissue engineering is an increasingly popular technique to solve bone defect challenges. This study aimed to investigate the interactions between matrix composition and appropriate cell type, focusing on hydroxyapatite (HA), to achieve a more effective combination for bone regeneration.
Methods: Human unrestricted somatic stem cells (USSCs) were isolated from placental cord blood. The cellular and molecular events during the osteo-induction of USSCs were evaluated for 21 d under the following conditions: (1) in basal culture, (2) supplemented with hydroxyapatite nanoparticle (nHA) suspension, and (3) seeded on electrospun aligned nanofibrous poly-ε-caprolactone/poly-*L*-lactic acid/nHA (PCL/PLLA/nHA) scaffolds. The scaffolds were characterized using scanning electron microscope (SEM), fourier transform infrared spectroscopy (FTIR) and tensile test.
Results: Maintenance of USSCs for 21 d in basal or osteogenic culture resulted in significant increase in osteoblast differentiation. With nHA suspension, even soluble osteo-inductive additives were ineffective, probably due to induced apoptosis of the cells. In contrast to the hindrance of proliferation by nHA suspension, the scaffolds improved cell growth. The scaffolds mimic the nanostructure of natural bone matrix with the combination of PLLA/PCL (organic phase) and HA (inorganic phase) offering a favorable surface topography, which was demonstrated to possess suitable properties for supporting USSCs. Quantitative measurement of osteogenic markers, enzymatic activity and mineralization indicated that the scaffolds did not disturb, but enhanced the osteogenic potential of USSCs. Moreover, the alignment of the fibers led to cell orientation during cell growth.
Conclusion: The results demonstrated the synergism of PCL/PLLA/nHA nanofibrous scaffolds and USSCs in the augmentation of osteogenic differentiation. Thus, nHA grafted into PCL/PLLA scaffolds can be a suitable choice for bone tissue regeneration.

Keywords: human unrestricted somatic stem cells; electrospun aligned nanofibrous poly-ε-caprolactone/poly-*L*-lactic acid/nHA scaffolds; bone regeneration; tissue engineering

Introduction

Bone defects caused by injury or disease are one of the major health concerns of human society. Current practice mainly relies on tissue repair by autograft and allograft or application of synthetic bone implants[1, 2]. However, many limitations, such as donor morbidity, limited availability of tissue suppliers, potent immune response, disease transfer, or insufficient bioactivity, have led this field to tissue engineering as an excellent alternative approach[3–7].

Cell transplantation in combination with supportive matrices for re-establishment of altered constructs is emerging as a new strategy for bone tissue engineering[2, 8, 9]. Unique features such as high porosity with proper interconnections, large surface area and enhanced recruiting of cells make nanofibrous scaffolds suitable for tissue engineering[10, 11]. Because of the importance of nano-sized structures of the extracellular matrix (ECM) in the regulation of many cell functions, scaffolds with nanoscale morphology have been vigorously studied[9, 10]. In this regard, developing nanofibrous scaffolds that mimic the architecture of tissue at the nanoscale can potentially meet this challenge[12]. Irrespective of the method of synthesis, nanofibers have been used as scaffolds for musculoskeletal tissue engineering (including bone, cartilage, ligament, and skeletal

muscle), vascular tissue engineering, and skin tissue engineering, as well as carriers for proteins and DNA[2, 4].

Electrospinning is one of the most broadly considered techniques to process polymeric biomaterials into nanofibers. Control over the thickness and composition of the porous nanofibers is an important aspect of this technique[10].

Hydroxyapatite (HA) composites have received a great deal of attention for bone regeneration because they possess excellent biodegradability, biocompatibility, osteoconductivity and direct bone-binding capability[1, 3]. Yang *et al*[13] demonstrated that the incorporation of HA into PCL/gelatin nanofibers enhanced dental pulp stem cell differentiation toward an odontoblast-like phenotype *in vitro* and *in vivo*. Osteogenic induction properties of HA has also been proven using goat and rat MSCs[14, 15]. Finally, it has been shown that incorporation of HA nanofibers as a second component in β-tricalcium phosphate significantly improves the mechanical strength of composite scaffolds[16].

However, owing to brittleness and poor mechanical stability, the use of HA without additional ingredients is limited[17]. As a solution, HA has been blended with poly-ε-caprolactone (PCL) and poly-*L*-lactic acid (PLLA). To overcome the possible masking of hydroxyapatite nanoparticle (nHA) osteoinductive properties due to it being embedded inside the polymer, the electrospun nanofiber technique has been strongly suggested[11].

PCL is a synthetic, biodegradable polymer with a slow degradation rate[5]. It has been used in fields such as skin tissue engineering and axonal regeneration and as a support for fibroblast and osteoblast growth[18]. It has been reported that adhesion and proliferation of fibroblasts and protein adsorption are improved in PCL/HA scaffolds compared to unmodified HA and pure PCL controls[19]. Yoshimoto *et al*[20] have reported that mesenchymal stem cells (MSCs) seeded on electrospun PCL scaffolds migrated inside the scaffold and produced a rich extracellular matrix. Shin *et al*[21] replicated this experiment in a rat model and demonstrated ECM production all over the scaffold, along with mineralization and osteogenic differentiation.

PLLA, the *L*-form of poly-lactic acid (PLA), is an FDA-approved polyester that has been studied extensively as a biodegradable surgical material; however, because of its poor biocompatibility and mechanical properties, its use is limited[8, 22]. The PLLA/HA nanocomposite improves the interface mechanical property and biocompatibility, and it is applied widely for bone fixation materials[23]. Also, incorporation of HA into PLLA enhances protein adsorption and increases the compressive modulus in comparison with pure PLLA scaffolds[24]. In one study, mouse fibroblasts cultured on PLLA/HA scaffolds showed a reduction in the inflammatory response compared with pure PLLA[25].

The stress-shielding problem is a result of elastic modulus mismatch between metallic materials and natural bone. Consequently, creation of polymer-ceramic composites that match the modulus of bone more closely has been suggested as a solution[26]. In one study, researchers successfully produced PLLA/HA/PCL composites with flexural moduli near the lower range of bone[27]. Hence, various nanofibers of chitosan/HA, PCL/collagen/HA, PCL/gel/HA, gel/HA, PCL/HA/gel, PCL/HA, and PHBV/HA have been generated for bone tissue engineering[28–32].

In this study, both the cell type that was loaded and the scaffold composition were important factors to consider when attempting to achieve a more effective combination for bone tissue regeneration. In previous reports on bone tissue engineering, hMSCs, preosteoblast cell lines and human osteoblasts have been routinely cultured. In contrast to adult bone marrow, human unrestricted somatic stem cells (USSCs) are less mature, with an extended length of life and longer telomeres. In addition to these biological advantages, USSCs are abundantly available and routinely harvested without risk to the donor[33–35].

This adherent HLA class II and CD45–negative stem cell can be stimulated to differentiate into bone, cartilage, hematopoietic cells, neural cells, liver and heart[2, 34]. It is worth noting that spontaneous differentiation of USSCs into osteoblasts has been demonstrated[36]. As a result, a USSC-based tissue engineering strategy seems to be an ideal approach for bone regeneration. However, the effect of nHA-containing nanofibers on differentiation and mineralization of USSCs has yet to be investigated.

We electrospun blends of nHA with both PCL and PLLA to create an *in vitro* environment that resembles the lowest level of hierarchical organization of bone for tissue engineering. The dispersion and effects of nHA on the tensile and morphological properties of nanofibers were investigated. In addition, the effects of PLLA/PCL/nHA nanofibers or an nHA suspension on the proliferation and osteogenic differentiation of USSCs were assessed.

Materials and methods
Materials
PCL (M_n=80), PLLA (M_n=99), and nHA were obtained from Sigma-Aldrich. The solvents *N*,*N*-dimethylformamide (DMF) and chloroform were purchased from Merck. All other chemicals were purchased from Sigma Co (St Louis, MO, USA) and used as received, unless stated otherwise.

Cell seeding
Collection, isolation and propagation of human USSCs were performed as described by Kogler *et al*[34]. Growth and expansion of the cells were performed in high glucose Dulbecco's modified Eagle's medium (DMEM) supplemented with 10% fetal bovine serum and 1% antibiotic (100 U/mL penicillin) under a humidified atmosphere of 95% air with 5% CO_2 at 37 °C. USSCs were cultured in 3 groups (6 subgroups) as described in Table 1. Five duplicate wells were prepared for each sample. Prior to cell seeding, scaffolds were placed in 4-well tissue culture polystyrene (TCPS) and sterilized in 70% ethanol. The scaffolds were then incubated with basal medium overnight to facilitate cell attachment. An initial cell density of 10^4 cm^{-1} was used for all groups. The average size of

Table 1. Description of different media of USSC cultivation.

Group	Subgroup	Matrix	Media	Additional material
1	TCPS	4-well plate	High glucose DMEM, FBS	–
	Osteo-TCPS	4-well plate	Osteo-inductive media	–
2	Osteo-nHA	4-well plate	Osteo-inductive media	HA nanoparticle suspension
	nHA	4-well plate	High glucose DMEM, FBS	HA nanoparticle suspension
3	Scaffold	HA scaffold	High glucose DMEM, FBS	–
	Osteo-Scaffold	HA scaffold	Osteo-inductive media	–

* tissue culture polystyrene.

the nHA was less than 200 nm. For group 2, after the cells had anchored to the plates, the culture medium was replaced with an nHA suspension (500 mg/L). The medium was exchanged twice a week.

Fabrication of nanofibrous scaffolds

We constructed PCL/PLLA and PCL/PLLA/nHA nanofibrous webs by electrospinning. Electrospinning solutions were prepared by dissolving PCL to a concentration of 8% (*w/w*) and PLLA to a concentration of 4% (*w/w*) in a solvent mixture of chloroform and DMF (8:2, *v/v*). For PCL/PLLA/nHA scaffolds, nHA (20% of polymer weight (*w/w*)) was dispersed in chloroform to form a suspension, and then the polymer was dissolved in the suspension. Finally, the second solvent (DMF) was added, and the mixture was homogenized by stirrer and ultrasonic homogenizer. A 10 mL disposable syringe was used to stock each of the prepared solutions. Two syringe pumps were used to feed the solutions through extension tubes capped with blunted 21-gauge needles. The collecting surface consisted of a cylindrical stainless steel collector rotating at 2300 revolutions per minute. The collector was located a fixed distance (15 cm) from the needle. A high voltage potential (20 kV) was also applied between the needle and the collector. The polymer solution was forced through the needle and collected as nanofibers on the rotating cylinder. The aligned nanofibrous membranes were separated from the collector surface and used for further analysis and application. Oxygen plasma treatment was performed by a low frequency plasma generator of 44 kHz frequency with a cylindrical quartz reactor (Diener Electronics, Germany). Pure oxygen was introduced into the reaction chamber at 0.4 mbar pressure, and then the glow discharge was ignited for 3 min.

Cell and fiber morphology

For the evaluation of nanofiber morphology, the specimens were gold coated using a sputter coater and then scanned by a scanning electron microscope (SEM, LEO 1455VP, Cambridge, UK). The fiber diameter was determined from SEM images using image analysis software (imageJ, NIH, USA). The cell-loaded scaffolds were rinsed with PBS after 14 d of culture and fixed in 2.5% glutaraldehyde for 1 h. For dehydration, the cell-loaded scaffolds were placed in a gradient series of increasing alcohol concentrations and then dried. Then, as for the pure

scaffold, they were gold coated and scanned by SEM.

Mechanical properties

The tensile properties were measured on the electrospun PCL/PLLA and PCL/PLLA/nHA nanofibrous webs in the parallel direction using Galdabini testing equipment. Prepared scaffolds were cut into 10 mm×50 mm×0.12 mm specimens and the tensile test was conducted at 20 mm/min crosshead speed at room temperature.

ATR-FTIR spectroscopy

Fourier transform infrared (FTIR) spectroscopy was performed to investigate the incorporation of nHA into the electrospun nanofibers. FTIR spectra were obtained with an Equinox 55 spectrometer (Bruker Optics, Germany) with a resolution of 2 cm^{-1}.

Osteogenic differentiation

For induction of USSCs into osteoblasts, the growth medium was supplemented with 250 nmol/L dexamethasone, 50 µg/mL ascorbic acid 2-phosphate, and 10 mmol/L beta-glycerol phosphate.

Differential staining

To determine calcium deposition, cultured cells were treated with alizarin red S. Briefly, samples were rinsed in PBS, fixed with 4% paraformaldehyde (1 h, room temperature), washed with PBS and stained with fresh 1% alizarin red S, pH 4.1, for 10 min at room temperature. Wells were then rinsed with a 0.1% HCl solution to remove excess stain and visualized using a light microscope.

Cell proliferation assay

The total protein content of each sample was determined using the Pierce BCA Protein Assay Kit (Thermo Scientific, USA) according to the manufacturer's instructions. After lysis, centrifugation and incubation of the mixture at 37 °C for 30 min, absorbance was measured at 562 nm.

Real–time quantitative RT–PCR

Total cellular RNA was extracted using QIAzol (Qiagen, USA). Synthesis of cDNA was carried out with M-MuLV reverse transcriptase (RT) and random hexamers as primers, accord-

ing to the manufacturer's instructions (Fermentas).

Reaction mixtures for PCR included 2.5 µL cDNA (5 µmol/L), 1×PCR buffer (AMS™, Cinnagen, Iran), 200 µmol/L dNTPs, 0.5 µmol/L of both the forward and the reverse primer and 1 U Taq DNA polymerase (Fermentas, MD, USA). PCR amplification was performed using a standard procedure with denaturation at 94 °C for 15 s, annealing at 53–61 °C (depending on the primers) for 30 s, and extension at 72 °C for 45 s. The number of cycles varied between 30 and 40, depending on the abundance of the particular mRNA (Table 2). Amplified DNA fragments were electrophoresed on a 2% agarose gel. The gels were stained with ethidium bromide (10 µg/mL) and photographed on a UV trans-illuminator (UVIdoc, UK).

Table 2. Primers used for RT-PCR and quantitative real-time PCR.

Gene	Primer sequences Sense, top; antisense, bottom	Tm (°C)	Size (bp)
Osteonectin	5'-AGGTATCTGTGGGAGCTAATC-3' 5'-ATTGCTGCACACCTTCTC-3'	60	223
BMP-2	5'-TGCGGTCTCCTAAAGGTC-3' 5'-AACTCGAACTCGCTCAGG-3'	60	185
ALPase	5'-GCACCTGCCTTACTAACTC-3' 5'-AGACACCCATCCCATCTC-3'	48	161
HPRT	5'-CCTGGCGTCGTGATTAGTG-3' 5'-TCAGTCCTGTCCATAATTAGTCC-3'	58	125
Osteocalcin	5'-TCACACTCCTCGCCCTATTGG-3' 5'-GATGTGGTCAGCCAACTCGTCA-3'	58	250
Osteopontin	5'-AGTTTCGCAGACCTGACATC-3' 5'-ACCATTCAACTCCTCGCTTTC-3'	54.6	82

For real-time PCR, mixtures of synthesized cDNA, specific primers and a master mix (Maxima, SYBR Green/Fluorescein, Fermentas) were prepared according to the manufacturer's instructions. Measurements were done using a RotorGene 6000 instrument (Corbett), and the data were normalized to an endogenous control gene (HPRT). The relative mRNA expression levels were calculated based on the delta Ct method.

Alkaline phosphatase activity measurement
Levels of alkaline phosphatase activity were determined in cell lysates using *p*-nitrophenyl phosphate as the substrate (Anaspect). The procedure was carried out as recommended by the manufacturer. Briefly, cells growing in 24-well plates (NUNC, Wiesbaden, Germany) were washed with PBS and incubated with 1% Triton X-100 for 30 min at 37 °C. The resulting lysate was then incubated with the substrate and the amount of liberated *p*-nitrophenol (pNP) was measured at 405 nm (Genios plate reader, TECAN). Alkaline phosphatase activity values were normalized to the total protein content.

Calcium content assay
The amount of calcium minerals deposited on TCPS and the scaffolds by USSCs under osteogenic induction was measured

using the cresolphthalein complex one method. Calcium extraction was performed by homogenization of the scaffolds in 0.6 mol/L HCl (Merck) followed by shaking for 4 h at 4 °C. Optical density was measured at 570 nm after the addition of the reagent to the calcium solutions. Calcium content was obtained from a standard curve of concentrations of serial dilutions of calcium versus corresponding *OD*.

Statistical analysis
The Student's *t*-test was used to determine whether there is a significant difference between the groups. To compare the multiple groups, ANOVA test was applied; the difference was regarded as significant if the *P* value was lower than 0.05. Samples were run in triplicate for the biochemical assays and for molecular analysis, if not stated. All data are shown as means±standard deviation (SD).

Results
Morphology and differentiation of USSCs
The morphology of USSCs on TCPS was studied on d 3 and d 21 of cultivation, with or without nHA suspension or osteogenic medium (Figure 1). According to our observations, in dense culture (21-d culture without any passage) USSCs proliferate and produce layers. Alizarin red staining of amorphous calcium deposits revealed strong mineralization in 21 d osteogenic medium induced USSCs while unstimulated USSCs did not show any calcium deposition on d 1 (Figure 2). In this regard, in cells seeded on a scaffold, mineral deposition was noticeable with vividly porous structure composed from the aggregation of globular mineral accretions. Furthermore, PCR analysis of osteogenic marker genes, such as BMP2, ALPase, osteocalcin and osteopontin, confirmed osteogenic differentiation (Figure 3, Table 2). All of these marker genes showed low expression at d 1 in unstimulated USSCs. The schematic
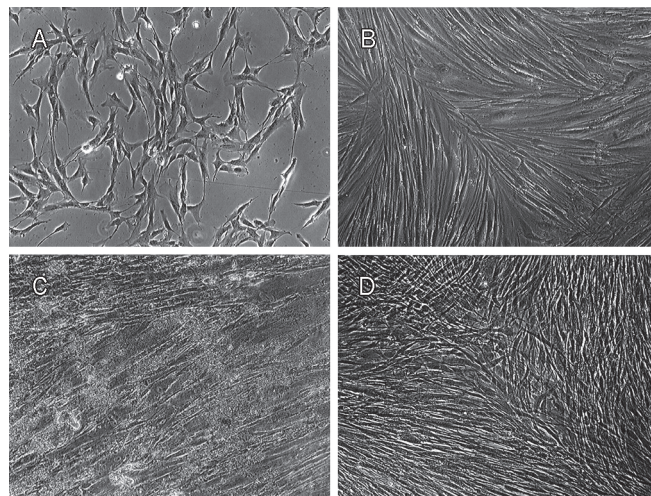
Figure 1. Phase microscopy for USSCs. Spindle-shaped USSCs on TCPS (A) on d 3, (B) Confluent multi-layer fibroblast-like shapes of USSCs on d 21 (self-differentiated), (C) in HA nanoparticle suspension and (D) in osteogenic medium (Bars: 100 µm. Magnification: ×40).
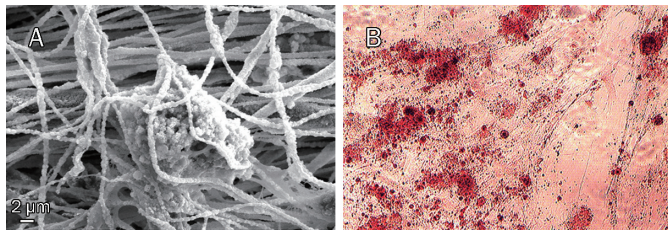
**Figure 2.** (A) Mineral deposition of USSC after 21 d of osteogenic differentiation on scaffold. (B) Alizarin red staining of calcium mineral deposited in the extracellular matrix after 21 d of osteogenic induction on TCPS.
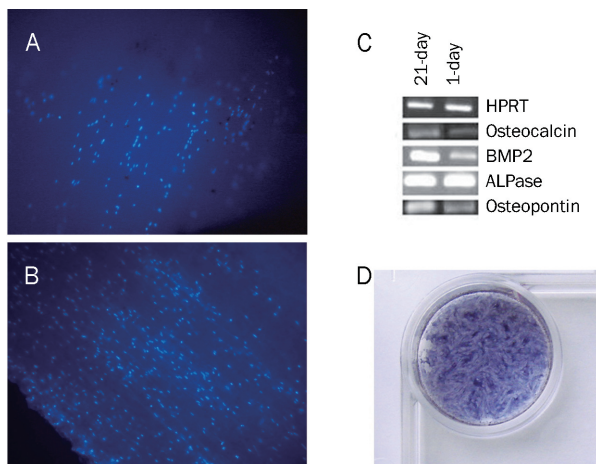
Figure 3. In order to show the high density and alignment of adherent cells on the scaffold, DAPI (4′,6-diamidino-2-phenylindole dilactate, Invitrogen, CA, USA) was utilized for staining the nuclei of the fixed cultured cells (0.25 mL/well of 1 µg/mL DAPI) after 1 d (A) and 7 d (B) for 30 min at room temperature. Photography was done with fluorescence microscope (Motic, Hong Kong, China) at ×100 magnification. (C) Transcription of genes involved in osteogenic differentiation of USSCs. RT-PCR analysis of the expression of genes related to the osteogenic differentiation in 1-d and 21-d cultures on TCPS under osteogenic stimulation. Differentiated USSCs express the osteoblastic phenotype markers osteocalcin, osteopontin, BMP-2 and Alkaline phosphatase. HPRT was measured as internal control. (D) Staining USSCs to demonstrate multilayer proliferation after 21 d of culture by 500 µL of sterile MTT dye (5 mg/mL, incubated for 4 h at 37 °C).

figure of expected multilayer growth of USSCs in nHA suspension culture is represented in Figure 4. Contrary to our expectation, apoptotic cells and cell debris were abundant in cultures containing the nHA suspension (Figure 1).
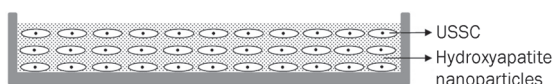
Figure 4. Schematic figure of trapped HA nanoparticle inside the USSCs layers.

Characterization of nanofibers

FTIR spectra of PCL/PLLA nanofibers, PCL/PLLA/nHA composite nanofibers, and nHA are shown in Figure 5. Characteristic peaks at 630 and 1016 cm^{-1} in the spectrum of nHA could be attributed to the vibrations of PO$_4^{3-}$ groups. In the PCL/PLLA/nHA composite scaffold spectrum, the latter peak overlapped with the vibration peak of PCL/PLLA at 1039 cm^{-1}, which leads to a more intense peak in this region. For the PCL/PLLA/nHA scaffold, the vibration peak of nHA near 630 cm^{-1} could be confirmed and did not appear in the case of PCL/PLLA nanofibers.
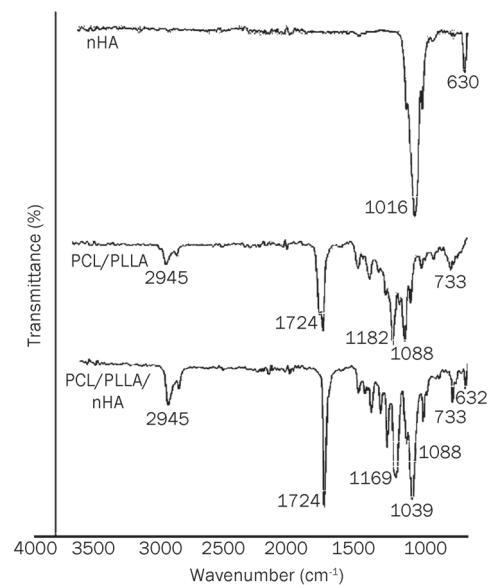
Figure 5. ATR-FTIR spectra of n-HA, PCL/PLLA, and PCL/PLLA/nHA.

PCL/PLLA nanofibers showed tensile strength of about 12 MPa and elongation at break of 55%, which decreased to a tensile strength of 4 MPa and elongation at break of 38% after nHA was blended into the PCL/PLLA/nHA scaffolds (Figure 6).

Moreover, SEM micrographs (Figure 7) of the scaffold revealed an aligned morphology of porous, beadless and nano-scaled fibrous structures formed under controlled condi-
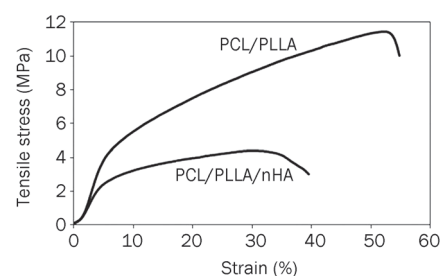
Figure 6. Stress-strain curves of aligned nanofibrous scaffolds along the fiber axis.
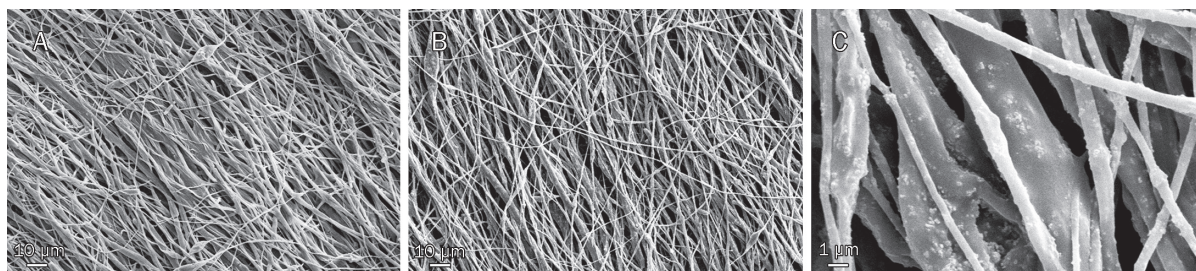
Figure 7. Morphology of fabricated scaffolds, PCL/PLLA (A, ×500), and PCL/PLLA/nHA (B, ×500) and (C, ×5000) nanofibers. As shown in the micrographs, electrospun scaffolds have a bead-free and oriented structure and HA nanoparticles are obvious within fibers. Thicker fibers are blends of PCL/HA and thinners are PLLA/HA.

tions. In addition, nHA appeared to be homogenously dispersed throughout the scaffolds.

Morphology evaluation of seed cells on nanofibers

The capacity of electrospun PCL/PLLA/nHA scaffolds to support the adhesion, proliferation and oriented growth of USSCs was investigated via nucleus staining of 1 d and 7 d cultures with DAPI (Figure 3). On d 1, the USSCs appeared to spread and adhere well, and on d 7 the majority of the scaffold surface was covered by USSCs. In addition, the cells displayed oriented growth along the direction of fiber orientation on d 14, a finding that was also confirmed by SEM (Figure 8).

Figure 8. SEM micrographs of cell seeded nHA scaffolds after 14 d at ×500 (A) and ×2000 (B). It is obviously clear that the orientation of the cultured USSCs is aligned along the nanofibers.

Cell proliferation

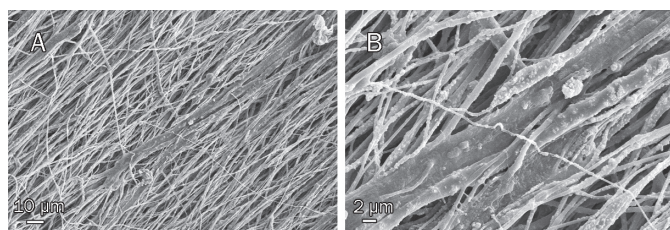We evaluated the effect of PCL/PLLA/nHA composite nanofibers and nHA suspension on the proliferation of USSCs by measuring the total protein contents of cultured USSCs in all mentioned groups on d 1, 7, 14, and 21 of cultivation (Figure 9). The total protein content at d 21 was significantly higher than that on d 7 in all subgroups. Particularly in the TCPS and osteo-TCPS subgroups, the increase in total protein content between d 7 and d 14 was significant. In contrast, the total protein content of each subgroup from d 1 to d 7 did not change considerably. Furthermore, the rates of cell proliferation in the TCPS and osteo-TCPS subgroups were higher compared to the other groups. In addition, the rate of proliferation within group 2 (nHA and osteo-nHA subgroups) was less than that in the other groups.
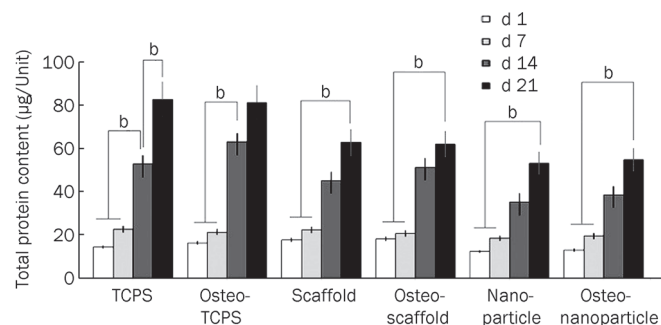
Figure 9. Comparison among total protein contents of USSCs on scaffolds and TCPS during osteogenic differentiation. $^{b}P<0.05$.

ALPase activity measurement

We analyzed ALPase activity to assess the progress of differentiation in all 6 subgroups (Figure 10). As illustrated, the highest ALPase activity belonged to the osteo-scaffold subgroup. Remarkably, the scaffold and osteo-scaffold subgroups demonstrated a decrease in ALPase activity on d 3 when compared to d 1 and d 7; such a decrease was not observed in the other subgroups.

Osteonectin transcription analysis

We assessed osteonectin (ON) transcription quantitatively in all groups on d 7 and d 21. As shown in Figure 11, the scaffold
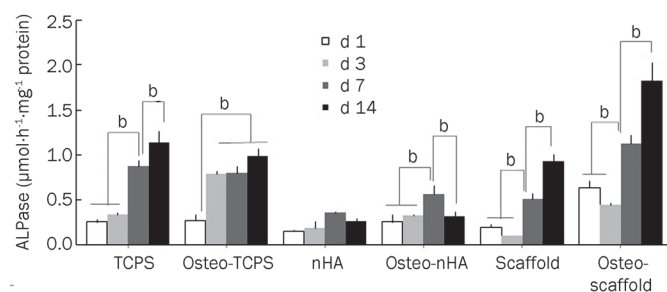
Figure 10. Measurement of alkaline phosphatase (ALPase) activity of USSCs after culturing for 1, 3, 7, 14, and 21 d in different conditions. Normalization is respect to total protein. It is clear that d 14 and osteo-scaffold subgroup have the higher activity of ALPase. $^{b}P<0.05$.

and osteo-scaffold subgroups demonstrated the highest levels on d 21. Conversely, the nHA and osteo-nHA subgroups transcribed osteonectin the least. Also, the transcription of osteonectin on d 21 was collectively higher than that on d 7. Overall, similar increasing trends in ON transcription were observed for all groups.
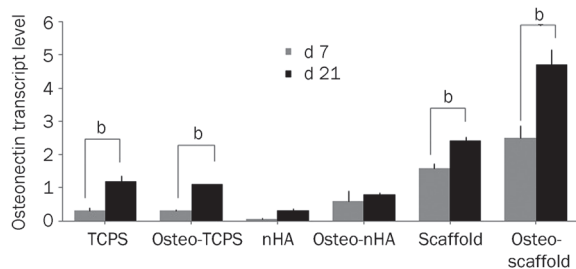
Figure 11. Relative expression of osteonectin on d 1, 3, 7, 14, and 21 in USSC on scaffolds and TCPS in different conditions. Normalization was done in respect to HPRT as an internal control. It is clear that osteo-scaffold subgroup has the highest level of osteonectin transcript. In addition levels of osteonectin transcripts on d 21 is generally higher than d 7. $^{b}P<0.05$.

Calcium content quantity

As the last osteogenic assessment, the calcium deposition (a late bone differentiation marker for the mineralization of USSCs) on d 21 of culture was examined and normalized to the total protein content (Figure 12). We know that calcium ions exist in the chemical structure of the nHA and HA scaffolds. To prevent this inherent calcium from introducing error into our measurements, we subtracted the amount of calcium deposited by the pure HA scaffold (6 μg/scaffold) or nHA suspension (10 μg/well) from related samples before normalization. The results indicate that calcium deposition increased significantly over time. In addition, the osteo-scaffold subgroup deposited the highest amount of calcium in comparison with the others, while the least calcium deposition was detected in the nHA subgroup.

Discussion

An important challenge in the regeneration of large bone
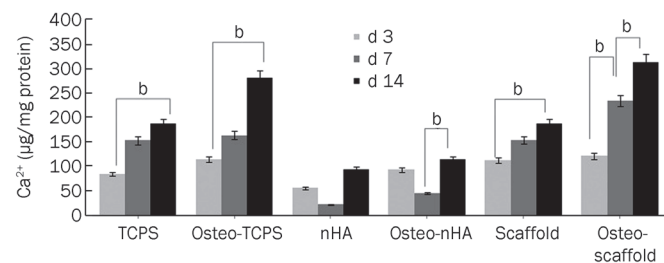
Figure 12. This figure represented the calcium content per total protein of different treatments of USSCs. It is obvious that d 14 has the highest content of calcium precipitate. Both osteo-induction and osteo-scaffold subgroups show the higher value for calcium precipitate. $^{b}P<0.05$.

defects is a sufficient supply of tissue from suitable cells. In order to integrate hard tissue implants into defected bone, appropriate cells must bind to the implant matrices, differentiate, and form a new bone[37–39]. Hence, in this study we investigated both matrix combination and type of cell loaded into the matrix.

One of the most important aspects of bone tissue engineering is the introduction of appropriate cells into the matrices. In this regard, USSCs have unique biological characteristics and are able to undergo extensive replication in culture as well as differentiation under controlled conditions into multiple stromal lineages. USSCs can be considered a preferable alternative, allogenic source to MSCs for stem cell regeneration. Compared to MSCs, USSCs are easily accessible and routinely HLA matched after their isolation. Furthermore, their use does not raise ethical concerns[2, 33, 34].

The differentiation potential of USSCs into the osteogenic lineage is well known and has been verified by many research groups[36, 40, 41]. They can be differentiated into the osteogenic lineage both spontaneously and when cultured with specific supplements[36]. The control of osteogenic differentiation of USSCs is important for *in vitro* culture or delivery by matrices.

Although Kogler *et al* had declared in their primary publication in 2004[34] that USSCs did not differentiate spontaneously, in 2009[36] they stated that USSCs spontaneously differentiated into osteoblasts. The results of our study demonstrate that in dense culture (21 d culture without any passage) USSCs proliferate and they produce some layers (Figure 1). This high compactness facilitates their spontaneous differentiation into the osteogenic lineage. In 2004, Kogler *et al*[34] had cultured USSCs to less than 80% confluency. Therefore, self-differentiation had not occurred. Also, Kogler *et al*[42] reported that once USSCs started to develop into osteogenic cells, they failed at neural and endodermal differentiation. In another study, they showed that USSCs initiated bone formation in the orthotropic site[34].

Another research team has reported that USSCs were significantly engrafted into bone marrow, survived within a collagen-TCP scaffold for up to 4 weeks, and increased local bone formation in the femoral defect of a nude rat[2]. According to these reports and our prior observations about their osteogenic potential, using USSCs in bone tissue engineering appears to be appropriate. To examine this hypothesis, we analyzed some osteogenic markers over a period of 21 d in USSCs cultured in either growth medium (TCPS subgroup) or osteo–inductive supplements (osteo-TCPS subgroup).

For a closer look at the osteogenic behavior of USSCs, Alizarin red staining of amorphous calcium deposits (Figure 2) and the expression of osteogenic marker genes, such as BMP2, ALPase, osteocalcin and osteopontin, were analyzed in cells seeded on TCPS or scaffolds (Figure 3, Table 2). The results support the observation of osteogenic differentiation under stimulation. It is noteworthy that all of these marker genes showed little expression on d 1 (unstimulated USSCs). This result supports the osteoblastic potential of USSCs.

Handschel *et al*[43] reported that the combination of insoluble

collagenous bone matrix (ICBM) scaffolds and USSCs led to bone formation in immunocompromised rats. Nevertheless, the use of ICBM or any other donor-derived tissue or tissue portion raises the danger of immunological rejection. This risk makes the use of artificial matrices more appealing.

There are two main approaches to the design of support matrices. The first approach is the administration of large amounts of osteogenically predifferentiated cells in microsphere form[1, 36]. But this technique is hampered by the limited volume of microspheres administered into the area of defect and the risk of effluence into other, unfavorable sites. Therefore, we have designed a new improvement in this field.

Because HA adsorbs adhesive proteins present within body fluids, HA containing scaffolds improve implant integration into bone defects. Many researchers have shown that protein adsorption is an important determinant of cell adhesion in early phases. Also, initial cell adhesion is critical for the functional improvement of anchorage-dependent cells because it mediates subsequent cellular responses, including proliferation and differentiation[3, 44–47].

In this study, our main objective was to evaluate the influence of nHA on osteogenic induction in USSCs. So, we chose TCPS as the reference surface for cultivation. Then, nHA grafted scaffolds and nHA suspensions were selected as two different approaches for the application of nHA and comparison for their osteogenic induction. This aim was based on a literature review of previous studies concerning applicable and suitable influences of HA in osteogenic induction.

In this regard, first the osteogenic influence of nHA particles in suspension was investigated (the sizes of the HA nanoparticles used were less than 200 nm). This test was carried out because the osteogenic induction of nHA suspension has not been investigated in prior studies.

For the nHA suspension (group 2) approach, we added nHA once a week for 3 weeks into the culture plates of USSCs (Figure 4). We expected that proliferating USSCs retained these hard particles inside their layers, much like fillings in a sandwich. We had aimed to strengthen the USSCs multi-layer culture for use in bone regeneration. Practically, we achieved a transportable multi-layer of USSCs after 21 d culture, but it was not as suitable as we had anticipated. The cell population did not expand according to our prediction, which may be explained by the nHA-induced apoptosis.

In contrast to our expectation, we observed broad apoptosis of USSCs before suitable osteogenic differentiation in cultures treated with the nHA suspension. Yuan *et al*[48] reported induction of apoptosis by nHA while analyzing the effects of different concentrations of HA nanoparticles on HepG2 cells. Chen *et al*[49] reported that HA nanoparticle-induced apoptosis was mediated through the mitochondrial- and caspase-dependent pathway. In yet another study, Sun *et al*[50] showed that HA nanoparticles could induce p53 expression; this activated downstream genes and finally resulted in cell apoptosis.

Considering that our observation is in agreement with the above-mentioned studies, it is feasible that the entry of USSCs into an apoptotic phase was induced by nHA. One explana-

tion for this could be the fact that USSCs have to consume most of their cellular matter and energy to overcome the apoptotic phenomenon. Therefore, USSCs were forced to avoid apoptotic cascades before responding to growth signals or osteogenic induction. Our analyses on the expression of osteogenic markers and proliferation (total protein content) of USSCs under nHA suspension support our suggestion (Figure 9).

According to these findings, in our future research we propose the use of other concentrations of nHA suspensions or larger osteo-inductive particles, such as HA micro-rods, which cause no pinocytosis and consequent apoptosis in the USSCs.

Our second approach to matrix design is the fabrication of a nanofibrous scaffold. This method is considered a revolution in tissue engineering. Nanofibrous scaffolds loaded with the proper cells have been used in several studies, with various animal models and materials, ranging from chemical ceramics to biodegradable cages. These developments have resulted in a superior regeneration capacity for bioengineered bone compared to pure implants[37, 38, 51].

The ability to mimic the chemical, physical and mechanical properties of the natural extra-cellular matrix is a key requirement for scaffolds to be successfully applied. Electrospun nanofibrous scaffolds have gained recognition in recent years because they are biomimetics of the nanoscale features of natural bone, such as high porosity, interconnected pores and large surface area[52].

In this study, we successfully fabricated aligned electrospun PCL/PLLA/nHA nanofibrous scaffolds to evaluate the effects of grafted-nHA within biocomposite nanofibers on attachment, proliferation, and osteogenic differentiation of USSCs.

Analyses of FTIR spectra of PCL/PLLA nanofibers, PCL/PLLA/nHA composite nanofibers and nHA indicated successful incorporation of nHA into the PCL/PLLA nanofibers (Figure 5). Incorporation of nHA into PCL/PLLA nanofibers causes a decrease in tensile strength and elongation at break. These changes occur because of low compatibility between nHA and these polymeric fibers. The large difference between the modulus of soft polymeric matrices and the modulus of hard nanoparticles leads to differences between the strains of these phases when tension is applied. Different strains and poor interfacial bonding between polymeric matrices and inorganic nHA lead to formation of voids at the interfaces. Growth of these voids leads to tearing of samples and decreased tensile properties of HA–filled nanofibers. Conversely, the large amount of inorganic nanoparticles (20% of polymer weight (w/w)) resulted in agglomeration of filler particles, which caused some defects during application of tension. As a result, the PCL/PLLA/nHA nanofibrous scaffold was highly flexible and allowed USSCs to penetrate into the scaffolds. Characteristics such as a porous, beadless structure and nano–scale aligned fibers, as revealed by SEM micrographs make this scaffold suitable for tissue engineering applications. Moreover, nHA was effectively presented on the surface and helped to attain the rough surface morphology ideal for cell attachment and proliferation.

Adherent cells convert signals sensed about matrix topography into morphological changes and cell-fate decisions concerning the direction of differentiation[53]. It has been suggested that the extracellular matrix and integrin collaborate to modulate both cell shape and intracellular signals[54, 55]. However, the mechanisms by which topographical signals manage cell orientation and morphology are still poorly understood.

Findings on the effects of fiber orientation on cell morphology and growth have been published by various researchers. Because bone has significant anisotropic mechanical properties, with a highly oriented ECM and bone cells, the arrangement of the ECM mimicked by aligned nanofibrous scaffold is greatly preferred[56, 57].

In agreement with the findings of Yin *et al*[7], aligned electrospun PLLA nanofibers provide an ideal microenvironment for hTSPCs to differentiate into the teno-lineage. An assay on electrospun polyester PCL–based polyurethane elastomer and PLLA demonstrated that alignment of electrospun fibers controlled the directional spreading of mouse fibroblasts[58].

Other reports have investigated the effect of oriented PCL electrospun fibers on promoting Schwann cell maturation, astrocyte alignment and directed axonal outgrowth for encouraging neural repair in the future[59, 60]. Finally, yet another study reported that unidirectionally oriented nanofibers significantly induced muscle cell alignment and myotube formation compared to randomly oriented nanofibers[61].

Cell infiltration into an electrospun nanofibrous matrix is often limited due to the relatively small pore size between the fibers. Aligned nanofibers provide relatively suitable pore size so that cell infiltration into the nanofibrous matrices can be significantly enhanced. The effect of aligned nanofibers on promoting infiltration of endothelial cells into scaffolds was reported by Kurpinski *et al*[62]. The present study investigated whether aligned nanofibers influenced the infiltration of USSCs and the orientation of their differentiation.

The impact of fabricated scaffolds on cell adhesion, growth and production of an aligned morphology of seeded USSCs on nanofibers was investigated by nucleus staining and SEM micrographs (Figures 3 and 8). Our results suggest that this scaffold is a biocompatible matrix. Such aligned scaffolds may lead to the development of desirable engineered bony tissue composed of favorable stem cells and smart scaffolds that can organize and align cell populations to facilitate osteogenic differentiation.

The consequence of our chosen conditions on cell proliferation was investigated by measuring the total protein content of cultured USSCs. Because we had used the same initial number of cells for all groups, we can consider the "total protein content" an indicator of proliferation. All groups showed an increase in total protein content during differentiation (Figure 9). The most important reason for the reduction in proliferation rate (decrease in total protein content) of two group (nHA and osteo-nHA subgroups) could be attributed to apoptosis induced by HA nanoparticles.

Compared to TCPS, the nHA scaffold demonstrated a decreased capacity to support proliferation of USSCs. To explain this insignificant difference, we should consider the modifications to the scaffold surface; further improvement may be required. Collectively, our findings showed biocompatibility and the capacity of this scaffold to support the proliferation of USSCs over a 21-d period of monitoring.

High–level expression of certain genes, which occurs at discrete time points during the differentiation process, is thought to contribute to the differentiated state of osteoblasts. Alkaline phosphatase (ALPase), collagen 1 (Col I) and osteonectin (ON) are expressed at high levels near the end of the proliferative period and during the period of extracellular matrix deposition and maturation. Genes expressed at or near the time of mineralization include osteopontin and osteocalcin[63].

Measuring the ALPase activity, as an indicator of progress in osteogenic differentiation, showed the highest levels of this factor at d 14 (Figure 10). Similar results were obtained by Jones *et al*[64], where the ALPase activity for human osteoblast cells (HOB) was highest on d 14, after which a decrease was observed due to the beginning of mineralization in HOB. In an experiment by Babister *et al*[1], both the activity and the transcription of ALPase in hMSCs were highest on d 21. Conversely, Degistirici *et al*[41] found that USSCs expressed the most active ALPase on d 7 during osteogenic differentiation.

Based on the fact that USSCs tend to differentiate into the osteo–lineage potentially, we can assume that USSCs passaged for longer will express osteogenic markers sooner. Consequently, the USSC line used by Degistirici *et al*[41] may have been older than ours.

To explain the decrease of ALPase activity on d 3, when compared to d 1 and d 7 in the scaffold group, it is worth mentioning that USSCs are adherent cells. Therefore, the properties of the matrix affect its function and destination. After seeding on a scaffold, USSCs need some time to adapt to the new matrix. As a consequence, seeded USSCs on HA scaffolds show a delay in responding to environmental cues. The similarity in the ALPase activity in the TCPS and osteo-TCPS subgroups could be another strong piece of evidence for the hypothesis that USSCs tend to spontaneously differentiate into the osteo–lineage.

The results of the ALPase activity assay were further confirmed by qPCR analysis of osteonectin and calcium content analysis in all conditions (Figures 11 and 12). Similar increasing trends in ON transcription were observed in all groups, with maximum transcription on d 21. As the final osteogenic evaluation, calcium deposition was examined and normalized to the total protein contents. In accordance with the previous results, calcium deposition increased significantly over time. Considering all the results, seeding USSCs on PCL/PLLA/nHA nanofibers synergistically improved the ALPase activity, osteonectin transcription and calcium deposition of USSCs in osteogenic culture conditions.

Conclusion

In the present study, nHA in both aligned electrospun nanofibrous PCL/PLLA scaffolds and in suspension was investigated to determine the most effective condition for the control

of osteogenic differentiation and mineralization of USSCs. SEM images indicated homogenous dispersion of nHA throughout this multi-component scaffold and aligned growth of USSCs on the scaffold. The incorporation of HA into the scaffold had no negative impact on USSC initial adhesion, proliferation, spreading or viability.

In conclusion, relying on these data, the described scaffold, in combination with an osteogenic medium, enhances osteogenesis in USSCs more effectively than the other analyzed conditions. These enhancements were confirmed by biochemical and gene expression analysis. Therefore the synergism of USSCs and the PCL/PLLA/nHA scaffold can be used to fill up spaces in bony defects and is a promising candidate for a novel bone regeneration approach.

Acknowledgements

Author contribution

Behnaz BAKHSHANDEH designed and performed the research, Masoud SOLEIMANI designed the research, and Nasser GHAEMI and Iman SHABANI contributed new reagents or analytic tools.

References

1 Babister JC, Hails LA, Oreffo RO, Davis SA, Mann S. The effect of pre–coating human bone marrow stromal cells with hydroxyapatite/amino acid nanoconjugates on osteogenesis. Biomaterials 2009; 30: 3174–82.

2 Jager M, Degistirici O, Knipper A, Fischer J, Sager M, Krauspe R. Bone healing and migration of cord blood–derived stem cells into a critical size femoral defect after xenotransplantation. J Bone Miner Res 2007; 22: 1224–33.

3 Lee JH, Rim NG, Jung HS, Shin H. Control of osteogenic differentiation and mineralization of human mesenchymal stem cells on composite nanofibers containing poly[lactic-co-(glycolic acid)] and hydroxyapatite. Macromol Biosci 2010; 10: 173–82.

4 Yang F, Murugan R, Wang S, Ramakrishna S. Electrospinning of nano/micro scale poly(L-lactic acid) aligned fibers and their potential in neural tissue engineering. Biomaterials 2005; 26: 2603–10.

5 Shor L, Guceri S, Wen X, Gandhi M, Sun W. Fabrication of three-dimensional polycaprolactone/hydroxyapatite tissue scaffolds and osteoblast-scaffold interactions *in vitro*. Biomaterials 2007; 28: 5291–7.

6 Jose MV, Thomas V, Xu Y, Bellis S, Nyairo E, Dean D. Aligned bioactive multi-component nanofibrous nanocomposite scaffolds for bone tissue engineering. Macromol Biosci 2010; 10: 433–44.

7 Yin Z, Chen X, Chen JL, Shen WL, Hieu Nguyen TM, Gao L, *et al*. The regulation of tendon stem cell differentiation by the alignment of nanofibers. Biomaterials 2010; 31: 2163–75.

8 Ge Z, Yang F, Goh JC, Ramakrishna S, Lee EH. Biomaterials and scaffolds for ligament tissue engineering. J Biomed Mater Res A 2006; 77: 639–52.

9 Hashemi SM, Soleimani M, Zargarian SS, Haddadi-Asl V, Ahmadbeigi N, Soudi S, *et al*. *In vitro* differentiation of human cord blood-derived unrestricted somatic stem cells into hepatocyte-like cells on poly(epsilon–caprolactone) nanofiber scaffolds. Cells Tissues Organs 2009; 190: 135–49.

10 Vasita R, Katti DS. Nanofibers and their applications in tissue engineering. Int J Nanomedicine 2006; 1: 15–30.

11 Gupta D, Venugopal J, Mitra S, Giri Dev VR, Ramakrishna S. Nano-structured biocomposite substrates by electrospinning and electro-spraying for the mineralization of osteoblasts. Biomaterials 2009; 30: 2085–94.

12 Li LH, Kommareddy KP, Pilz C, Zhou CR, Fratzl P, Manjubala I. *In vitro* bioactivity of bioresorbable porous polymeric scaffolds incorporating hydroxyapatite microspheres. Acta Biomater 2010; 6: 2525–31.

13 Yang X, Yang F, Walboomers XF, Bian Z, Fan M, Jansen JA. The performance of dental pulp stem cells on nanofibrous PCL/gelatin/nHA scaffolds. J Biomed Mater Res A 2010; 93: 247–57.

14 Liu X, Li X, Fan Y, Zhang G, Li D, Dong W, *et al*. Repairing goat tibia segmental bone defect using scaffold cultured with mesenchymal stem cells. J Biomed Mater Res B Appl Biomater 2010; 94: 44–52.

15 Niu X, Feng Q, Wang M, Guo X, Zheng Q. Porous nano-HA/collagen/PLLA scaffold containing chitosan microspheres for controlled delivery of synthetic peptide derived from BMP-2. J Control Release 2009; 134: 111–7.

16 Ramay HR, Zhang M. Biphasic calcium phosphate nanocomposite porous scaffolds for load-bearing bone tissue engineering. Biomaterials 2004; 25: 5171–80.

17 Wang M. Developing bioactive composite materials for tissue replacement. Biomaterials 2003; 24: 2133–51.

18 Marletta G, Ciapetti G, Satriano C, Pagani S, Baldini N. The effect of irradiation modification and RGD sequence adsorption on the response of human osteoblasts to polycaprolactone. Biomaterials 2005; 26: 4793–804.

19 Yu H, Wooley PH, Yang SY. Biocompatibility of Poly-epsilon-caprolactone-hydroxyapatite composite on mouse bone marrow-derived osteoblasts and endothelial cells. J Orthop Surg Res 2009; 4: 5.

20 Yoshimoto H, Shin YM, Terai H, Vacanti JP. A biodegradable nanofiber scaffold by electrospinning and its potential for bone tissue engineering. Biomaterials 2003; 24: 2077–82.

21 Shin M, Yoshimoto H, Vacanti JP. *In vivo* bone tissue engineering using mesenchymal stem cells on a novel electrospun nanofibrous scaffold. Tissue Eng 2004; 10: 33–41.

22 Wright-Charlesworth DD, King JA, Miller DM, Lim CH. *In vitro* flexural properties of hydroxyapatite and self-reinforced poly(*L*-lactic acid). J Biomed Mater Res A 2006; 78: 541–9.

23 Woo KM, Seo J, Zhang R, Ma PX. Suppression of apoptosis by enhanced protein adsorption on polymer/hydroxyapatite composite scaffolds. Biomaterials 2007; 28: 2622–30.

24 Wang X, Song G, Lou T. Fabrication and characterization of nano-composite scaffold of PLLA/silane modified hydroxyapatite. Med Eng Phys 2010; 32: 391–7.

25 Hunt JA, Callaghan JT. Polymer-hydroxyapatite composite *versus* polymer interference screws in anterior cruciate ligament reconstruction in a large animal model. Knee Surg Sports Traumatol Arthrosc 2008; 16: 655–60.

26 Sun JJ, Bae CJ, Koh YH, Kim HE, Kim HW. Fabrication of hydroxyapatite-poly(epsilon-caprolactone) scaffolds by a combination of the extrusion and bi-axial lamination processes. J Mater Sci Mater Med 2007; 18: 1017–23.

27 Charles LF, Shaw MT, Olson JR, Wei M. Fabrication and mechanical properties of PLLA/PCL/HA composites via a biomimetic, dip coating, and hot compression procedure. J Mater Sci Mater Med 2010; 21: 1845–54.

28 Ngiam M, Liao S, Patil AJ, Cheng Z, Yang F, Gubler MJ, *et al*. Fabrication of mineralized polymeric nanofibrous composites for bone graft materials. Tissue Eng Part A 2009; 15: 535–46.

29 Zhang Y, Venugopal JR, El–Turki A, Ramakrishna S, Su B, Lim CT. Electrospun biomimetic nanocomposite nanofibers of hydroxyapatite/chitosan for bone tissue engineering. Biomaterials 2008; 29: 4314–22.

30 Venugopal JR, Low S, Choon AT, Kumar AB, Ramakrishna S. Nanobioengineered electrospun composite nanofibers and osteoblasts for bone regeneration. Artif Organs 2008; 32: 388–97.

31 Ito Y, Hasuda H, Kamitakahara M, Ohtsuki C, Tanihara M, Kang IK, *et al*. A composite of hydroxyapatite with electrospun biodegradable nanofibers as a tissue engineering material. J Biosci Bioeng 2005; 100: 43–9.

32 Wutticharoenmongkol P, Pavasant P, Supaphol P. Osteoblastic phenotype expression of MC3T3-E1 cultured on electrospun polycaprolactone fiber mats filled with hydroxyapatite nanoparticles. Biomacromolecules 2007; 8: 2602–10.

33 Kogler G, Radke TF, Lefort A, Sensken S, Fischer J, Sorg RV, *et al*. Cytokine production and hematopoiesis supporting activity of cord blood-derived unrestricted somatic stem cells. Exp Hematol 2005; 33: 573–83.

34 Kogler G, Sensken S, Airey JA, Trapp T, Muschen M, Feldhahn N, *et al*. A new human somatic stem cell from placental cord blood with intrinsic pluripotent differentiation potential. J Exp Med 2004; 200: 123–35.

35 Buchheiser A, Liedtke S, Looijenga LH, Kogler G. Cord blood for tissue regeneration. J Cell Biochem 2009; 108: 762–8.

36 Langenbach F, Naujoks C, Kersten-Thiele PV, Berr K, Depprich R, Kubler N, *et al*. Osteogenic differentiation influences stem cell migration out of scaffold free microspheres. Tissue Eng Part A 2010; 16: 759–66.

37 Kadiyala S, Young RG, Thiede MA, Bruder SP. Culture expanded canine mesenchymal stem cells possess osteochondrogenic potential *in vivo* and *in vitro*. Cell Transplant 1997; 6: 125–34.

38 Bruder SP, Kurth AA, Shea M, Hayes WC, Jaiswal N, Kadiyala S. Bone regeneration by implantation of purified, culture-expanded human mesenchymal stem cells. J Orthop Res 1998; 16: 155–62.

39 Bruder SP, Kraus KH, Goldberg VM, Kadiyala S. The effect of implants loaded with autologous mesenchymal stem cells on the healing of canine segmental bone defects. J Bone Joint Surg Am 1998; 80: 985–96.

40 Vacanti V, Kong E, Suzuki G, Sato K, Canty JM, Lee T. Phenotypic changes of adult porcine mesenchymal stem cells induced by prolonged passaging in culture. J Cell Physiol 2005; 205: 194–201.

41 Degistirici O, Jager M, Knipper A. Applicability of cord blood–derived unrestricted somatic stem cells in tissue engineering concepts. Cell Prolif 2008; 41: 421–40.

42 Kogler G, Sensken S, Wernet P. Comparative generation and characterization of pluripotent unrestricted somatic stem cells with mesenchymal stem cells from human cord blood. Exp Hematol 2006; 34: 1589–95.

43 Handschel J, Naujoks C, Langenbach F, Berr K, Depprich R, Ommerborn M, *et al*. Comparison of ectopic bone formation of embryonic stem cells and cord blood stem cells *in vivo*. Tissue Eng Part A 2010; 16: 2475–83.

44 Lind M, Feller J, Webster KE. Tibial bone tunnel widening is reduced by polylactate/hydroxyapatite interference screws compared to metal screws after ACL reconstruction with hamstring grafts. Knee 2009; 16: 447–51.

45 Hennessy KM, Pollot BE, Clem WC, Phipps MC, Sawyer AA, Culpepper BK, *et al*. The effect of collagen I mimetic peptides on mesenchymal stem cell adhesion and differentiation, and on bone formation at hydroxyapatite surfaces. Biomaterials 2009; 30: 1898–909.

46 Wilson CJ, Clegg RE, Leavesley DI, Pearcy MJ. Mediation of biomaterial-cell interactions by adsorbed proteins: a review. Tissue Eng 2005; 11: 1–18.

47 Romberger DJ. Fibronectin. Int J Biochem Cell Biol 1997; 29: 939–43.

48 Yuan Y, Liu C, Qian J, Wang J, Zhang Y. Size-mediated cytotoxicity and apoptosis of hydroxyapatite nanoparticles in human hepatoma HepG2 cells. Biomaterials 2010; 31: 730–40.

49 Chen S, Zhao Y, Han W, Zhao G, Zhu L, Wang J, *et al*. Mitochondria-dependent signalling pathway are involved in the early process of radiation-induced bystander effects. Br J Cancer 2008; 98: 1839–44.

50 Sun J, Ding T. p53 reaction to apoptosis induced by hydroxyapatite nanoparticles in rat macrophages. J Biomed Mater Res A 2009; 88: 673–9.

51 Kon E, Muraglia A, Corsi A, Bianco P, Marcacci M, Martin I, *et al*. Autologous bone marrow stromal cells loaded onto porous hydroxyapatite ceramic accelerate bone repair in critical-size defects of sheep long bones. J Biomed Mater Res 2000; 49: 328–37.

52 Murugan R, Ramakrishna S. Design strategies of tissue engineering scaffolds with controlled fiber orientation. Tissue Eng 2007; 13: 1845–66.

53 Gao L, McBeath R, Chen CS. Stem cell shape regulates a chondrogenic versus myogenic fate through Rac1 and N-cadherin. Stem Cells 2010; 28: 564–72.

54 Engler AJ, Sen S, Sweeney HL, Discher DE. Matrix elasticity directs stem cell lineage specification. Cell 2006; 126: 677–89.

55 Boudreau NJ, Jones PL. Extracellular matrix and integrin signalling: the shape of things to come. Biochem J 1999; 339: 481–8.

56 Li WJ, Mauck RL, Cooper JA, Yuan X, Tuan RS. Engineering controllable anisotropy in electrospun biodegradable nanofibrous scaffolds for musculoskeletal tissue engineering. J Biomech 2007; 40: 1686–93.

57 Zhu B, Lu Q, Yin J, Hu J, Wang Z. Alignment of osteoblast-like cells and cell-produced collagen matrix induced by nanogrooves. Tissue Eng 2005; 11: 825–34.

58 Truong YB, Glattauer V, Lang G, Hands K, Kyratzis IL, Werkmeister JA, *et al*. A comparison of the effects of fibre alignment of smooth and textured fibres in electrospun membranes on fibroblast cell adhesion. Biomed Mater 2010; 5: 25005.

59 Horne MK, Nisbet DR, Forsythe JS, Parish C. Three dimensional nanofibrous scaffolds incorporating immobilized BDNF promote proliferation and differentiation of cortical neural stem cells. Stem Cells Dev 2010; 19: 843–52.

60 Nisbet DR, Rodda AE, Horne MK, Forsythe JS, Finkelstein DI. Neurite infiltration and cellular response to electrospun polycaprolactone scaffolds implanted into the brain. Biomaterials 2009; 30: 4573–80.

61 Choi JS, Lee SJ, Christ GJ, Atala A, Yoo JJ. The influence of electrospun aligned poly(epsilon-caprolactone)/collagen nanofiber meshes on the formation of self-aligned skeletal muscle myotubes. Biomaterials 2008; 29: 2899–906.

62 Kurpinski KT, Stephenson JT, Janairo RR, Lee H, Li S. The effect of fiber alignment and heparin coating on cell infiltration into nanofibrous PLLA scaffolds. Biomaterials 2010; 31: 3536–42.

63 Beck GR Jr, Zerler B, Moran E. Phosphate is a specific signal for induction of osteopontin gene expression. Proc Natl Acad Sci U S A 2000; 97: 8352–7.

64 Jones JR, Tsigkou O, Coates EE, Stevens MM, Polak JM, Hench LL. Extracellular matrix formation and mineralization on a phosphate-free porous bioactive glass scaffold using primary human osteoblast (HOB) cells. Biomaterials 2007; 28: 1653–63.

npg

Original Article

Epigallocatechin-3-gallate regulates cell growth, cell cycle and phosphorylated nuclear factor-κB in human dermal fibroblasts

Dong-Wook HAN[1, #], Mi Hee LEE[2, 3, #], Hak Hee KIM[2, 4], Suong-Hyu HYON[4], Jong-Chul PARK[2, 3, *]

[1]Department of Nanomedical Engineering, College of Nanoscience & Nanotechnology, Pusan National University, Busan 609–735, Korea; [2]Cellbiocontrol Laboratory, Department of Medical Engineering, [3]Brain Korea 21 Project for Medical Science, Yonsei University College of Medicine, Seoul 120–752, Korea; [4]Department of Medical Simulation Engineering, Research Center for Nano Medical Engineering, Institute for Frontier Medical Sciences, Kyoto University, Kyoto 606-8507, Japan

Aim: To investigate the effects of (–)epigallocatechin-3-gallate (EGCG), the main polyphenol in green tea, on cell growth, cell cycle and phosphorylated nuclear factor-κB (pNF-κB) expression in neonatal human dermal fibroblasts (nHDFs).
Methods: The proliferation and cell-cycle of nHDFs were determined using WST-8 cell growth assay and flow cytometry, respectively. The apoptosis was examined using DNA ladder and Annexin V-FITC assays. The expression levels of pNF-κB and cell cycle-related genes and proteins in nHDFs were measured using cDNA microarray analyses and Western blot. The cellular uptake of EGCG was examined using fluorescence (FITC)-labeled EGCG (FITC-EGCG) in combination with confocal microscopy.
Results: The effect of EGCG on the growth of nHDFs depended on the concentration tested. At a low concentration (200 μmol/L), EGCG resulted in a slight decrease in the proportion of cells in the S and G_2/M phases of cell cycle with a concomitant increase in the proportion of cells in G_0/G_1 phase. At the higher doses (400 and 800 μmol/L), apoptosis was induced. The regulation of EGCG on the expression of pNF-κB was also concentration-dependent, whereas it did not affect the unphosphorylated NF-κB expression. cDNA microarray analysis showed that cell cycle-related genes were down-regulated by EGCG (200 μmol/L). The expression of cyclins A/B and cyclin-dependent kinase 1 was reversibly regulated by EGCG (200 μmol/L). FITC-EGCG was found to be internalized into the cytoplasm and translocated into the nucleus of nHDFs.
Conclusion: EGCG, through uptake into cytoplasm, reversibly regulated the cell growth and expression of cell cycle-related proteins and genes in normal fibroblasts.

Keywords: (–)epigallocatechin-3-gallate (EGCG); polyphenol; green tea; cell cycle; fibroblasts; nuclear factor-κB (NF-κB)

Introduction

Food bioactives with strong antioxidant properties have been shown to be contained in green tea, grapes, and turmeric and have shown cancer chemopreventive and chemotherapeutic effects in many animal tumor bioassays, cell culture systems, and epidemiological studies[1–3]. These biological activities of green tea polyphenols are believed to be mostly mediated by (–)epigallocatechin-3-gallate (EGCG), the predominant catechin present therein[4]. Some previous reports have shown that treatment with EGCG or its derivatives results in G_0/G_1 phase cell cycle arrest and apoptosis of several types of cancer

cells, but not of normal cells[5–7]. However, the mechanism of this differential response to EGCG in cancer cells *vs* normal cells has not been fully elucidated. Many previous studies have reported the incorporation of EGCG into the cytosol and/or even the nucleus of cancer cells. The EGCG tissue distribution and metabolism in animals has also been assessed using radioisotope-labeled EGCG, *eg*, [^{3}H]EGCG[8–11]. This cellular incorporation of EGCG is considered involved in the mechanism of the anti-cancer activity of EGCG because catechins exert proapoptotic and antiproliferative activities on cancer cells.

Dietary agents that can suppress the cancer cells via apoptosis (a programmed cell death) but do not affect normal cells may have a therapeutic advantage for the elimination of cancer cells. At present, only a few agents are known to possess the potential for selective/preferential elimination of cancer

---

cells without affecting the normal cells[6, 7, 12, 13]. EGCG has been shown to have suppressive effects on various cancer cells by inducing cell cycle arrest and inhibiting proliferation[14, 15], whereas less attention has been paid to its cytoprotective effects on normal cells. Our previous reports have demonstrated that EGCG induces cellular hibernation with high cell survival rates through inhibiting apoptosis by scavenging free radicals harmful to the cells and protecting the fragile cell membrane by simply adhering to and reinforcing it[16–18].

In the present study, we investigated (i) the regulatory effects of low- and high-dose treatments of EGCG on the cellular responses and expression of phosphorylated nuclear factor-κB/p65 (pNF-κB/p65) in neonatal human dermal fibroblasts (nHDFs), (ii) the reversible effects of EGCG on the expression of cell cycle-related genes and proteins, and (iii) the involvement of the cellular uptake pattern of EGCG as a mechanism for these dose-differential responses to EGCG in nHDFs. Our data imply that the proliferation, cell cycle progression, apoptosis and pNF-κB/p65 expression of nHDFs are dose-differentially regulated in response to EGCG (200–800 μmol/L). Cell cycle-related genes and proteins, such as cyclin A (CCNA), CCNB, cyclin-dependent kinase 1 (CDK1) and CDK inhibitor A1 (CDKN1A or p21), were reversibly regulated when the cells were subjected to EGCG exposure and removal. EGCG conjugated with fluorescein isothiocyanate (FITC) was found to be incorporated into the cytoplasm of nHDFs with further nuclear translocation. The dose-differential regulatory activity of EGCG may be exploited to craft strategies for the cytoprotection of normal cells and cancer chemoprevention by EGCG.

Materials and methods
Cell cultures
Neonatal human dermal fibroblasts (nHDFs) were kindly provided by Dr Dong Kyun RAH (Department of Plastic and Reconstructive Surgery, Yonsei University College of Medicine, Seoul, Korea). The cells were routinely maintained in Dulbecco's modified Eagle's medium (D6429, Sigma-Aldrich Co, St Louis, MO, USA) supplemented with 10% fetal bovine serum (Sigma-Aldrich Co) and a 1% antibiotic antimycotic solution (including 10 000 units penicillin, 10 mg streptomycin and 25 μg amphotericin B per mL, Sigma-Aldrich Co) at 37 °C in a humidified atmosphere of 5% CO_2 in air as previously described[19]. Studies were performed with nHDFs within 10 passages.

EGCG treatment
EGCG (Teavigo™), a major polyphenolic constituent of green tea, was purchased from DSM Nutritional Products Ltd (Basel, Switzerland), and its purity exceeded 98%. To examine the dose-based differential effects of EGCG on growth, cell cycle progression, apoptosis and pNF-κB/p65 expression of nHDFs, the cells were seeded into well plates and incubated in the presence of increasing concentrations (100–800 μmol/L) of EGCG in complete medium for 24 h. Upon determining the effects of EGCG on the expression of cell cycle-related genes or proteins, cultured cells were treated with 200 μmol/L EGCG in complete medium for 24 h. After EGCG treatment, EGCG was removed from the culture medium and the cells were further incubated for 24 to 72 h.

Cell growth assay
The number of viable cells was quantified indirectly using a highly water soluble tetrazolium salt [WST-8, 2-(2-methoxy-4-nitrophenyl)-3-(4-nitrophenyl)-5-(2,4-disulfophenyl)-2H-tetrazolium, monosodium salt] (Dojindo Lab, Kumamoto, Japan) that is reduced to a formazan dye by mitochondrial dehydrogenases. Cell growth was found to be directly proportional to the metabolic reaction products obtained in the WST-8 assay. Briefly, WST-8 assays were conducted as follows. nHDFs cultures treated with increasing concentrations of EGCG were incubated with WST-8 for the last 4 h of the culture period (24 h) at 37 °C in the dark. To avoid a direct reaction between the antioxidant EGCG and the WST-8 to be reduced, the cell cultures were thoroughly washed with phosphate-buffered saline (PBS, pH 7.2) and refreshed with a fresh medium containing WST-8. Parallel sets of wells containing freshly cultured, non-treated nHDFs were regarded as the controls. Absorbance was determined at 450 nm using an ELISA reader (SpectraMax© 340, Molecular Device Co, Sunnyvale, CA, USA). At the end of incubation, the cellular morphologies were observed under an Olympus IX70 inverted microscope (Olympus Optical Co, Osaka, Japan).

Cell cycle analysis
For cell cycle analysis, cultured nHDFs, following treatment with increasing concentrations of EGCG for 24 h, were collected and washed with cold PBS (pH 7.2). The cells were resuspended in 95% cold methanol for 1 h at 4 °C and then centrifuged at 120×*g* for 5 min. The resultant pellet was washed twice with cold PBS, suspended in PBS and incubated with RNase (20 Units/mL, final concentration, Sigma-Aldrich Co) at 37 °C for 30 min. Afterward, the cells were chilled on ice for 10 min and stained with 100 μg/mL propidium iodide (PI, Sigma-Aldrich Co) for 1 h. At least 10 000 cells were counted by a flow cytometer (FACSCalibur™, BD Biosciences, San Jose, CA, USA), and the data obtained were analyzed using ModFit™ LT for Mac version 3.0 software (Verity Software House, Topsham, ME, USA).

Apoptosis analysis
After treatment of nHDFs with increasing concentrations of EGCG for 24 h, the cellular DNA was isolated and resolved over a 1.5% agarose gel to assess DNA ladder formation (fragmentation) using a standard procedure. Briefly, following EGCG treatment, the cells were washed twice with PBS (pH 7.2) and incubated with 1.0 mL of cytoplasm extraction buffer (10 mmol/L Tris, pH 7.5, 150 mmol/L NaCl, 5 mmol/L $MgCl_2$, and 0.5% Triton X-100) on ice for 15 min. The cells were centrifuged (14 000×*g*) at 4 °C and then incubated with 1.0 mL of DNA lysis buffer (10 mmol/L Tris, pH 7.5, 400 mmol/L NaCl, 1 mmol/L EDTA, and 1% Triton X-100) for 20 min on ice. The

lysate was cleared by centrifugation (14 000×*g*) at 4 °C, and the supernatant was incubated overnight with RNase (0.2 mg/mL) at room temperature and then with Proteinase K (0.1 mg/mL, Sigma-Aldrich Co) for 2 h at 37 °C. DNA was extracted using phenol:chloroform (1:1) and precipitated with 95% ethanol. The DNA precipitate was centrifuged at 14 000×*g* (4 °C) for 15 min, and the pellet was air-dried and dissolved in 20 mL of TE buffer (10 mmol/L Tris–HCl, pH 8.0, and 1 mmol/L EDTA). The total amount of DNA obtained was resolved over a 1.5% agarose gel containing 0.3 mg/mL ethidium bromide in Tris-borate-EDTA buffer. The bands were visualized under a UV transilluminator followed by Polaroid photography.

Apoptosis of nHDFs treated with EGCG for 24 h was also determined by the TACS™ Annexin V-FITC assay (R&D Systems Inc, McKinley Place, MN, USA). Phosphatidylserines exposed on the membrane surface of apoptotic cells were stained with Annexin V-FITC according to the manufacturer's instructions. The late apoptotic (or necrotic) cells were stained with PI. Parallel sets of wells containing non-treated nHDFs were regarded as the (+) controls. The results were acquired and analyzed with CellQuest© software (BD Biosciences). The population of apoptotic cells was characterized by its high mean fluorescence of Annexin V-FITC in a flow cytometric histogram.

Western blotting

After treatment with increasing concentrations of EGCG for 24 h, nHDFs were washed twice with cold PBS (10 mmol/L, pH 7.4), and ice-cold RIPA lysis buffer (Santa Cruz Biotechnology Inc, Santa Cruz, CA, USA) was added to the cells. After 5 min, the cells were scraped, and the lysate was centrifuged at 14 000×*g* for 20 min at 4 °C. Proteins were extracted from the total lysate, and the protein concentration was determined by a BCA™ protein assay using the manufacturer's protocol (Pierce, Rockford, IL, USA). For immunoblot analysis, 35–40 μg of protein was run on a 4/20 polyacrylamide-SDS gel (Daiichi Pure Chemicals Co, Ltd, Tokyo, Japan) for 1 h at 30 mA and blotted to a PVDF membrane for 50 min at 35 mA. The membrane was blocked in a blocking buffer (Nacalai Tesque Inc, Kyoto, Japan) for 1 h at room temperature and incubated with rabbit anti-human NF-κB/p65 and pNF-κB/p65 (Ser 536) polyclonal antibodies (Cell Signaling Technology Inc, Danvers, MA, USA) and, as the reference, mouse anti-human glyceraldehyde-3-phosphate dehydrogenase (GAPDH) monoclonal antibody (International Inc, Temecula, CA, USA). The membrane was treated with either an anti-mouse IgG (Amersham Biosciences, Buckinghamshire, UK) or an anti-rabbit IgG secondary antibody (Santa Cruz Biotechnology Inc), horseradish peroxidase-conjugated. Protein expression was detected by a Chemilumi-one chemiluminescent kit (Nacalai Tesque Inc) and X-ray film (Fujifilm, Tokyo, Japan).

In the cases of immunoblot analysis for cell cycle-related proteins, such as CCNA, CCNB1, CDK1, and CDKN1A, nHDFs were treated with 200 μmol/L EGCG for 24 h; the EGCG was then removed for further incubation for up to 72 h. Afterward, each protein was extracted from the cell lysate and blotted to the membrane. The membrane was blocked and incubated with primary antibodies, including either mouse anti-human CCNA, CCNB1, and CDK1 monoclonal antibodies (BD Biosciences) or rabbit anti-human CDKN1A monoclonal antibody (Cell Signaling Technology Inc), followed by incubation with horseradish peroxidase-conjugated secondary antibodies. Protein expression was detected as described above.

Microarray analysis

The effect of EGCG on gene expression of nHDFs was investigated using a Platinum Human Cancer 3.0K oligo microarray (GenoCheck, Ansan, Gyunggi-do, Korea). This microarray consisted of 3096 oligonucleotide spots including Operon (Operon, Huntsville, AL, USA), human oligo subsets, housekeeping genes and *Arabidopsis* DNA as controls. All oligonucleotide probes were designed from the UniGene Database Build Hs 184 and the Human Reference Sequence Database, both developed and maintained at the National Center for Biotechnology Information. The probes were resuspended in spotting solution (GenoCheck) at a final concentration of 50 pmol/L and spotted onto CMT-GAPS II silane slide glass (Corning, NY, USA) with a PixSys 5500 arrayer (Cartesian Technologies, Irvine, CA, USA) using 6 stealth micro spotting pins. The printed slides were processed according to the CMT-GAPS II slide protocol.

Confocal laser scanning microscopy

To determine the cellular uptake patterns of EGCG in nHDFs upon treatment with low and high doses of EGCG, the cells were treated for 24 h with 100 or 400 μmol/L FITC-conjugated EGCG (FITC-EGCG) as described previously[20]. After FITC-EGCG treatment, the cells were washed thoroughly with PBS, fixed with 3.5% paraformaldehyde (Sigma-Aldrich Co) in 0.1 mol/L phosphate buffer (pH 7) for 5 min at room temperature and immediately observed under a confocal laser scanning microscope (LSM 510, Carl Zeiss Advanced Imaging Microscopy, Jena, Germany). Cell nuclei were counterstained with 5 μmol/L PI immediately before 3 to 5 min of observation.

Statistical analyses

All variables were tested in three independent cultures for each experiment, and each experiment was repeated twice (*n*=6). The results are reported as the mean±standard deviation (SD) compared with the non-treated controls. A one-way analysis of variance (ANOVA), which was followed by a Tukey HSD test for the multiple comparisons, was used to detect the dose-based differential effects of EGCG on nHDFs. A *P* value < 0.05 was considered statistically significant.

Results

Effects of EGCG on growth, morphology and cell cycle progression of nHDFs

Proliferation was inhibited in nHDFs in a dose-differential manner in response to EGCG treatment (Figure 1A). The cells partially lost their proliferation feedback control mechanism during EGCG treatment with lower than 200 μmol/L for 24 h,

but the proliferation control was slowly recovered by the cell to cell contact and returned to a normal level after the removal of EGCG from the medium (data not shown). However, upon treatment with greater than 400 µmol/L EGCG, the proliferation control was not recovered in spite of EGCG removal.

A dose-differential modulation of cell cycle progression of nHDFs by EGCG treatment was also found. As shown in Figure 1B, EGCG treatment triggered an appreciable dose-dependent increase in the Sub-G_1 phase (*ie*, 5.4%, 56.7%, and 69.9% at 200 µmol/L, 400 µmol/L, and 800 µmol/L, respectively), which corresponds to apoptotic cells, and a concomitant decrease in S phase cells. Interestingly, 200 µmol/L EGCG resulted in a slight decrease in the population of S and G_2/M phases of the cell cycle, leading to cell cycle delay at the G_0/G_1 phase. However, EGCG treatment at a concentration greater than 400 µmol/L resulted in a significant increase in the Sub-G_1 phase of the cell cycle with a remarkable decrease in the proportion of cells in both the S and the G_2/M phases. Accordingly, the cells could not enter the S phase during treatment with higher concentrations of EGCG, which might induce cell cycle arrest as well as apoptosis.

This dose-differential antiproliferative response of EGCG in nHDFs was evident from the morphological observations (Figure 1C). The non-treated control and the lower doses (100 and 200 µmol/L) of EGCG caused only slight alterations, if any, in the cellular morphologies of nHDFs. At the higher doses
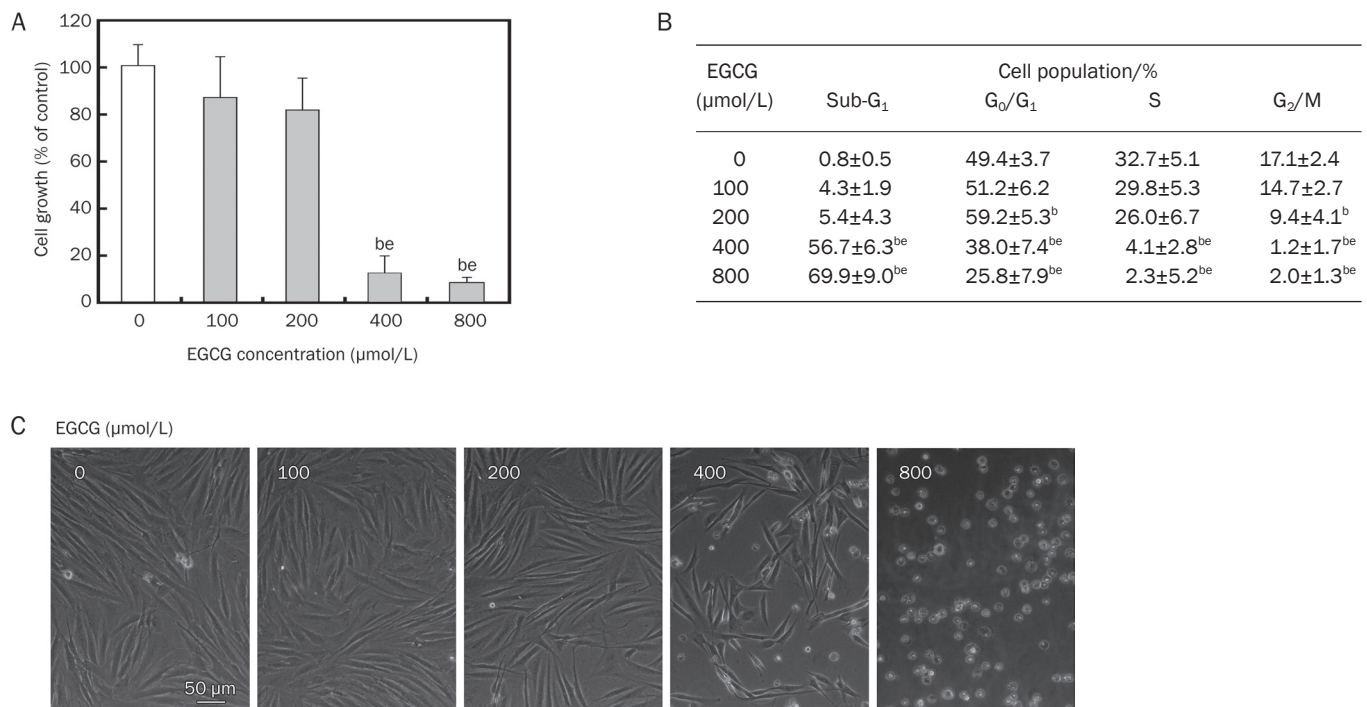
(400 and 800 µmol/L), however, the number of attached cells was markedly decreased, indicating that the EGCG treatments might result in apoptotic detachment of the cells.

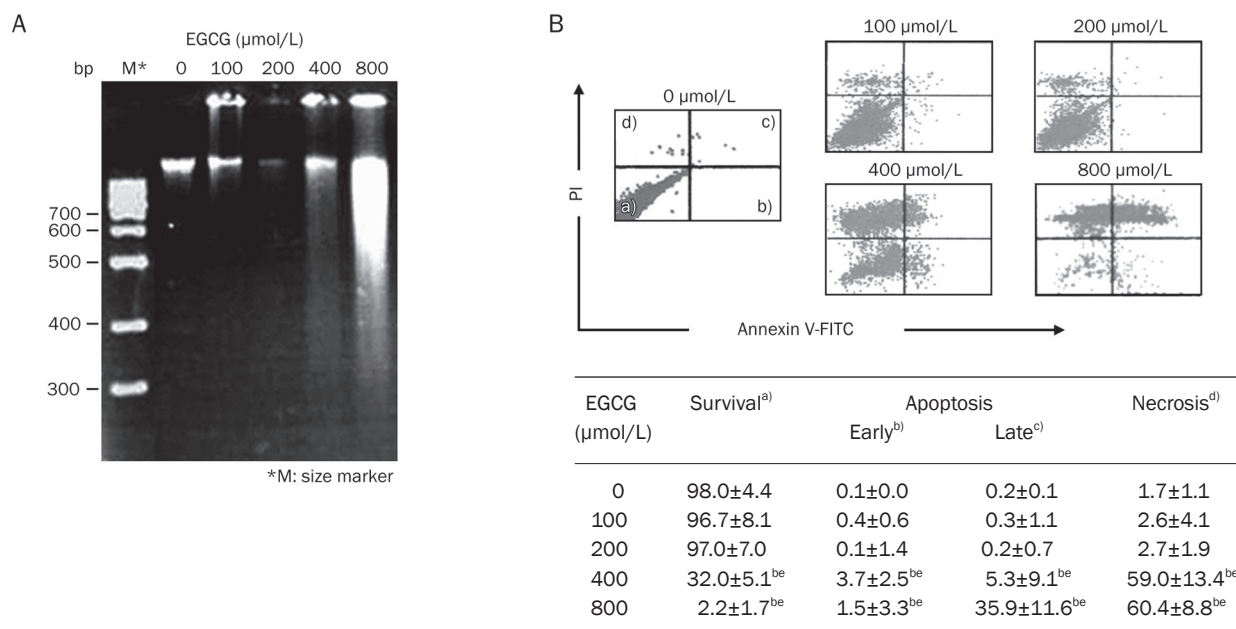## Effects of EGCG on apoptosis of nHDFs

The dose-differential effects of EGCG on apoptosis of nHDFs were evident from a DNA ladder assay, which showed the induction of DNA fragmentation with increasing concentrations of EGCG treatment (Figure 2A). The Annexin V-FITC assay showed that neither apoptosis nor necrosis was seen at doses lower than 200 µmol/L EGCG (Figure 2B). However, treatment of nHDFs with higher concentrations of EGCG resulted in late apoptosis and necrosis as evident by the formation of internucleosomal DNA fragments and high fluorescence of Annexin V-FITC and PI. Overall, this dose-differential pattern of apoptosis induced by EGCG in nHDFs agreed well with that of cell growth regulation, as shown in Figure 1.

Effects of EGCG on pNF-κB/p65 expression in nHDFs

To evaluate differential effects of EGCG on the expression of constitutive NF-κB/p65 and pNF-κB/p65 in nHDFs, an antibody directed against the RelA/p65 subunit of each protein was employed. EGCG treatment did not result in any significant alternation in the inactive, unphosphorylated form of NF-κB/p65 protein expression (Figure 3). However, a very strong inhibition of pNF-κB/p65 expression was observed at

A

B

EGCG	Cell population/%			
(µmol/L)	Sub-G_1	G_0/G_1	S	G_2/M
0	0.8±0.5	49.4±3.7	32.7±5.1	17.1±2.4
100	4.3±1.9	51.2±6.2	29.8±5.3	14.7±2.7
200	5.4±4.3	59.2±5.3[b]	26.0±6.7	9.4±4.1[b]
400	56.7±6.3[be]	38.0±7.4[be]	4.1±2.8[be]	1.2±1.7[be]
800	69.9±9.0[be]	25.8±7.9[be]	2.3±5.2[be]	2.0±1.3[be]

C EGCG (µmol/L)

Figure 1. Dose-based differential effects of EGCG on proliferation, morphology, and cell cycle progression of nHDFs. Cells were incubated with increasing concentrations (100–800 µmol/L) of EGCG for 24 h. The proliferation (A), cell cycle progression (B), and morphology (C) of EGCG-treated nHDFs were measured by WST-8 assay, flow cytometry and optical microscopy, respectively. The results are reported as a mean±SD and analyzed by a Tukey HSD test. [b]$P<0.05$ *vs* non-treated control, [e]$P<0.05$ *vs* 100 or 200 µmol/L EGCG group, respectively (A and B). The data shown in this figure are representative of 6 independent experiments, showing similar results.

A

B

EGCG (µmol/L)	Survival[a)]	Apoptosis		Necrosis[d)]
		Early[b)]	Late[c)]	
0	98.0±4.4	0.1±0.0	0.2±0.1	1.7±1.1
100	96.7±8.1	0.4±0.6	0.3±1.1	2.6±4.1
200	97.0±7.0	0.1±1.4	0.2±0.7	2.7±1.9
400	32.0±5.1[be]	3.7±2.5[be]	5.3±9.1[be]	59.0±13.4[be]
800	2.2±1.7[be]	1.5±3.3[be]	35.9±11.6[be]	60.4±8.8[be]

Figure 2. Dose-based differential apoptotic responses of nHDFs to EGCG. Cells were incubated with increasing concentrations (100–800 µmol/L) of EGCG for 24 h. DNA fragmentation (A) and apoptosis (B) in EGCG-treated nHDFs were measured by DNA ladder and Annexin V-FITC assays, respectively. The results are reported as a mean±SD and analyzed by a Tukey HSD test. $^{b}P<0.05$ *vs* non-treated control, $^{e}P<0.05$ *vs* 100 or 200 µmol/L EGCG group, respectively (lower table in B). The data shown in this figure are representative of 6 independent experiments, showing similar results.
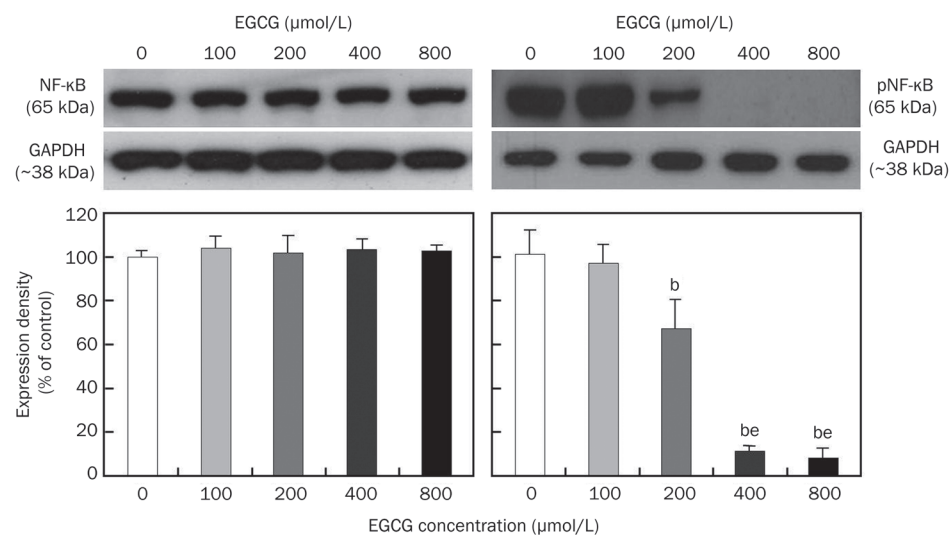
Figure 3. Dose-based differential modulation of pNF-κB expression in nHDFs by EGCG. Cells were incubated with increasing concentrations (100–800 µmol/L) of EGCG for 24 h. Expression levels of NF-κB/p65 and pNF-κB/p65 proteins in EGCG-treated nHDFs were detected by immunoblot analysis as described in Materials and methods. Results from representative experiments were normalized to GAPDH expression by densitometry. The quantitative results are shown in the lower panel. The results are reported as a mean±SD and analyzed by a Tukey HSD test. $^{b}P<0.05$ *vs* non-treated control, $^{e}P<0.05$ *vs* 100 or 200 µmol/L EGCG group, respectively.

higher concentrations (400 and 800 µmol/L) of EGCG, while at 200 µmol/L, slight inhibition of pNF-κB/p65 expression occurred. This EGCG-mediated pattern of regulation of the pNF-κB/p65 in the cells was somewhat similar to the pattern of regulation of proliferation. These results suggest that pNF-κB/p65 activation and translocation may be dose-differentially regulated by EGCG.

Effect of EGCG on the expression of cell cycle-related genes and proteins in nHDFs

A cDNA microarray analysis was employed to evaluate the effect of EGCG on the expression level of cell cycle-related genes. The microarray contained oligonucleotide probes representing 3096 human genes and included 50 cell cycle-related genes. Although a total of 3096 genes were screened in EGCG-treated nHDFs, the expression of 1520 genes was statistically reliable with respect to the control. The expression of only 23 genes was more than 2-fold up-regulated and that of only 61 genes was 2-fold down-regulated in response to 200 µmol/L EGCG compared with non-treated cells. Among the cell cycle-related genes, some genes were significantly down-regulated in response to EGCG treatment (Table 1). These

Table 1. List of significantly down-regulated/up-regulated cell cycle-related genes in nHDFs after EGCG treatment.

Gene (Symbol)	Role	Fold
Cyclin A2 (CCNA2)	Essential for S phase & G_2/M phase transition	0.2
Cyclin B1 & B2 (CCNB1 & CCNB2)	Essential for mitosis, associates with cell division cycle 2 (CDC2)	0.3
Cyclin-dependent kinase 1 (CDK1 or CDC2)	Complexes with cyclin A & B, essential for G_2/M phase transition	0.2
Protein kinase, membrane associated tyrosine/threonine 1 (PKMYT1)	Inactivates CDC2 and negatively regulates cell cycle G_2/M transition	0.3
CDK inhibitor 1A (CDKN1A or p21)	Inhibits cyclin-CDK2 or -CDK4 complexes, regulates G_1 phase	3.3

genes included cyclin (CCN) A2, CCNB1/B2 and their regulatory kinase, cyclin-dependent kinase 1 (CDK1), which function at S phase and the G_2/M phase transition. Protein kinase, membrane associated tyrosine/threonine 1 (PKMYT1), which inactivates the cell division cycle 2 (CDC2 or CKD1) protein and negatively regulates the cell cycle G_2/M transition, was also significantly down-regulated. In contrast, CDK inhibitor A1 (CDKN1A or p21), a G_1 phase regulator, was significantly up-regulated upon EGCG treatment. Other cell cycle-related genes, such as CCNC, CCND3, CCNF, CDC20, and CKS2 (CDC28 protein kinase regulatory subunit 2), were slightly down-regulated (Table 2). Interestingly, CDK2 and CDK6, which complex with CCNE and CCND, respectively, and are essential for the G_1/S phase transition and early G_1 phase, were not affected by EGCG treatment. The expression levels of the other cell cycle-related genes are listed in Supplementary Table S1. The detailed expression levels of other genes significantly changed by EGCG treatment relative to the controls are listed in Supplementary Tables S2 and S3.

Figure 4 demonstrates the regulatory effects of EGCG on the expression level of cell cycle-related proteins in nHDFs. The protein expression levels of CCNA, CCNB1, and CDK1 were significantly decreased by 200 μmol/L EGCG treatment for 24 h, but they were noticeably restored after 72 h of EGCG removal. In contrast, the expression level of CDKN1A was slightly suppressed after EGCG treatment, but remained at low levels 72 h after the removal of EGCG. These data suggest that the expression of cell cycle-related genes and proteins

can be reversibly regulated by EGCG exposure and removal. These results agreed well with those of the cell cycle profile, which showed that the cell cycle of cells treated with EGCG for 24 h was delayed at G_0/G_1 phase and restored after EGCG removal.

Cellular uptake of FITC-EGCG in nHDFs
To determine and compare the incorporation of FITC-EGCG into the cytoplasm of nHDFs and its further nuclear translocation between low- and high-dose treatments, confocal microscopy was performed in the cells treated with 100 and 400 μmol/L FITC-EGCG. The cellular uptake of FITC-EGCG was not observed until approximately 4 h of culture and was most dramatic between 4 and 6 h (data not shown). As the incubation time progressed, FITC-EGCG became concentrated in the cytoplasm and then localized to different sites within the cells. Although the cellular response to FITC-EGCG and its binding pattern to receptors would be different from those of EGCG, the low dose (100 μmol/L) of FITC-EGCG was clearly observed to be adsorbed onto the membrane and internalized into the cytoplasm of nHDFs, particularly with intense bright green fluorescence after 24 h (Figure 5A). At higher magnification, FITC-EGCG was clearly found to be widely distributed in the cytosol of the cells and partially translocated into the nucleus, bound to endosome-like structures. However, the incorporation of FITC-EGCG into the cells was appreciably decreased by pretreatment with free EGCG (data not shown), suggesting that a negligible amount of conjugate accumulates

Table 2. List of minimally regulated or unaffected cell cycle-related genes in nHDFs after EGCG treatment

| Gene (Symbol)	Role	Fold
Cyclin C (CCNC)	Important regulator of G_1 phase	0.8
Cyclin D1 (CCND1)	Essential for G_1 phase, with CDK4 and CDK6	0.9
Cyclin D3 (CCND3)	Essential for G_1 phase, with CDK4 and CDK6	0.7
Cyclin F (CCNF)	Important regulator of cell cycle transitions	0.6
Cyclin T1 (CCNT1)	Functions as regulators of CDKs	0.9
Cyclin-dependent kinase 2 (CDK2)	Complexes with cyclin A & E, essential for G_1/S phase transition	0.6
Cyclin-dependent kinase 6 (CDK6)	Complexes with cyclin D1, D2 & D3, essential for early G_1 phase	0.6
Cyclin-dependent kinase 9 (CDK9)	Complexes with CCNT and CCNK	0.9
Cyclin-dependent kinase 10 (CDK10)	Regulator of G_2/M phase	0.9
Cell division cycle 20 (CDC20)	Functions at multiple points in the cell cycle	0.7
Cell division cycle 23 (CDC23)	Essential for cell cycle progression through the G_2/M transition	0.9
CDC28 protein kinase regulatory subunit 2 (CKS2)	Binds to CDKs, essential for their biological functions	0.6
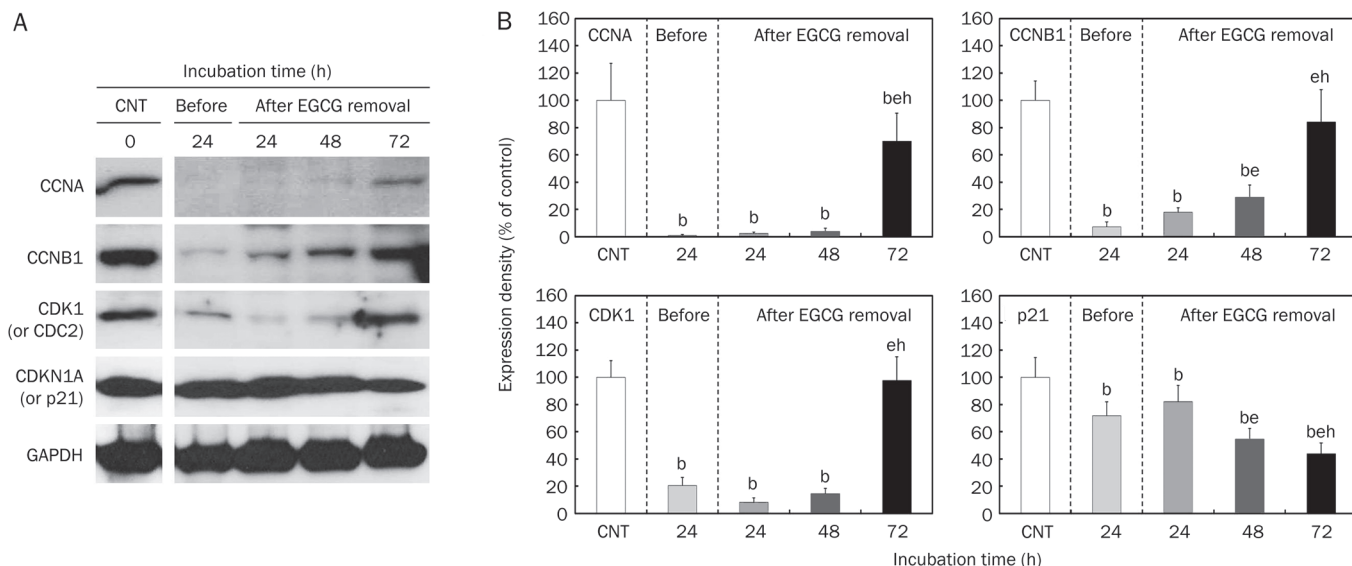
Figure 4. Effects of EGCG on expression of cell cycle-related proteins in nHDFs. After treatment with 200 µmol/L EGCG for 24 h, EGCG was removed from the cultured cells followed by further incubation for up to 72 h. The expression of cell cycle-related proteins in nHDFs (A) was determined by Western blotting as described in Materials and methods. Results from representative experiments were normalized to GAPDH expression by densitometry. The quantitative results are shown in the right panel (B). The results are reported as a mean±SD and analyzed by a Tukey HSD test. [b]$P<0.05$ *vs* non-treated control, [e]$P<0.05$ *vs* 24 h after EGCG treatment group, [h]$P<0.05$ *vs* 24 or 48 h after EGCG removal group.

within cells by virtue of competition with unlabelled EGCG for membrane binding sites. This cellular uptake pattern of FITC-EGCG in normal fibroblasts was completely different from the pattern in human fibrosarcoma (HT-1080) cells (as their cancer counterparts)[21] and murine fibroblastic (L-929) cells (Supplementary Figure S1)[20]. Additional fluorescence microscopic observation demonstrated the time course of cellular uptake of FITC-EGCG in cultured nHDFs. FITC-EGCG was clearly observed in both the membrane and the cytoplasm of the cells until 10 d, despite the removal of FITC-EGCG from the culture medium (Supplementary Figure S2).

Confocal micrographs of nHDFs detached due to apoptosis mediated by a higher dose (400 µmol/L) of FITC-EGCG showed that FITC-EGCG was still incorporated into the cytoplasm and even into the nucleus of the detached cells (Figure 5B). Both the membrane and the nucleus of detached nHDFs were too damaged to delineate due to apoptosis. Furthermore, the cells that were still attached but adversely affected by FITC-EGCG showed typical apoptotic appearances, including blebbing, nuclear swelling, and membrane deterioration, whereas they were subjected to the nuclear translocation of FITC-EGCG like their cancer counterparts[21]. These results imply that FITC-EGCG at an almost non-toxic concentration can be incorporated into the cytosol of the cells through binding to specific receptors and forming complexes with them. Furthermore, FITC-EGCG may be differentially translocated into the nucleus in nHDFs *vs* HT-1080 cells and L-929 cells, which contributes to the reversible regulation of the cell cycle and leads to cytoprotection.

Discussion

In the present study, we demonstrated that the dose-differential effects of EGCG were associated with the reversible regulation of the expression of cell cycle-related genes and proteins in nHDFs. Although several studies comparing the effects of EGCG on cancer cells and their normal counterparts have been reported previously[5–7], it has not been clear whether these pharmacological effects of EGCG are related to the reversible regulation of the cell cycle mediated by EGCG incorporated into the cells. Natural dietary anti-cancer chemopreventive compounds, such as polyphenols (*eg*, EGCG and curcumin), isothiocyanates (*eg*, sulforaphane and phenethyl isothiocyanate) and their combinations, are known to possess redox-mediated differential signaling mechanisms that lead to cytoprotection of normal cells *vs* cytotoxicity in tumor cells[22]. Our studies have shown that EGCG did not induce growth inhibition, cell cycle deregulation, or apoptosis of normal fibroblasts at 200 µmol/L, which is a concentration that would be high enough to affect their cancer counterparts (Figures 1 and 2). This result suggests that EGCG or its derivatives can be developed as agents to selectively eliminate cancer cells without affecting normal cells. Other previous studies have primarily used concentrations of 40 to 100 µmol/L to demonstrate differential effects of EGCG on cancerous cells *vs* their normal counterparts[5–7]. Even these concentrations are not physiological[23], but provide a framework for understanding the differential effects of EGCG. Here, we employed 200 µmol/L as a critical concentration to define the mechanistic basis of the differential effects of EGCG. Although this concentration is much higher than that used in other studies,
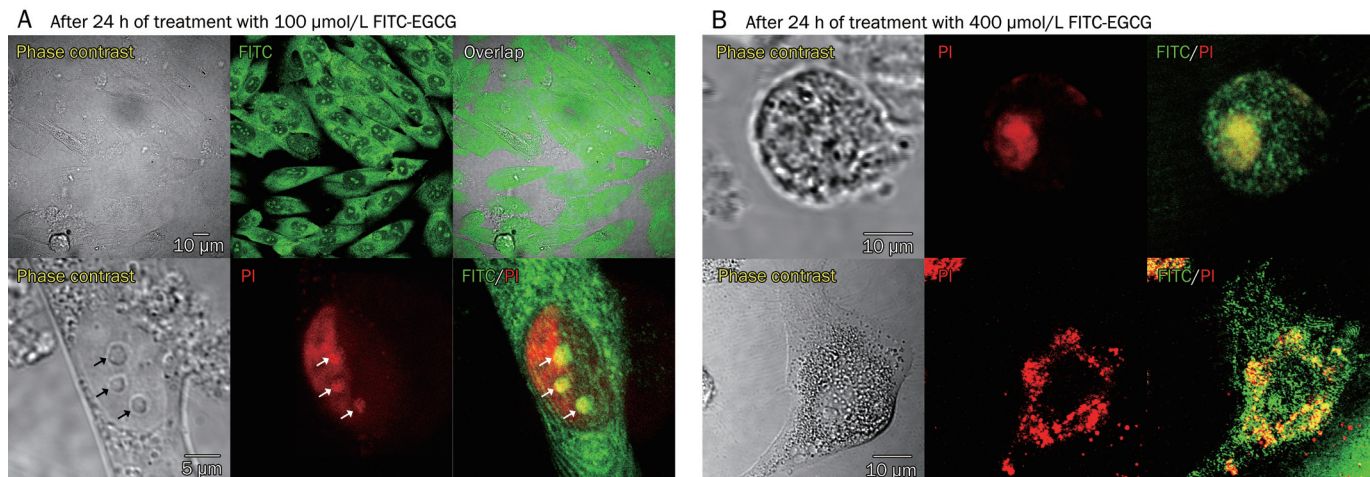
Figure 5. Cellular uptake of FITC-EGCG in nHDFs. Cells were incubated with 100 μmol/L (A) and 400 μmol/L (B) FITC-EGCG for 24 h and then observed under a confocal laser scanning microscope. The micrographs shown in this figure are representative of 6 independent experiments, showing similar results [Original magnification: ×500 and ×2000 (A, upper and lower, respectively), and ×1800 (B)]. Arrows in A indicates FITC-EGCG translocated into the nucleus.

the LC$_{50}$ value of EGCG on growth inhibition was estimated to be approximately 600 μmol/L in nHDFs (Supplementary Table S4). Moreover, HT-1080 cells were more sensitive to EGCG and had a much lower LC$_{50}$ value (200 μmol/L) than that of nHDFs[21]. Therefore, 200 μmol/L EGCG was considered suitable for understanding the dose-differential effects of EGCG on normal *vs* cancer fibroblasts. These results suggest the possibility that appropriate concentrations of EGCG may inhibit the growth of certain cancer cells, but have no apparent adverse effect on the growth of their normal counterparts.

We also showed that EGCG displayed a dose-differential regulatory effect on pNF-κB expression, but not on NF-κB expression (Figure 3). Perkins *et al* have found that specific CDKs regulate NF-κB-mediated transcriptional activation through interactions with the coactivator p300 and that the transcriptional activation domain of RelA (p65) interacts with an amino-terminal region of p300 that is distinct from a carboxyl-terminal region of p300 required for binding to the CCNE-CDK2 complex[24]. According to their report, CDKN1A or a dominant negative CDK2, which inhibits p300-associated CCNE-CDK2 activity, stimulates NF-κB-dependent gene expression, and the interaction of NF-κB and CDKs through the p300 and CREB-binding protein coactivators provides a mechanism for the coordination of transcriptional activation with cell cycle progression. Increasing evidence has indicated that the development of selective NF-κB inhibitors may represent a promising therapeutic tool to sensitize tumor cells to apoptosis and increase the efficacy of conventional anticancer drugs in a wide spectrum of malignancies[25].

In general, cDNA microarray analysis provides extensive information on global gene expression. Indeed, the data presented here demonstrated the global regulation of multiple genes involved in cell survival, cell cycle, and apoptosis that are considered some of the most important factors for cytoprotection[16]. The genes that changed over 2-fold, namely either

≥2 or ≤1/2, constituted only 5.5% (84 genes) of the genes with statistical reliability (Table 1 and Supplementary Tables S1–S3). Our findings from the cDNA microarray showed that 20% (10 genes) of cell cycle-related genes were strongly affected by EGCG treatment. Among the cell cycle-related genes, those that were the most affected by EGCG treatment were CCNs and CDKs directly involved in cell cycle regulation. Interestingly, a substantial difference in the response to EGCG among the cell cycle-related genes was present. CCNA2, CCNB1/B2, and CDK1, essential for the G$_2$/M phase transition, were strongly suppressed, whereas CCNC, CCND1/3, CDK2, and CDK6, essential for G$_1$ phase and the G$_1$/S phase transition, were less suppressed (Tables 1 and 2). This cell cycle delay at the G$_0$/G$_1$ phase showed a proper correlation with the result of the cell cycle assay (Figure 1B). Based on the results of a cell growth assay and cytometry, cellular responses such as proliferation and cell cycle progression can be predicted to be regulated by cell cycle-related genes that were changed over 2-fold upon EGCG treatment. Therefore, the reversible effects of EGCG may allow its safe usage in cell protection for chemotherapy[16, 18]. Our hypothesis was further verified by finding highly positive correlations with the results from immunoblotting that showed similar patterns to those of the microarray data (Figure 4). Removal of EGCG from the culture medium restored the expression of cell cycle-related proteins to the levels before EGCG treatment, which suggests that the effect of EGCG on the cell cycle is reversible. EGCG reduced the number of proliferating nHDFs cells by slowing the transit through the S and G$_2$/M phases, by delaying cell cycle at the G$_1$ phase, or even by inducing apoptotic cell death.

We also showed that the cellular uptake of FITC-EGCG in normal fibroblasts was different from that in a fibroblastic cell line (Figure 5 and Supplementary Figure S1) in their cancer counterparts (HT-1080 cells)[21]. These cellular uptake patterns were involved as important contributors to the dose-

differential growth inhibitory, cell cycle regulatory, and apoptotic responses of EGCG. Although the exact mechanism of the incorporation of EGCG into cells has not been fully elucidated, some evidence has been reported that EGCG is bound to the membrane and incorporated into the cytosol and the nucleus of cancer cell lines (such as PC-9 and HT-29 cells) treated with [³H]EGCG[8, 26]. These quantitative results using [³H]EGCG agree well with our qualitative results showing that the FITC-EGCG was incorporated into the cytosol of fibroblastic cells[20, 21]. However, the nuclear translocation pattern of FITC-EGCG was quite different in nHDFs *vs* HT-1080 cells and L-929 cells (Supplementary Figure S2), which would lead to the reversible regulation of the cell cycle and cytoprotection of normal fibroblasts. These phenomena can be related in part to the intrinsic characteristics of EGCG as a polyphenolic compound. EGCG is amphipathic and easily binds to extracellular matrices, lipid membranes or any type of intracellular protein[27-29]. Therefore, EGCG seems to be able to be incorporated into the cytosol of fibroblastic cells and further translocated into the nucleus and may modulate the exogenous signals directed to genes required for the survival and apoptosis of the cells. Recent studies have demonstrated that expression of the metastasis-associated 67 kDa laminin receptor might confer EGCG responsiveness to cancer cells at physiologically relevant concentrations, suggesting that the gallate moiety of EGCG may be critical for receptor binding and subsequent activity[30, 31]. Moreover, the observation that nucleic acids extracted from catechin-treated cells were colored implied that because both galloyl and catechol groups of EGCG were essential for DNA and RNA binding, both groups seemed to hold strands of DNA and RNA via their branching structure[32, 33].

Taking these results into consideration, we conclude that EGCG internalized into normal fibroblasts can dose-differentially regulate the expression of cell cycle-related genes and proteins and exert cytoprotective effects on the cells through a feasible mechanism of action (Supplementary Figure S3). This dose-differential regulatory activity of EGCG may be exploited to craft strategies using EGCG for the cytoprotection of normal cells and the chemoprevention of cancer cells.

Abbreviations

CCN, Cyclin; CDC, cell division cycle; CDK, cyclin-dependent kinase; CDKN1A, CDK inhibitor 1A; CKS2, CDC28 protein kinase regulatory subunit 2; EGCG, (–)epigallocatechin-3-gallate; FITC, fluorescein isothiocyanate; FITC-EGCG, FITC-conjugated EGCG; GAPDH, glyceraldehyde-3-phosphate dehydrogenase; nHDFs, neonatal human dermal fibroblasts; PBS, phosphate-buffered saline; pNF-κB/p65, phosphorylated nuclear factor-κB/p65; PI, propidium iodide; PKMYT1, protein kinase, membrane associated tyrosine/threonine 1; SD, standard deviation; WST-8, water soluble tetrazolium salt.

Acknowledgements

Author contribution

Dong-Wook HAN, Mi Hee LEE, and Jong-Chul PARK conceived and designed the study; Dong-Wook HAN and Mi Hee LEE performed the research and analyzed the data; Dong-Wook HAN, Hak Hee KIM, and Suong-Hyu HYON wrote the manuscript; Jong-Chul PARK edited the manuscript and provided the funding support for the studies.

Supplementary information

Additional experimental details for the microarray analysis and cytotoxicity assay are provided with the results for significantly down-regulated cell cycle-related genes in nHDFs after EGCG treatment (Table S1), significantly down-regulated/up-regulated apoptosis-related genes in nHDFs after EGCG treatment (Table S2), significantly down-regulated/up-regulated signal transduction-related genes in nHDFs after EGCG treatment (Table S3), and LC_{50} values of EGCG against various phenotypes of primary cells or cell lines (Table S4). Other experimental details for confocal and fluorescence microscopy are provided with the results for the cellular uptake of FITC-EGCG in L-929 cells (Figure S1) and the time course of cellular uptake of FITC-EGCG in cultured nHDFs (Figure S2) as well as a discussion of the feasible mechanism of action of EGCG (Figure S3).

These are available at Acta Pharmacologica Sinica website of NPG.

References

1 Na HK, Surh YJ. Intracellular signaling network as a prime chemopreventive target of (–)-epigallocatechin gallate. Mol Nutr Food Res 2006; 50: 152–9.

2 Khan N, Afaq F, Saleem M, Ahmad N, Mukhtar H. Targeting multiple signaling pathways by green tea polyphenol (–)-epigallocatechin-3-gallate. Cancer Res 2006; 66: 2500–5.

3 Kwon KH, Barve A, Yu S, Huang MT, Kong AN. Cancer chemoprevention by phytochemicals: potential molecular targets, biomarkers and animal models. Acta Pharmacol Sin 2007; 28: 1409–21.

4 Nair S, Barve A, Khor TO, Shen GX, Lin W, Chan JY, *et al*. Regulation of Nrf2- and AP-1-mediated gene expression by epigallocatechin-3-gallate and sulforaphane in prostate of Nrf2-knockout or C57BL/6J mice and PC-3 AP-1 human prostate cancer cells. Acta Pharmacol Sin 2010; 31: 1223–40.

5 Ahmad N, Feyes DK, Nieminen AL, Agarwal R, Mukhtar H. Green tea constituent epigallocatechin-3-gallate and induction of apoptosis and cell cycle arrest in human carcinoma cells. J Natl Cancer Inst 1997; 89: 1881–6.

6 Ahmad N, Gupta S, Mukhtar H. Green tea polyphenol epigallocatechin-3-gallate differentially modulates nuclear factor-κB in cancer cells versus normal cells. Arch Biochem Biophys 2000; 376: 338–46.

7 Chen ZP, Schell JB, Ho CT, Chen KY. Green tea epigallocatechin gallate shows a pronounced growth inhibitory effect on cancerous cells but not on their normal counterparts. Cancer Lett 1998; 129:

173–9.

8   Okabe S, Suganuma M, Hayashi M, Sueoka E, Komori A, Fujiki H. Mechanisms of growth inhibition of human lung cancer cell line, PC-9, by tea polyphenols. Jpn J Cancer Res 1997; 88: 639–43.

9   Kohri T, Nanjo F, Suzuki M, Seto R, Matsumoto N, Yamakawa M, *et al*. Synthesis of (−)-[4-^{3}H]epigallocatechin gallate and its metabolic fate in rats after intravenous administration. J Agric Food Chem 2001; 49: 1042–8.

10 Suganuma M, Okabe S, Oniyama M, Tada Y, Ito H, Fujiki H. Wide distribution of [^{3}H](−)-epigallocatechin gallate, a cancer preventive tea polyphenol, in mouse tissue. Carcinogenesis 1998; 19: 1771–6.

11 Swezey RR, Aldridge DE, LeValley SE, Crowell JA, Hara Y, Green CE. Absorption, tissue distribution and elimination of 4-[^{3}H]-epigallo-catechin gallate in beagle dogs. Int J Toxicol 2003; 22: 187–93.

12 Ahmad N, Gupta S, Husain MM, Heiskanen KM, Mukhtar H. Differential antiproliferative and apoptotic response of sanguinarine for cancer cells versus normal cells. Clin Cancer Res 2000; 6: 1524–8.

13 Donnerstag B, Ohlenschlager G, Cinatl J, Amrani M, Hofmann D, Flindt S, *et al*. Reduced glutathione and S-acetylglutathione as selective apoptosis-inducing agents in cancer therapy. Cancer Lett 1996; 110: 63–70.

14 Khan N, Adhami VM, Mukhtar H. Apoptosis by dietary agents for prevention and treatment of cancer. Biochem Pharmacol 2008; 76: 1333–9.

15 Ramos S. Cancer chemoprevention and chemotherapy: dietary polyphenols and signalling pathways. Mol Nutr Food Res 2008; 52: 507–26.

16 Bae JY, Kanamune J, Han DW, Matsumura K, Hyon SH. Reversible regulation of cell cycle-related genes by epigallocatechin gallate for hibernation of neonatal human tarsal fibroblasts. Cell Transplant 2009; 18: 459–69.

17 Hyon SH, Kim DH. Hibernation of mammalian cells at a living body temperature. Biotechnol Bioprocess Eng 2001; 6: 289–92.

18 Matsumura K, Kim JY, Tsutsumi S, Hyon SH. Hibernation, reversible cell growth inhibition by epigallocatechin-3-O-gallate. J Biotechnol 2007; 127: 758–64.

19 Park JC, Park BJ, Suh H, Park BY, Rah DK. Comparative study on motility of the cultured fetal and neonatal dermal fibroblasts in extracellular matrix. Yonsei Med J 2001; 42: 587–94.

20 Han D-W, Matsumura K, Kim B, Hyon SH. Time-dependent intracellular trafficking of FITC-conjugated epigallocatechin-3-O-gallate in L-929 cells. Bioorg Med Chem 2008; 16: 9652–9.

21 Lee MH, Han DW, Hyon SH, Park JC. Apoptosis of human fibrosarcoma HT-1080 cells by epigallocatechin-3-O-gallate via induction of p53 and caspases as well as suppression of Bcl-2 and phosphorylated nuclear factor-κB. Apoptosis 2011; 16: 75–85.

22 Nair S, Li W, Kong AN. Natural dietary anti-cancer chemopreventive compounds: redox-mediated differential signaling mechanisms in cytoprotection of normal cells versus cytotoxicity in tumor cells. Acta Pharmacol Sin 2007; 28: 459–72.

23 Chow HH, Cai Y, Hakim IA, Crowell JA, Shahi F, Brooks CA, *et al*. Pharmacokinetics and safety of green tea polyphenols after multiple-dose administration of epigallocatechin gallate and polyphenon E in healthy individuals. Clin Cancer Res 2003; 9: 3312–9.

24 Perkins ND, Felzien LK, Betts JC, Leung K, Beach DH, Nabel GJ. Regulation of NF-κB by cyclin-dependent kinases associated with the p300 coactivator. Science 1997; 275: 523–7.

25 Piva R, Belardo G, Santoro MG. NF-κB: a stress-regulated switch for cell survival. Antioxid Redox Signal 2006; 8: 478–86.

26 Hong J, Lu H, Meng X, Ryu JH, Hara Y, Yang CS. Stability, cellular uptake, biotransformation, and efflux of tea polyphenol (−)-epigallocatechin-3-gallate in HT-29 human colon adenocarcinoma cells. Cancer Res 2002; 62: 7241–6.

27 Palermo CM, Westlake CA, Gasiewicz TA. Epigallocatechin gallate inhibits aryl hydrocarbon receptor gene transcription through an indirect mechanism involving binding to a 90 kDa heat shock protein. Biochemistry 2005; 44: 5041–52.

28 Uekusa Y, Kamihira M, Nakayama T. Dynamic behavior of tea catechins interacting with lipid membranes as determined by NMR spectroscopy. J Agric Food Chem 2007; 55: 9986–92.

29 Yang D, Liu J, Tian C, Zeng Y, Zheng YH, Fang Q, *et al*. Epigallocatechin gallate inhibits angiotensin II-induced endothelial barrier dysfunction via inhibition of the p38 MAPK/HSP27 pathway. Acta Pharmacol Sin 2010; 31: 1401–6.

30 Tachibana H, Koga K, Fujimura Y, Yamada K. A receptor for green tea polyphenol EGCG. Nat Struct Mol Biol 2004; 11: 380–1.

31 Umeda D, Yano S, Yamada K, Tachibana H. Green tea polyphenol epigallocatechin-3-gallate signaling pathway through 67-kDa laminin receptor. J Biol Chem 2008; 283: 3050–8.

32 Kuzuhara T, Sei Y, Yamaguchi K, Suganuma M, Fujiki H. DNA and RNA as new binding targets of green tea catechins. J Biol Chem 2008; 281: 17446–56.

33 Kuzuhara T, Tanabe A, Sei Y, Yamaguchi K, Suganuma M, Fujiki H. Synergistic effects of multiple treatments, and both DNA and RNA direct bindings on, green tea catechins. Mol Carcinog 2007; 46: 640–5.

npg

Original Article

Sulfated polymannuroguluronate inhibits Tat-induced SLK cell adhesion via a novel binding site, a KKR spatial triad

Yan-lin WU[1, #], Jing AI[2, #], Jing-ming ZHAO[3], Bing XIONG[4], Xiao-jie XIN[2], Mei-yu GENG[2], Xian-liang XIN[2, *], Han-dong JIANG[3, *]

[1]Department of Pharmacology and Glycobiology, School of Medicine and Pharmacy, Ocean University of China, Qingdao 266003, China; [2]Division of Anti-tumor Pharmacology, State Key Laboratory of Drug Research, Shanghai Institute of Materia Medica, Chinese Academy of Sciences, Shanghai 201203, China; [3]Division of Respiratory Medicine, Affiliated Hospital of Medical College, Qingdao University, Qingdao 266003, China; [4]Department of Medicinal Chemistry, State Key Laboratory of Drug Research, Shanghai Institute of Materia Medica, Chinese Academy of Sciences, Shanghai 201203, China

Aim: Sulfated polymannuroguluronate (SPMG), a candidate anti-AIDS drug, inhibited HIV replication and interfered with HIV entry into host T lymphocytes. SPMG has high binding affinity for the transactivating factor of the HIV-1 virus (Tat) via its basic domain. However, deletion or substitution of the basic domain affected, but did not completely eliminated Tat-SPMG interactions. Here, we sought to identify other SPMG binding sites in addition to the basic domain.
Methods: The potential SPMG binding sites were determined using molecular simulation and a surface plasmon resonance (SPR) based competitive inhibition assay. The effect of SPMG on Tat induced adhesion was evaluated using a cell adhesion assay.
Results: The KKR domain, a novel high-affinity heparin binding site, was identified, which consisted of a triad of Lys12, Lys41, and Arg78. The KKR domain, spatially enclosed SPMG binding site on Tat, functions as another binding domain for SPMG. Further functional evaluation demonstrated that SPMG inhibits Tat-mediated SLK cell adhesion by directly binding to the KKR region.
Conclusion: The KKR domain is a novel high-affinity binding domain for SPMG. Our findings provide important new insights into the molecular mechanisms of SPMG and a potential therapeutic intervention for Tat-induced cell adhesion.

Keywords: sulfated polymannuroguluronate; transactivating factor of the HIV-1 virus (Tat); binding site; Kaposi's sarcoma; heparin; mutation; HIV-1

Introduction

Kaposi's sarcoma (KS) is the most common tumor in human immunodeficiency virus (HIV)-infected patients and is a leading cause of mortality and morbidity in acquired immune deficiency syndrome (AIDS)[1–3]. KS is much more frequent and aggressive in the setting of HIV-1 infection, suggesting that HIV itself, or molecules produced during HIV infection, might play important roles in KS development and progression[4]. The transactivating factor of the HIV-1 virus (Tat), a polypeptide of 86–102 amino acids released from HIV-1 infected cells, contributes directly to KS pathogenesis[5]. In addition to the transactivation of HIV-1 gene expression, Tat can promote KS

cell adhesion through binding to integrins[6, 7]. Therefore, the inhibition of Tat activity could be a useful way to inhibit the development and progression of KS in AIDS patients.

Tat-driven activities depend precisely on its interaction with cell surface heparan sulfate (HS) and heparin through their negatively charged sulfate groups[8]. Conversely, free heparin inhibits the uptake of intracellular Tat and affects the cell surface interaction mediated by Tat[9–11]. The basic domain constituted by a stretch of repeated Arg and Lys residues has long been recognized as the sole contributor to this interaction, which is mediated by its heparin binding properties[9, 11–13]. However, our previous studies have challenged this notion by identifying a novel heparin-binding KKR domain (Lys12, Lys41, and Arg78) that helps facilitate Tat-driven β1 integrin activation and subsequent adhesion in a heparan sulfate proteoglycan (HSPG)-dependent manner[14]. These important insights into the binding profile between heparin and Tat will provide a more precise understanding of the comprehensive

---

# These two authors contributed equally to this work.
* To whom correspondence should be addressed.
E-mail jianghd@163.com (Han-dong JIANG);
      xinxianliang@hotmail.com (Xian-liang XIN)

roles of Tat and aid in the design of new therapeutic agents. Moreover, growing evidence shows that heparin and many heparin analogs represent potent extracellular Tat antagonists of possible therapeutic value[10, 15].

Sulfated polymannuroguluronate (SPMG), a new heparin-like sulfated polysaccharide extracted from brown algae, is rich in 1,4-linked β-*D*-mannuronate, with an average of 1.5 sulfates and 1.0 carboxyl groups per sugar residue and an average molecular weight of 10 kDa. SPMG has entered Phase II clinical trials in China, making it the first marine sulfated polysaccharide with the potential to be approved as an anti-AIDS drug. Our previous *in vitro* and *in vivo* studies demonstrated that SPMG inhibited HIV replication and interfered with HIV entry into host T lymphocytes. We further demonstrated that Tat exhibited a high binding affinity for SPMG via its basic domain, thereby inhibiting Tat-induced AIDS-KS[16, 17]. We also found that substitution of the basic domain affected, but failed to completely eliminate, Tat-SPMG interactions. These results led us to hypothesize that there might exist other SPMG binding sites in addition to the basic domain. In this article, using molecular simulation combined with a surface plasmon resonance (SPR)-based competitive inhibition assay, we found that the KKR domain, a newly identified high-affinity heparin binding site[14], functioned as another binding domain for SPMG. Further functional evaluation demonstrated that SPMG inhibited Tat-mediated SLK cell adhesion by directly binding to the KKR region.

Materials and methods
Materials
SPMG, depolymerized by acidic hydrolysis, and then sulfatation (M_w about 8000 Da), was provided by the Marine Drug and Food Institute (Ocean University of China, Qingdao, China). Heparin, HS, chondroitin sulfates A (CSA) and C (CSC), and hyaluronic acid (HA) were obtained from Sigma (St Louis, MO, USA). Anti-GST antibody (sc-459) was purchased from Santa Cruz Biotechnology, Inc (Santa Cruz, CA, USA).

Cell culture
SLK cells (derived from an endothelial-origin Kaposi's sarcoma) were kindly provided by the NIH AIDS Research Division. The cells were maintained in RPMI-1640 medium supplemented with 10% heat-inactivated fetal calf serum (FCS, Gibco Gaithersburg, MD, USA), 2 mmol/L *L*-glutamine, 100 U/mL penicillin, and 100 μg/mL streptomycin at 37 °C in a humidified incubator with 5% CO_2.

Computational docking modeling
The amino acid sequence of human T-lymphotropic virus 3 (Tat-III protein) was retrieved from the appropriate NCBI protein database (GI: 328765) and used to search for homologs in the Protein Data Bank (http://www.rcsb.org). Through a BLASTP search, it was found that the NMR structure of Tat-I (PDB entry: 1JFW) was the most homologous protein (83/86 aa, 96% identity)[18]. Therefore, the structure of Tat-I was used

as the template to create a 3D model of Tat-III using the MODELLER program[19]. Ten models were generated, and these 3D structures were optimized with a conjugate gradient minimization scheme followed by a restrained annealing molecular dynamics simulation. The model with the lowest value for the objective function was selected as the most representative Tat-III model for further study.

Structure-based analysis of our homology model of Tat-III was performed to search for SPMG binding sites using the newly developed AutoDock Vina program[20]. This program is two orders of magnitude faster than AutoDock4 and enabled us to search for binding sites over the whole surface of Tat-III. Additionally, it is based on the fast iterated local search global optimization of protein-ligand interactions, so the search time increases linearly with atom number. The input PDBQT files of Tat-III and three ligands (2-, 4-, and 8-SPMG) were prepared with AutoDockTools, and the docking operation algorithm was performed in a consistent manner. A large box encompassing the entire Tat-III structure, with dimensions 48 Å×48 Å×42 Å, was generated to take all possible SPMG binding sites into account. Then, the Vina program was applied to account for protein-ligand interactions using a newly developed scoring function that includes the terms gauss type steric interaction, repulsion interaction, hydrogen bond, and torsional free energy. Through large scale validation, the Vina program can significantly improve the accuracy of binding mode predictions[20]. Finally, the evaluation with the lowest binding energy was used to analyze ligand pose, and the interaction model of SPMG/Tat-III was illustrated with the program Pymol based on the docked complex structure[21].

Preparation of Tat and its mutants
Plasmid pGEX-2T (Amersham Pharmacia, Uppsala, Sweden) and pGST-Tat were kindly provided by Prof M GIACCA and M PRESTAI (International Centre for Genetic Engineering and Biotechnology, Trieste, Italy). Tat mutants were constructed using site-directed mutagenesis, yielding a series of GST-Tat mutants (Table 1).

Recombinant wild type HIV-1 Tat and the different Tat mutants were expressed in *Escherichia coli* as glutathione *S*-transferase (GST) fusion proteins and purified to homoge-

Table 1. Summary of mutated amino acids in the set of GST-Tat mutants.

Mutant name	Amino acids change
GST-Tat(G48-R57)A	Amino acids 48–57 (basic domain) → Ala
GST-TatK(12,41)A/R78A	Lys12, Lys41, Arg78 → Ala
GST-TatK12A	Lys12 → Ala
GST-TatK41A	Lys41 → Ala
GST-TatR78A	Arg78 → Ala
GST-TatK(12,41)A	Lys12, Lys41 → Ala
GST-TatK12A/R78A	Lys12, Arg78 → Ala
GST-TatK41A/R78A	Lys41, Arg78 → Ala
GST-Tat(G48-R57)A/K(12,41)A/R78A	Amino acids 48–57, Lys12, Lys41, Arg78 → Ala

neity from bacterial lysates by glutathione-sepharose affinity chromatography (Amersham Pharmacia) as described previously[14]. The purity and integrity of the protein product were routinely checked by SDS-polyacrylamide gel electrophoresis and 0.25% Coomassie brilliant blue R-250 staining. The identification of mutant products was further carried out by MS-MS spectral analysis. In addition, the similarity of the secondary structure of the mutated products to the native Tat protein was predicted using a position-specific scoring method[14]. The purified proteins were stored in aliquots at -80 °C until use[9].

Surface plasmon resonance assay

To characterize Tat binding with SPMG, kinetic properties and competitive inhibition were examined using a surface plasmon resonance assay (SPR, BIAcore X, Uppsala, Sweden). For this purpose, SPMG was immobilized to a CM5 sensor chip according to the established method[22, 23]. The immobilization procedure was carried out at 25 °C and at a constant flow rate of 5 µL/min in HBS-EP [0.01 mol/L HEPES, pH 7.4, 0.15 mol/L NaCl, 3 mmol/L EDTA, and 0.005% polysorbate 20 (*v/v*)]. To assess the real-time binding capacity, 50 µL of GST-Tat or the relevant mutant was injected over the sensor chip surface with the immobilized SPMG, followed by 5 min of washing with HBS-EP buffer. The sensor chip surface was regenerated using 2 mol/L NaCl. All binding experiments were performed at 25 °C with a constant flow rate of 15 µL/min HBS-EP. To correct for nonspecific binding and bulk refractive index change, a blank channel (FC2) without SPMG was employed as a control for each experiment. Sensorgrams for all binding interactions were recorded in real time and analyzed after subtraction of channel blanks. Changes in mass due to the binding response were recorded as resonance units (RU). Binding kinetics and affinities were calculated using BIAcore software 3.1. Competitive inhibition experiments were conducted with the same protocol, except that a 50 µL mixture of GST-Tat or the relevant mutant and inhibitors that had been preincubated for 3 min at 37 °C was used.

Cell adhesion assay

To guarantee that plates were coated with the same amount of each tested protein, anti-GST antibody was adsorbed to polystyrene microplates (Costar, Cambridge, MA, USA) by overnight incubation at 4 °C in 100 mmol/L carbonate buffer (pH 9.6) at a concentration of 10 µg/mL. The plates were subsequently washed three times with Tris-buffered saline+Tween 20 (TBS-T) and then filled with 1.25% BSA-PBS and incubated for 2 h at 37 °C. After three washes with TBS-T, 40 µg/mL of GST alone, GST-Tat or the relevant mutant Tat protein was added to the wells and incubated for 1 h at 37 °C. The plate was next washed three times with PBS-T. Then, 100 µL of SLK cell suspension was added to each well (3×10^5 cells/mL in RPMI-1640 with 10 % FCS). After incubation for 1 h at 37 °C in a 5% CO_2 atmosphere, non-adherent cells were removed by careful aspiration and three washes with RPMI 1640. Adherent cells were fixed, stained, and quantified as previously described[24]. A SPMG competition cell adhesion assay was conducted with the same procedure, except that SPMG at defined concentrations was added to each well. Each experiment was performed in triplicate and replicated three times.

Statistical analysis

Data were presented as means±SD, and differences were considered significant when $P<0.05$ as determined by Student's *t*-tests.

Results

Lys12, Lys41, and Arg78 triad is predicted as a novel SPMG binding site

Computational modeling was first employed with the aim of identifying potential SPMG binding sites. The homology model of Tat protein (Tat-III) constructed on the basis of NMR data was used as the target structure, and several SPMG oligosaccharides including di-, tetra-, and octa-saccharides were selected as docking probes. In the disaccharide SPMG model, SPMG was noted to preferentially interact with a triad of basic residues (Lys12, Lys41, and Arg78 (KKR); Figure 1A–1C, highlighted in yellow in Figure 1C).

Modeling of interactions with tetra- and octa-saccharides revealed similar results; the positively charged KKR triad plays an important role in the molecular recognition of SPMG probes by producing a highly conserved interaction with Tat-III. It should be noted that the oligosaccharide chain begins to stretch toward the basic domain (green for comparison, Figure 1D and 1E) as the probe length increases. As the length increases to a tetramer, a delicate interaction with residue Arg56 of the basic domain is established. The octamer follows the same path and approaches residue Arg53 (Figure 1D and 1E). Ideally, SPMG, if long enough, is proposed to fully extend to encompass both the KKR region and the whole basic domain.

The KKR domain is spatially enclosed to bind to SPMG

To characterize the Tat KKR triad engagement with SPMG, a series of Tat mutants were expressed in *E coli* as GST-Tat fusion proteins, purified from bacterial lysates by glutathione-agarose affinity chromatography, and checked by SDS-PAGE.

First, the EC_{50} binding capacity was evaluated. For this evaluation, a series of GST-Tat solutions with a range of concentrations (0.25, 0.5, 1, 2, or 4 µmol/L) were injected over an SPMG-immobilized sensor chip surface. RU_{max} values were generated using BIAcore evaluation 3.1 software, yielding an EC_{50} value of 1.5 µmol/L (data not shown); this value was used as a reference for subsequent experiments.

We next investigated whether KKR was an SPMG binding site, as predicted. A series of comparative studies were performed using all relevant mutants. We found that GST-Tat binding to SPMG exhibited a multi-phasic binding profile (Figure 2A), indicating the existence of more than one SPMG binding site. Notably, mutation of the basic domain still produced monophasic binding, further supporting the notion that a binding site for SPMG exists in addition to the basic domain (Figure 2B). Accordingly, the mutation of Lys12, Lys41, and
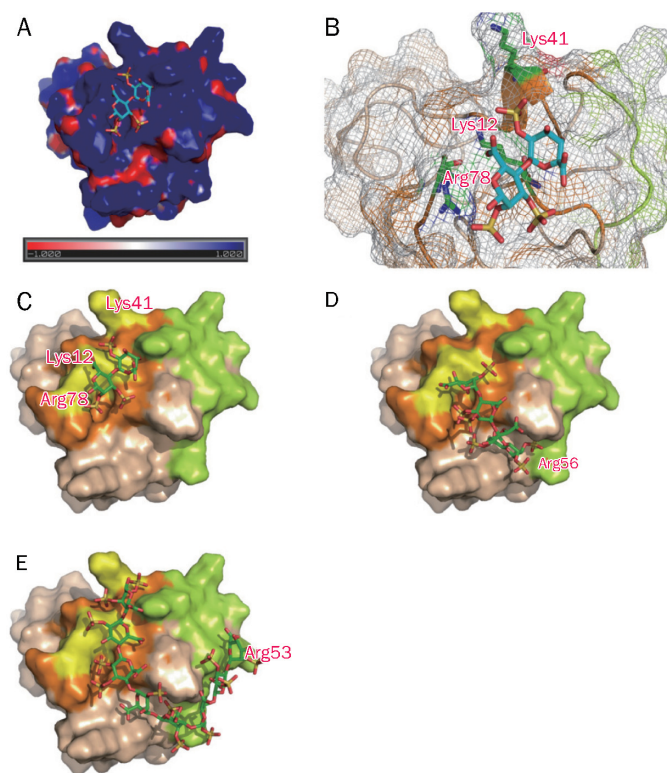
Figure 1. Computational docking model of HIV-Tat with SPMG-derived fragments. Predicted interactions between HIV-Tat and SPMG-derived fragments, including di- (A, B, and C), tetra- (D), and octa-saccharide (E) are indicated. Tat is represented by a surface and oligosaccharides by stick model. The Tat surface is colored by electrostatic potential in A. In C-E, it is wheat-colored, with the KKR region and basic domain highlighted in yellow and green, respectively. A close-up view of the binding interface between the di-saccharide and the KKR (Lys12, Lys41, and Arg78) region is shown in B, where Tat is shown in mesh form and the protein main chain is shown in cartoon style.

Arg78 to alanine [GST-Tat$_{K (12,41)A/R78A}$] displayed a markedly decreased binding potency for SPMG when compared to

wild-type GST-Tat (Figure 2C). Moreover, double-mutant GST-Tat$_{(G48-R57)A/K(12,41)A/R78A}$ led to complete abolishment of Tat-SPMG interactions (Figure 2C). These findings substantiate our hypothesis that Tat possesses another SPMG binding site, the KKR region.

We next clarified the contribution of the three basic residues as a whole and separately. Single, double, and triple mutations of the KKR region were constructed and their binding affinities (K_D) for immobilized SPMG were recorded and compared. K_D values were calculated using BIAcore evaluation 3.1 software. Mutation of a single residue (GST-Tat$_{K12A}$, GST-Tat$_{K41A}$, or GST-Tat$_{R78A}$) led to only a partial loss of SPMG binding affinity (K_D 0.112 nmol/L, 0.174 nmol/L, or 0.0729 nmol/L, respectively), with the Arg78 mutation (GST-Tat$_{R78A}$) influencing binding affinity the least (Table 2). Mutation of any two KKR residues (GST-Tat$_{K(12,41)A}$, GST-Tat$_{K12A/R78A}$, or GST-Tat$_{K41A/R78A}$) led to a significant loss of binding affinity with correspondingly decreased K_D values (1.04 nmol/L, 0.435 nmol/L and 0.205 nmol/L, respectively), with the Lys12, Lys41 mutation (GST-Tat$_{K(12,41)A}$) affecting binding the most (Table 2). Most significantly, concurrent mutation of all three residues produced a dramatic drop in SPMG binding affinity, with a resultant K_D value of 11 nmol/L (Table 2). These findings collectively indicated that Lys12, Lys41 and Arg78 cooperated as a whole to profoundly impact SPMG binding.

The KKR triad binds specifically to SPMG in a high affinity manner

We next sought to delineate the nature of the interaction between KKR and SPMG. We first assessed binding affinity. Various concentrations of GST-Tat, GST-Tat$_{(G48-R57)A}$, and GST-Tat$_{K(12,41)A/R78A}$ were injected over an SPMG-immobilized sensor chip surface (Figure 3A–3C). We found that GST-Tat bound to SPMG (K_D=24.2 pmol/L) (Table 2). Mutation of the basic domain (leaving the KKR domain intact and thus solely responsible for the strength of the Tat KKR-SPMG interaction) had little effect on binding affinity (K_D=26.5 pmol/L). Nota-
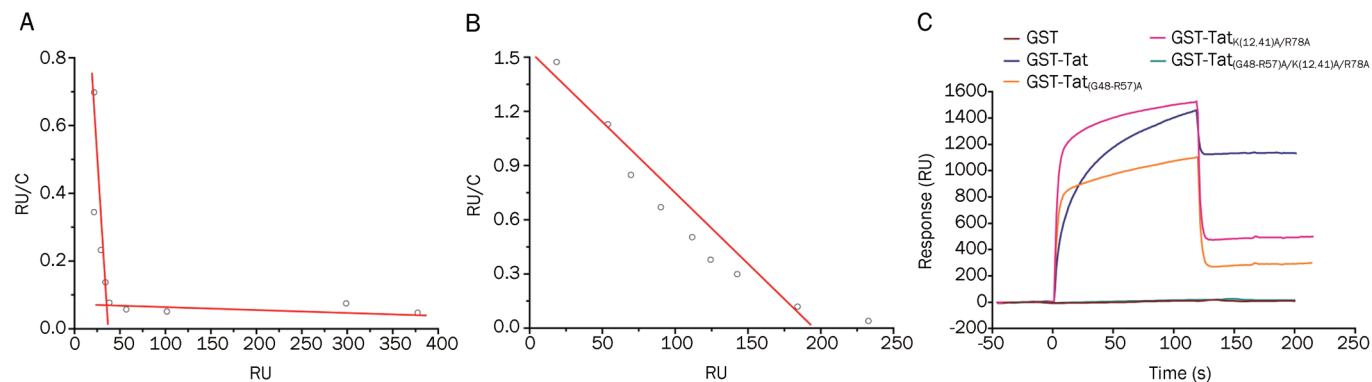
Figure 2. Identification of the Tat Lys12, Lys41, Arg78 (KKR) domain as a new SPMG binding site. (A, B) Scatchard plot analysis of GST-Tat (A) and GST-Tat$_{(G48-R57)A}$ (B) with immobilized SPMG. A series of concentrations of GST-Tat or GST-Tat$_{(G48-R57)A}$ were injected over the SPMG-immobilized sensor chip surface. The binding potency/concentration (RU/C) was plotted *versus* RU. (C) Interaction of GST-Tat and its mutants with biotinylated SPMG immobilized on a CM5 sensor chip. GST-Tat or the appropriate mutants (1.5 μmol/L) were injected over the SPMG-immobilized sensor chip. The binding RU was recorded as binding potency.

Table 2. The affinity parameters for binding of GST-Tat and its mutants to SPMG.

Analyte	K_A [1/(mol·L^{-1})]	K_D (mol/L)
GST-Tat	4.13×10^{10}	2.42×10^{-11}
GST-Tat$_{(G48-R57)A}$	3.77×10^{10}	2.65×10^{-11}
GST-Tat$_{K(12, 41)A/R78A}$	9.08×10^{7}	1.10×10^{-8}
GST-Tat$_{K12A}$	8.93×10^{9}	1.12×10^{-10}
GST- Tat$_{K41A}$	5.73×10^{9}	1.74×10^{-10}
GST- Tat$_{R78A}$	1.37×10^{10}	7.29×10^{-11}
GST- Tat$_{K(12, 41)A}$	9.65×10^{8}	1.04×10^{-9}
GST-Tat$_{K12A/R78A}$	2.30×10^{9}	4.35×10^{-10}
GST- Tat$_{K41A/R78A}$	4.88×10^{9}	2.05×10^{-10}

K_A: equilibrium association constant; K_D: equilibrium dissociation constant. Data shown are representative of three independent experiments with similar results.

bly, mutation of the KKR region caused a remarkable decrease in GST-Tat-SPMG binding (K_D=11 nmol/L), representing the K_D value of the basic domain in isolation. This K_D represents a 500 fold decrease in binding affinity compared with that of wild-type GST-Tat (Table 2). Based on this comparison, we conclude that the KKR spatial region dominates Tat-SPMG binding compared to the basic domain.

For further confirmation, we conducted a series of competitive inhibition assays. Wild-type GST-Tat or the appropriate Tat mutants (1.5 µmol/L) were injected over an SPMG-immobilized chip in the presence of varying concentrations of SPMG as a competitive inhibitor. Free SPMG was able to inhibit the binding of either GST-Tat or the corresponding mutant to immobilized SPMG in a dose-dependent manner (Figure 4A–4C). Notably, mutation of the basic domain (GST-Tat$_{(G48-R57)A}$) produced an IC$_{50}$ value (1.803 µg/mL) comparable to that of GST-Tat (1.808 µg/mL), while mutation of the KKR region (GST-Tat$_{K(12,41)A/R78A}$) yielded an IC$_{50}$ value of 3.259 µg/mL, almost twice that of GST-Tat. These data further support the notion that the KKR spatial domain contributes dramatically to SPMG binding and represents an extremely high-affinity SPMG binding site.

We then characterized KKR binding specificity via the introduction of soluble glycosaminoglycans (GAGs). Both heparin and HS were able to compete for KKR binding to SPMG, yielding IC$_{50}$ values of 0.633 µg/mL and 41.314 µg/mL, respectively. By contrast, other GAGs including CSA, CSC, and HA, even at concentrations up to 125 µg/mL, showed little or no inhibition of this interaction (Figure 4D). These findings suggest the binding specificity of the KKR region for SPMG is high.

Collectively, these data support the hypothesis that the KKR region of Tat, distinct from the well-recognized linearly contiguous basic domain, serves as a binding motif for SPMG that has extremely high affinity and is highly specific.

SPMG inhibits KKR-facilitated Tat-mediated SLK cell adhesion.
Because the KKR region facilitates Tat-mediated SLK cell
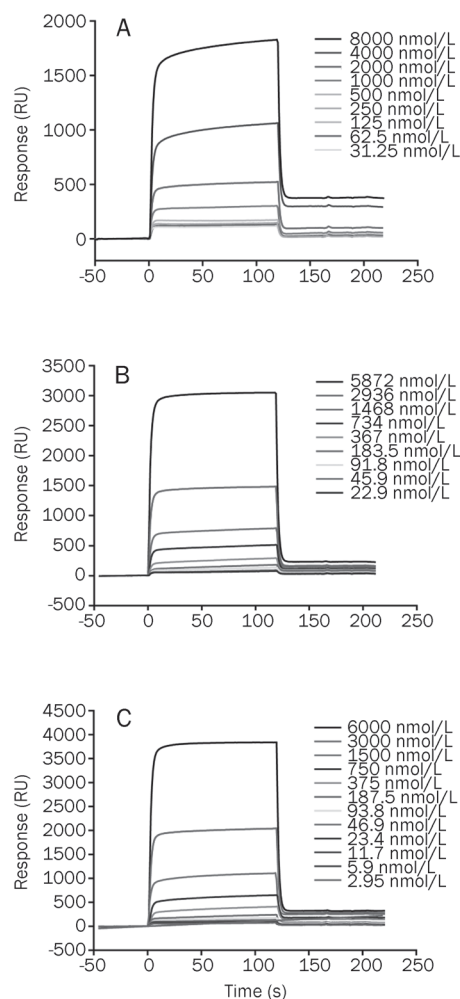
Figure 3. Characterization of the intrinsic properties of the Tat KKR SPMG binding domain. (A-C) Sensorgrams of GST-Tat and its mutants with immobilized SPMG. Serial concentrations of GST-Tat and its mutants were injected over the SPMG-immobilized sensor chip surface. The real time binding was recorded as response (RU) versus time. (A), (B) and (C) represent sensorgrams for GST-Tat, GST-Tat$_{(G48-R57)A}$, and GST-Tat$_{K(12,41)A/R78A}$, respectively.

adhesion in a cell surface HSPG-dependent manner[14], we then examined the effects of SPMG on SLK cell adhesion. We found that both Tat and KKR-dominant Tat (GST-Tat$_{(G48-R57)A}$) significantly induced the adhesion of SLK cells, although the KKR-dominant Tat induced cell adhesion to a lower extent. Notably, 200 µg/mL of SPMG dramatically inhibited SLK adhesion (Figure 5). Together, these findings clearly support the idea that SPMG inhibits KKR region-facilitated SLK cell adhesion by directly binding to the KKR region.

Discussion
In the present study, we demonstrated that the triad of Lys12, Lys41, and Arg78 functioned as a crucial determinant of Tat-SPMG interaction in addition to the basic domain.

Using an SPR assay, a multiphasic binding mode between Tat and SPMG was observed. With mutation of the basic
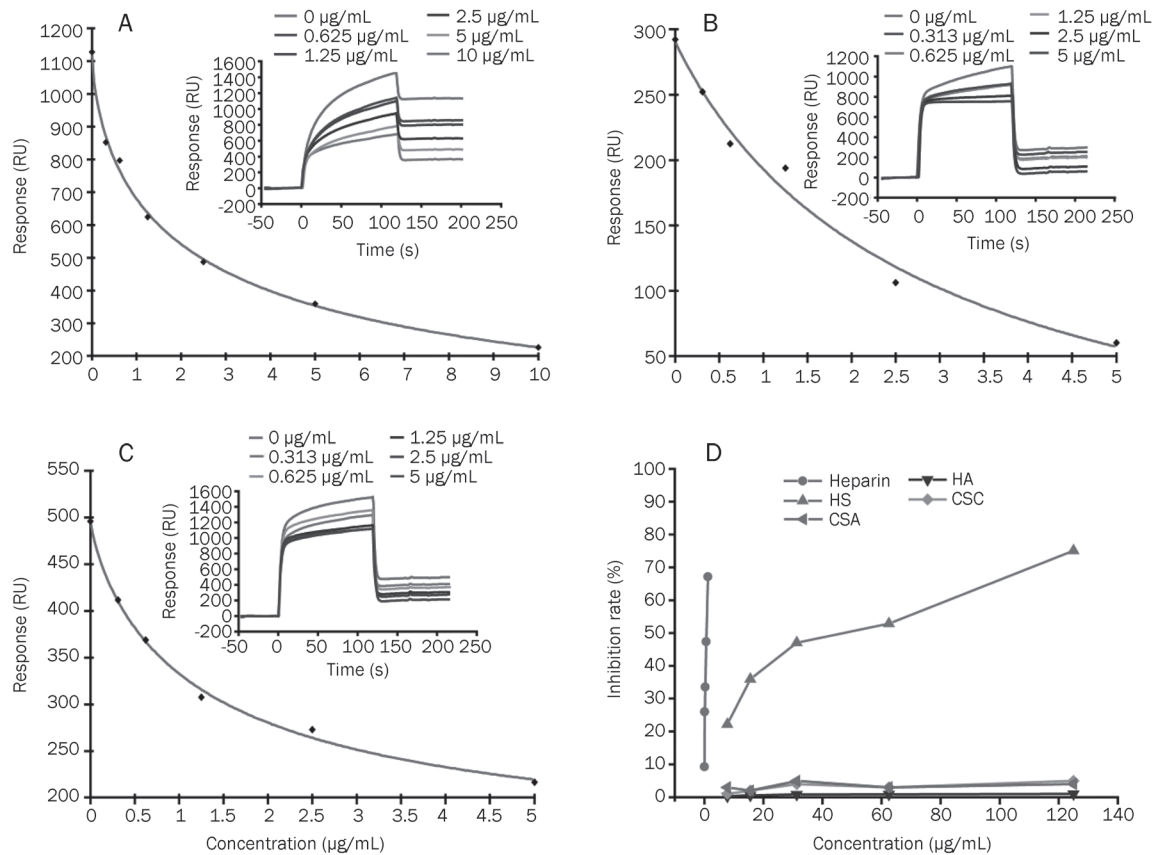
Figure 4. SPMG competitively inhibits binding of GST-Tat and its mutants with immobilized SPMG. GST-Tat (A), GST-Tat$_{(G48-R57)A}$ (B) and GST-Tat$_{K(12,41)A/R78A}$ (C) (1.5 µmol/L) alone or in the presence of serial concentrations of SPMG were injected over an SPMG immobilized chip surface. The responses (in RU) were plotted versus the concentration of SPMG. Insets show the overlay of sensorgrams showing the binding of GST-Tat and its mutants to immobilized SPMG in the presence of increasing concentrations of SPMG. (D) The inhibitory action of different glycosaminoglycans on GST-Tat$_{(G48-R57)A}$-SPMG interaction. GST-Tat$_{(G48-R57)A}$ (1.5 µmol/L) was preincubated with the indicated concentrations of free heparin, heparan sulfate (HS), chondroitin sulfates A (CSA), C (CSC), or hyaluronic acid (HA) and injected over a biotinylated SPMG surface.
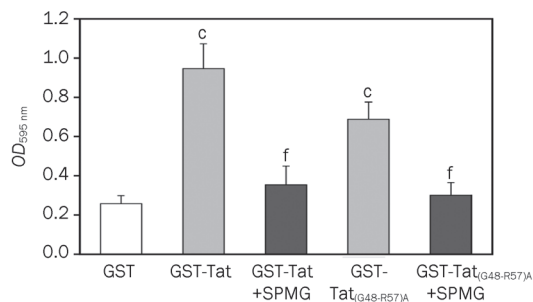
Figure 5. Inhibitory effects of SPMG on Tat-mediated SLK cell adhesion (*n*=3). $^{c}P<0.01$ *vs* GST; $^{f}P<0.01$ *vs* GST-Tat or GST-Tat$_{(G48-R57)A}$.

domain, a monophasic binding series became evident. A complete loss of binding capacity for SPMG was then noted following double mutation of both KKR and the basic domain. These findings collectively support the idea that the Tat protein offers two binding sites for SPMG. One is the well-recognized basic domain, and the other is the newly identified

KKR region. This model is congruent with our simulation-based predictions. Notably, the mutants with either a single or a double substitution of KKR residues did not dramatically affect SPMG binding affinity, while a triple mutation significantly did. This finding highlights the importance of all three residues in this triad for functionality.

By kinetic analysis, the dissociation constant (K_D value) was calculated as 26.5 pmol/L, which represents an extremely high-affinity binding interaction (about 500 times that of the basic domain). The disparity in binding affinity between the KKR and the basic domain, in principle, should allow SPMG to preferentially occupy KKR. *In silico* simulation clearly demonstrated that SPMG could specifically recognize the KKR region when the disaccharide probe was used. As the length of the oligosaccharide increased, the oligomer stretched toward and along the basic domain; it began to form interactions with Arg56 when the tetramer probe was used and reached Arg53 as the sugar length increased to 8. Ideally, SPMG at its typical length would simultaneously bind to both KKR and the whole basic domain.

An interesting feature of the KKR domain is its specificity

for SPMG, as evident from the observation that only heparin/HS but not other GAGs, including CSA, CSC and HA, were able to produce a dose-response-based competitive inhibitory effect on Tat-SPMG interactions. Sugar-protein interactions are predominantly dependent on saccharide composition and the extent and distribution of sulfation of the sugar backbone[25, 26]. SPMG is a heparin-like sulfated polysaccharide and is rich in 1, 4-linked β-D-mannuronate. The high affinity of Tat for SPMG might be the outcome of both its defined sulfate groups and its specific saccharide composition. In addition, unlike the linearly contiguous sequence of the basic domain, the KKR residues of the novel SPMG binding site, although distant in sequence, are brought into close spatial proximity via Tat conformational folding. This finding is highly consistent with current views, which hold that heparin binding sites are commonly recognized on the external surface of proteins and correspond to shallow pockets of positive charge that are often linearly contiguous or, alternatively, may be distant in sequence yet closely spatially orientated when the protein assumes its native tertiary structure[27–29].

The KKR region facilitates Tat-mediated SLK cell adhesion in a cell surface HSPG-dependent manner[14]. In the present study, we found that SPMG dramatically inhibited SLK adhesion induced by Tat and KKR-dominant Tat (GST-Tat$_{(G48-R57)A}$) as well, suggesting the interaction of SPMG with the KKR region competitively abrogated Tat-mediated cell adhesion.

In sum, we herein show that a domain consisting of a triad of Lys12, Lys41, and Arg78 is a novel, high-affinity, spatially enclosed SPMG binding site on Tat. This finding, together with the fact that SPMG inhibits Tat-induced AIDS-KS, provides important new insights into the molecular mechanism of SPMG and a potential therapeutic intervention for Tat-related Kaposi's sarcoma.

Acknowledgements

Author contribution

Han-dong JIANG and Xin-liang XIN conceived and designed the experiments. Yan-lin WU, Jing AI, Xin-liang XIN, Jing-ming ZHAO, and Xiao-jie XIN performed the experiments. Yan-lin WU, Jing AI, Mei-yu GENG, Han-dong JIANG, and Xin-liang XIN analyzed the data. Han-dong JIANG and Jing AI wrote the paper. And Bing XIONG designed and executed molecular docking.

References

1 Dezube BJ. Management of AIDS-related Kaposi's sarcoma: advances in target discovery and treatment. Expert Rev Anticancer Ther 2002; 2: 193–200.

2 Aversa SM, Cattelan AM, Salvagno L, Crivellari G, Banna G, Trevenzoli M, et al. Treatments of AIDS-related Kaposi's sarcoma. Crit Rev Oncol Hematol 2005; 53: 253–65.

3 Sullivan RJ, Pantanowitz L, Dezube BJ. Targeted therapy for Kaposi sarcoma. BioDrugs 2009; 23: 69–75.

4 Aoki Y, Tosato G. HIV-1 Tat enhances Kaposi sarcoma-associated herpesvirus (KSHV) infectivity. Blood 2004; 104: 810–4.

5 Pati S, Foulke JS Jr, Barabitskaya O, Kim J, Nair BC, Hone D, et al. Human herpesvirus 8-encoded vGPCR activates nuclear factor of activated T cells and collaborates with human immunodeficiency virus type 1 Tat. J Virol 2003; 77: 5759–73.

6 Barillari G, Sgadari C, Fiorelli V, Samaniego F, Colombini S, Manzari V, et al. The Tat protein of human immunodeficiency virus type-1 promotes vascular cell growth and locomotion by engaging the alpha5beta1 and alphavbeta3 integrins and by mobilizing sequestered basic fibroblast growth factor. Blood 1999; 94: 663–72.

7 Rusnati M, Presta M. HIV-1 Tat protein and endothelium: from protein/cell interaction to AIDS-associated pathologies. Angiogenesis 2002; 5: 141–51.

8 Ziegler A, Seelig J. Interaction of the protein transduction domain of HIV-1 TAT with heparan sulfate: binding mechanism and thermodynamic parameters. Biophys J 2004; 86: 254–63.

9 Rusnati M, Coltrini D, Oreste P, Zoppetti G, Albini A, Noonan D, et al. Interaction of HIV-1 Tat protein with heparin. Role of the backbone structure, sulfation, and size. J Biol Chem 1997; 272: 11313–20.

10 Rusnati M, Tulipano G, Spillmann D, Tanghetti E, Oreste P, Zoppetti G, et al. Multiple interactions of HIV-I Tat protein with size-defined heparin oligosaccharides. J Biol Chem 1999; 274: 28198–205.

11 Rusnati M, Tulipano G, Urbinati C, Tanghetti E, Giuliani R, Giacca M, et al. The basic domain in HIV-1 Tat protein as a target for polysulfonated heparin-mimicking extracellular Tat antagonists. J Biol Chem 1998; 273: 16027–37.

12 Tyagi M, Rusnati M, Presta M, Giacca M. Internalization of HIV-1 tat requires cell surface heparan sulfate proteoglycans. J Biol Chem 2001; 276: 3254–61.

13 Fittipaldi A, Giacca M. Transcellular protein transduction using the Tat protein of HIV-1. Adv Drug Deliv Rev 2005; 57: 597–608.

14 Ai J, Xin X, Zheng M, Wang S, Peng S, Li J, et al. A triad of Lys12, Lys41, Arg78 spatial domain, a novel identified heparin binding site on Tat protein, facilitates Tat-driven cell adhesion. PLoS One 2008; 3: e2662.

15 Rusnati M, Urbinati C, Caputo A, Possati L, Lortat-Jacob H, Giacca M, et al. Pentosan polysulfate as an inhibitor of extracellular HIV-1 Tat. J Biol Chem 2001; 276: 22420–5.

16 Hui B, Xia W, Li J, Wang L, Ai J, Geng M. Sulfated polymannuroguluronate, a novel anti-acquired immune deficiency syndrome drug candidate, blocks neuroinflammatory signalling by targeting the transactivator of transcription (Tat) protein. J Neurochem 2006; 97: 334–44.

17 Lu CX, Li J, Sun YX, Qi X, Wang QJ, Xin XL, et al. Sulfated polymannuroguluronate, a novel anti-AIDS drug candidate, inhibits HIV-1 Tat-induced angiogenesis in Kaposi's sarcoma cells. Biochem Pharmacol 2007; 74: 1330–9.

18 Peloponese JM Jr, Gregoire C, Opi S, Esquieu D, Sturgis J, Lebrun E, et al. ^{1}H-^{13}C nuclear magnetic resonance assignment and structural characterization of HIV-1 Tat protein. C R Acad Sci III 2000; 323: 883–94.

19 Sali A. Comparative protein modeling by satisfaction of spatial restraints. Mol Med Today 1995; 1: 270–7.

20 Trott O, Olson AJ. AutoDock Vina: improving the speed and accuracy of docking with a new scoring function, efficient optimization, and multithreading. J Comput Chem 2010; 31: 455–61.

21 DeLano WL. The PyMOL Molecular Graphics System. 2002. Available from: http://www.pymol.org.

22 Li FC, Qi X, Geng MY. A novel method of Immobilization of 911 for surface plasmon resonance biosensor. Chin J Anal Chem 2003; 31:

266–9.

23 Liu H, Geng M, Xin X, Li F, Zhang Z, Li J, *et al*. Multiple and multivalent interactions of novel anti-AIDS drug candidates, sulfated polymannuronate (SPMG)-derived oligosaccharides, with gp120 and their anti-HIV activities. Glycobiology 2005; 15: 501–10.

24 Hutchings H, Ortega N, Plouet J. Extracellular matrix-bound vascular endothelial growth factor promotes endothelial cell adhesion, migration, and survival through integrin ligation. FASEB J 2003; 17: 1520–2.

25 Mulloy B. The specificity of interactions between proteins and sulfated polysaccharides. An Acad Bras Cienc 2005; 77: 651–64.

26 Katsuraya K, Nakashima H, Yamamoto N, Uryu T. Synthesis of sulfated oligosaccharide glycosides having high anti-HIV activity and the relationship between activity and chemical structure. Carbohydr Res 1999; 315: 234–42.

27 Capila I, Linhardt RJ. Heparin-protein interactions. Angew Chem Int Ed Engl 2002; 41: 391–412.

28 Hileman RE, Fromm JR, Weiler JM, Linhardt RJ. Glycosaminoglycan-protein interactions: definition of consensus sites in glycosaminoglycan binding proteins. Bioessays 1998; 20: 156–67.

29 Munoz EM, Linhardt RJ. Heparin-binding domains in vascular biology. Arterioscler Thromb Vasc Biol 2004; 24: 1549–57.

npg

Original Article

Metabolic and pharmacokinetic studies of scutellarin in rat plasma, urine, and feces

Jian-feng XING[1], Hai-sheng YOU[2], Ya-lin DONG[2, *], Jun LU[2], Si-ying CHEN[2], Hui-fang ZHU[2], Qian DONG[2], Mao-yi WANG[2], Wei-hua DONG[2]

[1]Department of Pharmacy, Medical College, Xi-an Jiaotong University, Xi-an 710061, China; [2]Department of Pharmacy, the First Affiliated Hospital, Medical College, Xi-an Jiaotong University, Xi-an 710061, China

Aim: To study the metabolic and pharmacokinetic profile of scutellarin, an active component from the medical plant *Erigeron breviscapus* (Vant) Hand-Mazz, and to investigate the mechanisms underlying the low bioavailability of scutellarin though oral or intravenous administration in rats.

Methods: HPLC method was developed for simultaneous detection of scutellarin and scutellarein (the aglycone of scutellarin) in rat plasma, urine and feces. The *in vitro* metabolic stability study was carried out in rat liver microsomes from different genders.

Results: After a single oral dose of scutellarin (400 mg/kg), the plasma concentrations of scutellarin and scutellarein in female rats were significantly higher than in male ones. Between the female and male rats, significant differences in AUC, t_{max2} and C_{max2} for scutellarin were found. The pharmacokinetic parameters of scutellarin in the urine also showed significant gender differences. After a single oral dose of scutellarin (400 mg/kg), the total percentage excretion of scutellarein in male and female rats was 16.5% and 8.61%, respectively. The total percentage excretion of scutellarin and scutellarein in the feces was higher with oral administration than with intravenous administration. The *in vitro* $t_{1/2}$ and CL_{int} value for scutellarin in male rats was significantly higher than that in female rats.

Conclusion: The results suggest that a large amount of ingested scutellarin was metabolized into scutellarein in the gastrointestinal tract and then excreted with the feces, leading to the extremely low oral bioavailability of scutellarin. The gender differences of pharmacokinetic parameters of scutellarin and scutellarein are due to the higher CL_{int} and lower absorption in male rats.

Keywords: scutellarin; scutellarein; metabolism; pharmacokinetics; excretions; gender differences

Introduction

Breviscapines are flavones extracted from the medical plant *Erigeron breviscapus* (Vant) Hand-Mazz. One of the active components of breviscapine is scutellarin ($C_{21}H_{18}O_{12}$; 4′,5,6-hydroxyl-flavone-7-glucuronide). Scutellarin is hydrolyzed *in vivo* to form scutellarein (4′,5,6,7-hydroxyl-flavone), an aglycone of scutellarin, and it is further metabolized to form conjugated metabolites. Scutellarin has been extensively used for the clinical treatment of cardiovascular and cerebrovascular diseases in China for many years. Pharmacological research indicates that scutellarin is associated with anti-hypertrophic effects[1], fibrinolysis and anticoagulant effects[2], protective effects in the brain and heart[3], hypercholesterolemia suppression[4], and endothelium-independent relaxation induction[5]. Scutellarin produces an anti-inflammatory

effect via actions on arachidonic acid metabolism[6]. The compound has also been shown to have some anti-HIV effects[7] and to attenuate hepatocellular damage[8]. It is interesting that scutellarin exhibits weak estrogenic properties[9, 10], similar to genistein and apigenin. Many phytoestrogen compounds, such as genistein, apigenin, daidzein, glycitein, and their metabolites, have been demonstrated pharmacokinetic differences between male and female in humans and rats.

Gender differences affect the metabolism, excretion, and bioavailability of soy isoflavones in humans and rats[11]. To date, the pharmacokinetic profiles of scutellarin and scutellarein in different genders are unknown. Therefore, this study represents to investigate preliminary pharmacokinetics in male and female rats following administration of single oral and intravenous doses of scutellarin.

There are increasing benefits for scutellarin use in patients; however, problems with its analysis in biological samples have been reported in many studies. Pharmacological profiles of the parent drug and its metabolites in plasma[12, 13], tissues[14],

urine[15], and bile[16] in humans and rats have been evaluated using high-performance liquid chromatography (HPLC) with ultraviolet detector or HPLC with mass spectrometer. After oral administration of scutellarin, only a minute amount of the compound was detected in human blood[13], and its bioavailability was estimated to be only 10.67%[17]. However, substantial amounts of scutellarein were present in blood and urine in humans[18]. Scutellarein has similar pharmacological effects to scutellarin, but it is more potent than scutellarin. Previous studies have shown that scutellarin consistently displays double peaks in its plasma concentration-time curves[14]. Although the pharmacokinetics and metabolism of scutellarin have been extensively studied in humans and animals, the reasons for its extremely low oral bioavailability have not been elucidated. Prior to this study, there was very limited information available on the excretion dynamics of scutellarin. Most studies focused on excretion through the urine[19] with less emphasis on excretion through the feces. Scutellarin and scutellarein were found to be negligible in the urine in this present study. Hao *et al*[20] asserted that the gastrointestinal tract played an important role in scutellarin's bioavailability. Accordingly, fecal excretion of scutellarin and scutellarein was investigated in this study, and this is the first report on the fecal excretion process and the pharmacokinetics in different genders of rats for these compounds. This study provides evidence that improving the formulation design of scutellarin in a drug delivery system would result in better bioavailability and efficacy.

Materials and methods
Chemicals and reagents
Scutellarin (95% purity) was obtained from Gejiu Bio-Medicine Industry Ltd (Yunnan, China). Quercetin, the internal standard (batch N$\underline{o}$ 100081-200406; 97.3% purity by HPLC) was purchased from the National Institute for the Control of Pharmaceutical and Biological Products (Beijing, China). Scutellarein (98% purity) was obtained from DELTA Medicine Science Ltd (Anhui, China). β-NADPH was purchased from Sigma Chemical Co (St Louis, Mo, USA). HPLC-grade methanol was purchased from Fisher Scientific Co (Somerville, NJ, USA), and acetic ether was purchased from the National Medicine Corporation (Shanghai, China). Triple-distilled water was used throughout the experiments.

Animals
Sprague-Dawley rats were obtained from the Experimental Animal Center of Xi-an Jiaotong University (Xi-an, China). All rats were maintained under standard conditions with access to food and water *ad libitum*. They were housed in stainless steel cages in standard laboratory conditions (a regular 12 h day-night cycle in a well-ventilated room with an average temperature of 25–28 °C and a relative humidity of 40%–60%). The animal experimental protocol was approved by the University Ethics Review Committee for Animal Experimentation.

Intravenous and oral administrations
Pharmacokinetics
Twenty Sprague-Dawley rats (weighing 280 to 320 g; 10 males and 10 females, 4–6 months old) were fasted for 16 h but allowed water *ad libitum* the day before drug administration. Scutellarin was resuspended in 0.5% carboxymethylcellulose sodium, and it was administered to rats (400 mg/kg) by oral gavage. Blood samples (0.2 mL) were collected from the tail vein of each rat before dosing and at 5, 10, 20, 40, and 80 min and 2, 4, 6, 8, 11, 16, 24, and 36 h post-dosing. Plasma samples (0.1 mL) were obtained by centrifugation immediately after blood collection and were stored at -20 °C until analysis.

Excretion
Forty Sprague-Dawley rats (weighing 200 to 220 g; 20 males and 20 females, 3–4 months old) were housed in metabolic cages and used to study the fecal and urinary excretions of scutellarin. They were fasted for 16 h but allowed water *ad libitum* the day before drug administration. The urine and feces samples were collected 0–4, 4–8, 8–12, 12–16, 16–24, 24–32, 32–40, 40–48, 48–60, and 60–72 h after intragastric or intravenous administration of scutellarin (400 or 40 mg/kg, respectively). The volume of urine and weight of the dried feces were recorded.

Instruments
The Waters HPLC system (Milford, MA, USA) consisted of a Waters 515 pump, a Waters 717 autosampler, and a Waters 2996 diode-array-detector. The HPLC system was interfaced to a computer through Empower Pro software. A refrigerated centrifuge (Beckman Coulter™, Allegra™ X-ZZR), the Nano-drop 1000 spectrophotometer (Thermo Scientific, Wilmington, DE, USA) and a pressurized gas blowing evaporator (HBC-12) were used to process the samples.

Chromatographic conditions
An ODS-2 HYPERSIL C_{18} analytical column (250 mm×4.6 mm, 5 μm) (Thermo Scientific Corporation, USA) with a C_{18} guard column (4 mm×3 mm, 5 μm) (Phenomenex Corporation, Torrance, CA, USA) was used in chromotography. The mobile phase consisted of methanol and water at a ratio of 1:1 (*v/v*), and the pH was adjusted to 2.5 with phosphoric acid (1 mol/L). The mobile phase was delivered at a flow rate of 1 mL/min. The diode array detector was operated at 335 nm.

Sample preparation
Preparation of standard solutions
Stock solutions of scutellarin (250 μg/mL), scutellarein (50 μg/mL), and quercetin (the internal standard (190 μg/mL)) were prepared in methanol. A series of standard working solutions (scutellarin 20, 10, 5, 2.5, 1.25, 0.625 μg/mL; scutellarein 5, 2.5, 1.25, 0.625, 0.312, 0.156 μg/mL) were prepared by further diluting the standard stock solution in the mobile phase (pH 2.5). Appropriate amounts of the working solution were diluted in the pooled blank plasma, urine, and fecal

samples to cover the respective calibration standard ranges. All samples were stored at 4 °C and brought to room temperature before use.

Preparation of plasma samples

Quercetin stock solution (10 µL; 2.5 µg/mL) was transferred to a 10 mL tapered glass tube and evaporated to dryness under a stream of nitrogen. Plasma (100 µL) and phosphoric acid (50 µL; 1 mol/L) solutions were then added to the glass tube and mixed for 1 min before being extracted with acetic ether (1 mL) by vortex mixing for another 3 min. The glass tubes were then centrifuged at 3000 revolutions per minute for 10 min. The upper organic phase was transferred to a clean tube and evaporated to dryness at 35 °C under a stream of nitrogen. The residue was immediately reconstituted in the mobile phase (100 µL) and centrifuged at 10000 revolutions per minute at 4 °C for 10 min. The supernatant (80 µL) was transferred into an autosampler vial, and 50 µL of it was injected into the HPLC system.

Preparation of the urine and feces samples

The blank urine and feces samples were collected from rats housed in metabolic cages. Quercetin (10 µL; 2.5 µg/mL) was transferred to a 10 mL tapered glass tube and evaporated to dryness under a stream of nitrogen. The collected urine samples were centrifuged at 10 000 revolutions per minute for 10 min, and the urine sample (200 µL) and phosphoric acid solution (100 µL; 1 mol/L) were added to the glass tube. This mixture was sonicated for 1 min, vortexed for 5 min, and centrifuged at 10000 revolutions per minute for 10 min. Then the mixture (20 µL) was injected into the HPLC system for analysis.

The rat feces were first dried at room temperature and ground to powder with a mortar. The dry feces powder (0.2 g) was then sonicated in methanol (2 mL) for 10 min. Distilled water (1 mL) was then added to the sample, and another sonication step was performed. The samples were centrifuged at 10000 revolutions per minute for 10 min, and the supernatant was filtered through a 0.45 µm membrane and transferred into an autosampler vial. Samples (20 µL) were injected into the HPLC system for analysis.

Mechanistic study on gender differences
Liver microsomal preparation

Pooled rat liver microsomes from both genders were prepared according to the method reported previously[21]. Three male and three female rats (weighing 200 to 220 g; 3–4 months old) were euthanized with CO_2 after a 24-h fasting period. The pooled, extracted liver microsomes were suspended in Tris buffer (0.1 mol/L; pH 7.4) and stored at -80 °C before use. Rat microsomal protein contents were determined by a Nanodrop 1000.

Liver microsomal incubations

The scutellarin stock solution in dimethyl sulfoxide was added to Tris buffer (0.1 mol/L; pH 7.4) with the rat liver microsomes. The mixture was first shaken for 5 min to equilibrate in a shaking water bath at 37 °C. Incubation was then initiated by adding a β-NADPH solution. The final concentrations of scutellarin, NADPH and the microsomal protein in the incubation mixture (1.5 mL) were 30 µmol/L, 1 mmol/L and 2 mg/mL, respectively. The percentage of dimethyl sulfoxide in the incubation mixture was kept less than 0.5% (v/v). Incubation sample mixtures (50 µL) were collected at 0, 10, 20, 30, 40, 50, 60, and 90 min. The reactions were terminated with ice-cold methanol (100 µL) to precipitate the proteins, and the samples were subsequently centrifuged at 16000×g for 15 min. Negative controls were prepared by adding NADPH, which was followed by immediate termination using ice-cold methanol and considered the 0 min aliquots. Supernatants (50 µL) were collected and analyzed by HPLC.

Pharmacokinetic and statistical analyses

The pharmacokinetic parameters in plasma and urine were estimated using the DAS2.0 software (Drug and Statistics, version 2.0, Mathematical Pharmacology Professional Committee of China, Shanghai)[22]. Differences in the plasma scutellarin concentrations at each time point and differences in the pharmacokinetic parameters (AUC, $t_{1/2}$, t_{max}, C_{max}) in the plasma and urine between male and female rats were analyzed using ANOVA and a Student's t-test with the SSPS 11.5 software pack. $P<0.05$ was considered statistically significant. Data are presented as the mean±SD.

Results
Selectivity

Six individual, blank rat plasma, urine, and feces samples were analyzed to determine if anything in the matrix interfered with the analytes. Under the optimized HPLC conditions, scutellarin, an unknown metabolite, scutellarein, and quercetin were separated chromatographically with retention times of 5.1, 6.4, 8.9, and 11 min, respectively. No interference was observed at these retention times (Figure 1).

Linearity of the calibration curves and lower limit of quantification

Calibration curves were constructed based on the peak area ratios of the analytes to the internal standard *versus* the concentrations. These were made using a weighted (1/c) liner regression analysis. Good linear relationships were established for both scutellarin and scutellarein in the plasma (0.1 mL), urine (0.2 mL), and fecal (0.2 mL) homogenates. The lower limits of quantification (LLOQ) were defined as signal-to-noise ratios (S/N) greater than 10, and they were evaluated by analyzing six replicates of the biological samples spiked with scutellarin and scutellarein. The results of the calibration curves and LLOQ are summarized in Table 1.

Precision and accuracy

Intra-day accuracy and precision were evaluated by analyzing the quality control (QC) samples (n=5) at different time points in the same day. They were determined by repeated
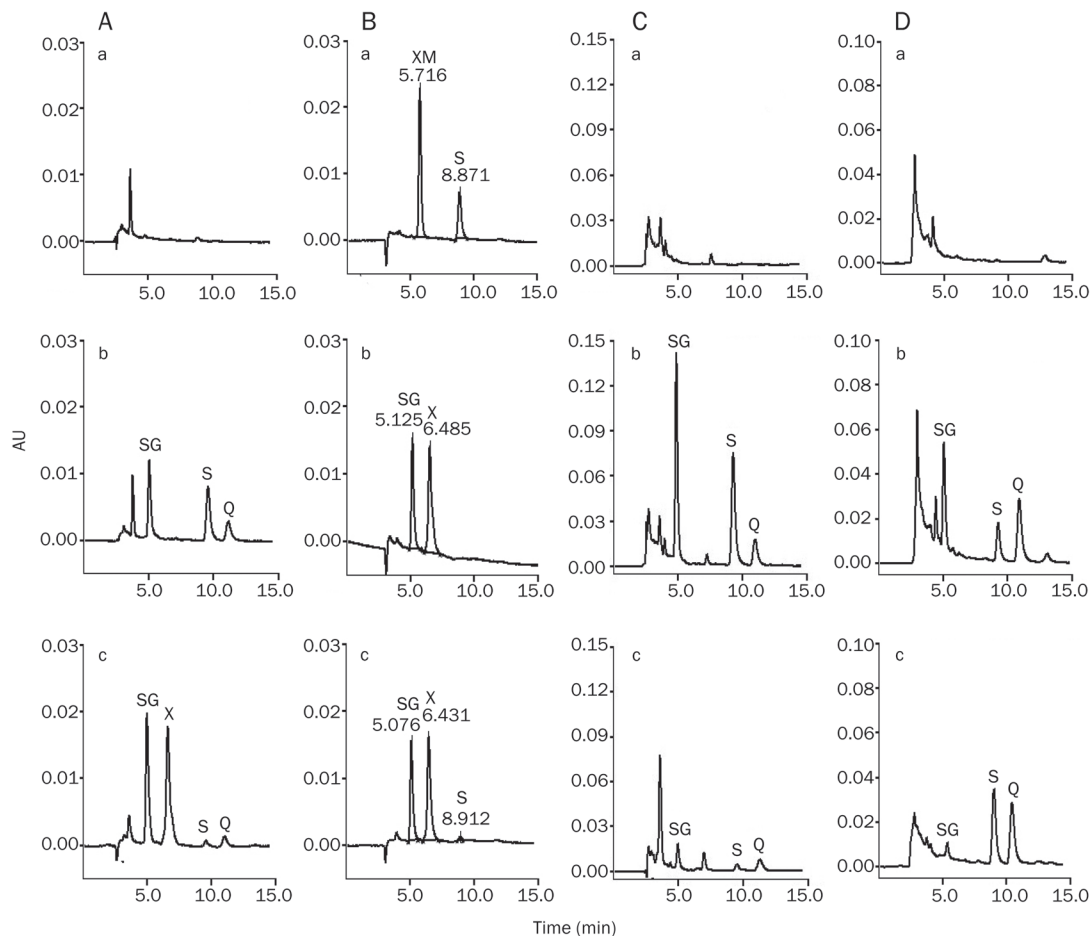
Figure 1. HPLC chromatograms of scutellarin and scutellarein in biological samples. Panel A: (a) Blank plasma sample; (b) Blank plasma spiked with scutellarin, scutellarein and internal standard; (c) Plasma sample at 8 h after an oral administration of scutellarin (400 mg/kg). Panel B: (a) Plasma sample collected at 8 h after treatment with β-glucuronidase; (b) Plasma sample at 8 h after treatment with sulfatase; (c) Plasma sample at 8 h without any enzyme treatment and no internal standard added to the sample. Panel C: (a) Blank urine sample; (b) Blank urine spiked with scutellarin, scutellarein and internal standard; (c) Urine sample at 0–4 h after oral administration of scutellarin (400 mg/kg). Panel D: (a) Blank feces solution; (b) Blank feces solution spiked with scutellarin, scutellarein and internal standard; (c) Blank feces solution sample collected at 8–12 h after oral administration of scutellarin (400 mg/kg). SG, scutellarin; X, scutellarin metabolite; XM: compound formed after treatment with β-glucuronidase; S, scutellarein; Q, quercetin.

Table 1. The calibration curves and LLOQ of scutellarin and scutellarein in the respective matrix of plasma, urine, and feces.

Samples	Calibration curve	Linear range (µg/mL)	r	LLOQ (µg/mL)
Plasma	y(scutellarin)=0.0009684 x+0.0228	0.06–2.0	0.9980	0.06
Plasma	y(scutellarein)=0.007873 x+0.2151	0.02–0.50	0.9977	0.02
Urine	y(scutellarin)=0.0955 x+0.0658	0.64–41.0	0.9997	0.64
Urine	y(scutellarein)= 0.3320 x+0.0355	0.16–10.4	0.9996	0.16
Feces	y(scutellarin)=0.0831 x+0.0203	0.64–41.0	0.9999	0.64
Feces	y(scutellarein)= 0.2418 x−0.0157	0.16–10.4	0.9998	0.16

analyses of the QC samples on three different days (*n*=5). The concentration of each sample was determined with newly prepared calibration standards. To determine the absolute recovery, non-extracted samples (pure sample freshly pre-

pared in methanol) and a set of post-extracted spiked samples were analyzed in the same run. These post-extracted spiked samples were at three concentrations in the plasma (2, 0.5, and 0.12 µg/mL for scutellarin and 0.5, 0.12, and 0.03 µg/mL for

scutellarein, respectively) and in the urine and feces (20.5, 5.13, and 1.28 µg/mL for scutellarin and 5.2, 1.3, and 0.32 µg/mL for scutellarein, respectively). Absolute recovery was determined by measuring the peak-area ratio of a post-extracted sample against the non-extracted samples. The results of these analyses are shown in Table 2.

Stability

Scutellarin has a structure almost identical to baicalin and is stable in acidified biological samples[23]; however, baicalin lacks the 4′-hydroxyl group that scutellarin has. Oxidation-reduction reactions, which are mediated by phenol radicals, are the major cause for the degradation of these compounds in biological samples. Previous studies have shown that acidic conditions can stabilize these flavonoids in solutions and biological samples[24]. The pH is responsible for degrading baicalin[24] but not the matrix. Therefore, in this study, scutellarin and scutellarein were stabilized by adjusting the pH to 2.5 in all samples with phosphoric acid (1 mol/L).

The stability of scutellarin and scutellarein during sample storage and processing was evaluated by analyzing the QC samples. At room temperature for 8 h, the scutellarin and scutellarein concentrations in the biological samples varied by less than ±9.90%, and the responses did not vary by more than 7.74% after 24 h of storage at 4 °C. The concentration variations were within ±11.13% of the nominal concentrations after three cycles of freezing at -20 °C, and thawing at 20 °C showed no significant loss of scutellarin or scutellarein. The processed samples were reconstituted in the mobile phase and placed at room temperature (25 °C) in the autosampler for

8 h, and scutellarin and scutellarein showed very good post-preparation stabilities with RSDs less than 10.43%. When the processed samples were stored at -20 °C for two weeks, scutellarin and scutellarein showed good stabilities at the concentrations studied with RSDs of ±11.44%.

Pharmacokinetic and excretion studies in rats
Pharmacokinetics

The mean plasma concentration-time curves exhibited double peaks in both male and female rats after oral administration of scutellarin (400 mg/kg) (Figures 2 and 3). Significantly higher plasma concentrations of scutellarin were measured in females
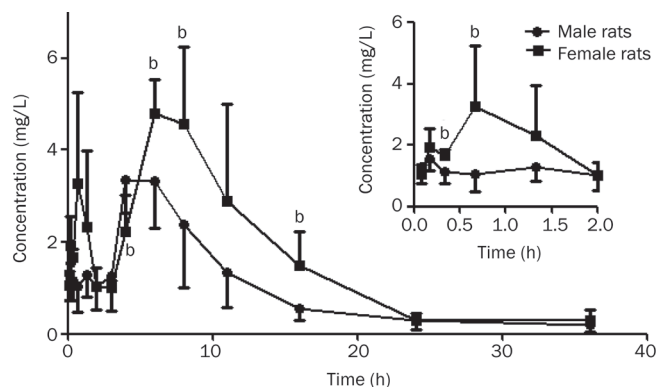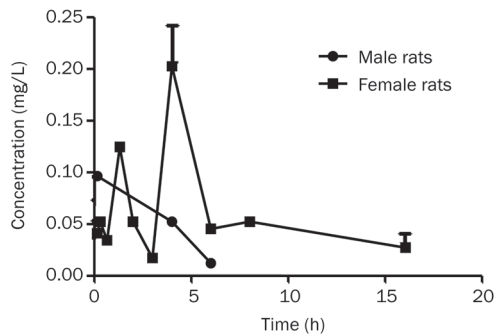

Figure 2. Plasma concentration-time curve of scutellarin after a single oral dose of 400 mg/kg scutellarin in both male and female rats (*n*=10). The smaller figure enlarged the original one whose data started to from 0 h to 2.0 h. Mean±SD. [b]*P*<0.05 *vs* male rats.

Table 2. Precision of the assays and recoveries of scutellarin and scutellarein from the respective biological samples (mean±SD, *n*=5).

Samples	Added (µg/mL)	Intra-day Measured (µg/mL)	Intra-day RSD/%	Inter-day Measured (µg/mL)	Inter-day RSD/%	Relative recovery/%	Absolute recovery/%
Scutellarin in plasma	2.00	1.95±0.11	5.86	1.99±0.12	5.90	99.10±6.40	52.50±1.60
	0.50	0.47±0.04	7.70	0.49±0.04	8.80	95.60±8.10	62.10±1.80
	0.12	0.126±0.01	5.10	0.129±0.01	5.09	100.90±5.20	57.30±3.50
Scutellarein in plasma	0.50	0.50±0.01	2.00	0.525±0.02	3.81	100.52±2.12	59.81±2.78
	0.12	0.137±0.00	2.30	0.125±0.01	0.81	105.71±9.01	65.03±7.13
	0.03	0.029±0.00	7.20	0.029±0.00	7.80	94.73±8.41	59.82±2.70
Scutellarin in urine	20.50	20.15±0.19	0.94	20.37±0.60	2.93	98.29±0.92	77.64±0.37
	5.13	4.74±0.11	2.29	4.80±0.32	6.62	92.42±2.11	78.42±1.26
	1.28	1.12±0.01	1.12	1.12±0.01	0.96	87.45±0.98	87.23±1.30
Scutellarein in urine	5.20	5.31±0.05	0.92	5.35±0.07	1.37	102.04±0.94	73.22±0.23
	1.30	1.21±0.03	2.87	1.21±0.05	3.87	93.31±2.68	69.46±0.86
	0.32	0.33±0.01	2.45	0.30±0.02	5.41	100.10±2.45	70.01±2.25
Scutellarin in feces	20.50	20.61±0.41	2.01	20.38±0.63	3.09	100.53±2.02	94.56±5.16
	5.13	5.35±0.08	1.50	4.91±0.36	7.30	104.31±1.56	105.50±9.22
	1.28	1.17±0.05	4.37	1.19±0.09	7.25	90.94±3.97	92.55±6.33
Scutellarein in feces	5.20	5.11±0.45	8.82	5.53±0.40	7.14	98.34±8.67	66.17±2.80
	1.30	1.29±0.16	12.41	1.31±0.15	11.34	98.91±12.27	67.52±8.34
	0.32	0.34±0.80	0.83	0.33±0.02	6.09	106.01±0.88	66.48±6.77

RSD: relative standard deviation.

Figure 3. Plasma concentration-time curve of scutellarein after a single oral dose of 400 mg/kg scutellarin in both male and female rats. Mean±SD. *n*=10.

Table 3. Parmacoknetics parameters for scutellarin after oral administration in both male and female rats (mean±SD, *n*=10). [b]*P*<0.05, [c]*P*<0.01 *vs* male rats.

Pharmaco-kenetics parameters	Units	Scutellarin	
		Male	Female
$AUC_{(0-t)}$	mg/L·h	34.71±9.88	56.08±9.28[c]
$AUC_{(0-\infty)}$	mg/L·h	35.71±9.72	57.30±10.46[c]
$t_{1/2}$	h	6.14±2.79	5.26±1.55
t_{max1}	h	0.18±0.09	0.43±0.23
t_{max2}	h	5.60±1.67	8.80±2.17[b]
C_{max1}	mg/L	1.78±0.37	3.56±1.86
C_{max2}	mg/L	3.96±0.77	5.29±0.97[b]

(P<0.05) at 20 and 40 min and at 4, 6, 8, and 16 h (Figure 2). Similar results were also noted for scutellarein in female rats (Figure 3). Significant differences for scutellarin in AUC, t_{max2}, and C_{max2} were noted between the male and female rats (P<0.05 or P<0.01) (Table 3).

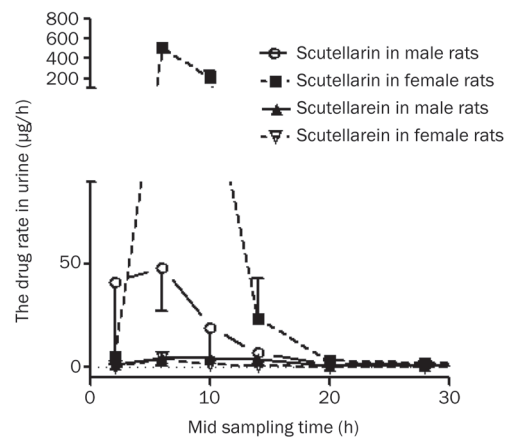*Excretion*

The urinary pharmacokinetic parameters of scutellarin and suctellarein after the oral administration of 400 mg/kg scutellarin and intravenous administration of 40 mg/kg scutellarin are shown in Table 4 and Table 5, and the urinary excretion rates of scutellarin and scutellarein are shown in Figure 4 and Figure 5. The percentages of the accumulated excretion of scutellarin and scutellarein in urine and feces are shown in Figure 6–9.

Table 4 and Table 5 show that the excretion percentage of scutellarein was lower than that of scutellarin. Scutellarin was excreted quickly, but scutellarein was excreted slowly from 0
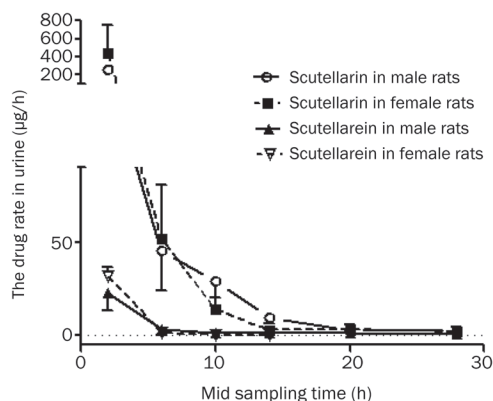

Figure 4. The mean excretion rate-time curve in male and female rats urine for both scutellarin and scutellarein after oral administration of 400 mg/kg scutellarin (*n*=10). Mean±SD.

Table 4. The pharmacokinetic parameters scutellarin and scutellarein in urine after oral administration of 400 mg/kg scutellarin in rats (mean±SD, *n*=10). [b]*P*<0.05, [c]*P*<0.01 *vs* male rats.

Pharmacokenetics parameters	Units	Male		Female	
		Scutellarin	Scutellarein	Scutellarin	Scutellarein
$t_{1/2}$	h	4.46±1.99	19.52±9.55	7.52±1.10[b]	13.89±2.81
Ke	1/h	0.18±0.06	0.04±0.02	0.09±0.01[b]	0.05±0.01
The drug accumulation excretion in urine	%	0.53±0.21	0.11±0.05	0.96±0.20	0.02±0.00[c]

Table 5. The pharmacokinetic parameters scutellarin and scutellarein in urine after intravenous administration of 40 mg/kg scutellarin in rats (mean±SD, *n*=10). [b]*P*<0.05, [c]*P*<0.01 *vs* male rats.

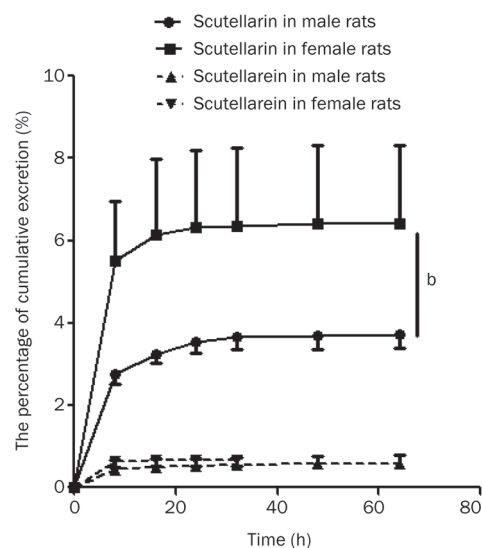| Pharmacokenetics parameters	Units	Male		Female	
		Scutellarin	Scutellarein	Scutellarin	Scutellarein
$t_{1/2}$	h	3.37±0.16	5.29±0.48	3.42±1.26	1.65±0.37[c]
Ke	1/h	0.21±0.01	0.13±0.01	0.22±0.07	0.43±0.09[c]
The drug accumulation excretion in urine	%	3.72±0.33	0.58±0.20	6.42±1.89	0.67±0.15[b]

Figure 5. The mean excretion rate-time curve in male and female rats urine for both scutellarin and scutellarein after intravenous administration of 40 mg/kg scutellarin (n=10). Mean±SD.
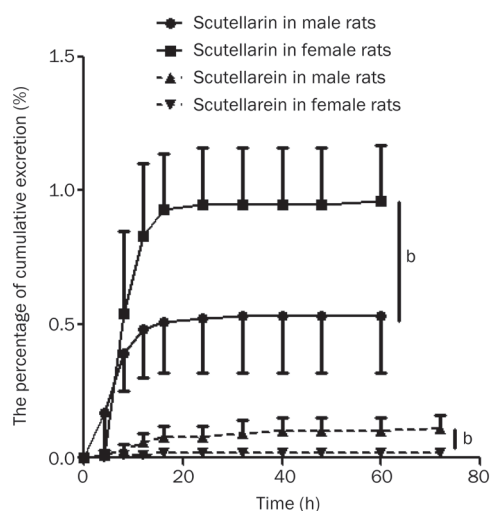
Figure 6. The percentage of cumulative excretion of scutellarin and scutellarein in male and female rats urine after administration of a single oral dose of 400 mg/kg scutellarin (n=10). Mean±SD. [b]$P<0.05$ vs male rats.

Figure 7. The percentage of cumulative excretion of scutellarin and scutellarein in male and female rats urine after administration of a single intravenous dose of 40 mg/kg scutellarin (n=10). [b]$P<0.05$ vs male rats. Mean±SD.
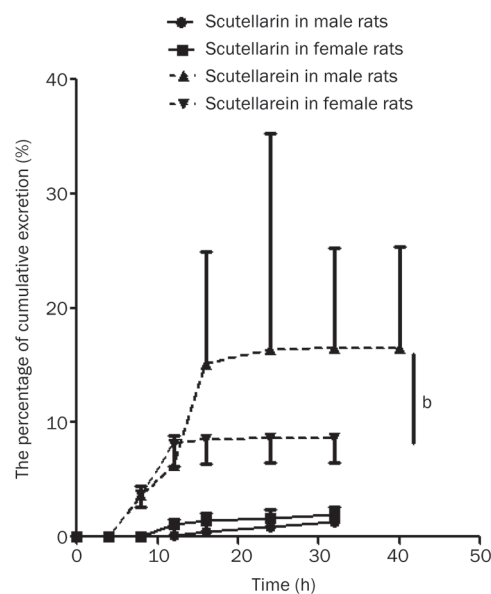

Figure 8. The percentage of cumulative excretion of scutellarin and scutellarein in male and female rats feces after administration of a single oral dose of 400 mg/kg scutellarin (n=10). Mean±SD. [b]$P<0.05$ vs male rats.

to 16 h (Figures 4 and 5). The elimination half-life of scutellarein was much longer than scutellarin with oral administration. The cumulative amounts of scutellarin recovered in the urine were 0.53% in male rats and 0.96% in female rats ($P<0.05$), and they were 0.11% and 0.02% in male and female rats, respectively, for scutellarein ($P<0.05$, Figure 6). After intravenous administration of scutellarin (40 mg/kg), the cumulative amounts of scutellarin recovered in the urine were 3.72% and 6.42% in male and female rats, respectively ($P<0.05$, Figure 7).

The amounts of scutellarin and scutellarein recovered in the feces were much higher than those recovered from the urine after oral scutellarin administration (Figure 8); however, less amounts were recovered by the intravenous route than the oral route (Figure 9). These results indicate that most of the

scutellarein that was excreted in the feces was unabsorbed after oral administration of scutellarin. Although the plasma level of scutellarein was very low, a substantial amount of scutellarein was recovered in the feces after oral administration. Thus, we conclude that the bulk of scutellarin is hydrolyzed by the intestinal microflora or transformed by enzymes in the gastrointestinal tract into scutellarein, which leads to the low bioavailability. Hao et al[20] hypothesized that the site of
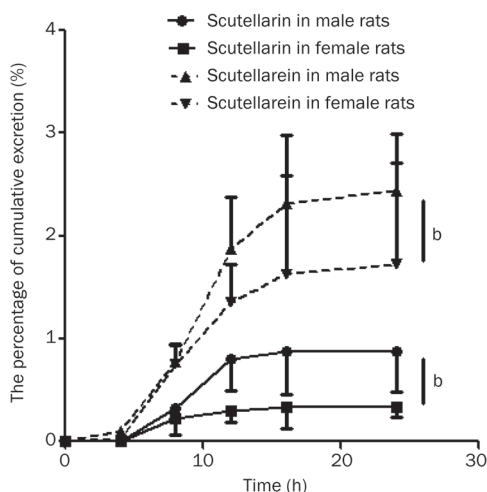
Figure 9. The percentage of cumulative excretion of scutellarin and scutellarein in male and female rats feces after adminstration of a single intravenous dose of 40 mg/kg scutellarin (*n*=10). Mean±SD. [b]*P*<0.05 vs male rats.

the first-pass effect was not the liver but in the gastrointestinal tract. Therefore, scutellarein could be partially excreted in the feces without being absorbed. The percentages of scutellarin and scutellarein that were cumulatively excreted were different according to gender for both oral and intravenous administrations (Figures 8 and 9).

Mechanism study on gender differences

Gender-specific rat liver microsomes were used in an *in vitro* metabolic study of scutellarin. These microsome experiments were performed in triplicate at eight time points between 0 and 90 min. Scutellarin was rapidly metabolized in both genders, and the starting concentrations of scutellarin that remained in female and male rat liver microsomes were 16.16%±1.02% and 8.08%±1.90%, respectively. The calculated *in vitro* scutellarin $t_{1/2}$ in female and male rats were 75.5±1.78 min and 75.6±0.33 min, respectively. The CL_{int} values for scutellarin in male rats (5.56±0.11 mL·min^{-1}·kg^{-1}) was much higher than that in female rats (4.51±0.02 mL·min^{-1}·kg^{-1}, *P*<0.01).

Discussion

Scutellarin, an unknown metabolite and scutellarein were detected simultaneously in rat plasma 5 min after oral administration of scutellarin. This indicates that scutellarin is immediately absorbed and rapidly transformed into other metabolites *in vivo*. Scutellarin and the unknown metabolite can be hydrolyzed completely by β-glucuronidase from bovine liver (essentially sulfatase-free) but not by sulfatase from *Aerobacter aerogenes* (no β-glucuronidase activity at pH 7). Huang *et al*[25] reported that scutellarin was hydrolyzed and transformed into scutellarein. Therefore, after hydrolysis by β-glucuronidase, the scutellarin peak disappeared, but the scutellarein peak increased. Additionally, when the unknown metabolite disappeared, another compound formed after glucuronidase hydro-

lysis, and the retention time of the second unknown metabolite was 5.72 min [Figure 1, panel B (a)].

After oral administration of scutellarin, its plasma concentrations at 20 and 40 min and at 6, 8, and 16 h were significantly higher in female than in male rats (Figure 2), and the $AUC_{(0-t)}$ and C_{max2} for scutellarin were much higher in female than in male rats. Similar results were also noted for scutellarein in female rats (Figure 3). Due to the absence of calibration standards for the unknown metabolite, its plasma concentrations could not be quantified. It is interesting to note that the plasma levels, which were estimated by the peak ratios, appeared to be higher in females than in males. Identifying the structural and pharmacological effects of the unknown metabolite warrants further investigation. The plasma concentrations of scutellarein were very sporadic and low, and they were quantified at a few time points. However, the scutellarein concentrations still appeared to be higher in female than in male rats, which was similar to the findings for scutellarin and the unknown metabolite.

After oral administration, the plasma concentration–time profile for scutellarin in rats was present as double peaks (Figure 2). The first peak was at 0.18 and 0.43 h in male and female rats, respectively. This suggests that scutellarin is absorbed in the stomach or upper intestinal lumen and mucosa to produce the first concentration peak because the lower pH conditions favor the liposolubility of scutellarin and its absorption. The second peak emerged at 5.6 and 8.8 h in male and female rats, respectively, and its peak concentration was higher than the first peak. These results indicate that scutellarin is transformed in the inferior part of the intestines and the colon by bacterial enzymes into the corresponding aglycone, which is absorbed. The aglycone is then followed by a regioselective glucuronidation to transform scutellarin to enter the bloodstream[13].

The observed gender effect on the pharmacokinetics of scutellarin is similar to another flavonoid, genistein[26, 27]. It is suggested that these effects on genistein are due to higher CYP1A2 activity in male rats[27, 28]. Similar to other flavonoids, scutellarin could also be metabolized by CYP1A2 enzymes. The involvement of CYP1A2 in the metabolism of scutellarin will be studied in the future.

Conclusion

This study demonstrates that a substantial amount of scutellarin is converted to scutellarein before absorption. The presystemic transformation of scutellarin could be partially responsible for its low bioavailability. The gender effect was identified in the pharmacokinetics of scutellarin, and the plasma levels of scutellarin were much higher in female than in male rats. The observed differences in plasma, urine, and feces levels could be due to gender-related differences in enzyme activity.

Acknowledgements

Author contribution

Jian-feng XING and Ya-lin DONG designed the study, performed the research and wrote the paper. Hai-sheng YOU, Jun LU, Si-ying CHEN, Hui-fang ZHU, Qian DONG, Mao-yi WANG, and Wei-hua DONG performed some of the research.

References

1 Pan ZW, Zhang Y, Mei DH, Zhang R, Wang JH, Zhang XY, *et al*. Scutellarin exerts its anti-hypertrophic effects via suppressing the Ca^{2+}-mediated calcineurin and CaMKII signaling pathways. Naunyn Schmiedebergs Arch Pharmacol 2010; 381: 137–45.

2 Zhou QS, Zhao YM, Bai X, Li PX, Ruan CG. Effect of new-breviscapine on fibrinolysis and anticoagulation of human vascular endothelial cells. Acta Pharmacol Sin 1992; 13: 239–42.

3 Lin LL, Liu AJ, Liu JG, Yu XH, Qin LP, Su DF. Protective effects of scutellarin and breviscapine on brain and heart ischemia in rats. J Cardiovasc Pharmacol 2007; 50: 327–32.

4 Li Q, Wu JH, Guo DJ, Cheng HL, Chen SL, Chan SW. Suppression of diet-induced hypercholesterolemia by scutellarin in rats. Planta Med 2009; 75: 1203–8.

5 Pan Z, Feng T, Shan L, Cai B, Chu W, Niu H, *et al*. Scutellarin-induced endothelium-independent relaxation in rat aorta. Phytother Res 2008; 22: 1428–33.

6 Wang ZY, Chen DC, He Y, Ruan CG, Zhang RW. Differential effects of new breviscapine on arachidonic acid metabolisms in blood cells and endothelial cells. Acta Pharmacol Sin 1993: 14: 148–51.

7 Zhang GH, Wang Q, Chen JJ, Zhang XM, Tam SC, Zheng YT. The anti-HIV-1 effect of scutellarin. Biochem Biophys Res Commun 2005; 334: 812–6.

8 Tan ZH, Yu LH, Wei HL, Liu GT. The protective action of scutellarin against immunological liver injury induced by concanavalin A and its effect on pro-inflammatory cytokines in mice. J Pharm Pharmacol 2007; 59: 115–21.

9 Zhu JT, Choi RC, Li J, Xie HQ, Bi CW, Cheung AW, *et al*. Estrogenic and neuroprotective properties of scutellarin from *Erigeron breviscapus*: a drug against postmenopausal symptoms and Alzheimer's disease. Planta Med 2009; 75: 1489–93.

10 Zhu JT, Choi RC, Chu GK, Cheung AW, Gao QT, Li J, *et al*. Flavonoids possess neuroprotective effects on cultured pheochromocytoma PC12 cells a comparison of different flavonoids in activating estrogenic effect and in preventing beta-amyloid-induced cell death. J Agric Food Chem 2007; 55: 2438–45.

11 Sepehr E, Cooke G, Robertson P, Gilani GS. Bioavailability of soy isoflavones in rats Part I: application of accurate methodology for studying the effects of gender and source of isoflavones. Mol Nutr Food Res 2007; 51: 799–812 .

12 Lv W, Guo J, Ping Q, Song Y, Li J. Comparative pharmacokinetics of breviscapine liposomes in dogs, rabbits and rats. Int J Pharm 2008; 359: 118–22.

13 Chen X, Cui L, Duan X, Ma B, Zhong D. Pharmacokinetics and metabolism of the flavonoid scutellarin in humans after a single oral administration. Drug Metab Dispos 2006; 34: 1345–52.

14 You HS, Dong YL, Xing JF, Zhang CL, Wang MY. Pharmacokinetic and tissue distribution study of scutellarin in rats. Zhongguo Zhong Yao Za Zhi 2007; 32: 1688–92.

15 Liu Q, Shi Y, Wang Y, Lu J, Cong W, Luo G, *et al*. Metabolism profile of scutellarin in urine following oral administration to rats by ultra performance liquid chromatography coupled to time-of-flight mass spectrometry. Talanta 2009; 80: 84–91.

16 Che QM, Chen Y, Pan LY, He H. Study on bile excretion of scutellarein. Zhongguo Zhong Yao Za Zhi 2006; 31: 1710–2.

17 Huang JM, Weng WY, Huang XB, Ji YH, Chen E. Pharmacokinetics of scutellarin and its aglycone conjugated metabolites in rats. Eur J Drug Metab Pharmacokinet 2005; 30: 165–70.

18 Ju WZ, Zhang J, Tan HS, Jiang M, Chen M, Xiong NN. Determination of scutellarin in human plasma by LC-MS method and its clinical pharmacokinetics in Chinese healthy volunteers. Chin J Clin Pharmacol Ther 2005; 10: 298–301.

19 Zhang JL, Che QM, Li SZ, Zhou TH. Study on metabolism of scutellarin in rats by HPLC-MS and HPLC-NMR. J Asian Nat Prod Res 2003; 5: 249–56.

20 Hao X, Cheng G, Yu JE, He Y, An F, Sun J, *et al*. Study on the role of hepatic first-pass elimination in the low oral bioavailability of scutellarin in rats. Pharmazie 2005; 60: 477–8.

21 Huang M, Ho PC. Identification of metabolites of meisoindigo in rat, pig and human liver microsomes by UFLC–MS/MS. Biochem Pharmacol 2009; 77: 1418–28.

22 Sun Y, Cheng ZY, Zheng QS. Drug and Statistics Software (DAS), version 2.0. Mathematical pharmacology professional. Am J Pharm Edu 2005; 69: 397–8.

23 Shi SL, Xu LY, Mao ZK, Li WL, Ye JY, Gao M. Study on physicochemical properties and influence factors on stability of breviscapine. Zhongguo Zhong Yao Za Zhi 2009; 34: 843–7.

24 Xing J, Chen XY, Zhong DF. Stability of baicalin in biological fluids *in vitro*. J Pharm Biomed Anal 2005; 39: 593–600.

25 Huang J, Li N, Yu Y, Weng W, Huang X. Determination of aglycone conjugated metabolites of scutellarin in rat plasma by HPLC. J Pharm Biomed Anal 2006; 40: 465–71.

26 Slikker WJ, Scallet AC, Doerge DR, Ferguson SA. Gender-based differences in rats after chronic dietary exposure to genistein. Int J Toxicol 2001; 20: 175–9.

27 Wang R, Zhou S, Mei Q, Yang Z, Zhang BE, Liu Z. Study on gender-based differences in pharmacokinetics of genistein. Chin Phar J 2005; 40: 1575–8.

28 Waxman DJ, Holloway MG. Sex differences in the expression of hepatic drug metabolizing enzymes. Mol Pharmacol 2009; 76: 215–28.

Original Article

Novel liver-specific cholic acid-cytarabine conjugates with potent antitumor activities: Synthesis and biological characterization

Dan-qi CHEN, Xin WANG, Lin CHEN, Jin-xue HE, Ze-hong MIAO, Jing-kang SHEN*

State Key Laboratory of Drug Research, Shanghai Institute of Materia Medica, Chinese Academy of Sciences, Shanghai 201203, China

Aim: Cytarabine is an efficient anticancer agent for acute myelogenous leukemia, but with short plasma half-life and rapid deamination to its inactive metabolite. The aim of this study was to design and synthesize novel cholic acid-cytarabine conjugates to improve its pharmacokinetic parameters.

Methods: The *in vitro* stability of novel cholic acid-cytarabine conjugates was investigated in simulated gastric and intestinal fluid, mouse blood and liver homogenate using HPLC. The portacaval samples of the conjugates were examined in male Sprague-Dawley rats using LC/MS, and *in vivo* distribution was examined in male Kunming mice using LC/MS. Antitumor activities were tested in HL60 cells using MTT assay.

Results: Cholic acid-cytarabine compounds with four different linkers were designed and synthesized. All the four cholic acid-cytarabine conjugates could release cytarabine when incubated with the simulated gastric and intestinal fluid, mouse blood and liver homogenate. The conjugates **6**, **12**, and **16** were present in the portacaval samples, whereas the conjugate **7** was not detected. The conjugates **6** and **16** showed high specificity in targeting the liver (liver target index 34.9 and 16.3, respectively) and good absorption *in vivo*, as compared with cytarabine. In cytarabine-sensitive HL60 cells, the conjugates **6**, **12**, and **16** retained potent antitumor activities.

Conclusion: Three novel cholic acid-cytarabine conjugates with good liver-targeting properties and absorption were obtained. Further optimization of the conjugates is needed in the future.

Keywords: cytarabine; cholic acid; liver; antitumor drug

Introduction

1-β-*D*-Arabinofuranosylcytosine (cytarabine, Ara-C) is an efficient anticancer agent for acute myelogenous leukemia[1, 2]. However, its usefulness is limited by its short plasma half-life and rapid deamination to the biologically inactive metabolite, 1-β-*D*-arabinofuranosyluracil (Ara-U) by cytidine deaminase[3]. Cytidine deaminase is a ubiquitous enzyme found in high concentrations in the intestine, liver, spleen, and kidneys[4]. When administered by iv, systemic elimination is biphasic with an initial plasma half-life ($t_{1/2\alpha}$) of 7–20 min and a terminal half-life ($t_{1/2\beta}$) of 2–3 h[5]. Cytarabine derivatives and conjugates have been designed with the intention of increasing its stability and lipophilicity as well as avoiding rate-limiting cytarabine phosphorylation while maintaining its biological

activity[6]. For example, ancitabine (cyclocytidine), enocitabine and fostabine have been used clinically in Japan (Figure 1)[7–9].

The conjugation of cytarabine through the formation of a bond with its amino group at the N^4 position may protect the amino group from deamination and change the pharmacokinetic parameters of the cytarabine because new molecules are often more lipophilic. Behenoyl-Ara-C (Enocitabine, **4**), one of the N^4-acyl derivatives of saturated fatty acids, has been found to be superior to its parent compound, cytarabine, likely because of the resistance to cytidine deaminase and the liberation of Ara-C over a period of time[8]. N^4-peptidyl-Ara-C, like *L*-valyl-Ara-C, was reported to increase cellular uptake of cytarabine through the involvement of various transporters[10]. Relatively high activity of cytarabine conjugates was achieved through the coupling of amino groups of cytarabine with carboxyl groups of polysaccharide molecules (*eg*, polygalacturonic acid (PGA) and carboxymethylated yeast beta-*D*-glucan (CMG)); the *in vitro* antileukemic activity of these

conjugates was comparable or higher than the activity of non-conjugated/free cytarabine combined with a polysaccharide[11] (Figure 2).

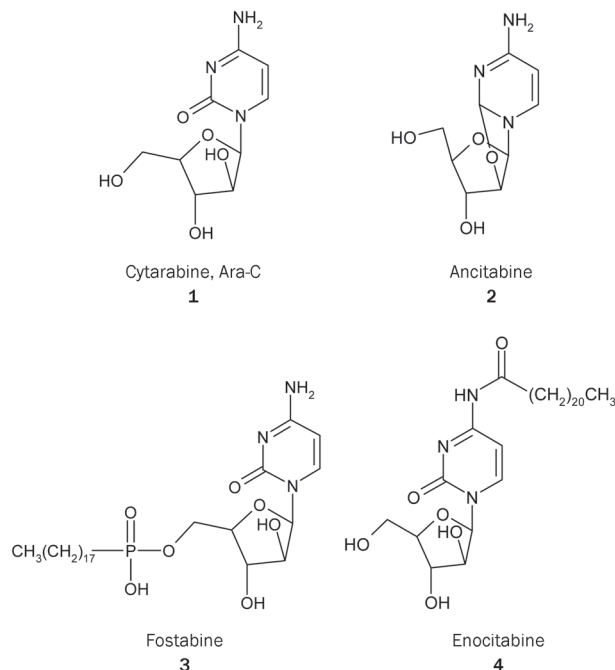The 5′-hydroxyl group is essential for the biological activity

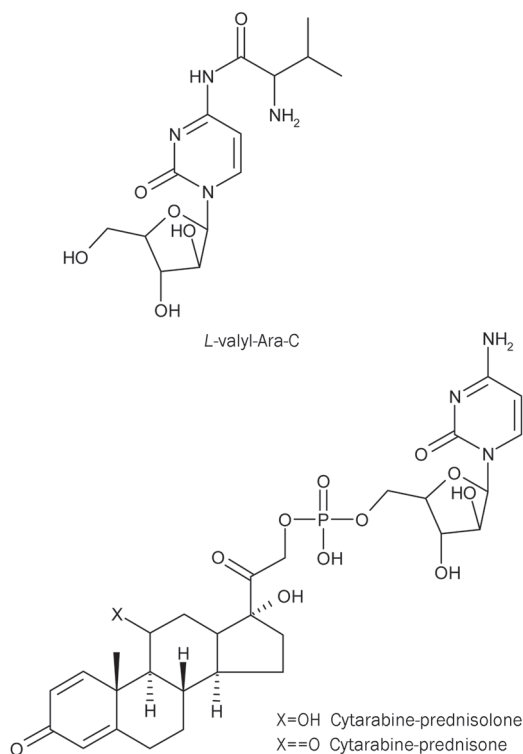
Figure 1. Cytarabine and its derivatives.

Figure 2. Conjugates of cytarabine with other moleculars.

of cytarabine because the activation of cytarabine to triphosphate occurs at this position; thus, if the 5′-hydroxyl group is blocked by conjugation, it would prevent its phosphorylation until free cytarabine is liberated, which would result in changed pharmacokinetic parameters. The attachment of a lipidic structure to cytarabine is usually achieved through the remains of phosphates as in Ara-CDP (arabinosylcytosine diphosphate), which is a normal cytarabine metabolite preceding activation to its active metabolite Ara-CTP. Steroid-cytarabine conjugates are small molecular conjugates that deserved attention. For example, conjugating cytarabine with prednisolone or prednisone by forming a phosphodiester bond at the 5′ position has produced increased activities in L1210 leukemia models[12].

Individual bile acids are endogenous markers of liver transport and synthesis function. The enterohepatic circulation of bile acid makes it an attractive tool in designing pharmacological hybrid molecules and prodrugs with the view of improving intestinal absorption, increasing the metabolic stability of pharmaceuticals, specifically targeting drugs to organs involved in enterohepatic circulation, and sustaining therapeutically reasonable systemic concentrations of active agents[13–19]. In light of these characteristics of bile acids, cholic acid was chosen to modify cytarabine to improve its *in vivo* function and to achieve improved liver-targeting, which would make it possible to use cytarabine for treating liver cancer.

Herein, the synthesis of several cholic acid-cytarabine conjugates is described with different linkers. *In vitro* stability, portacaval samples and *in vivo* distribution were tested to investigate the metabolic process. Furthermore, the antitumor activities of the conjugates were also tested.

## Materials and methods
Chemistry
Conjugate **6** consisted of cholic acid linked to cytarabine with a direct amide bond from cholic acid to cytarabine via ethyl chloroformate[20]. Cholic acid was linked to cytarabine with a direct ester bond in conjugate **7** and was synthesized via general conditions using dicyclohexylcarbodiimide and 4-dimethylaminopyridine (Scheme 1).

Conjugates **12** and **16** were designed to have a β-Alanine as the linker between cholic acid and cytarabine. The N-terminal of β-Alanine was attached to cholic acid with an amide bond, whereas the carboxyl group was linked to cytarabine via an ester bond or an amide bond to form **12** and **16**, respectively. As shown in Scheme 2, commercially available β-Alanine was directly converted to an ester by thionyl chloride and EtOH. The resulting ester was coupled to cholic acid through isobutyl chloroformate to yield **10**. After the hydrolysis of **10** by NaOH, compound **12** was then synthesized in similar manner as **7** using the corresponding acid, **11**. Cytarabine was first coupled to a Boc-protected β-Alanine to obtain **14**. After deprotection by HCl in EtOH, the resulting compound, **15**, was reacted with cholic acid to produce **16**.

The formation of the amide and ester bonds was determined by ¹H-NMR. The chemical shift, δ, of hydrogen on
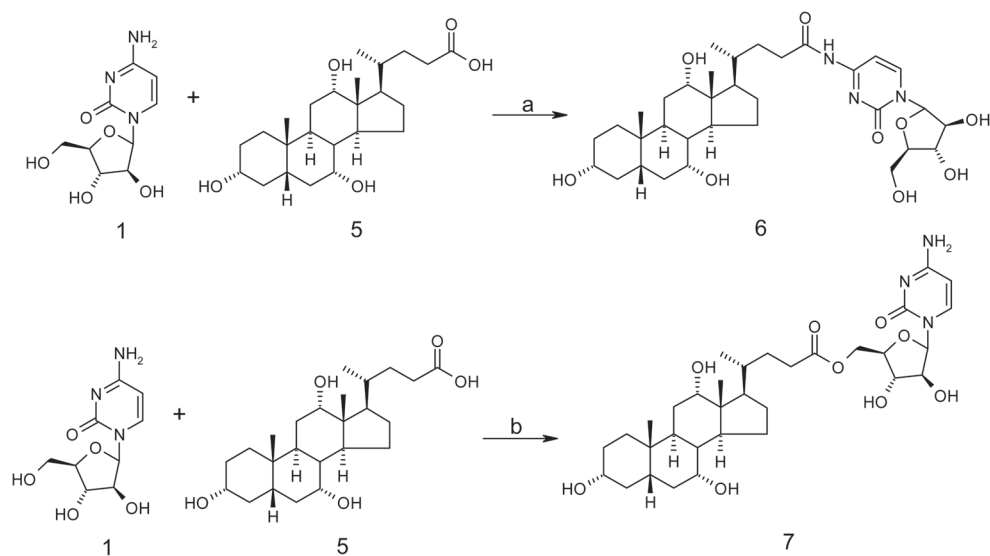
Scheme 1. Reagents and conditions: (a) ethyl chloroformate, triethylamine, *N,N*-dimethylformamide, -15 °C to RT; (b) dicyclohexylcarbodiimide, 4-dimethylaminopyridine, *N,N*-dimethylformamide.
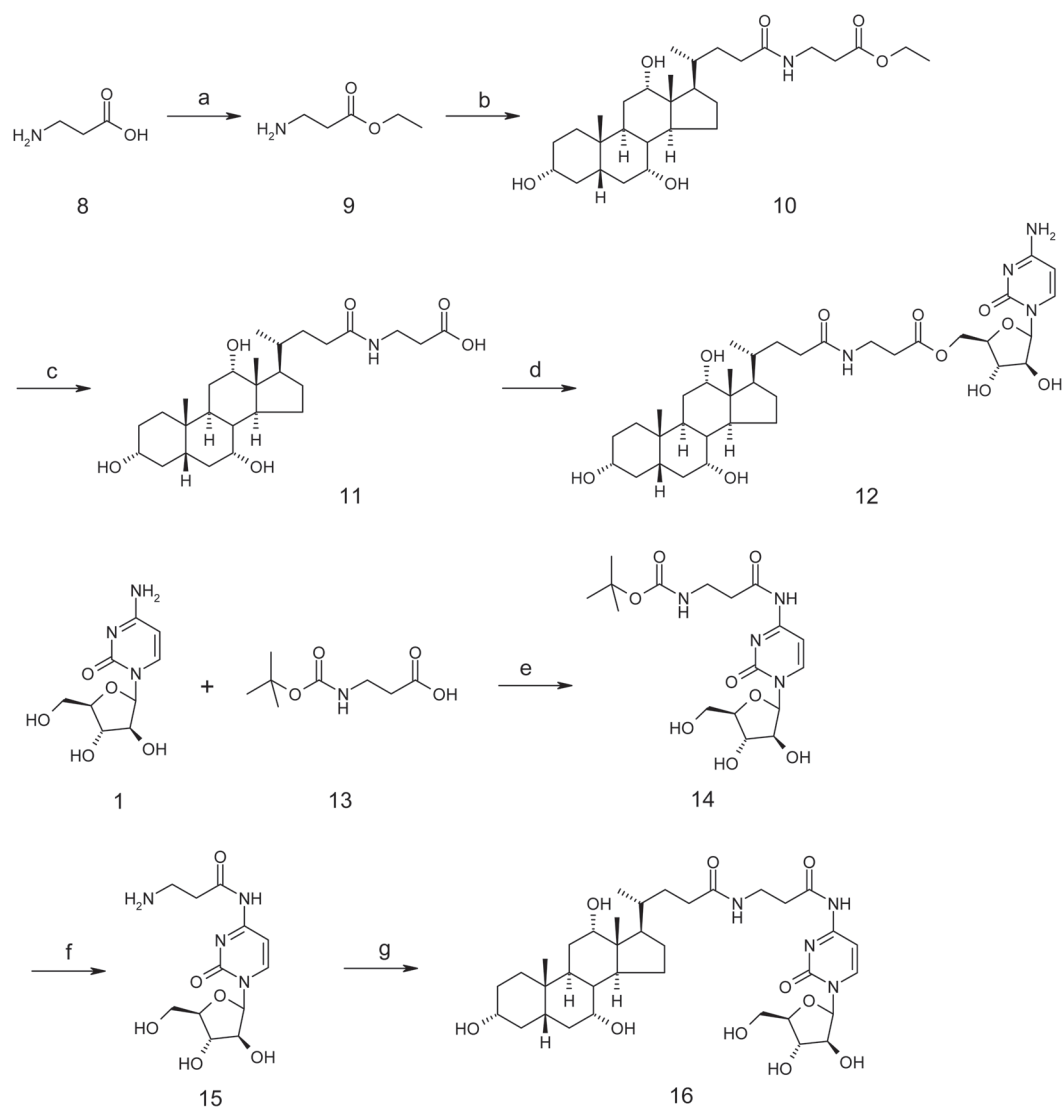
Scheme 2. Reagents and conditions: (a) thionyl chloride, EtOH; (b) **5**, isobutyl chloroformate, triethylamine, *N,N*-dimethylformamide, -15 °C to RT; (c) 10% NaOH, EtOH; (d) **1**, dicyclohexylcarbodiimide, 4-dimethylaminopyridine, *N,N*-dimethylformamide; (e) ethyl chloroformate, triethylamine, *N,N*-dimethylformamide, -15 °C to RT; (f) HCl in EtOH; (g) **5**, ethyl chloroformate, triethylamine, *N,N*-dimethylformamide, -15 °C to RT.

the 5-, 6-, and 5'-carbon of cytarabine was 6.0, 7.78, and 3.85, respectively. When N^4 was coupled with the carboxyl group of cholic acid (compounds **6** and **7**), δ of 5- and 6-hydrogen moved to 7.4 and 8.2, respectively; when the 5'-OH was coupled with the carboxyl group of cholic acid, δ of 5'-H shifted to 4.2 (Figure 3). Similar changes were observed in compounds **12** and **14**.
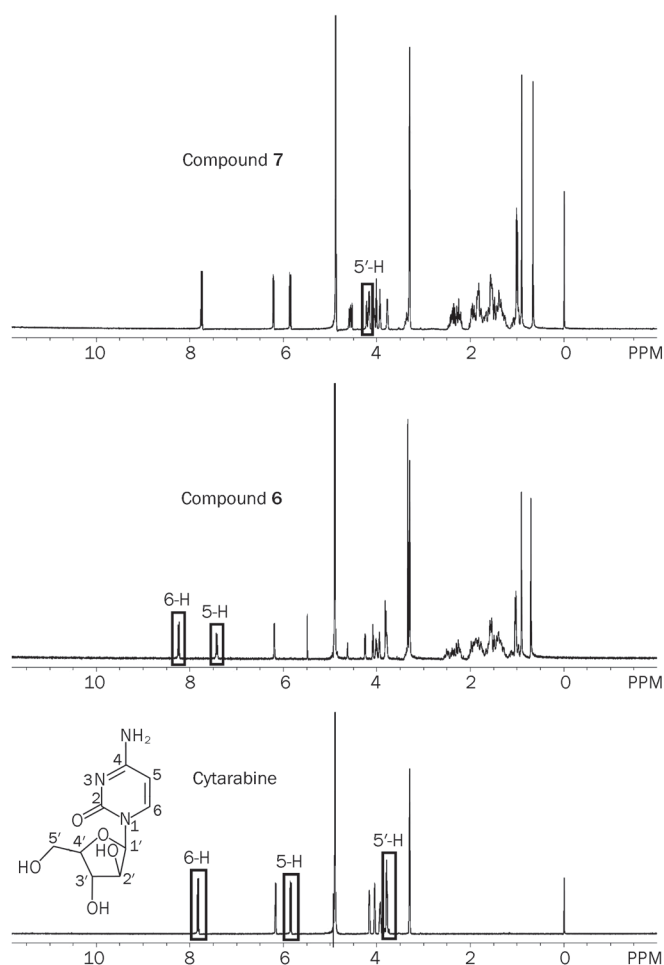

Figure 3. ^{1}H-NMR spectrum of cytarabine, compound **6** and **7**.

In vitro stability

Taking into account the possibility of the oral administration of the conjugates, the stability of all the newly synthesized compounds was tested in simulated gastric and intestinal fluids, mouse blood and liver homogenate. After incubation with the four matrixes, samples at different time points were subjected to HPLC to determine the extent of metabolism.

Simulated gastric and intestinal fluids were prepared according to the Chinese Pharmacopoeia. Mouse blood was collected, and heparin was added; the solution was then incubated at 37 °C. Mouse liver homogenate was prepared using a buffer containing 50 mmol/L HEPES (pH 7.4), 150 mmol/L NaCl, 10% glycerol, 1% Tween 20, 1.5 mmol/L $MgCl_2$, 10 mmol/L Na_3PO_4, 100 mmol/L NaF, and 2 mmol/L Na_3VO_4[21].

Cytarabine, **6**, **7**, **12**, and **16** were weighed (2 mg each), dissolved in 50 μL DMSO and added to an 800 μL matrix solution described above. The mixtures were incubated at 37 °C, and the samples were obtained at different time points (gastric and intestinal fluid: 0, 2, 5, and 24 h; blood and liver homogenate: 0, 1, 3, 5, and 24 h). All target compounds were analyzed using an HPLC system (HP1100) with UV-detection at 214 nm. The separation was performed using a ZORBAX SB-C_{18} (5 μm, 4.6 mm×150 mm) with a 5 mmol/L ammonium acetate solution/methanol gradient at a flow rate of 1.0 mL/min (column temperature was set to 35 °C).

Portacaval sampling

It has been reported that cytarabine deaminates rapidly in the liver[4]. To determine the forms of the conjugates after intestinal absorption and before reaching liver, portacaval blood samples were investigated by LC/MS after oral administration.

Four male Sprague-Dawley rats, weighing 200 to 230 g, were orally administered conjugates **6**, **7**, **12**, and **16** separately (each compound was equivalent to 50 mg/kg cytarabine). The compounds administered were prepared by dissolving the compounds in propanediol and diluting them with the same volume of 0.5% carboxyl methyl cellulose (CMC) to 35 mmol/L. The rats were anaesthetized by barbital and the abdominal cavity was opened. The portavacal vein was intubated and blood samples were collected at 0.25, 0.5, and 1 h. All of the samples were examined by LC-MS/MS. The analysis was performed using a LCQ Deca XP ion trap mass spectrometer (ThermoFinnigan, San Jose, CA, USA), an Atlantis analytical HILIC Silica column (2.1 mm×100 mm, 5 μm) from Waters (made in Ireland); a mixture of methanol, 5 mmol/L ammonium acetate solution, water and acetonitrile containing 0.1% acetic acid was used as the mobile phase [Mobile phases A and B consisted of methanol and 5 mmol/L ammomium acetate; Mobile phases C and D consisted of water and acetonitrile containing 0.1% acetic acid, respectively. Gradient chromatographic separation using mobile phases A, B, C, and D was as follows: 0 min (2% A, 5% B, and 93% D), 2.1 min (2% A, 5% B, and 93% D) , 2.5 min (2% A, 5% B, 60% D, and 33% C), 3.0 min (2% A, 5% B, 60% D, and 33%C), 3.5 min (2% A, 5% B, and 93% D) and finished at 6.5 min at a constant flow rate of 0.3 mL/min]. The MS/MS reactions selected to monitor cytarabine and Acyclovir (internal standard) were the transitions from m/z 244 → m/z 112 and m/z 226 → m/z 152 with collision energies of 32% and 30% of the instrumental maximum for MS^2 experiments, respectively.

In vivo distribution

Male Kunming mice, weighing 18 to 20 g, were administered cytarabine (50 mg/kg), compound **6** or **16** orally, which was equivalent to 50 mg/kg cytarabine. Blood and liver samples were collected at different time points. All of the samples were examined by LC/MS.

The liver target index was calculated by the following formula:

$$\text{Liver target index (LTI)} = \frac{\text{AUC}_{0-t} \text{ in liver}}{\text{AUC}_{0-t} \text{ in plasma}}$$

Normal, non-fasted male Kuming mice were administered ig with a dose of 50 mg/kg of cytarabine, 130 mg/kg of **6** and 145 mg/kg of **16**, respectively. At specific times after administration, mice were anesthetized, and blood was drawn. The liver was removed, rapidly frozen on crushed ice and then stored at -20 °C. The livers were slit, added to methanol with THU (final concentration of 0.4 mmol/L) and homogenized. The centrifugation was carried out at 3500 revolutions per minute and 4 °C for 5 min. A 100 µL aliquot of supernatant was added to 25 µL of the internal standard (Acyclovir) and 100 µL of acetonitrile and mixed by vortexing for 1 min. After centrifugation, the supernatant was transferred to a glass tube and evaporated until dry using an evaporator at 40 °C under a stream of nitrogen. The dried extract was then reconstituted in 100 µL of the mobile phase and a 20 µL aliquot was injected into the LC-MS/MS system for quantitative analysis.

Blood was added to THU (final concentration of 0.1 mmol/L) and chilled on crushed ice. The plasma was then separated by centrifugation (11 000 revolutions per minute, 4 °C), frozen and stored at -20 °C. The mouse plasma samples were prepared using the protein precipitation technique. A 100 µL aliquot of an acetonitrile solution containing 25 µL of internal standard (2 µg/mL, Acyclovir) was added to 25 µL of plasma, and mixed by vortexing for 1 min. After centrifugation, the supernatant was transferred to a glass tube and evaporated at 40 °C under a stream of nitrogen. The dried extract was then reconstituted in 100 µL of mobile phase, and a 20 µL aliquot was injected into the proposed LC-MS/MS system for quantitative analysis. The analysis was performed using a triple quadrupole mass spectrometer, TSQ Quantum Ultra (ThermoFinnigan, San Jose, CA, USA), equipped with an ESI source. Cytarabine and internal standard (IS) were analyzed by a Waters HILIC column (150 mm×2.1 mm id, 5 µm) and protected by a SecurityGuard C_{18} guard column (4 mm×3.0 mm id). A mixture of acetonitrile-10 mmol/L ammonium acetate-formic acid (90:10:0.1, *v/v/v*) was used as the mobile phase at a flow rate of 0.70 mL/min. The retention time of cytarabine was approximately 6.6 min. Compounds **6**, **16**, and IS were analyzed by a Venusil ASB-C_{18} column (150 mm×4.6 mm id, 5 µm) and protected by a SecurityGuard C_{18} guard column (4 mm×3.0 mm id). A mixture of acetonitrile-10 mmol/L ammonium acetate-formic acid (70:30:0.1, *v/v/v*) was used as the mobile phase at a flow-rate of 0.60 mL/min. The retention time of **6** and **16** was approximately 4 min. The quantification was performed using the selective reaction monitoring (SRM) mode to study parent → product ion (*m/z*) transitions for cytarabine (244 → 112 and 212), **6** (634 → 112, 337, and 502), **16** (705 → 426 and 573) and IS (227 → 163), respectively.

Antitumor activity

Compounds were tested for their cytotoxic effects against a leukemia HL60 cell line by methyl-thiazol-tetrozolium (MTT) assays[22]. Cells were treated with different concentrations of compounds for 72 h. At the end of the treatment, 20 µL of MTT (5 mg/mL) was added to each well and the plates were incubated at 37 °C for 4 h. Then "triplex solution" (10% SDS-5% isobutanol-HCl 12 mmol/L) was added, and the plates were incubated at 37 °C for 12–20 h. The *OD* value was read on a plate reader at 570 nm. The inhibition rate was calculated by the following equation: inhibition rate of proliferation (%)=(OD_{control}–$OD_{\text{experiment}}$)/OD_{control}×100%.

Results and discussion

The *in vitro* stability test showed that all of the cholic acid-cytarabine conjugates might release cytarabine when incubated with the four matrixes (Table 1). According to the results, gradual degradations of **6** and **16**, which contain amide bonds, were found in acid gastric fluid ($t_{1/2}$<8 h); released cytarabine was detected in the sample of conjugate **12** in mouse blood and liver homogenate ($t_{1/2}$>8 h). Conjugate **7**, which had cytarabine directly linking to cholic acid via an ester bond, was completely converted into cytarabine in mouse blood within one hour.

The conjugated forms of **6**, **12**, and **16** were observed in portacaval samples, among which **16** had the most obvious MS characteristic peak. A small amount of cytarabine was detected at one hour only after the administration of conjugate **12**. Neither the conjugate nor released cytarabine was observed when conjugate **7** was administered. The results showed that either conjugate **7** was not absorbed by the intestine or was metabolized to an unknown form (Figure 4).

Table 2 showed *in vivo* pharmacokinetics results of cytarabine, **6**, and **16**. The concentration of the compounds in the plasma, after the administration of cytarabine, reached their peaks at 0.5 h, and only trace amounts were left in the blood after 4 h. The $C_{\max}$ was 1.14 µg/mL. The $C_{\max}$, $T_{\max}$, and Auc_{0-t} of the livers were all lower than those of the plasma; additionally, the elimination rate in liver was found to be much faster (Figure 5A). The released cytarabine of conjugate **6** was observed in the plasma samples but not in the liver. The $C_{\max}$ of the conjugate in the plasma and liver were 0.091 and 3.25 µg/mL respectively, and 0.188 µg/mL for released cytarabine in plasma (Figure 5B). Conjugate **16** also released cytarabine *in vivo*. The $C_{\max}$ of the conjugate in plasma and liver were 0.826 and 14.868 µg/mL, whereas released cytarabine levels in plasma and liver were 0.097 and 0.455 µg/mL (Figure 5C), respectively. Although **12** was present in the portacaval samples, only a small amount of the conjugate form could be detected in the liver, and it was not found in plasma. Released cytarabine was not detected in the liver or plasma. Thus, data on conjugate **12** were not provided. According to the calculation of AUC_{0-t}, the liver targeting index was 0.17 for cytarabine, 34.9 for **6**, and 16.3 for **16**.

Both conjugates **6** and **16** showed good liver targeting compared to cytarabine. The LTI of **6** reached 34.9, which was 200 times more than cytarabine. The LTI of **16** also reached 16.3, and the $C_{\max}$ was 14.868 µg/mL, which demonstrated good absorption. The stability of the amide bond prevented the conjugates from degradation through oral absorption,

Table 1. Results of the *in vitro* stability test.

| Tested Samples		Simulated gastric fluid				Simulated intestinal fluid				Mouse blood					Mouse liver homogenate				
		0 h	2 h	5 h	24 h	0 h	2 h	5 h	24 h	0 h	1 h	3 h	5 h	24 h	0 h	1 h	3 h	5 h	24 h
Ara-C		100	100	100	100	100	100	100	100	100	100	100	100	100	100	100	100	100	66.89
6	6	100	84.51	50.71	34.30	100	100	100	100	100	100	100	100	100	100	95.15	91.74	91.40	87.88
	Ara-C	0	15.49	49.29	65.70	0	0	0	0	0	0	0	0	0	0	4.85	8.26	8.60	12.12
7	7	100	100	100	78.14	100	100	100	100	100	0	0	NT	NT	100	100	100	100	100
	Ara-C	0	0	0	21.86	0	0	0	0	0	100	100	NT	NT	0	0	0	0	0
12	12	100	100	100	90.66	100	100	100	80.40	100	81.66	62.84	55.07	16.87	100	82.51	NT	78.83	72.25
	Ara-C	0	0	0	9.34	0	0	0	19.60	0	18.34	37.16	44.93	83.13	0	17.49	NT	21.17	27.75
16	16	100	78.48	56.12	21.34	100	100	100	100	100	100	100	100	100	100	NT	100	100	83.29
	Ara-C	0	21.52	43.87	78.66	0	0	0	0	0	0	0	0	0	0	NT	0	0	16.71

NT: not tested.

Table 2. Pharmacokinetic parameters of cytarabine, **6** and **16** after oral administration to Kunming mice.[*]

Compound	Ingredients	Matrix	t_{max} h	C_{max} μg/mL	AUC_{0-t} μg·h/mL	$AUC_{0-\infty}$ μg·h/mL	MRT h	$t_{1/2}$ h	LTI
Cytarabine	Cytarabine	Plasma	0.50	1.14	1.94	1.95	1.22	0.55	0.17
		Liver	0.25	0.361	0.339	0.562	1.59	1.02	
6	6	Plasma	1.0	0.091	0.177	0.188	1.67	0.86	34.9
		Liver	1.0	3.25	6.17	6.22	1.50	0.79	
	Cytarabine	Plasma	0.50	0.188	0.371	0.532	3.00	1.97	–
		Liver[**]	–	–	–	–	–	–	
16	16	Plasma	0.083	0.826	0.472	0.491	2.79	3.47	16.3
		Liver	0.083	14.868	7.716	7.962	1.37	1.73	
	Cytarabine	Plasma	2.0	0.097	0.387	0.443	3.27	2.35	1.25
		Liver	0.5	0.455	0.485	0.542	1.61	1.45	

[*]: All the pharmacokinetic parameters were calculated using DAS 2.0.
[**]: Not detected.
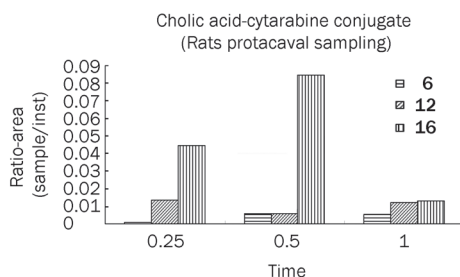
Figure 4. All the samples were detected by LC/MS. The ordinate represented the peak-area ratio of the conjugates to the internal standard (Acyclovir).

whereas *in vivo*, the bond could be metabolized, which made it an appropriate link. The C_{max} of **16** was approximately 4 times larger than conjugate **6**, which showed that using β-Alanine as the linker might increase cytarabine's absorption.

The antitumor activities of conjugates **6**, **16**, and **12** were tested on HL60 cells (Table 3). All three compounds showed potent antitumor activities on cytarabine-sensitive HL60 cells, which indicated that conjugating cytarabine to cholic acid allowed its antitumor activities to be retained.

In conclusion, a new series of cholic acid-cytarabine conjugates with antitumor activities have been described. Some of them exhibited excellent targeting of the liver and good absorption compared to cytarabine alone. Further studies will
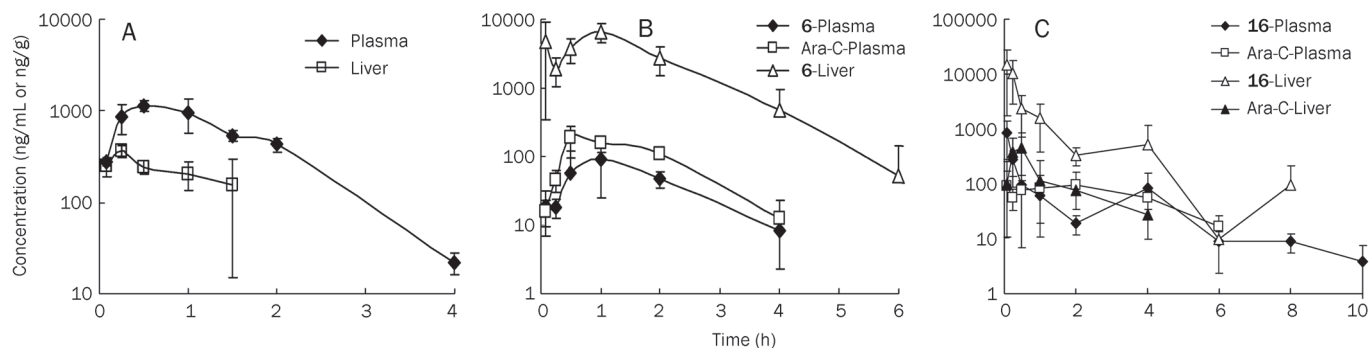
Figure 5. A) Plasma and liver concentrations following oral administration of Ara-C (50 mg/kg). B) Plasma and liver concentrations following oral administration of **6** (130 mg/kg). C) Plasma and liver concentrations following oral administration of **16** (145 mg/kg). Mean±SD. *n*=3.

Table 3. Antitumor activities on HL60 cells after 72 h. Mean±SD. *n*=3.

Compounds	IC$_{50}$ (µmol/L)
Cytarabine	0.19±0.13
6	2.09±1.23
12	0.99±0.65
16	2.96±2.03

continue by developing more conjugates with different linkers. Biological evaluations will be conducted on conjugates **6** and **16** in the near future.

Experimental

The reagents were purchased from Alfa-Aesar (Karlsruhe, Germany), Acros (Geel, Belgium) and Shanghai Chemical Reagent Company (Shanghai, China) and were used without further purification. Analytical thin-layer chromatography was performed on HSGF 254 (150–200 µm thickness; Yantai Huiyou Company, Yantai, Shandong, China). The IR spectra were recorded on a Nicolet Magna 750 FTIR spectrometer, and the ^{1}H NMR (300 MHz or 400 MHz) spectra were recorded on a Varian Mercury-300 or a 400 High Performance Digital FT-NMR using tetramethylsilane as an internal standard. The ^{13}C NMR (100 MHz) spectra were determined using a Varian Mercury-400 High Performance Digital FT-NMR. HPLC analysis was performed using a Gilson HPLC system with UV detection at 214 and 254 nm. UV scanning was performed on an Agilent HP1100. LC-MS spectra were obtained using a LCQ Deca XP ion trap mass spectrometer (ThermoFinnigan, San Jose, CA, USA). Accurate mass measurements were carried out on a Q-TOF ultima Globe mass spectrometer (Micromass, Manchester, UK).

(4R)-N-(1-((3S,4S,5R)-3,4-dihydroxy-5-(hydroxymethyl)tetrahydrofuran-2-yl)-2-oxo-1,2-dihydropyrimidin-4-yl)-4-((3R,5S,7R,12S,13R,14S,17R)-3,7,12-trihydroxy-10,13-dimethylhexadecahydro-1H-cyclopenta[a]phenanthren-17-yl)pentanamide (6)

Cholic acid (1.16 g, 3 mmol) and triethylamine (TEA, 0.39 mL, 3 mmol) were dissolved in dry *N,N*-dimethylformamide (DMF, 20 mL). The mixture was cooled to -15 °C, and ethyl chloroformate (0.31 mL, 3 mmol) was then added. After being stirred for 20 min, cytarabine (0.69 mg, 3 mmol) in 15 mL DMF was added the mixture, dropwise. The reaction mixture was stirred at -15 °C for 1 h and at RT overnight. The mixture was filtered, and the filtrate was concentrated. The residue was subjected to silica gel chromatography (dichloromethane/methanol, 10:1 to 4:1) to yield **6** as a white solid (1.34 g, 75%).

mp 190–192 °C.

IR (KBr cm^{-1}): 3396, 2933, 2868, 1711, 1649, 1566, 1493, 1389, 1315, 1117, 1076, 1047, 980, 951, 804, 609, 559.

^{1}H-NMR (CD$_3$OD, 300 MHz): δ 8.22 (d, 1H, J=7.6 Hz), 7.4 (d, 1H, J=7.1 Hz), 6.2 (d, 1H, J=3.8 Hz), 4.25 (m, 1H), 4.08 (t, 1H), 4.01 (m, 1H), 3.94 (s, 1H), 3.8 (m, 3H), 2.6–1.05 (m, 25H), 1.02 (d, 3H, J=6.2 Hz), 0.9 (s, 3H), 0.7 (s, 3H).

^{13}C NMR (100 MHz, d^6-DMSO) δ 174.5, 162.3, 154.7, 146.7, 94.5, 87.1, 85.3, 76.2, 74.7, 71.1, 70.6, 66.4, 61.1, 46.3, 45.8, 41.6, 41.5, 35.4, 35.3, 34.9, 34.5, 33.7, 31.0, 30.4, 28.6, 27.4, 26.3, 22.9, 22.7, 17.1, 12.4.

MS (ESI): *m/z* 634 (M+H)$^+$; HRMS calcd for C$_{33}$H$_{51}$N$_3$O$_9$Na: 656.3523 (M+Na)$^+$; Found: 656.3536.

(4R)-((2R,3S,4S)-5-(4-amino-2-oxopyrimidin-1(2H)-yl)-3,4-dihydroxytetrahydrofuran-2-yl)methyl-4-((3R,5S,7R,9S,10S,12S,13R,14S,17R)-3,7,12-trihydroxy-10,13-dimethylhexadecahydro-1H-cyclopenta[a]phenanthren-17-yl)pentanoate (7)

Cytarabine (1.46 g, 6 mmol) was dissolved in dry DMF (30 mL) and heated to 60 °C. Cholic acid (3.67 g, 9 mmol), dicyclohexylcarbodiimide (DCC, 1.79 g, 9 mmol) and 4-dimethylaminopyridine (DMAP, 109 mg, 0.9 mmol) were added. The mixture was cooled to RT and stirred for 2 d. Then, a second addition of cholic acid (3.67 g, 9 mmol), DCC (1.79 mg, 9 mmol) and DMAP (109 mg, 0.9 mmol) was made. The mixture was stirred continuously for 4 d. The reaction mixture was filtered, and the filtrate was concentrated. The residue was subjected to silica gel chromatography (dichloromethane/methanol, 15:1) to yield **7** as a white solid (310 mg, 10%).

mp 204–205 °C.

IR (KBr cm^{-1}): 3423, 2929, 2868, 1730, 1649, 1491, 1377, 1290, 1076, 1045, 795, 735, 609.

^{1}H-NMR (CD$_3$OD, 300 MHz): δ 7.76 (d, 1H, J=7.8 Hz), 6.22

(d, 1H, J=3.9 Hz), 5.86 (d, 1H, J=7.5 Hz), 4.57 (m, 1H), 4.20 (m, 2H), 4.07 (m, 1H), 4.01 (m, 1H), 3.94 (brs, 1H), 3.78 (d, 1H, J=2.8 Hz), 3.37 (m, 1H), 2.50–2.15 (m, 4H), 2.05–1.10 (m, 20H), 1.0 (d, 3H, J=6.5 Hz), 0.9 (s, 3H), 0.65 (s, 3H).

^{13}C NMR (100 MHz, CD$_3$OD) δ 176.2, 168.0, 158.6, 145.3, 95.3, 89.2, 84.8, 78.9, 76.8, 74.5, 73.3, 69.5, 65.3, 48.6, 48.0, 43.7, 43.5, 41.4, 41.0, 37.0, 36.4, 32.8, 32.6, 31.7, 30.1, 29.2, 28.4, 24.7, 23.7, 18.0, 13.4.

MS (ESI): *m/z* 634 (M+H)$^+$; HRMS calcd for C$_{33}$H$_{51}$N$_3$O$_9$Na: 656.3523 (M+Na)$^+$; Found: 656.3531.

Ethyl 3-((4R)-4-((3R,5S,7R,9S,10S,12S,13R,14S,17R)-3,7,12-trihydroxy-10,13-dimethylhexadecahydro-1H-cyclopenta[a]phenanthren-17-yl)pentanamido)propanoate (10)

Thionyl chloride (20 mL) was added dropwise to anhydrous ethanol (80 mL), and the temperature did not exceed 25 °C. β-Alanine (9 g, 0.1 mol) was then added. After stirring at 50 °C for 3 h, β-Alanine dissolved. The mixture was stirred at RT overnight. The solvent was evaporated and ether was added to the residue. A white solid was formed, filtered and then dried (Na$_2$SO$_4$) to yield 16 g **9** (100%). Cholic acid (5.57 g, 13.6 mmol) and triethylamine (TEA, 1.92 mL, 15 mmol) were dissolved in dry DMF (45 mL). The mixture was cooled to -15 °C, and isobutyl chloroformate (1.78 mL, 17 mmol) was added. After stirring for 5 min, **9** (2.3 g, 20 mmol) and TEA (3.84 mL, 30 mmol) were combined with 10 mL DMF, which was added dropwise. The reaction mixture was stirred at -15 °C for 1 h and at RT overnight. The mixture was filtered, and the filtration was concentrated. The residue was dissolved in ethyl acetate and washed with water 4 times (water/ethyl acetate, 1:2). The organic layer was combined and washed with 0.5 mol/L NaOH, 0.5 mol/L HCl and brine; it was then dried and concentrated to yield **10** as a white solid 5.67 g (87%).

^{1}H-NMR (CD$_3$OD, 300 MHz): δ 4.12 (m, 2H), 3.94 (brs, 1H), 3.78 (brs, 1H), 3.4 (m, 3H), 2.5 (t, 2H, J=6.6 Hz), 2.4–1.2 (m, 24H), 1.24 (t, 3H, J=7.2 Hz), 1.0 (d, 3H, J=6.4 Hz), 0.9 (s, 3H), 0.7 (s, 3H).

MS (ESI): *m/z* 1015 (2M+H)$^+$.

3-((4R)-4-((3R,5S,7R,9S,10S,12S,13R,14S,17R)-3,7,12-trihydroxy-10,13-dimethylhexadecahydro-1H-cyclopenta[a]phenanthren-17-yl)pentanamido)propanoic acid (11)

Compound **10** (3.9 g, 7.7 mmol) was dissolved in ethanol (30 mL) and added to a solution of 10% NaOH (30 mL). The reaction mixture was stirred at RT overnight and then poured into ice water and acidified with 1 mol/L HCl, which was extracted with ethyl acetate 3 times. The organic layer was combined and washed with brine, dried (Na$_2$SO$_4$) and concentrated to yield **11** as a white solid 3.2 g (87%).

^{1}H-NMR (CD$_3$OD, 300 MHz): δ 3.95 (brs, 1H), 3.8 (brs, 1H), 3.4 (t, 3H, J=7 Hz), 2.5 (t, 2H, J=6.8 Hz), 2.4–1.05 (m, 24H), 1.0 (d, 3H, J=6.1 Hz), 0.9 (s, 3H), 0.7 (s, 3H).

MS (ESI): *m/z* 959 (2M+H)$^+$.

((2R,3S,4S)-5-(4-amino-2-oxopyrimidin-1(2H)-yl)-3,4-dihydroxytetrahydrofuran-2-yl)methyl- 3-((4R)-4-((3R,5S,7R,9S,10S,12S,

13R,14S,17R)-3,7,12-trihydroxy-10,13-dimethylhexadecahydro-1H-cyclopenta[a]phenanthren-17-yl)pentanamido)propanoate (12)

Cytarabine (324 mg, 1.33 mmol) was dissolved in dry DMF (12 mL) and heated to 60 °C. Compound **11** (0.96 g, 2 mmol), DCC (453 mg, 2.2 mmol) and DMAP (24.4 mg, 0.2 mmol) were then added. The mixture was cooled to RT and stirred for 2 d. Another addition of **11** (0.96 g, 2 mmol), DCC (453 mg, 2.2 mmol) and DMAP (24.4 mg, 0.2 mmol) was made. The mixture continued to stir for 2 d and was then filtered. The filtration was concentrated, and the residue was subjected to silica gel chromatography (dichloromethane/methanol, 15:1) to yield **12** as a white solid 200 mg (15%).

mp 174–176 °C.

^{1}H-NMR (CD$_3$OD, 300 MHz): δ 7.72 (d, 1H, J=7.4 Hz), 6.20 (d, 1H, J=3.5 Hz), 5.87 (d, 1H, J=7.6 Hz), 4.51 (m, 1H), 4.27 (m, 1H), 4.18 (m, 1H), 4.08 (m, 1H), 4.02 (m, 1H), 3.93 (brs, 1H), 3.78 (m, 1H), 3.44 (t, 2H, J=6.9 Hz), 2.58 (t, 2H, J=6.3 Hz), 2.4–1.1 (m, 25H), 0.99 (d, 3H, J=6.4 Hz), 0.90 (s, 3H), 0.69 (s, 3H).

^{13}C NMR (100 MHz, CD$_3$OD) δ 177.5, 173.6, 168.0, 158.6, 145.0, 95.3, 89.2, 84.6, 79.0, 76.8, 74.5, 73.3, 69.5, 65.6, 55.3, 48.4, 47.9, 43.6, 43.4, 41.5, 40.9, 37.3, 36.9, 36.8, 36.4, 36.3, 35.4, 34.5, 33.7, 31.6, 30.0, 29.2, 28.3, 24.7, 23.7, 18.2, 13.5.

MS (ESI): *m/z* 705 (M+H)$^+$; HRMS calcd for C$_{36}$H$_{56}$N$_4$O$_{10}$Na: 727.3894 (M+Na)$^+$; Found: 727.3913.

tert-butyl 3-(1-((3S,4S,5R)-3,4-dihydroxy-5-(hydroxymethyl)tetrahydrofuran-2-yl)-2-oxo-1,2-dihydropyrimidin-4-ylamino)-3-oxopropylcarbamate (14)

Boc-β-Ala-OH (945 mg, 5 mmol) and triethylamine (0.6 mL, 5 mmol) were dissolved in dry DMF (30 mL). The mixture was cooled to -15 °C, and ethyl chloroformate (0.48 mL, 5 mmol) was added. After stirring for 30 min, cytarabine (1.22 g, 5 mmol) in 10 mL DMF was added dropwise to the mixture. The reaction mixture was stirred at -15 °C for 30 min and then at RT overnight. The reaction mixture was filtered, and the filtration was concentrated and subjected to silica gel chromatography (dichloromethane/methanol, 20:1) to yield **14** as a white solid (1.7 g, 82%).

^{1}H-NMR (CD$_3$OD, 300 MHz): δ 8.24 (d, 1H, J=7.5 Hz), 7.42 (d, 1H, J=7.5 Hz), 6.19 (d, 1H, J=3.9 Hz), 4.25 (m, 1H), 4.08 (t, 1H, J=2.4 Hz), 4.01 (m, 1H), 3.81 (d, 2H, J=4.8 Hz), 3.36 (t, 2H, J=6.6 Hz), 2.62 (t, 2H, J=6.3 Hz), 1.41 (s, 9H).

MS (ESI): *m/z* 415 (M+H)$^+$.

(4R)-N-(3-(1-((3S,4S,5R)-3,4-dihydroxy-5-(hydroxymethyl)tetrahydrofuran-2-yl)-2-oxo-1,2-dihydropyrimidin-4-ylamino)-3-oxopropyl)-4-((3R,5S,7R,9S,10S,12S,13R,14S,17R)-3,7,12-trihydroxy-10,13-dimethylhexadecahydro-1H-cyclopenta[a]phenanthren-17-yl)pentanamide (16)

Compound **14** (700 mg, 1.7 mmol) was dissolved in saturated HCl in ethanol (5 mL) and stirred at RT overnight. The solvent was evaporated and methanol (10 mL) was added to the residue then stirred for 1 h. The solid was filtered and washed with methanol. The white solid was dried, and the crude product **15** (400 mg) was obtained, which was used in

the next step without purification.

Cholic acid (408 mg, 1 mmol) and triethylamine (0.12 mL, 1 mmol) were dissolved in dry DMF (6 mL). The mixture was cooled to -15 $^{\circ}$C, and ethyl chloroformate (0.1 mL, 1 mmol) was added. After stirring for 20 min, compound **15** (351 mg, 1.1 mmol) was added to the mixture by a dropwise addition in 5 mL DMF. The reaction mixture was stirred at -15 $^{\circ}$C for 30 min and at RT overnight. The reaction mixture was filtered and concentrated. Subsequently, the residue was subjected to silica gel chromatography (dichloromethane/methanol, 20:1 to 5:1) to yield **16** as a white solid (300 mg, total yield: 82%).

mp 178–180 $^{\circ}$C.

^{1}H-NMR (CD$_3$OD, 300 MHz): δ 8.24 (d, 1H, J=7.8 Hz), 7.46 (d, 1H, J=7.7 Hz), 6.19 (d, 1H, J=4.1 Hz), 4.28 (m, 1H), 4.09 (m, 1H), 4.01 (m, 1H), 3.89 (s, 1H), 3.8 (m, 3H), 3.47 (t, 2H, J=6.4 Hz), 2.66 (t, 2H, J=6.2 Hz), 2.4-1.01 (m, 25H), 0.98 (d, 3H, J=6.3 Hz), 0.9 (s, 1H), 0.65 (s, 1H).

^{13}C NMR (100 MHz, d^6-DMSO) δ 172.9, 172.2, 162.1, 154.6, 146.7, 94.5, 87.1, 85.8, 76.2, 74.6, 71.1, 70.5, 66.4, 61.1, 46.2, 45.8, 41.6, 41.4, 36.5, 35.4, 35.2, 34.9, 34.5, 32.5, 31.8, 30.8, 30.4, 28.5, 27.4, 26.3, 22.9,22.7, 17.2, 12.4.

MS (ESI): *m/z* 705 (M+H)$^+$; HRMS calcd for C$_{36}$H$_{56}$N$_4$O$_{10}$Na: 727.3894 (M+Na)$^+$; Found: 727.3898.

Acknowledgements

Author contribution

Jing-kang SHEN and Dan-qi CHEN designed research; Dan-qi CHEN, Xin WANG, Lin CHEN, Jin-xue HE and Ze-hong MIAO performed research; Dan-qi CHEN and Xin WANG contributed new analytical tools and reagents; Dan-qi CHEN and Xin WANG analyzed data; and Dan-qi CHEN wrote the paper.

References

1   Pallavicini MG. Cytosine arabinoside: Molecular, pharmacokinetic and cytokinetic considerations. Pharmacol Ther 1984; 25: 207–38.

2   Rustum M, Raymakers RA. 1-β-Arabinofuranosylcytosine in therapy of leukemia: Preclinical and clinical overview. Pharmacol Ther 1993; 56: 307–21.

3   Beumer JH, Eiseman JL, Parise RA, Florian Jr JA, Joseph E, D'Argenio DZ, *et al*. Plasma pharmacokinetics and oral bioavailability of 3,4,5,6-tetrahydrouridine, a cytidine deaminase inhibitor in mice. Cancer Chemother Pharmacol 2008; 62: 457–64.

4   Hsi D, Ho W. Distribution of kinase and deaminase of 1-β-*D*-Arabino-furanosylcytosine in tissue of man and mouse. Cancer Res 1973; 33: 2816–20.

5   Hamada A, Kawaguchi T, Nakano M. Clinical pharmacokinetics of cytarabine formulations. Clin Pharmacokinet 2002; 41: 705–18.

6   Novotny L, Rauko P. Cytarabine conjugates with biologically active molecules and their potential anticancer activity. Neoplasma 2009; 56: 177–86.

7   Miller LP, Pyesmany AF, Wolff LJ, Rogers PCJ, Siegel SE, Wells RJ, *et al*. Successful reinduction therapy with amsacrine and cyclocytidine in acute nonlymphoblastic leukemia in children — A report from the childrens cancer study-group. Cancer 1991; 67: 2235–40.

8   Ueda T, Nakamura T, Ando S, Kagawa D, Sasada M, Uchino H, *et al*. Pharmacokinetics of *N*^{4}-Behenoyl-1-β-*D*-arabinofuranosylcytosine in patients with acute leukemia. Cancer Res 1983; 43: 3412–6.

9   Rosti G, Bonifazi F, Trabacchi E, Vivo A, BAssi S, Martinelli G, *et al*. A phase II study of α-interferon and oral arabinosyl cytosine (YNK01) in chronic myeloid leukemia. Leukemia 2003; 17: 554–9.

10 Cheon EP, Hong JH, Han HK. Enhanced cellular uptake of Ara-C via a peptidomimetic prodrug, *L*-valyl-Ara-C in Caco-2 cells. J Pharm Pharmacol 2006; 58: 927–32.

11 Kery V, Novotny L, Tihlarik K, Haplová J, Kacuráková M, Sandula J, *et al*. Preparation, properties and antileukemic activity of arabinosylcytosine polysaccharide conjugates. Int J Biochem 1990; 22: 1203–7.

12 Hong CI, Nechaev A, West CR. Nucleoside conjugates as potential antitumor agents. 2. Synthesis and biological activity of 1-(beta-*D*-arabinofuranosyl)cytosine conjugates of prednisolone and prednisone. J Med Chem 1979; 22: 1428–32.

13 Sievanen E. Exploitation of bile acid transport systems in prodrug design. Molecules 2007; 12: 1859–89.

14 Enhsen A, Kramer W, Wess G. Bile acids in drug discovery. Drug Discov Today 1998; 3: 409–18.

15 Tolle-Sander S, Lentz KA, Maeda DY, Coop A, Polli JE. Increased acyclovir oral bioavailability via a bile acid conjugate. Mol Pharm 2004; 1: 40–8.

16 Geldern TW, Tu N, Kym PR, Link JT, Jae H, Lai C, *et al*. Liver-selective glucocorticoid antagonists: A novel treatment for type 2 diabetes. J Med Chem 2004; 47: 4213–30.

17 Gabano E, Ravera M, Osella D. The drug targeting and delivery approach applied to Pt-Antitumour complexes. A coordination point of view. Curr Med Chem 2009; 16: 4544–80.

18 Jurcek O, Wimmer Z, Svobodova H, Bennettova B, Kolehmainen E, Drasar P. Preparation and preliminary biological screening of cholic acid-juvenoid conjugates. Steroids 2009; 74: 779–85.

19 Rohacova J, Marin ML, Martinez-Romero A, Diaz L, O'Connor JE, Gomez-Lechon MJ, *et al*. Fluorescent benzofurazan-cholic acid conjugates for *in vitro* assessment of bile acid uptake and its modulation by drugs. ChemMedChem 2009; 4: 466–72.

20 Hu P, Hou S, Jin H, Zhang J, Wang L. Synthesis and stability of bile acid conjugate lamivudine as a liver target prodrug. Central South Pharmacy 2005; 3: 13–5.

21 Ju J, Gitcho MA, Casmaer CA, Patil PB, Han D, Spencer SA, *et al*. Potentiation of insulin-stimulated glucose transport by the AMP-activated protein kinase. Am J Physiol Cell Physiol 2007; 292: 564–72.

22 Qing C, Miao ZH, Tong LJ, Zhang JS, Ding J. Actinomycin D inhibiting K562 cell apoptosis elicited by salvicine but not decreasing its cytotoxicity. Acta Pharmacol Sin 2003; 24: 415–21.